DESIGN, FABRICATION AND GEOMETRIC OPTIMIZATION OF GRAPHENE ELECTRODES FOR ELECTROCHEMICAL DETECTION

A Dissertation

Presented to the Faculty of the Graduate School

Of Cornell University

In Partial Fulfillment of the Requirements for the Degree of

Doctor of Philosophy

By

Nini L. Munoz

August 2014

© 2014 Nini L. Munoz

DESIGN, FABRICATION AND GEOMETRIC OPTIMIZATION OF GRAPHENE ELECTRODES FOR ELECTROCHEMICAL DETECTION

Nini L Munoz, Ph. D.

Cornell University 2014

Graphene has gained much attention as a biosensing material since its discovery and characterization due to its highly sensitive electronic properties. Reported work on graphene as a biological sensor has focused on solution-gated graphene transistors (SGGFETs) that can measure the perturbed channel conductivity in response to environmental changes in the proximity of the graphene surface. Electrodes present a simpler method of biological detection, both from the operation and the fabrication standpoint. Investigation of graphene's electrochemical properties has reported higher electron transfer kinetics occurring at the edges than at the basal plane of the carbon allotrope. Yet, inconsistencies in sample preparation impede an accurate comparison of electrode performance.

This thesis examines the fabrication and characterization of graphene microelectrode arrays made with a variety of graphitic materials that exhibit differences in the number of layers, domain size, defects and substrate. We examine, for the first time, the electrochemical properties of Van der Waals CVD graphene grown on sapphire substrates and electrode arrays made on epitaxial graphene grown on silicon carbide. We find no significant performance differences with mono-, bi- and multilayer graphene, but do observe microelectrode edge effects becoming more dominant in multilayer devices as they are scaled down. CVD graphene on sapphire, with domain sizes as small as 100-200 nm, show higher sensitivity and epitaxial electrodes display the lowest detection limit (1μM) and fastest electron transfer kinetics, with the latter presumed to be

effect of the high degree of corrugation in the material and consistent with reports that higher curvature leads to faster kinetics [1]. To further examine the effect of the edges, we patterned electrodes of the same area varying only the perimeter. For clean electrodes, the perimeter to area ratio had little effect on the electrode sensitivity. However, after exposure to a low-power 30-second ozone plasma, the electrode sensitivity and electron kinetics improved, increasing by almost by two-fold with increasing electrode length. This result is consistent with the graphene edges becoming more electroactive through functionalization and result implies that graphene electrode sensitivity can be increased by functionalization and optimization of the electrode geometry.

BIOGRAPHICAL SKETCH

Nini Lucia Muñoz was born and raised in Barranquilla, Colombia by Alberto Muñoz and Aracely Perez. As a child and young adult, she enjoyed math and the applied sciences, becoming a math Olympiad at age 9, and taking the national championship by age 13. She graduated first in her class at Colegio Karl C. Parrish and received a scholarship to attend Cornell University in 2001, where she graduated with a Bachelor's of Science in Electrical and Computer Engineering in 2005. She went on to pursue a Master of Engineering and quickly transitioned into the Ph. D program at Cornell. During her graduate career she became the instructor and assistant instructor for a wide range of courses, ranging from Microelectronics and Nanofabrication, all the way to Power Switching electronics, circuit design and robotics. Her graduate studies initially focused on CMOS-based sensors, but she ultimately transitioned into graphene bioelectronics, under the guidance of Dr. Michael Spencer. In his group, she fostered collaborations and friendships that defined her graduate career. Still as a graduate student, she took a job as a full-time intern for Applied Materials, and for about the last 17 months of her doctorate, worked while studying in Massachusetts, where she now resides. The challenges of such lifestyle proved key in overcoming any self-doubt and pushing her own academic research forward.

To my mother, who always reminded me that my education was the best thing she could ever give to me.

ACKNOWLEDGMENTS

As one completes such phase of an academic career, it is hard to not think of the people that have played a fundamental part of one's life as a graduate student. One's own work is important and mostly, self-driven, but, in a way, it is also the result of the contribution, both personal and professional, of friends, family, peers and mentors. During this time of growth and understanding, newfound knowledge, reprioritization of values and redefining of the self, I have been immensely blessed to have a strong support network to advise me, guide me or sometimes just celebrate life's highs and lows with me. The journey has not been easy but it has been worth it, particularly because of the people I have encountered and from whom I have learned valuable and unforgettable lessons about tolerance, responsibility, integrity, friendship, comprehensive research, and, about myself.

I would first like to express indebted gratitude to my parents, who never shunt my ideas, as silly as they were. I used to pull off these crazy projects while in school and not once did they stop nor tell me it could not be done. They believed in me and I pushed forward academically. My father taught me to be resourceful and have no expectations, while my mother taught me the importance of receiving an education, of being kind, remaining humble and most importantly, the importance of treating each and every single person as my equal, regardless of their background. I too have an amazing brother that took care of me. I want him to know that I love him very much, even though sometimes I have to give him tough love. I hope he continues to grow and pursue the things he loves the most. I would like to thank my aunts, who have been like a mother since I was born. Their presence and support have proven invaluable and irreplaceable in my own upbringing and performance. I lost my mother at a young age, but I had these amazing women to look after me, especially when I was at my worst. I hope that as I become my best, I can be there for them as they were for me. Nini and Martha have made my

life substantially better and I really don't know what course it would have taken without them. I am their daughter as much as I am my mother's and I love them both beyond what words can express here. My uncles, Ernesto and Rafael, have also been key figures in my development and growth, and I take this opportunity to tell them that I love them and am grateful for their unconditional love and support throughout the years. I want Ema Cecilia and Lucero, my mother's lifelong friends and kind, beautiful human beings, to know that I am blessed for them stepping in to watch out for me as my own mother would have done.

I would like to thank my faculty committee and group mates for always being so supportive and ubiquitous in my academic development. In particular, I want to thank Dr. Michael Spencer, who has proven to be more than an adviser and mentor. He has been an unconditional friend. I had so much self-doubt when I joined his group and he believed in me, from the very beginning. Soon enough I started believing in myself. My thesis work would not have taken off without him and I will be forever grateful. Professor Hector Abruña also deserves much credit in the work presented today. I enlisted in a field outside my own and. I had to learn new things to understand my results. He patiently answered every question I had (promptly too!). Had it not been for his insights it would have been much harder to put together the results presented in this dissertation. Thank you. Professor Carl Batt helped me make the right decisions, especially at a time when I was transitioning from one group to the next. Thank you for always listening, providing feedback and making recommendations to further improve my work. Professor Al Molnar's critiques were critical in getting me through the rough patches of my dissertation. He pushed me in the right direction so I could present my work and explain it more coherently. I appreciate his constant feedback and criticism. I grew as a researcher because of them and want to express a sincere thank you to him for it. I would also like to express many thanks to Jim Turner, who was key in the funding and development of this project. I would also like to thank Bruce Johnson, Wolfgang Sachse and Bruce Land for providing continuous mentorship through both my graduate and undergraduate careers at Cornell. They are a strong addition to the Cornell faculty and I feel

blessed to have met them and learned from them. My group mates Hussain, Shriram, Joon, Dorr, Jeff and Brian provided help and moral support as I was introduced into graphene electronics. They were there to assist me with cleanroom feedback, good questions and sometimes, just a shoulder to cry on. Life got tough and they were there for me as brothers and colleagues. Hussain is one of the most amazing gentlemen I have been lucky to meet. I hope nothing but the best for him and I look forward to spending more time together when time allows. Lastly, I want to thank Nicole Ritzert. She was my collaborator in the chemistry department. There was so much I did not know when I started this project and she continued to help me, answering questions and helping me get a dedicated setup for my experiments. I hope our paths run across each other in the future. She too will be graduating this year, is a phenomenal researcher and an outstanding human being. I want to wish her the best of luck in years to come.

While my immediate family is rather short, I have had the opportunity to foster a sense of community amongst my friendships and would like to mention those close friends who have seen me grow, often been patient with me and provided guidance, understanding, laughter or sometimes, just listened. I would like to thank Alex Cerruti, my closest friend from Cornell, for being there for me when I most needed a friend. Our memories together have been the best and through my interaction with him I have learned a significant amount about myself, others and friendship. I love him very much. Zhana and Paul: these two were there for me when I was at my worst. I only hope I can be nothing but my best for them. They are like a sister and a brother and I hope we continue to foster our friendship for many years. The latter has taught me about tolerance, patience and most importantly, the immense value that differences amongst each other contribute to the quality of our lives. I want to thank Timothy and Jeff for always making me feel I was part of a home. It was often hard to be so far away from my own family and they shared theirs with me. Their love and affection nurtured my self-confidence in more ways I have ever told them. To Farah, my soul mate and roommate, I want her to know our friendship goes for the long haul. I want to thank her for always bringing such positive energy and insights into my life.

Kate Brunick and I have unfinished stories. I am looking forward to more adventures with her. I am so glad we met. She is strong, confident, sexy and just one of a kind. Sarah Xu is an angel in disguise and I hold her very near in my heart. I hope I get to see her in Portland soon. To my friends in Ithaca, San Francisco and New York: Archit, Sara, Hugh, Lee, Sara Keen, Prantik, Andre, Ramon, Jason, Peter, Remy, Avana, Nima, Petko, Roland, Parin, Andrew and Robert – I want them to know that they made it being here so much better. I will miss them all and will always try to find an excuse to come back to see them. My new friends, Rafael Escalona and Lisa (and Curby), are one of a kind and I have a feeling there is a long future ahead for our friendship. Let's get ready for Detroit! Meenakshi is another close friend and admirable human being. He is also one of the smartest people I know. I send out much love to him and hope we can continue to be good friends for many years.

I had the opportunity of meeting wonderful people in the Boston area as well. Dee DeOliveira is my closest friend. We have had our ups and downs, but we stick together and grow together. I love her so much. She is like my big sister and I am her munchkin. I also feel blessed to have met Celia. We have not spent much time together lately but I will soon remedy that. I admire her persistence towards self-improvement and her positive outlook on everything. Alisha Quitt's emotional maturity is humbling. I want to thank her for always being so level-headed, charismatic and all-around fabulous. I want Erin Moore to know she is chosen. She should feel blessed for the changes life has bestowed upon her as they will make her life better. Remember, growth comes from change and when things bother us, it's because we are making them a reflection of ourselves. I have seen her grow so much this last year and know she is strong and wonderful. I am glad we have remained friends. I want Cheryl Blauth to know we need more runs and time together. We will have both. Bree and Lara bring so much positivity and excitement it would be hard not to mention them here. I want to thank them for their vibrant, outgoing and all-around fun nature. Lastly, I'd like to reach out to my newest friend Katie Giblin. She is a role model. Strong, positive, beautiful and did I mention, a neurology resident?

She exemplifies the ultimate work-life balance and in our short time as friends, has proven to be a loyal, outstanding and devoted individual. I look forward to many more well-spent times together.

I want to thank all the technical staff that provided me support and assistance throughout my graduate studies. Garry and Ed made my cleanroom days (and nights) so much better. Jerry Drumhheller shared all of his notes from the sixties. Mike Skvarla taught me how to work the system. Thank you. Daron Westly, Aaron Windsor, Rob Ilic, Vince Genova and Phil Infante, answered my dozens of questions. I feel incredibly lucky to have had such great group of guys to guide me through my fabrication process. At the NBTC I want to thank Teresa Porri, Brian Bowman and Penny Burke for helping me out so many times, even just going over equipment trainings and protocols repeatedly. Penny has been an incredible friend and support all these years. I will miss her and always remember what a wonderful, genuine human being she is and has been. In the ECE department, Patricia Gonyea has treated me like her own daughter and always watched out for my best interests. Thank you. Jamie Dal Cero and Carrie Ingersoll Wood were always there to listen and provide insight and feedback and I am incredibly happy to have fostered a friendship with them. Dave, our fourth floor custodian made it coming to work so much better. He always has a smile and a story to tell along with an extra set of keys to let me in the office the numerous times I was locked out.

Lastly I want to thank Ben Uyeda. Things did not work out as we had planned. In a way, they turned out to be better. Over the last few years I have had to grow at a much faster rate than I could handle at times and I was able to do it, in part, because of the lessons you bestowed upon me. I learned to look inward, take responsibility and create solutions through our interaction. I still often struggle when I obsess about the problem, but yet slowly and steadily, I am learning a better way. I want to thank him for his support, patience, hundreds of hours on the phone and chatting, and his affection, even when it has been presented in a tough format. I want to thank

him for being at commencement with me and being with me at my worst. I believe we will have many more adventures together and look forward to nurturing our friendship in the years to come.

TABLE OF CONTENTS

LIST OF FIGURES

LIST OF ILLUSTRATIONS

LIST OF TABLES

LIST OF ABBREVIATIONS

AA= ascorbic acid
AFM = atomic force microscopy
ALD = atomic layer deposition
C-face = Carbon face
CNT = Carbon nanotube
Cu = copper
CVD = Chemical vapor deposition
CPE = Carbon paste electrode
mCPE = Modified carbon paste electrode
CV = Cyclic voltammetry
DA= Dopamine
DE = Diamond electrode
DI = de-ionized
DNA = Deoxyribonucleic acid
DOS = density of states
DPV = Differential pulse voltammetry
FIA = Flow injection analysis
FIA with PAD = Flow injection analysis with pulsed amperometric detection
GaAs = Galium arsenide
GCE = Glassy carbon electrode
GCS= Gouy-Chapman-Stern
GE = Graphite electrode
HOPG = highly oriented pyrolitic graphite
IHP = inner Helmholtz plane
ISE = ion selective electrode
LSV = Linear sweep voltammetry
LOD = Limit of detection
mGold = Modified gold
m-indium tin oxide = modified indium tin oxide
MLG = Multilayer graphene
Ni = nickel
OHP = Outer Helmholtz plane
PCB = printed circuit board
PMMA = Poly(methyl methacrylate)
PR = photoresist
Pt = Platinum
PZT = piezoelectric
Si = silicon
Si-face = silicon face
SiC = Silicon carbide
SiO_2= Silicon Oxide

SLG = Single Layer graphene
SO= surface optical
SPE = screen-printed electrode
SWV = square wave voltammetry
TEM = transmission electron microscopy
TLM = transfer length method
UA = Uric Acid

LIST OF CONSTANTS

e	Elementary Charge	1.60218×10^{-19} C
F	Faraday constant	9.64853×10^{4} C
h	Planck constant	6.62607×10^{-34} J-s
k	Boltzmann constant	1.38065×10^{-23} J/K
N_A	Avogadro's number	6.602214×10^{23} mol^{-1}
R	Molar gas constant	8.31447 $mol^{-1}K^{-1}$
$f=F/RT$		38.92 V^{-1}
kT		25.69 meV

CHAPTER 1

INTRODUCTION

Graphene has come to the forefront of semiconductor research due to its highly cited and impressive list of electrical, mechanical and optical properties, which are far more remarkable than silicon. As the physical limits of downscaling have hindered Moore's Law, widespread resources have been allocated to alternative materials innovation and novel device designs to sustain trends in the industry. It doesn't come as a surprise that since its isolation in 2004 and the discovery of its outstanding electrical and mechanical properties, graphene has become a promising contender for the replacement of channel material in conventional field effect transistors. As such, the literature has exploded in a plethora of studies detailing everything from its conductance modulation to its charge transfer properties. The latter have received vast interest, as there is enormous potential for the material to work as an electrode material, with energy storage/conversion, biodetection and electrochemical applications in mind. To this end, the electron-transfer characteristics of graphene have been studied. Yet, to this date, complete understanding of the electrochemical properties of the two-dimensional carbon allotrope has not been gained. Much controversy still remains in regards to the relative electrochemical activity of the edge planes and basal plane of graphitic samples [1-5].

Much of the reported inconsistencies in the electrochemical behavior of graphene stems from irregularities seen in sample and process preparation [6]. The introduction of defects, dopants, cracks and event substrate choice can and will largely shift the properties of the material, as its

two-dimensional lattice is easily and strongly perturbed with small changes. Regardless, its other intrinsic properties, such as transparency, flexibility, Dirac-point modulation and biocompatibility, among others, have made it a front runner for biosensing applications, particularly electrochemical detection. Graphene is the first truly 2D crystal ever observed in nature. The existence of 2D crystals had often been doubted in the past. It has defied the Mermin-Wagner theorem which states that a 2D crystal loses its long-range order, and thus melts, at any small but non-zero temperature, due to thermal fluctuations [7].

1.1 Carbon versus Silicon and Other Materials

Most of the electrodes used in electroanalytical chemistry are based on metals, such as gold, platinum, bismuth, palladium, rhodium, copper, nickel, ruthenium and silver. These materials have a broad potential range, are readily produced, have low background current, low cost, rich surface, are suitable for various sensing and detection applications, and provide robust reproducible results [8, 9]. They can also be easily functionalized to add selectivity.

Despite their advantages, these materials are limited by their rather low hydrogen overvoltage for Pt, Au, Ru, Ag and others [8-12] (given a metal electrode and a reversible hydrogen electrode in the same solution, the hydrogen overvoltage is the potential difference between the hydrogen's equilibrium reactions in a solution and the hydrogen itself present in the solution when it begins to form a corrosive reaction with the metal electrode- a higher overpotential implies a slower corrosion reaction). Some of these materials also have the tendency to form surface oxides or readily dissolve. Oxides will generally interfere with the electron transfer reaction while dissolution of the metal in fluid may react with the analyte and give rise to unexpected behavior.

Of the noble metals, gold and platinum are the most commonly used, usually in the form of a wire or planar disc. Both materials exhibit a rather large anodic potential (potential at which the metal electrode starts to oxidize or break down into its ions, accepting its negative ions) range and very favorable electron transfer kinetics, but they also both display a cathodic potential (potential at which the metal electrode starts to reduce, or accept its own positive ions) range that is limited in the presence of aqueous solutions as compared to mercury electrodes [9, 10, 12]. Pt is advantageous due to its corrosion resistance and very clear separation of the potential regions for oxygen and hydrogen, but Au is more inert, and hence less likely to bear oxide formation or surface contamination, both important factors in the validity, reproducibility and stability of a measurement.

Carbon has several advantages over its solid-state electrode counterparts. Generally, it has slower electron transfer kinetics [12-14], but this also grants the material a wider potential window of operation (window at which electrode is not oxidizing or reducing into its constitutive ions). Other advantages include low cost, relatively inert electrochemistry, low background current and electrocatalytic activity for a variety of redox reactions [15]. Specifically, the oxidation and reduction of organic and biological molecules has been shown superior on carbon-based materials to those found in noble metals [16]. All carbon-based electrode materials exhibit the traditionally seen six-atom aromatic ring and sp^2 bonding with differing ratios of the edge to basal planes. The edge plane has been experimentally found to display faster electron transfer kinetics than the basal plane, as the high degree of delocalized π electrons, the weak Van der Waals forces and unterminated dangling bonds provide better electrical conductivity than the basal plane. Thus, the transfer kinetics for a specific redox analyte have been found to change

with different edge-to-basal plane ratios, with the edge plane carbon-based electrodes showing nearly reversible reactions (and voltammogram) and most basal plane electrodes depicting irreversible behavior [17-19]. One major advantage of carbon-based electrodes is that they do not interact with analytes or deposited compounds during electrolysis, eliminating errors derived from such reactions.

Carbon's diversity as an electrode material is rooted in its structural polymorphism [16]. Carbon-carbon bonds are extremely strong and chemically stable both inter-atomically and with other surface modifiers. The type of bond dictates not only the type of carbon material, but also its dimensionality.

There have been extensive studies and reviews of carbon electrode materials such as graphite, glassy carbon and carbon black [20]. However, recent years have brought on a new wave of essential innovations that have significantly enhanced the application of this excellent electrode material in organic and biological electrochemistry. Carbon nanotubes electrode arrays, fullerenes, carbon films deposited via chemical vapor deposition, boron-doped diamond, graphene and other microfabricated structures have enabled novel applications in electroanalysis and electronics.

1.2 Forms of Carbon

Carbon is the elementary unit of graphene and other carbon allotropes, such as diamond, graphite and fullerenes. This element has 6 protons, 6, 7or 8 neutrons and 6 electrons. Carbon isotropes

with 6 or 7 neutrons are stable whereas those with 8 are radioactive. Most importantly, carbon is the building block of all organic molecules and responsible for life on Earth. It is hence, inherently, a biocompatible material in of itself.

In its ground state, the 6 electrons are in the $1s^2 2s^2 2p^2$ configuration. Two electrons fill the innermost orbital 1s and the other 4 occupy the 2s and 2p orbitals. As an isolated system, it is energetically favorable to put 2 of the electrons in the 2s orbital and 2 in the 2p orbitals. However, in the presence of other carbon, oxygen or hydrogen atoms, it is energetically favorable to excite one electron from the 2s into the 2p orbital and form covalent bonds with the other atoms; as such the bonds are very strong. The gain in energy from this covalent bond is larger than the required energy of excitation. This is depicted in figure 1.1.

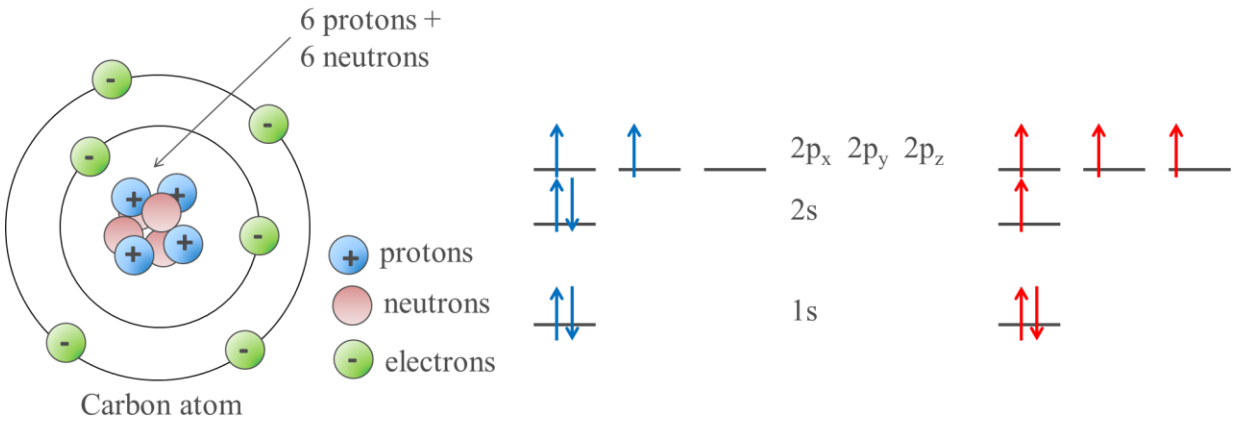

Figure 1.1 Representation of the carbon atom (left) electron arrangement of isolated carbon atoms (center) and in the presence of other atoms (right)

There are four energetically equivalent quantum-mechanical states, $|2s\rangle$, $|2p_x\rangle$, $|2p_y\rangle$ and $|2p_z\rangle$. A quantum-mechanical superposition of the state $|2s\rangle$ with a $|2p\rangle$ state is called sp^n hybridization and it is critical for covalent bond formation.

1.2.1 The sp^1 hybridization

In the sp^1 hybridization, the $|2s\rangle$ state hybridizes or mixes with one of the $|2p\rangle$ (let's say, $2p_x$) orbitals. The other 2p orbitals ($2p_y$ and $2p_z$) remain unaffected. The symmetric and anti-symmetric combinations of these states produce a new hybrid state.

$$|sp_+\rangle = \frac{1}{\sqrt{2}}(|2s\rangle + |2p_x\rangle \ , \ |sp_-\rangle = \frac{1}{\sqrt{2}}(|2s\rangle - |2p_x\rangle \tag{1.1}$$

The sp^1 orbitals overlap to form the covalent σ bond of the acetylene molecule. The remaining 2p orbitals form two additional π bonds, which are weaker than the σ bond. This is depicted in figure 1.2.

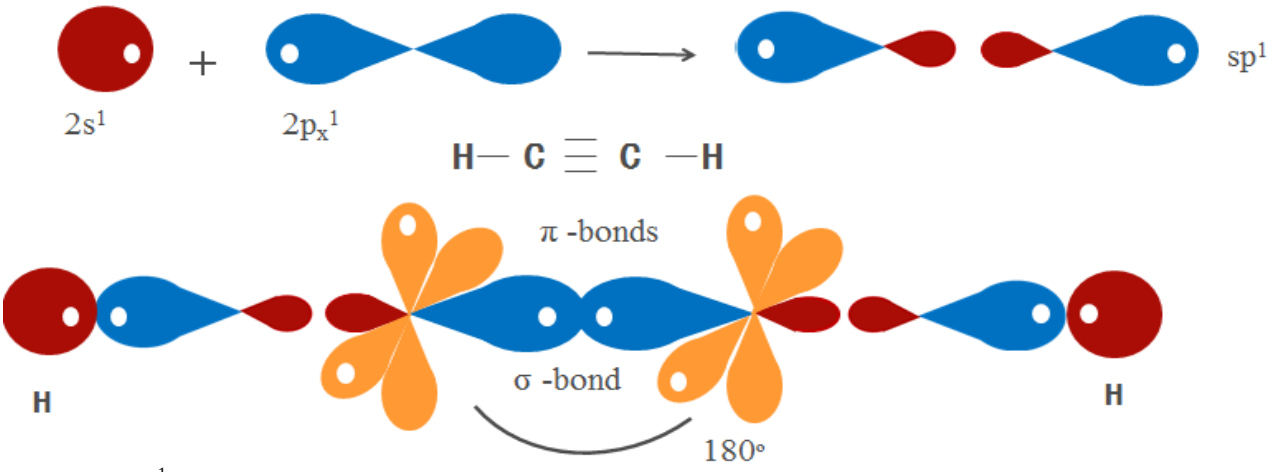

Figure 1.2 sp^1 hybridization and representation of the acetylene molecule, with one covalent bond and two additional π bonds

1.2.2 The sp^2 hybridization: Graphitic allotropes

In the sp^2 hybridization, the $|2s\rangle$ state hybridizes with two of the $|2p\rangle$ orbitals to form 3 hybridized orbitals. The sp^2 hybridization is planar in the xy-plane and the orbitals are oriented

120◦ from each other. The benzene molecule is an example of sp^2 hybridization. Six carbon atoms form a hexagon, with each carbon atom bonded to two others and to a hydrogen atom through a σ bond. The remaining $2p_z$ orbitals are perpendicular to the plane and form 3 π bonds. The resulting double bonds alternate with single bonds. The quantum-mechanical state of the benzene ring is depicted in figure 1.3. It is a superposition of the two possible arrangements of the single and double bonds around the benzene ring which differ by the position of the π bonds.

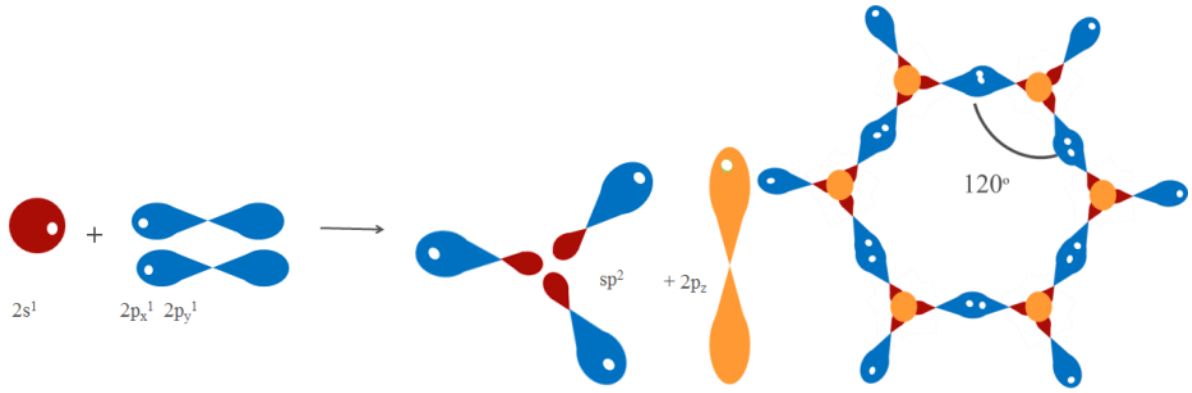

Figure 1.3 Depiction of the sp^2 hybridization and formation of a 6-carbon ring typically seen in graphitic allotropes

The quantum-mechanical states given by the hybridized $|2s\rangle$ state with two of the $|2p\rangle$ orbitals are given by:

$$|sp_1^2\rangle = \frac{1}{\sqrt{3}}(|2s\rangle - \frac{2}{\sqrt{3}}|2p_y\rangle, \tag{1.2a}$$

$$|sp_2^2\rangle = \frac{1}{\sqrt{3}}(|2s\rangle + \sqrt{\frac{2}{3}}\left(\frac{\sqrt{3}}{2}|2p_x\rangle + \frac{1}{2}|2p_y\rangle\right) \tag{1.2b}$$

$$|sp_2^2\rangle = -\frac{1}{\sqrt{3}}(|2s\rangle + \sqrt{\frac{2}{3}}\left(-\frac{\sqrt{3}}{2}|2p_x\rangle + \frac{1}{2}|2p_y\rangle\right) \tag{1.2c}$$

Graphene can be thought of as a collection of benzene rings that have been tiled next to each other. The hydrogen atoms, however, have been replaced by carbon atoms from the neighboring

hexagons and the π electrons are now delocalized over the whole lattice.

A graphene sheet is the building block of all graphitic compounds. Theoretically, it has existed for a very long time, but experimentally has gained most momentum since 2004, when it was successfully isolated [21]. Graphite, a stacking of graphene sheets has been around much longer. The sheets stick together through Van der Waals forces which are weaker than the in-plane covalent bonds. Graphite is considered the 3D graphitic allotrope, whereas graphene is considered the 2D. Figure 1.4 depicts graphene and graphite.

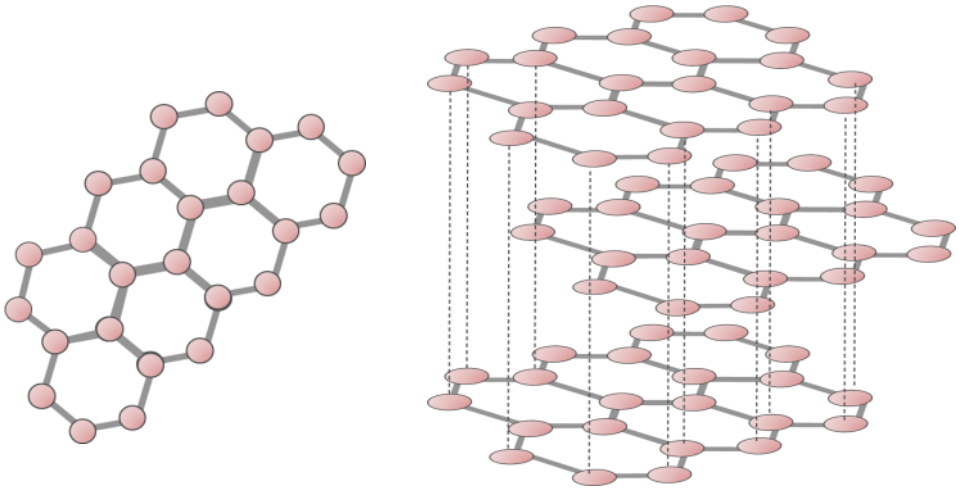

Figure 1.4 (left) A single layer of graphene composed of a honeycomb arrangement of carbon atoms. The solid lines represent the sigma bonds between carbon atoms (right) Graphite viewed as a stack of graphene layers. The dashed lines represent the $\pi - \pi$ stacking between graphene sheets.

Fullerenes, discovered in 1985 by Robert Curl, represent the 0D graphitic allotropes. C60 is the most common 0D allotrope. In it, some carbon hexagons have been replaced with pentagons. In planar graphene the sp^2-hybridized carbon atoms are at their energy minimum at 120◦ from each other. To form a sphere, the angle in planar graphite must be bent, or strained. This is possible by creating 2 σ-bonds from one π-bond, namely a double bond. This changes the sp^2-hybridized

carbons into sp^3-hybridized ones, causing the angles to decrease to 109.5°. As a result, the typical graphene sheet collapses onto itself and forms a sphere or "buckyball", as illustrated in Figure 1.5.

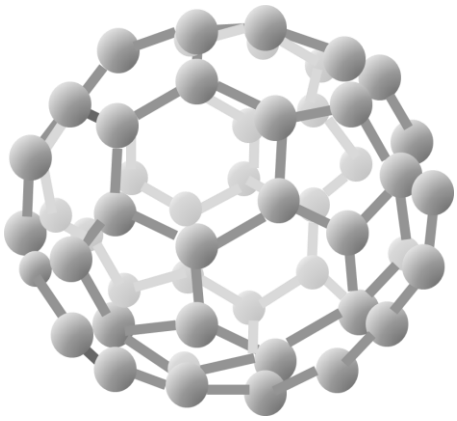

Figure 1.5 A "buckyball" or C60 molecule is a graphene sheet that has collapsed onto itself by straining the angle between carbon atoms to form a double bond from a π-bond.

Carbon nanotubes (CNT) constitute the 1D allotrope. CNTs are rolled up graphene sheets. The edge termination defines whether these are metallic or semiconducting, depending on whether the edges have a zigzag or armchair atomic placement on the carbon lattice. This is depicted in Figure 1.6. CNTs have gained tremendous popularity in the last few years due to their unique conducting and sensing properties. They were first reported in 1952 by Soviet Scientists Radushkevich and Lukyanovich, but formerly described by Sumio Iijima in the early 1990's [22-23].

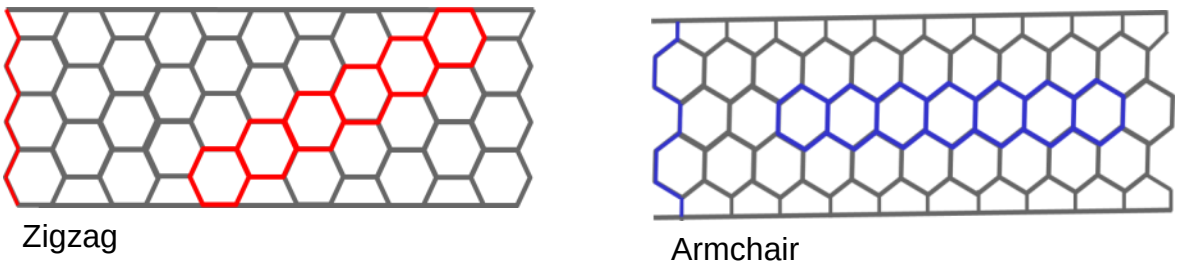

Figure 1.6. Armchair and zig-zag CNTs differ by their termination, leading to either semiconducting or metallic type properties, respectively.

1.2.3 The sp^3 hybridization: Diamond

If the $|2s\rangle$ state hybridizes with all three of the $|2p\rangle$ orbitals, the resulting four sp^3 hybridized orbitals form a tetrahedron. The angles between these orbitals are 109.5◦ (Figure 1.7). Diamonds have sp^3 hybridization. Its lattice consists of two intercalated face-centered-cubic (fcc) lattices. This is also shown in figure 1.7.

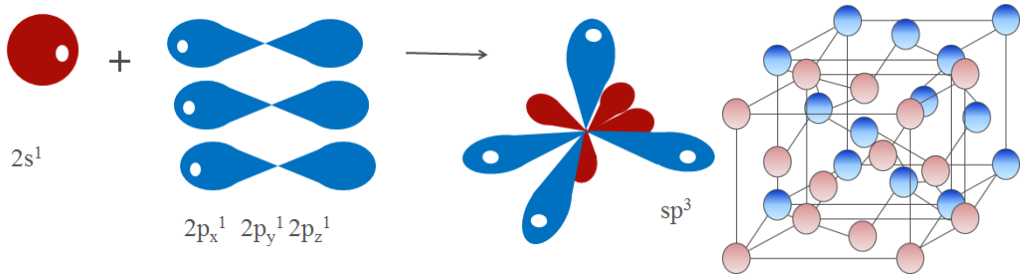

Figure 1.7 (left) Diamond sp^3 hybridization. (right)The carbon lattice is composed of two intercalating FCC carbon lattices.

Despite being made of the same constituent atom, namely, carbon, graphite and diamond are very different from one another. While graphite is soft due to the weak Van der Waals forces between the layered graphene sheets, diamond is extremely hard, as all the bonds are covalent σ bonds. This is because all of the 4 valence electrons in the outer atomic shell are used (all 2p orbitals are hybridized) in the formation of σ bonds. Because there are no delocalized (and thus conducting) electrons forming any π bonds in diamonds, the latter is generally a wide band gap semiconductor.

1.3 Types of Graphene

The theory of graphene was pioneered by P. R. Wallace in 1947 as an attempt to explain the electrical properties of three-dimensional graphite [24]. Since its discovery in 2004 by the conventional "scotch tape" method, which, namely, peels layers of graphene off 3D graphite, there have been substantial advances made in the growth of graphene via chemical vapor deposition (CVD) and epitaxial growth on silicon carbide (SiC). The resulting graphene types exhibit similar, yet not identical properties. In addition, the substrate on which the graphene is grown and/or transferred to may critically perturb the two-dimensional lattice, and thus the electronic properties, which, as we will see in the next section, are strongly linked to the geometrical properties of the two-dimensional allotrope.

1.3.1 Exfoliated Graphene

Attempts at isolating single graphene sheets date back to the 1990's. Single layer graphene, however, wasn't realized until 2004 by Andre Geim and Kostya Novoselov at the University of Manchester [25]. They were able to "peel" it off bulk graphite and transfer to an insulating substrate, silicon oxide. The later provided enough contrast to allow the graphene to be visible and electrically isolated to explore its properties.

In the exfoliation method thin samples are peeled off a graphite crystallite with scotch tape. Each

time the tape is peeled away the graphite piece is separated into two parts, each time being thinner. The process is iterated for several cycles until only one to a few layers of graphene remain stuck to the scotch tape. At this point, the scotch tape is adhered to a SiO_2 substrate. The tape is carefully peeled away and the graphene sheets remain glued to the substrate. Figure 1.8 shows a TEM image of exfoliated graphene adhered to 300 nm SiO_2 substrate.

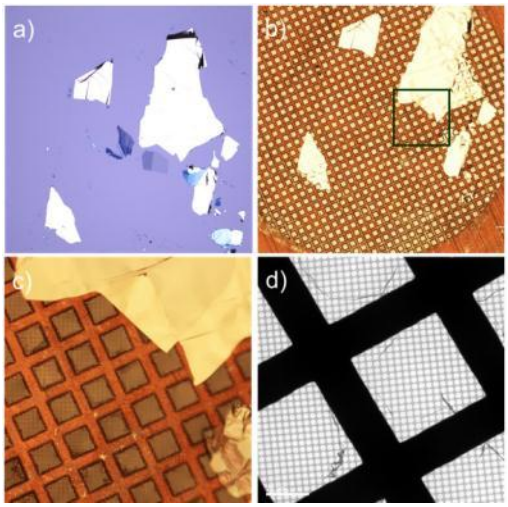

Figure 1.8 Graphene flakes a) as prepared on an oxidized silicon wafer, b) after transfer onto a TEM grid; c) magnified optical image of the green square indicated in (b) illustrating how suspended single layer regions are not easily visible; d) low magnification TEM image of a single layer area. Broken flakes and rolled up regions produce some visible contrast and hint at the presence of the single layer graphene sheet [25].

Despite it producing some of the best quality materials in regards to its electronic properties, there are a few drawbacks to the exfoliation method. For one, it is incredibly difficult to produce large scale area single layer graphene mainly because of the nature of exfoliation. Hence, it is unlikely to be a method implemented for industrial production. Also, the identification of the few single graphene layers, which are randomly distributed on the substrate, becomes cumbersome if not impossible.

Another type of exfoliation is liquid phase exfoliation. With this method the graphene flakes

float in solution and/or mixed with other chemicals that add specific functions, and then dispersed onto the substrate of interest. While the quality of this graphene is not as high as that made with other methods because of all the processing steps, it can potentially be scalable enough to yield well in the industry.

1.3.2 Epitaxial Graphene

The epitaxial growth of graphene by a thermal decomposition reaction through which the layers are immediately provided on a large scale on a semiconducting surface is an attractive alternative to other conventional methods of graphene production. [27-31]. While the quality is high, the high cost and limited size of the substrate prevent it from being a scalable method of graphene mass production. Annealing of SiC basal plane substrates yields to graphitization of the surface due to the enhanced sublimation of Si atoms [32, 33] and it is this technique that been utilized the most to produce epitaxial graphene monolayers on the Si-face of SiC (0001 plane) , at temperatures at or above 1200◦C. While graphene can also grow on the C-face, it is less preferred for most applications because it is much harder to control the number of layers.

The homogeneity of graphene layers has been better controlled by annealing the SiC samples at temperatures above 1600 ◦C in an Argon atmosphere.[30,34]. More recent attempts of growing epitaxial graphene have made use of an additional carbon supply similar to molecular beam epitaxy (MBE) at lower temperatures of about 950 ◦C.

Growth of graphene on SiC (0001) is mediated by a covalently bound carbon intermediate interface layer. The strong interaction yields a well-ordered epitaxial relationship between the

substrate and graphene, but also dopes the graphene n-type. To this end, several methods have been explored to reverse the Fermi-level shift and obtain charge neutrality. Transfer doping by Sb or B deposition has been found to reduce the n-doping to a degree, although not completely eradicate it [35]. Deposition of tetrafluoro-tetracyanoquinodimethane (F4-TCNQ) molecule has, however, been found to achieve charge neutrality [36].

Hydrogen intercalation, a method by which the dangling bonds of the SiC substrate are hydrogen passivated so that the interfacial carbon layer between the substrate and the graphene is decoupled from the substrate, can eliminate interface bonding [37] and has become widely popular in recent years. Figure 1.9 shows the typical AFM image of epitaxial graphene on the Si-face of SiC.

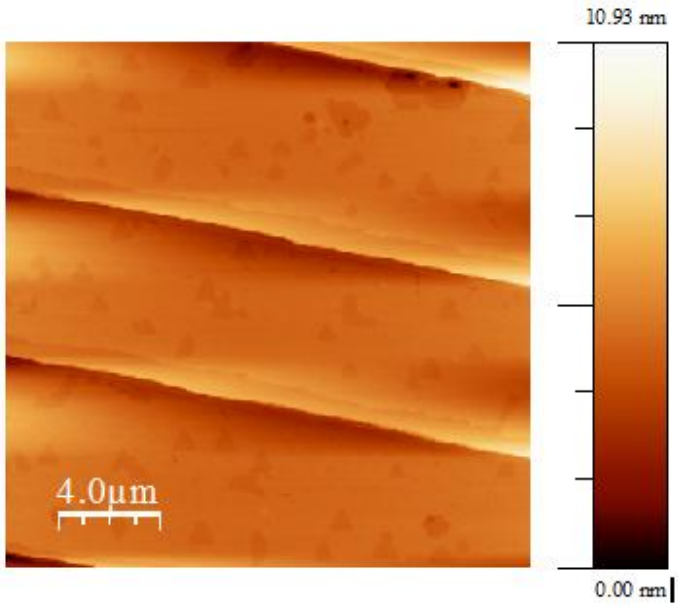

Figure 1.9 AFM Images of Epitaxial Graphene grown on 6H-SiC by silicon sublimation at 1600C at an Argon ambient of 750 Torr for 15 minutes

1.3.3 CVD (Chemical Vapor deposition) Graphene

The growth formation of graphene layers on metal surfaces has been around for almost 50 years. The formation of graphite from the combination of carbon with other materials was first put forward in 1896. In fact, graphite was first observed on Ni substrates when the films were exposed to carbon in the form of hydrocarbons or evaporated carbon [38, 39].

Generally, in chemical vapor deposition, growth takes place by surface segregation of carbon. That is, graphene is allowed to grow from carbon atoms that diffuse to the free surface sites of transition metals. These carbon atoms are introduced by chemical vapor deposition.

CVD growth offers a good compromise between film quality, size, and cost. The method is a chemical process that occurs in a well-controlled furnace, yielding layers of graphene up to 100 meters long, and of a solid quality. The films are usually grown on thin metal substrates, for example copper. The copper is later etched away and the graphene transferred onto any other substrate, depending on the application. The CVD method is versatile and the most commonly used method of making graphene films today. CVD graphene films that have been grown on copper and nickel substrates and subsequently transferred to SiO_2 are shown in Figure 1.10.

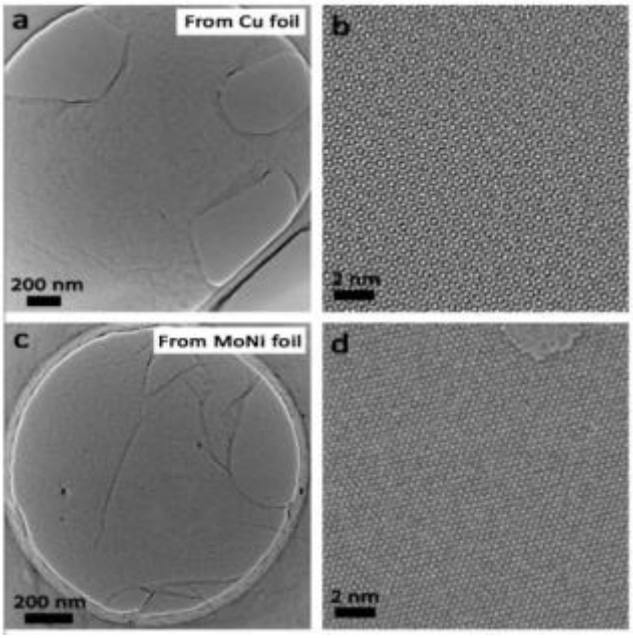

Figure 1.10. TEM micrographs of transferred graphene from different arbitrary growth substrates. Panel (a) shows the overview image of bi-layer graphene transferred from a Cu growth substrate. (b) The corresponding HRTEM image of the bi-layer graphene with rotational stacking (note the Moire pattern indicating a rotational stacking fault). Panels (c) and (d) respectively show the corresponding overview and HRTEM images of monolayer graphene transferred from MoNi.[40]

In addition to electrodes prepared with graphene grown via conventional CVD, we examine, for the first time, the electrochemical response of electrodes fabricated with graphene grown via a two-step CVD method on sapphire. We will examine this material in detail in Chapter 3.

1.4 Electrical Properties of Graphene

Graphene has captured the attention of the semiconductor industry and scientific community because of its unique electrical properties. Amongst them is its remarkably high electrical conductivity as well as the voltage modulation of its Dirac point. In graphene, the electron velocity has been found to be independent of energy; hence, the electrons move as if they were

light waves–that is, they behave like massless particles, even though it is known to contain particles known as massive chiral fermions, and particle theory has previously maintained that any particle with chirality must have mass [41].

1.4.1 Band Structure of Graphene

The electrical properties of graphene can be understood from its distinctly unique band structure rooted in its two-dimensional crystalline structure. As discussed before, carbon atoms form a hexagonal lattice made possible with the sp^2 hybridization of the 2s and 2p orbitals. Each carbon atom is roughly 1.42Å away from its nearest neighbor. Of its six electrons, 2 of them are in the ground state, or the 1s orbital. Three of them participate in covalent bonding with the 3 nearest neighboring atoms. These electrons occupy the hybridized orbitals. The remaining single electron occupies the $2p_z$ orbital, yielding the π-bond, which lies perpendicular to the plane of the carbon lattice (*xy*-plane). All the $2p_z$ orbitals from all neighboring atoms are hybridized to yield the π and π^* bands, which are responsible for graphene's unique electronic conduction properties. These bands, thus, have the conduction electrons in graphene, and hence, those near the Fermi level. The other three electrons that participate in covalent bonding do not contribute to conduction but rather give graphene's its trademark honeycomb lattice structure.

The hexagonal structure in graphene is not in itself a Bravais lattice, as every atom does not "see the same surrounding". Rather, we can think of it as the superposition of two triangular Bravais lattices, where we can classify carbon atom as type A or type B depending on which lattice they

belong to. Figure 1.11 shows a representation of the graphene lattice. Notice the difference in the nearest neighbors surrounding atoms of type A from those of type B. We will refer to this figure in our derivation and calculation of the band structure and dispersion relationship for graphene.

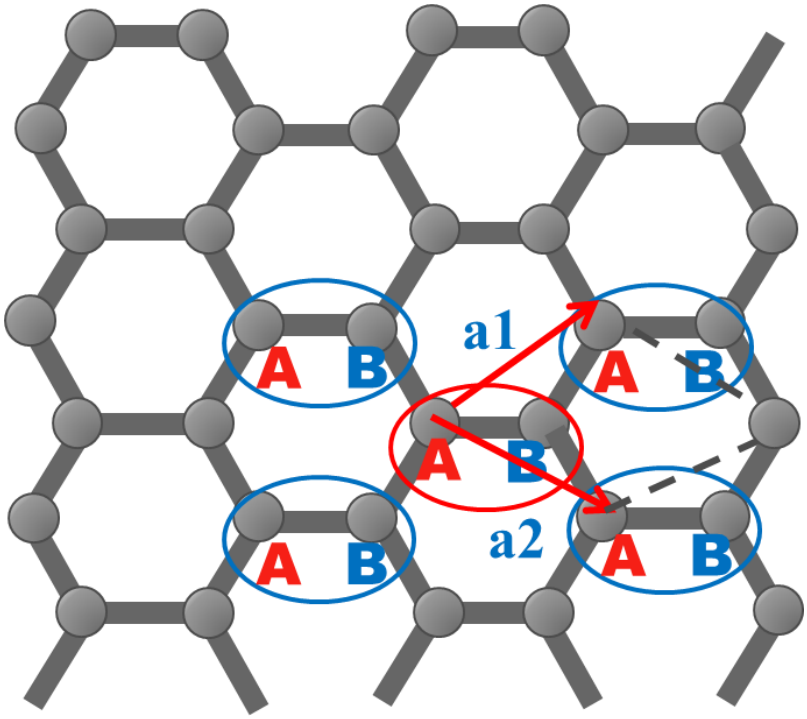

Figure 1.11 Hexagonal Arrangements of Carbon Atoms in Graphene. Lattice vectors $\mathbf{a_1}$ and $\mathbf{a_2}$ denote a triangular Bravais lattice with two atoms A and B per unit cell. Each atom in sublattice A has three nearest neighbors in sublattice B and vice versa.

A unit cell is thus constituted by both an atom A and an atom B, that is, 2 atoms per unit cell, with cell lattice vectors given by:

$$\vec{a}_1 = \frac{3}{2}a_o\hat{x} + \frac{\sqrt{3}}{2}a_o\hat{y} \quad , \quad \vec{a}_2 = \frac{3}{2}a_o\hat{x} - \frac{\sqrt{3}}{2}a_o\hat{y} \tag{1.3}$$

Each of these atoms has four valence electrons that participate in σ or π bonds, however, 3 of

these are tied up in covalent σ bonds and do not contribute to conduction, in other words they are not near the Fermi level or the electrochemical potential, μ.

By defining the basis functions for each of the atoms in the unit cell of graphene and solving the Schrödinger equation we can obtain a solution for the energy dispersion relationship.

$$E\Psi = (-\frac{\hbar^2}{2m}\nabla^2 + U)\Psi \tag{1.4}$$

$$E\{\Psi\} = [H]\{\Psi\} \tag{1.5}$$

The Hamiltonian, H, is a matrix with dimensions $Nb \times Nb$, where N is the number of unit cells and b is the number of basis functions per unit cell. This is a pretty big and complex matrix even for a small sample size. Fortunately, we can reduce this by taking into consideration that the lattice structure repeats itself in units of 2.

$$E\{\phi_n\} = \sum\nolimits_m [H_{nm}]\{\phi_m\} \tag{1.6}$$

$$\{\phi_n\} = \{\phi_o\} e^{i\vec{k}\cdot d\vec{n}} \tag{1.7}$$

$$[h]\{\phi_o\} = E\{\phi_o\} \tag{1.8}$$

$$h(k) = \sum_m [H_{nm}] e^{i\vec{k}\cdot(dm - d\vec{n})} \tag{1.9}$$

In graphene, any given unit cell composed of one A and one B type atom has four nearest neighbor unit cells. To find *h(k)* we only need consider the self-interacting and neighboring atoms. The Hamiltonian can be written as:

$$h(k)=\begin{bmatrix}\varepsilon_o & t\\ t & \varepsilon_o\end{bmatrix}+\begin{bmatrix}0 & 0\\ t & 0\end{bmatrix}e^{i\vec{k}\cdot\vec{a}_1}+\begin{bmatrix}0 & 0\\ t & 0\end{bmatrix}e^{i\vec{k}\cdot\vec{a}_2}+\begin{bmatrix}0 & t\\ 0 & 0\end{bmatrix}e^{-i\vec{k}\cdot\vec{a}_1}+\begin{bmatrix}0 & t\\ 0 & 0\end{bmatrix}e^{-i\vec{k}\cdot\vec{a}_2} \tag{1.10}$$

$$h[k]=\begin{bmatrix}\varepsilon_o & h_o\\ h_o* & \varepsilon_o\end{bmatrix}\quad where\ h_o=t(1+e^{i\vec{k}\cdot\vec{a}_1}+e^{i\vec{k}\cdot\vec{a}_1}) \tag{1.11}$$

$$\varepsilon=\varepsilon_o\pm|h_o| \tag{1.12}$$

Where *t* is the overlap integral, or ease with which one electron can go to an adjacent orbital. For graphene this is roughly 2.5-3eV. We care only about the eigenvalues right at the chemical potential, μ, more precisely, at ε_o, when the system is at equilibrium, alternatively when h_o is 0. Only electrons around the chemical potential contribute to conduction. The problem then simplifies to one where we find the values of k that make converge h_o to 0. Solving for *k*:

$$k=k_x\hat{x}+k_y\hat{y} \tag{1.13}$$

$$\vec{a}_1=a\hat{x}+b\hat{y}=\frac{3}{2}a_o\hat{x}+\frac{\sqrt{3}}{2}a_o\hat{y},\qquad \vec{a}_2=a\hat{x}-b\hat{y}=\frac{3}{2}a_o\hat{x}-\frac{\sqrt{3}}{2}a_o\hat{y} \tag{1.14}$$

$$h_o=t(1+2e^{ik_xa}(\cos k_yb)) \tag{1.15}$$

$$(k_xa,k_yb)=(0,\pm\frac{2\pi}{3}),\ (k_xa,k_yb)=(\pi,\pm\frac{\pi}{3}) \tag{1.16}$$

The values around $k_x a, k_y b$ represent the valleys, or points near the electrochemical potential. A Taylor series expansion around these point yields:

$$\frac{\partial h_o}{\partial x}(0,\pm\frac{2\pi}{3}) = iat, \quad \frac{\partial h_o}{\partial y}(0,\pm\frac{2\pi}{3}) = \sqrt{3}bt = at \tag{1.17}$$

Allowing us to express the Hamiltonian as:

$$h_o(k_x, k_y) = -iat[k_x - ib_y], b_y = k_y - \frac{2\pi}{3b} \tag{1.18}$$

where $\sqrt{3}b = a$. We can write our dispersion relationship for graphene near the Dirac points (Fermi level):

$$\varepsilon(\vec{k}) = \varepsilon_o \pm at\sqrt{k_x^{\,2} + b_y^{\,2}} = \varepsilon_o \pm t\sqrt{1 + 4\cos\left(\frac{\sqrt{3}k_x a}{2}\right)\cos\left(\frac{k_y a}{3}\right) + \cos^2\left(\frac{k_y a}{2}\right)} \tag{1.19}$$

The dispersion relation is linear with *k*. It is depicted in Fig. 1.12.

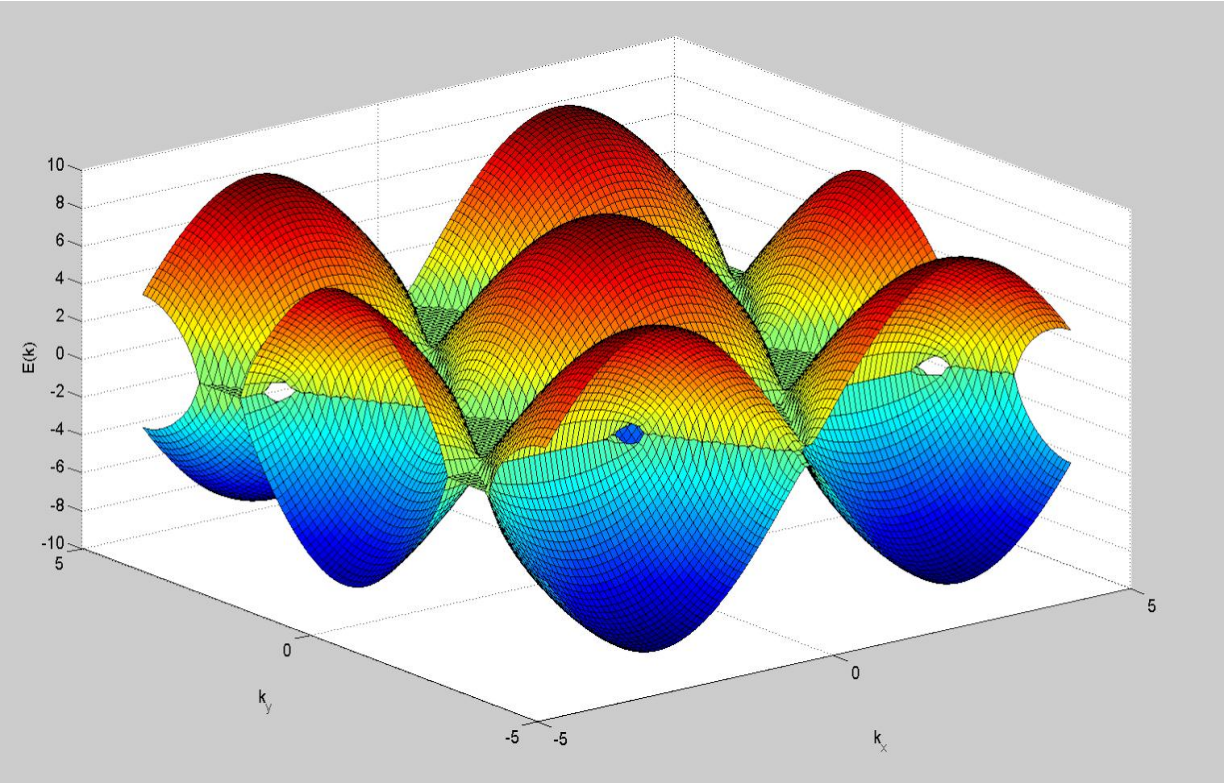

Figure 1.12 Dispersion relationship of monolayer graphene. The $E-\vec{k}$ relationship is linear around the conical points.

1.4.2 Massless fermions

We can take a look at the dispersion relation of graphene to extract the velocity and the mass from the first and second derivatives of the *E*-*k* relationship, respectively. From this analysis we can see the particles behave as massless fermions.

$$v = \frac{1}{\hbar}\frac{\partial E}{\partial k} = \frac{\partial E}{\partial p} = v_F \tag{1.20}$$

$$m = \frac{1}{\hbar}\frac{\partial^2 E}{\partial k^2} = \frac{\partial v}{\partial k} = 0 \tag{1.21}$$

1.4.3 Density of States

To calculate currents we need to convert our *E(k)* relationship to a density of states. There are several ways to do this but all use the number of available states *N(E).*

$$N(E) = \frac{\pi k^2}{\frac{2\pi}{W} \times \frac{2\pi}{L}} = \frac{|E|^2 \times Area}{\hbar^2 v_F^2 4\pi} \tag{1.22}$$

The density of states calculates the number of available state per unit of energy and is given by:

$$D(E) = \frac{dN(E)}{dE} = \sum_{\vec{k}} \delta(E - \varepsilon(\vec{k})) \rightarrow \iint \frac{dk_x dk_y}{\frac{2\pi}{L} \cdot \frac{2\pi}{W}} \delta(E - \varepsilon(\vec{k})) \tag{1.23}$$

Using the relationship:

$$\int dx \delta(x-a) f(a) = f(a) \quad and \quad \delta(x-a) = \delta(a-x) \tag{1.24}$$

We obtain:

$$\frac{LW}{4\pi^2} \int_0^{2\pi} k d\theta \int dk \delta(\varepsilon(\vec{k}) - E) \tag{1.25}$$

Using our expressions for the linear ε-$\vec{k}$ dispersion relationship:

$$\varepsilon(\vec{k}) = \pm at|\vec{k}| \quad and \quad d\vec{k} = \frac{d\varepsilon(\vec{k})}{at} \tag{1.26}$$

We can arrive at an expression for the density of states:

$$D(E) = \frac{g_s \cdot g_d \cdot Area}{2\pi} \frac{|E|}{a^2 t^2} = \frac{2 \cdot Area \cdot |E|}{\pi(\hbar v_F)^2} \tag{1.27}$$

The DOS is important because, as we will see in section 1.6, it contributes directly to the overall electrode performance. A higher DOS increases the probability that an electron of the correct energy is available for the electrodes to transfer. The D(E) is plotted in figure 1.13.

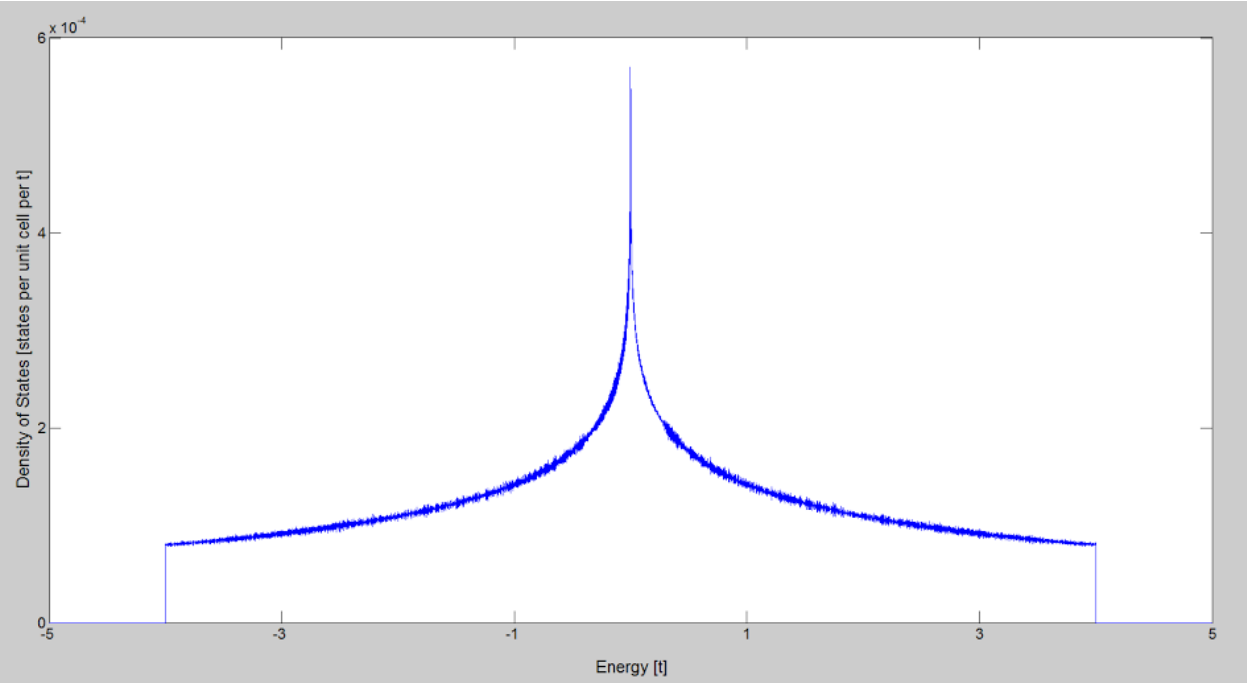

Figure 1.13 Density of State diagram for Graphene

1.4.4 Limitations on the Conductivity of Graphene

The carrier mobility in graphene is limited both by intrinsic and extrinsic factors. It is important to distinguish between these two, as these affect the overall device performance. Extrinsic mechanisms include charged impurities, neutral defects, interface roughness and graphene ripples. With proper materials growth and transfer controls these can be eliminated. The limiting value of the intrinsic room-temperature graphene mobility is therefore, of far more interest to the scientific community.

One of the dominant low-temperature extrinsic scattering mechanisms in graphene is due to Coulomb scattering by charged impurities present in the substrate, particularly in SiO_2 substrates used to transfer graphene and at the substrate-graphene interface. Short-range scattering mechanisms by neutral defects also have an impact on the overall carrier mobility, particularly at high carrier densities.

The scattering rate due to charged impurities present in the graphene-dielectric interface is given by [42]:

$$\frac{1}{\tau_{imp}} = \frac{n_{imp}}{\pi\hbar}\left(\frac{e^2}{2\varepsilon_o\,\kappa_{avg}}\right)\frac{2F(a)}{\varepsilon(k)} = \pi\alpha^2 F(a)\frac{n_{imp}v_F}{k} \tag{1.28}$$

where n_{imp} is the sheet density of impurities at the interface, $a = \alpha(\frac{k_F}{k})$ is a dimensionless parameter where α is the effective fine-structure constant defined as $\alpha = e^2/2\pi\epsilon_o\kappa_{avg}\hbar v_F$, v_F is the Fermi velocity, k_F is the Fermi wave vector, and the dimensionless function *F(a)* is defined as in [43]:

$$\frac{F(x)}{x^2} = \frac{\pi}{4} + 3x - \frac{3\pi x^2}{2} + \frac{x(3x^2-2)arcos(1/x)}{\sqrt{x^2-1}} \quad (1.29)$$

κ_{avg} is given by the average relative dielectric constant of the two regions sur- rounding graphene: κ_{avg} = (κ_{top}+κ_{bottom})/2. In typical cases, it is SiO_2 and air, implying κ_{avg}= (1+κ_{SiO2})/2 =2.45.

Intrinsic factors that affect the mobility are polar optical phonons and acoustic phonons. Unlike 2D GaAs systems, graphene lacks the strong long range polar optical phonons that limit the mobility in GaAs. Most of the intrinsic factors are really contingent on the weak deformation potential scattering from thermal lattice acoustic phonons. Chen et al showed that the acoustic phonon scattering is independent of the number of carriers and can place an intrinsic limit of the graphene resistivity of only 30 ohms at room temperature [44]. They also reported that extrinsic scattering by SiO_2 surface phonons can add a strong temperature dependent resistivity above 200K.

Low field mobility values for graphene are as high as 4000$cm^2/V\cdot s$ at room temperature and the highest value at greater than 10^{13} cm^{-2} carrier concentration is roughly 9000 $cm^2/V\cdot s$, as reported in the literature [45]. The electron-ionized charged impurity interaction varies with κ^{-2}, where κ is the dielectric constant of graphene's environment. Use of high- κ dielectric materials instead of SiO_2 can improve mobility at low fields, but it does at the cost of an extra scattering mechanism- the remote interface-phonons or surface optical phonons. The large electronegativity of its constituent atoms gives these high-κ materials high polar natures, which in turn create an electric field with vibrating dipoles. Such field decays exponentially away from the graphene-dielectric

interface. Graphene is an atomically thin material, thus sensitive to any kind of perturbation. Such decaying surface-phonon field will scatter carriers and limit the low-field mobility of carriers in graphene.(Jena reference) Thus, while with increasing dielectric constant damps out impurity scattering, SO phonon scattering increases. Figure 1.14(left) depicts the expected mobility for particular dielectrics in the absence of SO scattering. The filled circles show the degradation due to SO phonon scattering. The latter is independent of impurity concentration. Figure 1.14(right) plots the conductivity in SiO_2 and ZrO_2 The solid lines correspond to conductivity due to impurity scattering alone, while the dashed lines incorporate the effect of both impurity and surface-optical phonons [42].

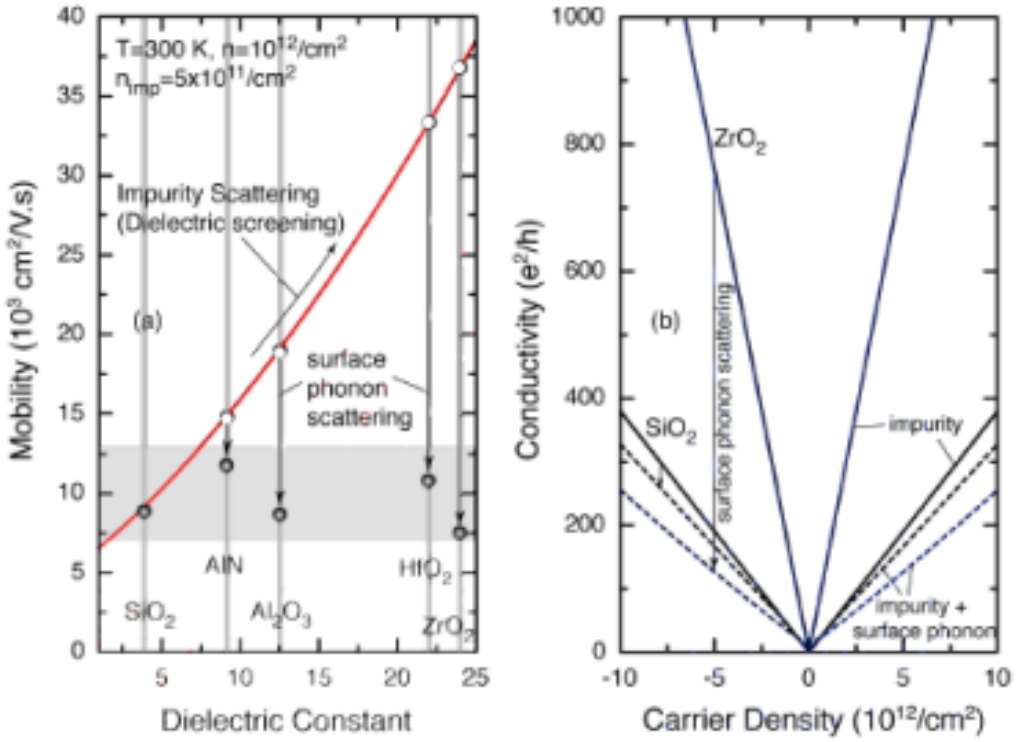

Figure 1.14. (left) Electron mobility in graphene as a function of the gate dielectric constant. High-k dielectrics reduce Coulombic impurity scattering, but strong SO phonon scattering by them reduces the RT mobilities to ~10^4 $cm^2/V{\cdot}s$. (right) Electron and hole conductivity as a function of carrier concentration for graphene on SiO_2 and ZrO_2 [42].

1.5 Raman Spectroscopy of Graphene

Perhaps the most integral and versatile characterization technique of graphene to date has been Raman spectroscopy. It offers a quick, robust and fairly simple method of detecting graphene on a surface. It does not destruct samples, offers high resolution, quality control and can convey both structural and electronic information. This all comes at the expense of data interpretation, which has evolved substantially over the last 6 years with new results on the effects of doping, edges, defects, chemical functionalization, electron-phonon and electron-electron interactions, interlayer coupling and many other phenomena found in graphene.

Raman spectroscopy, named after Sir C. V. Raman, is a spectroscopic technique that details the vibrational, rotational and other low frequency modes of a system [47]. It uses the inelastic scattering of monochromatic light as it interacts with vibrations of molecules, phonons or other excitations in the system. As a result of this interaction, the energy of the photons in the light, namely a laser, is shifted up or down. It is this shift in the energy that gives insightful information about the vibrational modes in a sample.

A Raman spectrum is distinguished by the positions of the measured peaks (wavelength), the peak area, A, the peak height or intensity, I, the full-width half maximum FWHM and the peak dispersion. The latter reflects the shift in the peak position with changing excitation energy. Single layer graphene (SLG) has a distinct Raman signature. The phonon dispersions of SLG comprise three acoustic (A) and three optical (O) modes. Out-of-plane modes (Z) are much softer than in-plane longitudinal (L) and transverse (T) modes. In the presence of defects,

additional peaks are observed. Figure 1.15 shows the Raman spectra for pristine SLG and defected MLG. The latter has observable defects.

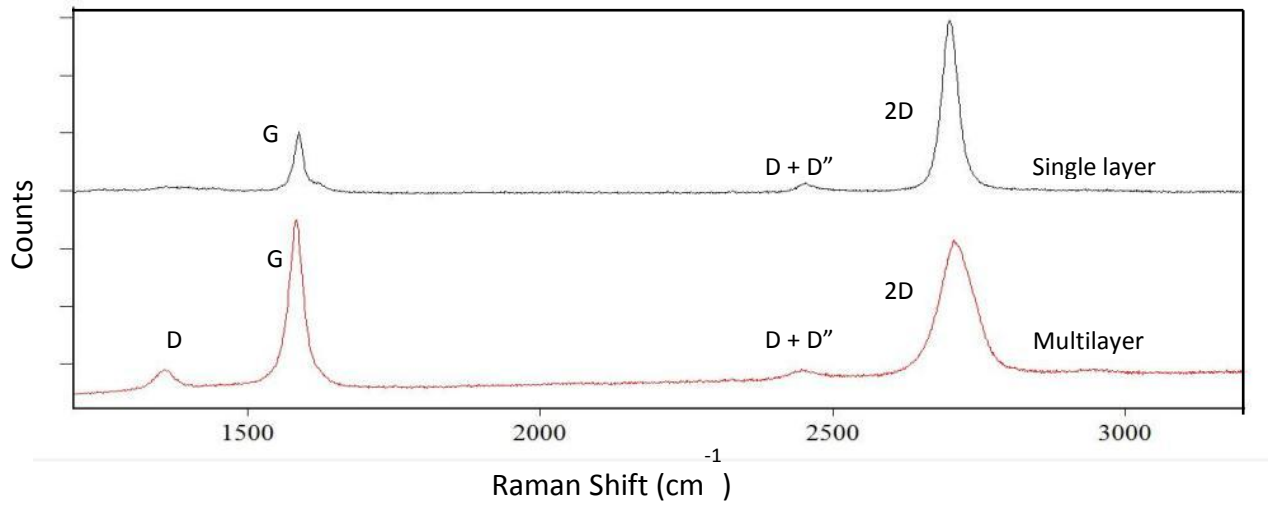

Figure 1.15 Raman spectra of single layer pristine (top) and defected multilayer (bottom) graphene.

The G peak seen in the Raman Spectra, at around 1582 cm^{-1} is due to the high frequency phonon at the Brillouin zone center. It is the primary mode in graphene and graphite and representative of the sp^2 configuration found in graphitic allotropes. The position of the G peak is independent of the laser excitation frequency, but not independent of the number of graphene sheets. As the layer thickness increases, the band positions shift to lower energy. The position of the G-band is also sensitive to doping and even strain in the graphene, so one must be careful when using this as a measure of graphene layer thickness.

The D-peak is otherwise known as the defect peak. It results from lattice vibrational processes from the breathing modes of the carbon rings and is usually seen around 1350 cm^{-1}. A strong d-peak indicates there are a lot of defects in the material, as its intensity is directly proportional to the level of defects in the sample. This could be due to dislocations, impurities or holes in the

material, but it is also correlated to domain size; as the domains get smaller, the number of edge defects increase. The D-band is a resonant band, exhibiting dispersive behavior. Generally this translates to position and shape dependence with excitation frequencies. In this work, the same laser, a 488 nm wavelength laser was used throughout all sample analysis. While the D peak represents intervalley scattering (double resonance, defect assisted), the D' peak represents intravalley scattering.

The 2D-band is often referred to as the G' band. It is the second order of the D band, or its overtone. The 2D band results from lattice vibrations that involve two phonons. In 2D and 2D' processes (intervalley and intravalley) two phonons with opposite wave vectors are scattered, momentum is conserved and no defects are needed. Thus, it does not need to be activated by a defect and is always present in graphene. Like the G-band, this band is used to estimate sample thickness. There is a general shift to higher wavenumbers with increasing layers. This relationship is seen in figure 1.16.

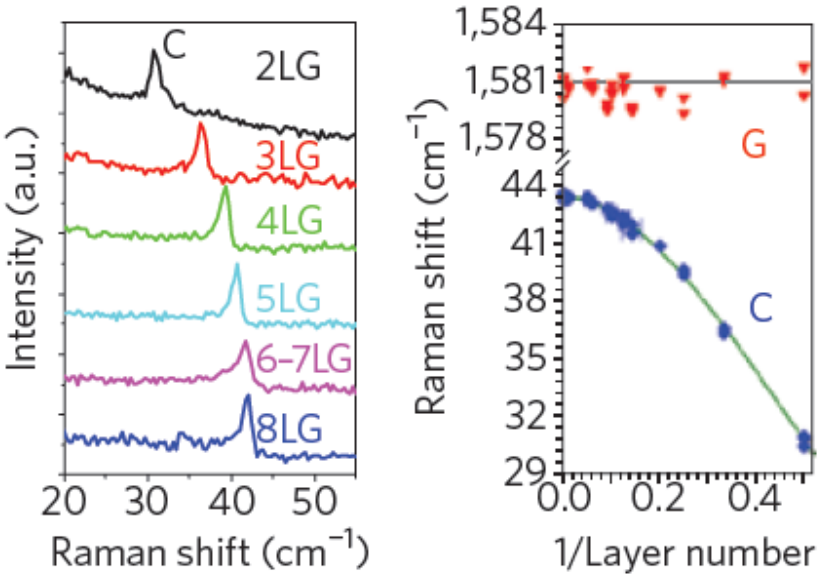

Figure 1.16 (Left) Peak as a function of layers. (Right) Fitted C- and G- peak position as a function of inverse number of layers [48].

More importantly, there are changes in the shape of the band with increasing number of layers. These changes are associated with the active components of the vibration. With single-layer graphene, there is only one component to the 2D band, whereas with bilayer there are four [48]. Like the D band, it exhibits dispersive behavior with changes in excitation frequency. Figure 1.17 shows the different type of one and two phonon processes responsible for the G, D and 2D bands and their overtones.

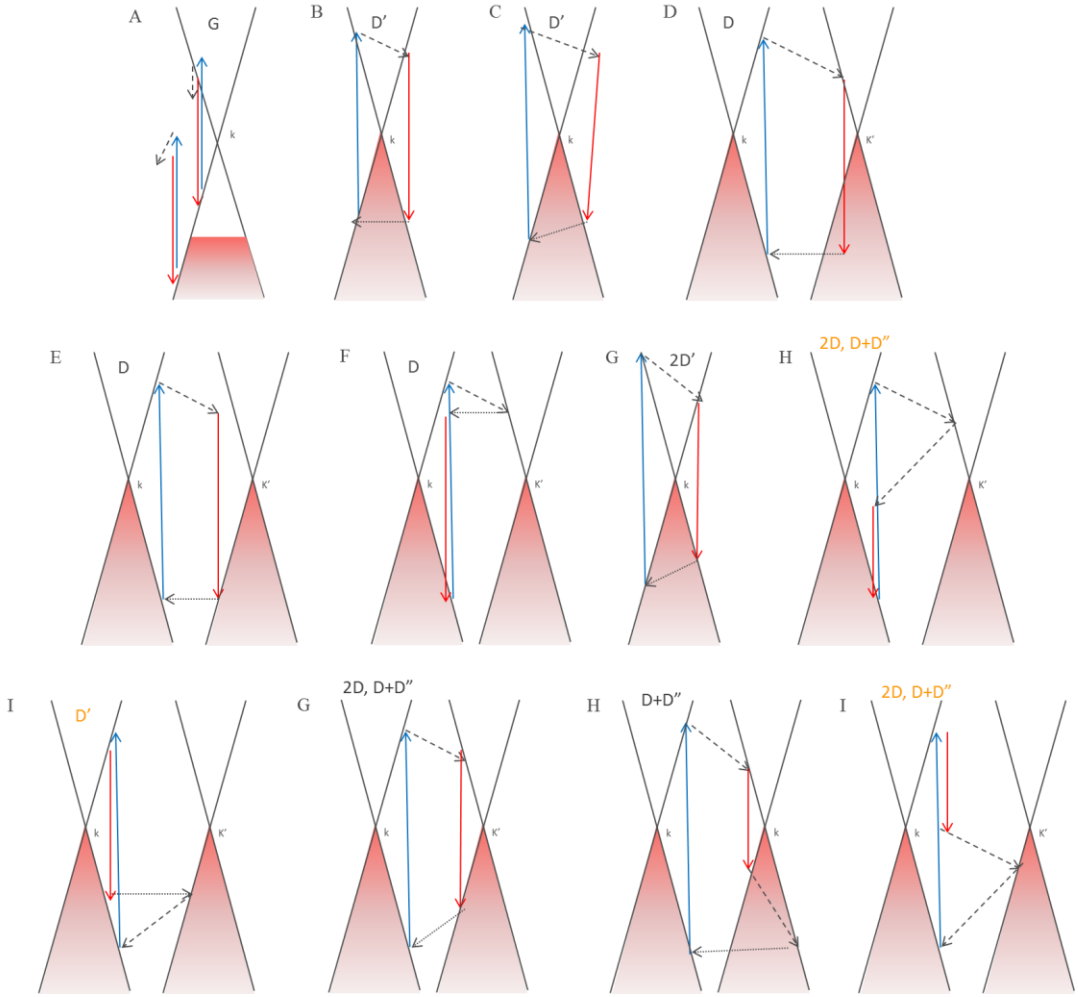

Figure 1.17 Raman Processes – Reproduced from Nature Nanotechnology, Ferrari and Basko, April 4 2013 with permission [48]. Electron dispersion (solid black lines), occupied states (shaded areas), interband transitions neglecting the photon momentum, accompanied by photon absorption (blue arrows) and emission (red arrows), intraband transitions accompanied by phonon emission (dashed arrows), electron scattering on a defect (horizontal dotted arrows). **A.** One-phonon processes responsible for the G peak. **B-F, I**, In the presence of defects, the phonon wave vector need not be zero, producing the D ' peak for intravalley scattering (**B, C, I**), and D peak for intervalley scattering (**D-F**). **G.** For two-phonon scattering, momentum can be conserved by emitting two phonons with opposite wave vectors, producing the 2D' peak for intravalley scattering and the **(H, I, G)** 2D, D + D" peaks for intervalley scattering.

1.6 Electrochemical Properties of Graphene

Graphene has received much attention in the area of electrochemistry, where it could be rather advantageous in a vast plethora of applications ranging from sensing to energy storage. The primary purpose of this thesis is to examine the electrochemical properties of a wide range of graphitic materials to determine the detection and sensitivity limits of its performance as an electrode sensor. In addition, we seek ways of improving upon such sensitivity. There have been many studies of single, bilayer and multilayer graphene reporting that there are no substantial differences in the electrochemical properties regardless of the number of layers [49]. Other studies have focused on the charge transfer kinetic differences between the edge and basal planes of graphene, mostly concluding that charge transfer is predominantly dominated at the edges [50-52]. Most recently it has been shown via scanning electrochemical cell microscopy (SECM) that the basal plane sites are highly time-dependent electroactive, with decreased electron transfer rates at the basal surface after one hour of cleaving [53].

1.6.1 Graphene as an Electrode Material

Graphene is an ideal electrode material for electrochemistry because it has the largest 2D electrical conductivity found in any organic material, and electrodes, in particular those for biodetection, are sought to be biocompatible, namely, made of carbon. It is robust, has a wide potential window and low electrical noise. In addition, it is transparent and flexible, hence being incredibly mechanically versatile for non-planar surfaces, such as those found in tissue and cell walls. Recently, it has been found that, through proper patterning, the elastic modulus can be

modified, rendering stretchable structures [54]. The latter could function as electrodes that could wrap around cells, thus circumventing the problem of being unable to make good close contact proximity and promote larger signal-to-noise ratio at lower concentration of measurable analyte or weaker action potentials.

Graphene is incredibly inert in its basal plane as compared with other solid-state electrodes and oxide interfaces, making it a model interface for biological fluids. The latter are usually saturated with molecules that can nonspecifically adsorb to sensor surfaces. Graphene is stable in both air and fluid, is nonreactive with biological species and has a relatively low cost as compared with its solid-state counterparts. Since its discovery in 2004 and further materials characterization in 2005, it has surfaced as a clear contender for choice of electrode material in applications pertaining to electrochemical analysis, biodetection and energy storage.

1.6.2 Graphene Charge Transfer Kinetics at the Edge vs. the Basal Plane

Electron transfer kinetics are measured with rate constants, often termed k_o. In a redox reaction couple, the rates at which the reagent A can oxidize (donate electrons) into B and B can reduce (gain electrons) back into A are related by the following expression:

$$A \rightleftharpoons_{k_b}^{k_f} B + e^- \tag{1.30}$$

where the rates of oxidative and reducing electron transfer, k_f and k_b, respectively can be much faster as compared to the rate of mass transport, depending on the electrode size, preparation and

surface characteristics. We will expand on this more in Chapter 2. It is important to note that throughout this thesis we will consider the oxidation step from reduced species (from *A* to *B+e-)* as the forward reaction and the reverse as the backward reaction, with transfer rate constant are given as defined above.

While there have been several efforts to study the electrochemical properties of graphene, definitive conclusions about charge transfer kinetics of the material have been hindered by the vast differences in sample preparation. There has been much speculation about charge transfer being more dominant along the edge sites of graphene than along the basal plane; however, few recent studies have revealed fast electron transfer kinetics at the pristine basal plane as well [53c].

At the molecular level one can identify two distinct regions in a graphene sheet: (1) the basal planes, consisting of two-dimensional conjugated sp^2 carbon atoms and (2) the edge regions, atom-thick line of carbon atoms with dangling bonds and other functional groups (hydrogen, hydroxyl, carbonyl and carboxyl). The two distinct regions can be seen in Figure 1.18. It has been reported by Yuan *et al.* [55] that the graphene edges show 4 orders of magnitude higher specific capacitance, much faster electron transfer rates and stronger electrocatalytic activity than the graphene basal plane [56-59]. It has also been reported that the surface defects of highly oriented pyrolytic graphite (HOPG) in the form of exposed edges exhibit a seven-fold increase in the transfer-rate constant as compared with the basal plane [60]. It is reasonable to think convergent diffusion is dominant at sub-nanometer graphene edge electrodes, whereas linear diffusional transport governs at the basal planes. However, very recent studies have shown that

the basal plane is not as inert as it has been thought to be and that electron transfer could also occur at the basal plane [61, 62].

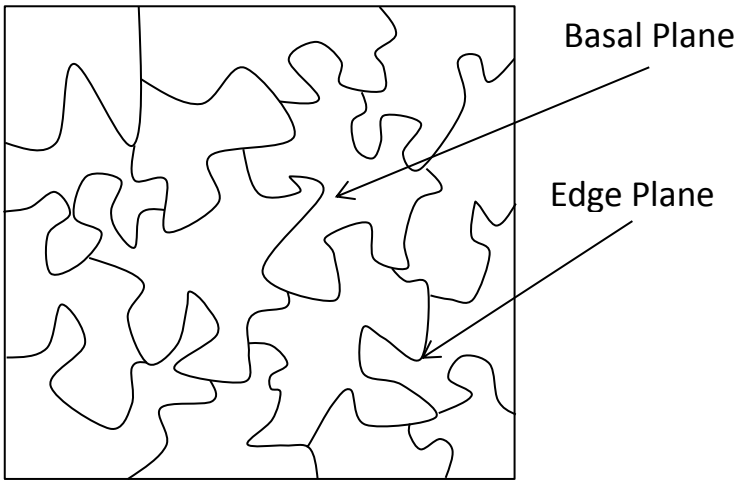

Figure 1.18 Schematic representation of graphitic surface showing the basal and edge plane islands

An important parameter of graphene as an electrode material is its Density of States (DOS). A higher DOS increases the probability that an electron of the correct energy is available for the electrodes to transfer. The DOS of gold is around 0.28 $atom^{-1}$ eV^{-1}. Gold's high conductivity stems from the combination of many atomic orbitals to form bands with a high density of states [16, 63]. HOPG (graphite) has a lower DOS than metal, being very low at the Fermi level, but can be increased through disorder; disorder increases the charge transfer rate by modifying the structure of carbon. A pristine basal surface area of HOPG has no edge planes, and thus no locations for functional groups nor dangling bonds. With disorder, such as roughening of the graphene surface to introduce holes or defects, the carbon symmetry is perturbed creating edge plane sites where electrochemical reactions can take place [63].

In terms of the DOS, HOPG can shed some light into understanding its electrochemical behavior.

For diffusional outer-sphere electron transfer processes, such as those explored in this thesis, the standard rate constant, k◦, can be defined as [64, 65]:

$$k^{\circ} = \frac{(2n)^2 \rho {H^{\circ}_{DA}}^2}{\beta h \sqrt{4\pi \Lambda}} exp\left[\frac{-\Lambda}{4}\right] I(\theta, \Lambda) \tag{1.31}$$

where ρ is the density of electronic states in the electrode material, ${H^{\circ}_{DA}}^2$is the electronic coupling matrix at the closest distance of approach, Λ = (F/RT) Λ, where Λ, is the reorganization energy, β is the corresponding electronic coupling attenuation coefficient, h is Planck's constant, F is Faraday's constant (96485 C mol^{-1}), R is the gas constant (8.314 J $mol^{-1}K^{-1}$) and T is the absolute temperature. $I(\theta, \Lambda)$ is an integral given by [65]:

$$I(\theta, \Lambda) = \int_{-\infty}^{\infty} \frac{\exp[-\frac{(\varepsilon-\theta)^2}{4\Lambda}]}{2\cosh\left(\frac{\varepsilon}{2}\right)} \tag{1.32}$$

where $\theta = F/RT(E - E_f^0)$, and E_f^0 is the formal potential. There is a direct relationship between the DOS and the electrochemical rate constant.

It has been reported that the DOS is 0 at the Fermi level for the basal plane of a pristine graphene sheet, and that the DOS increases with edge defects [66, 67]. Edge plane sites, thus, have been reported to have high DOS [67]. A variable DOS has been reported depending on the termination [68, 69]. This would imply pristine graphene with no defects would exhibit poor electrochemical performance and that with large number of defects would exhibit improvements in the transfer rate constant.

Calculations reported by Strano et al [70] suggest that double layer graphene is more reactive than single layer graphene as given by the DOS (1.6 times more reactive). However, experimental results confirm otherwise [71]. Those presented in this study show no significant difference at the macro-electrode scale. Higher electrode sensitivity, however, is observed in bi-layer and multi-layer electrodes that have been scaled down enough below 50 μm. This can be attributed to a "microelectrode edge" effect.

At a macroelectrode, electrolysis takes place across the entire electrode such that the diffusion is planar. Such current response is coined as "diffusion-limited". At the edges of the macroelectrode, diffusion is no longer onto a planar surface, but rather converges around a point, namely, the edge. Consequently, the flux and rate of mass transport are much larger at the edge. Such effect is negligible at larger electrodes because the contribution due to this type of "convergent diffusion" is small compared to the of planar diffusion activity. But as the electrode scales down to a few micron (~ < 30 microns or so), convergent diffusion becomes more significant and changes in the voltammetric response are noticeable, such that the traditional "peak" observed in diffusion-limited cyclic voltammetry is lost, and is replaced by a sigmoidal type of behavior. The different diffusional processes are depicted in Figure 1.19. We will examine the differences between linear and spherical diffusion in the Chapter 2 and Chapter 4.

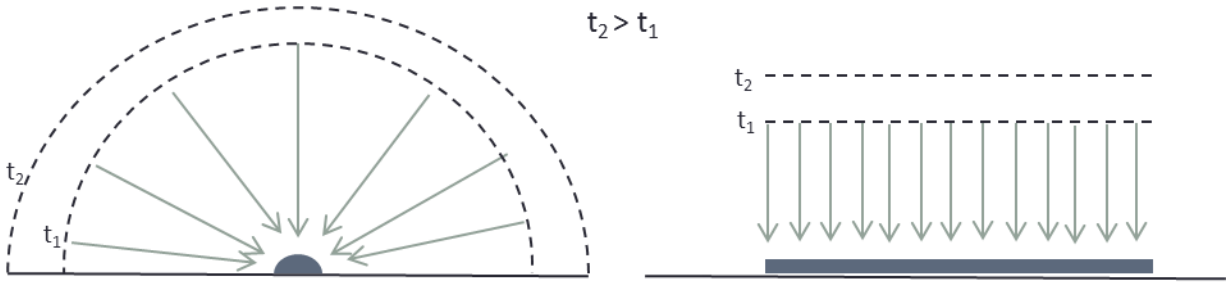

Figure 1.19 Depiction of radial diffusion processes (left) occurring in a spherical ultramicroelectrode versus linear diffusion of a planar large electrode.

Compton et al succeeded in fully characterizing HOPG [72, 73] confirming edges play a larger role than basal regions in the total electron transfer kinetics. They compared the responses to a simulated electrode assuming linear diffusion only, assuming all surface areas are uniformly electrochemically active. As expected, their findings show that the peak-to-peak separation is much greater for the simulated linear diffusion profile of Basal Plane Pyrolitic Graphite (BPPG) electrodes than for the edge plane pyrolitic graphene (EPPG) electrode.

Brownson et al. simulated HOPG as a heterogeneous surface consisting of basal plane islands and surrounding edge-plane bands, treated as a disc-shaped region of edge-plane graphite. Each island and its respective band is surrounded by other islands (and bands) and little to no net flux is assumed to take place from one island to the adjacent one [72, 74]. Thus, each island and edge bands are treated as an independent unit cell and the total voltammetric response it the sum all of all domains. Figure 1.20 illustrates this single unit diffusion domain in detail. The radius of the whole unit cell is termed R_o. It includes the width of the edge plane. The radius of the basal domain is R_b. Thus, the edge bands only occupy a fraction of the total surface coverage. This allows them to compute the effect of varying the edge planes, while keeping the total coverage constant.

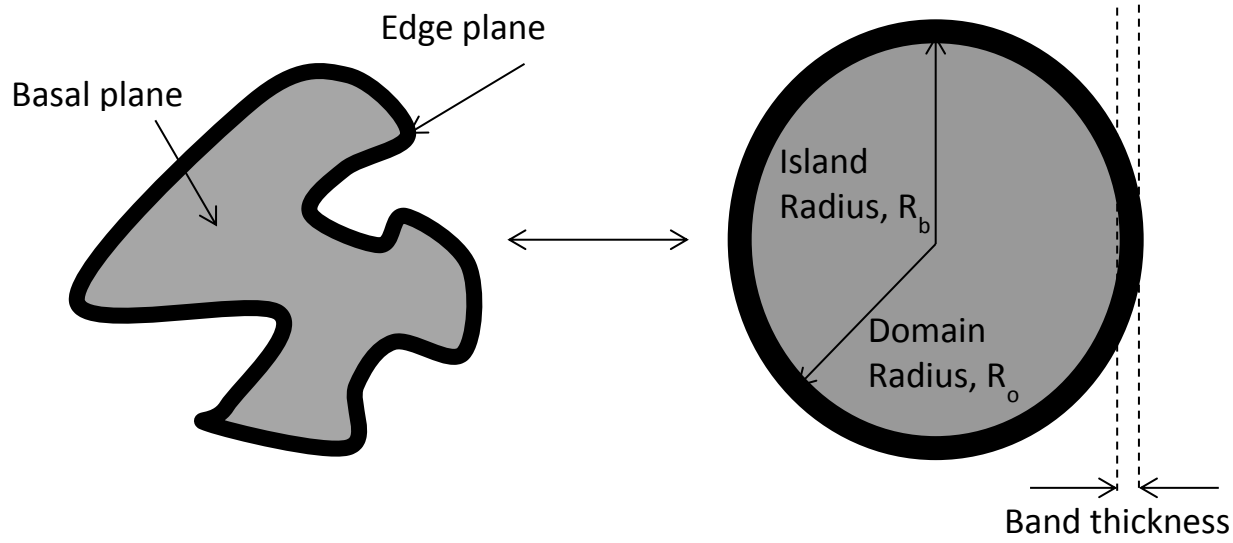

Figure 1.20 Schematic showing the approximation of a graphitic island and edge as a disc with the same area

They found that the peak-to-peak separation is strongly correlated to the edge plane coverage, independent of domain size for smaller domain sizes (<1 mm). This is expected, as the effect of convergent-diffusion plays less and less of a role as the domains increase. Their analysis concluded that most of electrocatalytic activity took place at the edge nanobands and that the basal islands were relatively inert to electroactivity for the redox of ferrocyanide. It is important to accurately define the meaning of the word "inert" in this context. Given that there are separate heterogeneous rate constants for basal and edge plane site reactions, it is expected that the voltammetric profile be the superposition of the voltammetry of the edge band and that of the basal plane. If these rate constants are similar in magnitude, two peaks at close enough potential would be observed such that they would merge into a larger peak. However, two separate peaks have never been observed. Thus, it has been concluded that the basal plane constant doesn't have measurable activity, that is, it is much slower than that of the edge plane and therefore, considered inert. Davies *et al.* and Ward *et. al* have examined this concept [72, 75]. Davies' work in particular [76] blocked the basal plane of HOPG and obtained identical voltammograms

to that obtained with the unmodified electrode.

1.6.3 Advantages of Carbon Electrodes over Solid State Electrodes

Carbon electrodes are preferred over solid-state electrodes for a variety of reasons. The single most important advantage is biocompatibility. Carbon is the unit cell of all organic compounds, and as such, is a preferred interface for biological specimens. It also has a wider potential window and is relatively nonreactive to measurements. In addition, it is robust, lower in cost and more readily available than it solid-state counter parts. Over the last 20 years carbon electrodes have seen extensive development, production and utilization for the same types of applications as their solid-state counterparts. These will be discussed in more detail in Chapter 2.

1.6.4 Advantages of Graphene Electrodes over other Carbon Electrodes

Graphene has several advantages over other carbon-based electrodes. Mainly, it's two-dimensional one atom thick hexagonal lattice structure grants it with flexibility and the largest 2D conductivity of any organic material. In addition, it doesn't require a metal catalyst for growth as do carbon nanotubes. Metal catalyst residues, such as iron, are cytotoxic to cells, and thus, undesirable in the fabrication process of any sensor whose intended use is to interface biological species.

1.7 Selection Criteria of Carbon Electrodes

The selection criteria of carbon-based electrode depend on the specified needs of an application. One of the most important criteria is that an electrode has low background noise, or namely, background currents. Like other electrode materials, carbon-based electrodes exhibit a small capacitive or charging current. Any excess currents over a given potential range are result of redox processes. Large capacitive currents can obscure any observable reactions taking place on the electrode surface [14, 77, 78].

A second critical performance criterion is the potential window. The potential window must be such that allows for a specific reaction to be observed without electrode oxidation/corrosion/degradation, etc.. Carbon has a competitive advantage over its solid-state counterparts because of its larger oxidation window, which comes at the cost of slower transfer kinetics, our third performance criterion [14, 77, 78].

An electrode must also be able to yield reproducible and stable results. Surface preparation and fabrication protocols play a major role in the latter. Lack of careful graphene transfer, adsorption of surface contaminants, or insufficient passivation can lead to false positive results and ghost currents, resulting from conductive electroactive impurities on the electrode surface or leakage currents through pores in the passivation layers on contact lines.

Lastly, and perhaps most important are the criteria of electrode performance are sensitivity, detection limit and linear range of detection. An electrochemical electrode's ultimate goal is to

detect miniscule quantities of an analyte linearly over a given range, and with sufficient signal amplification to detect small changes, regardless of background noise currents [79].

1.8 Organization of Thesis

This dissertation presents the design, fabrication, packaging and testing of a graphene microelectrode array on multiple substrates/graphene types for neurochemical detection. Chapter one has outlined some of the necessary background information for this work, starting from the different properties of carbon, specifically graphene, all the way to its inherent advantage as an electrode material. Chapter 2 will focus on the electrochemical properties and requirements of electrodes, focusing on the techniques for analyte detection and on the fundamental understanding of their respective reactions at the electrode-electrolyte interface. Chapter 3 describes the design, fabrication, packaging and testing protocols for the different microelectrode arrays. It also details the different obstacles associated with fabrication, device parasitics associated with materials and geometry and improvements to be made upon for future generation devices.

Chapter 4 describes the performance across all different types of devices, making a cross comparison across devices of 1, 2 and multiple layers on SiO_2, epitaxial material and CVD material grown on sapphire. The sensitivity, detection limit, effective electrode areas and electron-transfer kinetics are examined across the different types of graphene. Chapter 5 details the optimization of device performance through the increased exposure and functionalization of edges. Finally, Chapter 6 examines the potential use of such electrodes against neurochemical probes such as dopamine. We conclude with suggestions for future directions of this research.

CHAPTER 2

OVERVIEW OF ELECTROCHEMICAL SENSING

2.1 Electrochemical Sensors

Electrochemical sensors and sensing is an interdisciplinary subject that lies at intersection of the fields of physical and analytical chemistry, biochemistry, materials science, micro- and nanofabrication, solid-state physics, electrical engineering, signal processing, and even noise and statistical analysis. An electrochemical sensor is defined as a device or platform that is able to selectively and reversibly convert or transduce chemical or biological information in the proximity of its interface to the environment into an analytically relevant and useful signal. This is done by studying the phenomena that occur at the sensor surface with the passing of current through a solution electrolyte.

Chemical sensors target the measurement of a specific chemical or molecule, whereas biosensors, being a subset of the latter, are defined as sensors that use biomolecules and/or structures to measure something biologically significant.

Within the field of sensors, optical, thermal and mass-based sensors have also been well characterized and fully implemented [80-87]. Electrochemical sensors, however, are more desirable from the analytical perspective due to their ability of directly converting chemical information and events into an electrical signal in a robust, highly sensitive, inexpensive and experimentally simple way. Unlike their optical counterparts, electrochemical sensors do not

make use of complex instrumentation such as optics. Also important is the fact that detection depends on the activity at the electrode surface. Consequently, sample volumes can be fairly small and this lends itself to their miniaturization.

The widespread use of electrochemical sensors depicts the strong bearing they have cast in daily life, the industry and the academic sciences, where they have continued to be studied, improved thereupon and miniaturized to meet the demands of highly effective, fast, reproducible, portable and relatively low cost determination of analytes. Electrochemical sensing has been widely implemented in many different branches of the automotive, hygiene, process and quality control, environmental, clinical diagnostic, homeland security, and medical industries, among others [88]. Specific species, such as PO2, H_2O_2, CO_2 and pH can be traced purely through electrochemical methods [89]. Enzymatic sensors, a type of biosensor, are functionalized with enzyme catalysts alongside the electrochemical sensing element.[90-99] In neurophysiology, some electrodes can detect up to picomolar (pM) quantities of neurotransmitters [100-101], while others can track changes in ionic currents across the cell membrane of specific neurons. In all, electrochemical sensing is a robust and well-developed technique to gain real-time information by *in situ* measurements of chemical composition without sampling[2].

With the advent of photolithography and other nanofabrication techniques, the discovery and synthesis of new materials and the refinement of existing sensing techniques, instrumentation and data analysis, the path has been paved for the creation of new generations of electrochemical sensors with improved overall performance and biocompatibility.

2.1.1 History of Electrochemical Sensing

Electrochemical sensing dates back to the 1800's, when English chemists William Nicholson and Johann Wilhelm Ritter were able to separate water into its atomic components, hydrogen and water, by electrolysis. The first glass electrode was developed by Cremer in 1906 [102]. Glass electrodes are commonly used for pH measurements. There are also ion sensitive glass electrodes used for the detection of concentration of lithium, sodium, ammonium, and other ions. Haber and his student Klemensiewicz took up Cremer's idea and made the basis for analytical applications [103], publishing the results of their research on 28 January 1909 in The Society of Chemistry in Karlsruhe. While Cremer should be given full appreciation of the invention of the glass electrode, Haber dominates the literature [104].

By the early twentieth century, the concept of electroanalytical chemistry had also emerged as electrocapillary measurements were conducted with dropping mercury electrodes, otherwise known as polarography. Such technique enabled the beginning of voltammetry and granted Jaroslav Heyrovský the Nobel Prize in Chemistry [105]. Early voltammetry techniques suffered from many limitations, restraining their viability for everyday use in analytical chemistry. In 1942 Hickling designed and implemented the first three-electrode potentiostat [106].

Historically, the very first amperometric sensor was the oxygen electrode developed by L.C. Clark [107]. In his design, oxygen was allowed to enter through a gas-permeable membrane, and was then subsequently reduced to water at a noble metal cathode. Using his oxygen electrode design to determine the depletion of oxygen by the action of glucose oxidase on glucose [108],

Clark also put forward the designs for the first glucose biosensors in 1962.

With the invention of computers, many advances in the instrumentation of controlled systems in the 1960s and 1970s were possible. These, in turn, improved sensitivity and created new analytical methods. Since then, the industry has responded with the production of cheaper potentiostats, electrodes, and cells that could be effectively used in routine measurement work. Today, about 50 years after Clark invented the first oxygen sensor electrode, Hu *et al.* [109] have reported an oxygen sensor based on an inkjet-printed nanoporous gold electrode array on cellulose membranes using ionic liquid as electrolyte. The sensor looks like a piece of paper but possesses high sensitivity for O_2 in a linear range from 0.054 to 0.177 v/v%.

2.1.2 Principles of Electrochemical Sensing

An electrochemical cell is comprised of at least two electrodes separated by, though making contact to, a conducting (electrolyte) solution. An electrolytic cell is one in which reactions change in response to an applied external potential greater than the open-circuit potential of the cell. This applied potential drives chemical reactions at the electrode surfaces, mainly redox reactions, where sample analytes (usually the species of interest) found in the electrolyte oxidize (donate an electron) or reduce (accept an electron) with an applied potential. The electrode at which reductions occur is called the cathode, whereas the electrode at which oxidations occur is the anode. Cathodic currents are produced when electrons cross the electrode-electrolyte interface from the electrode to the species in the solution. In the opposite scenario, where electrons flow from the solution species to the electrode, an anodic current is produced.

The overall chemical reaction taking place in a cell is made of two independent half-reactions that describe the chemical changes at the two electrodes. Generally we only care about the reactions occurring at one of the electrodes, the working electrode (WE). To do so, the other electrode must be standardized by using an electrode of constant composition, the reference electrode (RE). At this electrode, the potential is fixed, and hence any changes observed in the cell can be attributed to chemical reactions taking place at the working electrode. It is thus said that the potential of the WE with respect to the RE is the one being changed. Lastly, there is an auxiliary electrode (AE) to supply current to the WE without changing the potential of the RE. In a two-electrode setup, the RE is also an AE, but it is harder to maintain a constant potential while supplying current. Therefore, three-electrode setups have become more popular in electroanalysis.

The electrolyte solution is the medium between the electrodes. Its main goal in controlled-potential experiments is to decrease the solution resistance, reduce or eliminate electromigration phenomena, and maintain a constant ionic strength. Typically, it consists of solvents with a high concentration of an ionized salt as well as the electro-active species being studied (termed the analyte). The choice of solvent depends of the solubility of the analyte and its oxidation (and reduction) activity, as well as the inherent solvent properties such as electrical conductivity. The solvents should be inert to the analyte (not react with it) and show stability over time. It can be an inorganic salt (potassium chloride), a mineral acid or a buffer (phosphate sodium bicarbonate). Figure 2.1 depicts a typical experimental setup in an electrolytic potential cell, both for a two- and three- electrode setup. A potentiostat is used to control the cell potential.

Sometimes a Faraday cage is used to reduce induced noise currents from other electromagnetic field sources in the laboratory. It is usually constructed form stainless steel and is designed to enclose the electrochemical cell and electrodes. When connected to the potentiostat ground it forms an extended electrical shield around the experimental setup.

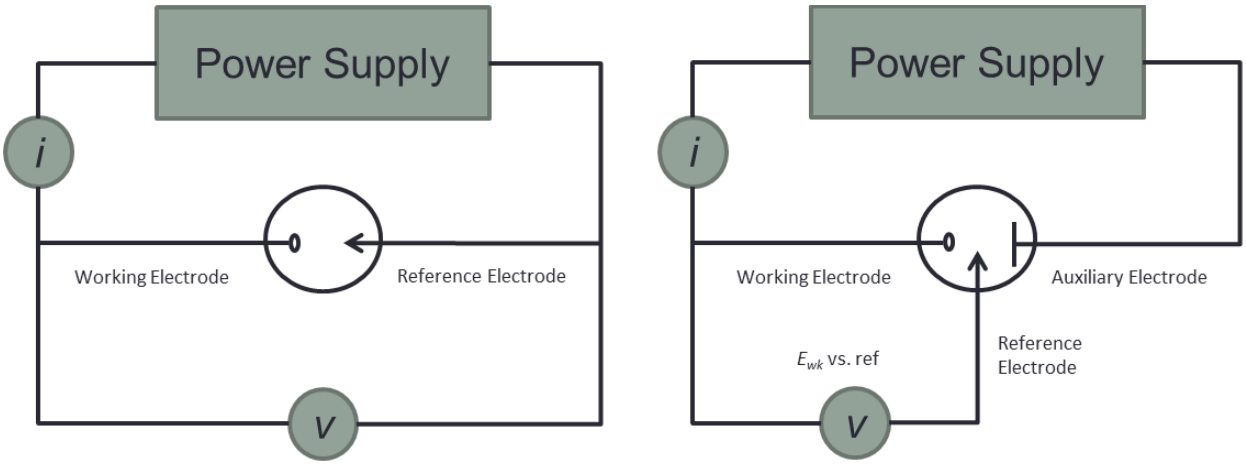

Figure 2.1: (Left) Two-electrode electrochemical cell. (Right) Three-electrode electrochemical cell.

2.1.3 Types of Electrochemical Sensors

Electrochemical sensors can generally be categorized as potentiometric, voltammetric, or conductimetric sensors. Their high selectivity, simplicity and low cost make potentiometric sensors desirable in field operations. However, their voltammetric counterparts have proven to be faster and more sensitive. An increasing amount of research being carried out on amperometric sensors has also shadowed the development and use of potentiometric devices. Other sensors rely on conductivity changes in ions, while others work by monitoring resistivity and impedance, such as chemiresistors and capacitive sensors. Conductimetric sensors do not really operate on an electrochemical reaction or basis and are thus usually referred to as chemical electrical sensors as

opposed to electrochemical sensors [110].

Electrochemical sensors are simply an electrochemical cell which makes use of a two or three-electrode setup. One electrode serves as a working electrode while the other is a reference electrode with respect to the fluid potential. It may also be used to supply electrons to the electrochemical reaction. However, in three-electrode setups an auxiliary electrode is also used to support the latter function, without perturbing the fixed potential of the reference electrode. Measurements can be made at steady-state or transient. The applied current or potential for electrochemical sensors may vary according to the mode of operation, and the latter is often chosen to improve the sensitivity and selectivity of a particular sensor.

2.1.3.1 Potentiometric Sensors

Potentiometric sensors work by converting the chemical reaction into a potential signal, which is logarithmically proportional to the concentration (activity) of species generated or consumed in the chemical reaction. The electrode potential is related to the concentration of species through the Nernst equation (as it relates to equation 1.30).

$$E = E^{o\prime} + \frac{RT}{nF} ln \frac{C_B^*}{C_A^*} \tag{2.1}$$

Where $E^{o\prime}$ is the standard electrode potential (relative to the Standard Hydrogen Electrode, SHE) and C_A^* and C_B^* are the respective concentrations of the reduced and oxidized species in the electrolyte at the bulk, R is the universal gas constant; T is the absolute temperature; F is the

Faraday constant; *n* is the number of electrons exchanged in the electrochemical reaction. We will derive the Nernst equation later in this Chapter. For now we will make note that the Nernst equation is usually written with forward reduction processes in mind and we have written it to conform to the experimental procedures in this thesis.

The most well-known potentiometric sensor is the ion selective electrode [111-118]. The ISE can selectively measure the concentration of a particular analyte ion. An ion-selective membrane at the tip of the electrode sensing surface measures a potential signal that is selective for the target ion. This potential signal is generated by a charge separation at the interface between the ion-selective membrane and the solution due to selective partitioning of the ionic species between these two phases.

2.1.3.2 Voltammetric Sensors

The current-potential (I-V) relationship of an electrochemical cell provides the basis for voltammetric sensors. Specifically, voltammetry examines the effect the concentration of the species of interest has on the current-potential response as it is oxidized or reduced in the vicinity of the electrode surface. The current-potential properties are directly affected by the rate of mass transfer of the detecting species in the reaction onto the electrode surface and the kinetics of the faradaic or charge transfer reaction at the electrode surface.

Amperometric sensors are a subset of voltammetric sensors. Unlike voltammetry, where the applied potential is increased (or decreased) linearly, the potential applied to the working electrode is held constant while the current is monitored.

The described voltammetric and amperometric sensors are very effective and robust to qualitatively and quantitatively detect and analyze chemical and biological species. The techniques are very well established. The main, yet exciting, challenge that remains is their applicability in complex and practical environments, such as tissue or blood. The measurements in this dissertation are voltammetric in nature.

2.1.3.3 Conductimetric Sensors

Conductance electrochemical sensors monitor changes in the conductance of an electrolyte, which changes as the specific conductivity changes in response to the concentration and magnitude of the charges in the ionic species in solution.

2.1.3.4 Other types of Electrode Sensors

In addition to the standard electrochemical sensors there are other classes of sensors that can transduce a biological or chemical signal without carrying out any electrochemical reactions. These include, but are not limited to:

- Optical/infrared: Monitor biological activity with light diffraction patterns. This sort of scheme is coupled with nanophotonics. For instance, by functionalizing nanopores or nanocavities with a target biological entity, it can then be identified through a signature diffraction pattern [119].

- Piezoelectric: Can monitor activity through changes in strain, pressure or acceleration. Makes use of a piezoelectric (PZT) material such as ceramics and single crystal materials that are sensitive to slight perturbations (i: mass changes) on the surface [120-127].

- Impedance: The working principle of this type of sensor is that the resistance of the sensor surface changes in response to chemical or biological activity [128-137]. The most prominent example of this is the semiconducting oxide sensor. When exposed to a target gas, it reacts with the metal oxide surface and changes its electronic properties. Such devices are sometimes called chemiresistors [88].

- Capacitance: These are usually integrated with Micro-Electrical-Mechanical Systems (MEM). Slight changes in mass on a cantilever beam can induce changes in the capacitance of a parallel plate capacitor defined with the cantilever. Other methods make use of a chemically sensitive polymer as a dielectric [138]. This polymer will swell and change the capacitance of the sensor element in presence of the analyte of interest.

- Ion-selective: Ion-selective electrodes (ISE) belong to the group of potentiometric sensors. They measure the change in interfacial potential at the electrode surface caused by an ion selective reaction [88].

- Solid-state electrodes: These types of electrodes replace the liquid electrolytic interface with a solid one, and are convenient for many high temperature type measurements. They are effective in the detection of liquid or gaseous analytes [88].

2.1.4 Applications of Electrochemical Sensors

Electrochemical sensors can be employed for the detection of solid, oxygen, hydrogen, carbon monoxide (and dioxide) and nitrogen oxides been have put forward in the steel, automotive, military and aerospace industry. Sensors to trace bacteria, fungal toxins, pH and humidity are prominent within the food industry as well as in environmental applications. Indoor air quality, toxic and combustible gases are detected with sensors in the industrial safety sectors and chlorine, lead and other mineral trace materials are constantly monitored with electrochemical sensors in water treatment processes. Table 2.1 summarizes the main applications and markets for chemical sensors to date [88].

Table 2.1: Exemplary Applications and Markets for Electrochemical Sensors [88]

Market/Application	Example of Detected Chemical Compounds
Automotive	CO, O_2 ,H_2 ,NO_2, HC_3
IAQ	CO, CH_4, CO_2, humidity, VOC_5
Food	Bacteria, fungal toxins, biologicals, chemicals, humidity, pH, CO_2
Agriculture	NH_3, CO_2, amines, humidity, pesticides, herbicides
Medical	Glucose, urea, O_2, CO_2, pH, Cl^-, K^+, Na^+, Ca^{2+}, infectious disease, bio-molecules, anesthesia gases
Water treatment	pH, Cl_2, CO_2, O_2, O_3, H_2S
Environmental	pH, CO_2, H_2S, HC_3, NH_3,heavy metal ions
Industrial Safety	Indoor air quality, toxic gases, combustible gases, O_2
Utilities (gas, electric)	O_2, CO, HC_x, NO_x, SO_x, CO_2
Petrochemical	HC_x, conventional pollutants
Steel	O_2, H_2, CO, conventional pollutants
Aerospace	O_2, H_2, CO_2, humidity
Military	Agents, explosives, propellants

A subset of electrochemical sensors is biosensors. These aim to use electrochemical techniques to detect biological processes using immobilized biomolecules as recognition elements on the surface of the electrode transducer. The specificity and selectivity that a biosensor delivers is due to this immobilized biological recognition group. To date, there are hundreds of different kinds of biosensor electrodes to detect glucose, cancer biomarkers, DNA and many other proteins of interest.

2.2 Kinetics of Electrode Reactions

This thesis examines the electrochemical response of graphene electrodes using cyclic voltammetry. In this section we want to quantitatively describe the electrode surface kinetics with respect to the electrode potential and concentration to then later arrive at a derivation of current with respect to these two experimental controls.

2.2.1 Essentials of Electrode Reactions

Electrode reactions are more complex than those occurring in solution or gas phase because they do not occur at the same rate everywhere within the medium. Such reactions are termed homogeneous. An electrode process is a heterogeneous reaction that occurs only at the electrode-electrolyte interface. Its rate is dependent on mass transfer to the electrode and surface effects, in addition to the typical kinetic parameters involved. Reaction rates are usually described in terms of mol/s per unit area:

$$\text{Rate}(\text{mol}\, s^{-1}\text{cm}^{-2}) = \frac{dN}{dtA} = \frac{i}{nFA} \tag{2.2}$$

Here i is the current, A is the area, F is Faraday's constant and n are the number of electrons consumed in the electrode reaction. Here we are letting the current $i = dQ/dt$ and the number of moles electrolyzed is given by $N = Q(coulombs)/nF(coulombs/mol)$.

It is often useful to express electrode reactions as a function of the applied potential. The term to describe the departure of the electrode potential from its equilibrium value upon passage of faradaic current is coined polarization. The extent of polarization is measured by the overpotential, η.

$$\eta = E - E_{eq} \tag{2.3}$$

Where E_{eq} is the equilibrium potential and *E* is the electrode potential.

2.2.2 Potential Barriers

If we consider the redox process given by equation (1.30) ($A \rightleftharpoons^{k_f}_{k_b} B + e^-$) we can relate the rate of the forward and reverse processes as:

$$v_f = k_f C_A \quad \text{and} \quad v_b = k_b C_B \tag{2.4}$$

Where the rate constants k_f and k_b have units of s^{-1} and the concentration of species A and B is given by C_A and C_B, respectively. These are the reciprocals of the mean lifetime of the species A and B. Rate constants of solution-phase solutions vary with temperature, with *ln k* being linear

with 1/T. The Arrhenius relationship allows us to express such rate constant as the probability of surmounting an energy barrier, the activation energy, E_A, time the number of attempts on it, otherwise known as the frequency factor, A.

The activation energy is the standard internal energy in going from initial reactants to a transition state or activated complex, prior to arriving to the final products of the reaction. It is often designated as the standard internal energy of activation, $\Delta E^{\ddagger}$. The standard enthalpy of activation, $\Delta H^{\ddagger}$ would then be given by $\Delta E^{\ddagger} + \Delta(PV)^{\ddagger}$, but $\Delta(PV)^{\ddagger}$, is usually negligible so $\Delta E^{\ddagger} \approx \Delta H^{\ddagger}$. The frequency factor can be expressed as the product $A'\exp(\Delta S^{\ddagger}/R)$, which involved the standard entropy of activation $\Delta S^{\ddagger}$. We can now rewrite our transfer rate constant as:

$$k = A' e^{\Delta H^{\ddagger} - T\Delta S^{\ddagger}/RT} = A' e^{\Delta G^{\ddagger}/RT} \tag{2.5}$$

Where $\Delta G^{\ddagger}$ is the standard free energy of activation.

The total reaction rate, as expressed in Equation 2.2 is the sum of the forward current and the reverse current. Throughout this thesis we define our forward current as the oxidation of species onto the electrode surface and thus, anodic. The backward reaction is a reduction process, thus yielding a cathodic current. In many texts the forward current can be defined as the cathodic current, whereas the anodic is considered the reverse current. The net reaction rate is then:

$$v_{net} = v_f - v_b = k_f C_A(0,t) - k_b C_B(0,t) = \frac{i}{nFA} \tag{2.6}$$

and we can express the current as:

$$i = i_a - i_c = nFA\left[k_f C_A(0,t) - k_b C_B(0,t)\right] \tag{2.7}$$

Reaction velocities in heterogeneous systems refer to unit interfacial area and have units of mol s^{-1} cm^{-2}. Thus heterogeneous rate constants must carry units of cm/s if the concentrations are expressed as mol/cm^3. The interface can only respond to its surroundings and the concentrations entering rate expression are always surface concentrations, which may differ from those of the bulk solution.

When the potential is changed to a new value by ΔE, the relative energy of the electron on the electrode surface changes by *-F ΔE=-F(E-E^o).* The barrier for oxidation under no applied bias, $\Delta G_{oa}^{\ddagger}$ is lowered (less energy required to donate an electron) and the barrier for reduction processes, $\Delta G_{oc}^{\ddagger}$ increases, as depicted in Figure 2.2, by a fraction of the total energy change.

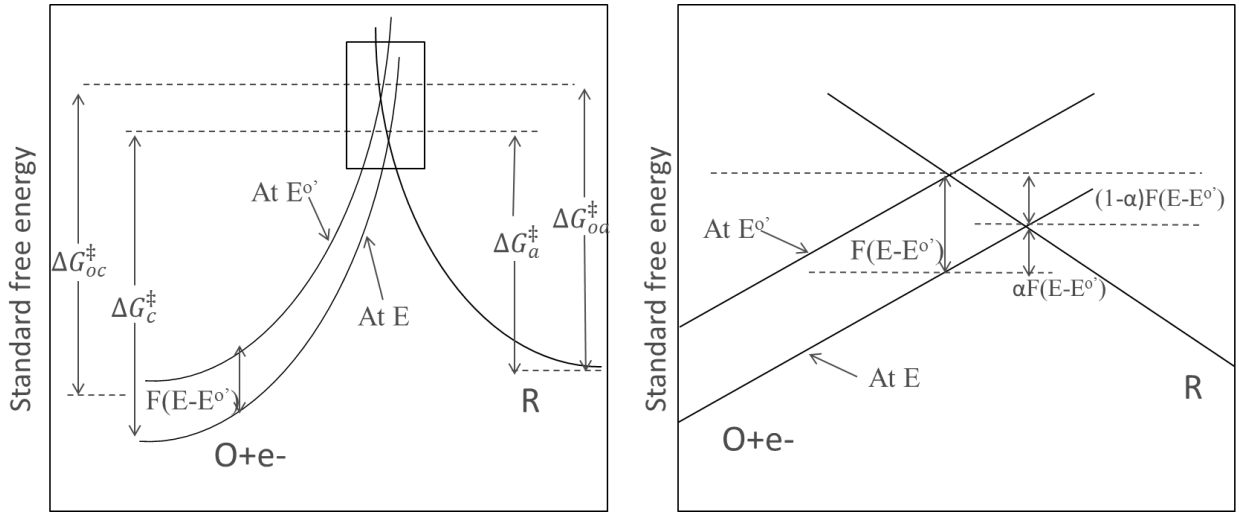

Figure 2.2 Effect of potential change on the standard free energies of activation for oxidation and reduction. The frame on the right is a magnified view of the boxed area on the frame on the left.

We call that fraction 1- α and α, respectively for the oxidative and reduction barriers (the barrier for a reduced species to oxidize to donate an electron and the barrier for an oxidized species to reduce by gaining an electron). α is the transfer coefficient and can range from 0 to unity. More specifically, it is a measure of the symmetry of the energy barrier between reactions. We can write the standard free energy for the anodic (oxidation process) and cathodic (reduction process) barriers as follow:

$$\Delta G_a^{\ddagger} = \Delta G_{oa}^{\ddagger} - (1-\alpha)F(E - E^{0'}) \tag{2.8}$$

$$\Delta G_c^{\ddagger} = \Delta G_{oc}^{\ddagger} + \alpha F(E - E^{0'}) \tag{2.9}$$

The transfer rate constants as given by equation 2.5 then become:

$$k_f = A_f \exp(-\Delta G_{oa}^{\ddagger}/RT)\exp[(1-\alpha)f\left(E - E^{0'}\right)] \tag{2.10}$$

$$k_b = A_b \exp(-\Delta G_{oc}^{\ddagger}/RT)\exp[-\alpha f\left(E - E^{0'}\right)] \tag{2.11}$$

Where we have let *f=F/RT*. Do note that the first 2 factors for a product independent of the potential and equal to the rate constant at $E=E^{0'}$. In the special case in which the interface is at equilibrium with a solution where the bulk concentrations, C_A and C_B are equal, $E=E^{0'}$, and $k_f C_A = k_b C_B$, the rate constants are also equal to one another. That value is called the standard rate constant, k^0. The rate constants at other potentials can then be expressed in terms of k^0.

$$k_f = k_0 \exp[(1-\alpha)f\left(E - E^{0'}\right)] \tag{2.12}$$

$$k_b = k_0 \exp[-\alpha f\left(E - E^{0'}\right)] \tag{2.13}$$

Insertion of these relations into equation 2.7 yields the complete current-potential equation:

$$i = i_a - i_c = nFAk_0[C_A(0,t)\exp[(1-\alpha)f\left(E - E^{0'}\right)] - C_B(0,t)\exp[-\alpha f\left(E - E^{0'}\right)]] \quad (2.14)$$

2.2.3 The Standard Rate Constant

The transfer rate constant has a very straightforward interpretation. It is but a measure of how easy a redox couple can react from and oxidized to a reduced state and vice-versa. A large value of k^0 will achieve equilibrium on a short time scale, whereas a system with a low value of k^0 will be sluggish. The range of values for k^o vary between 10 cm/s down to 10^{-9} cm/s/. Therefore, in electrochemistry there is a range of more than 10 orders of magnitude in kinetic reactivity.

2.2.4 The Transfer Coefficient

As mentioned, the transfer coefficient is a measure of the symmetry of the energy barriers. It can be understood by examining the geometry of the intersection region as depicted in Figure 2.3.

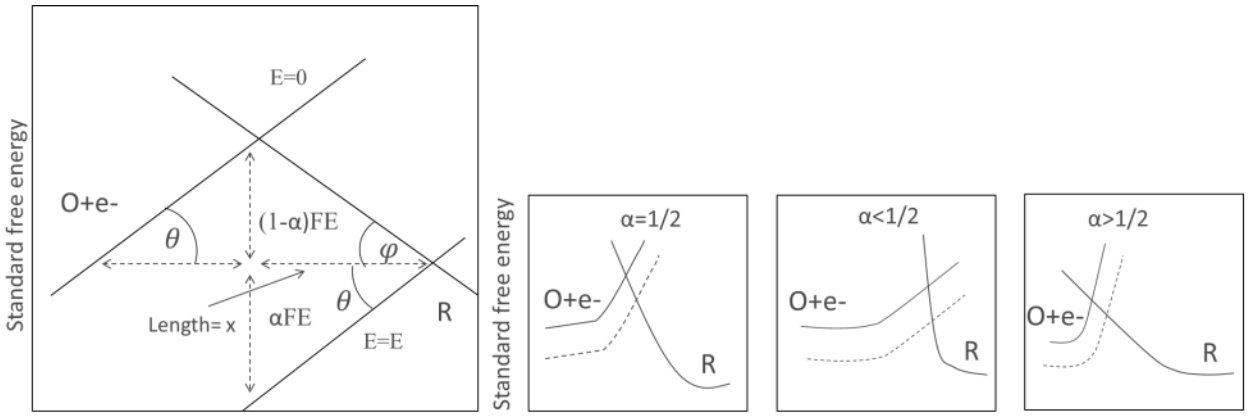

Figure 2.3(Left) Relationship of the transfer coefficient to the angles of intersection of the energy barrier curves. (Right) Transfer coefficient as an indicator of the symmetry of the barrier to reaction.

If the curves are locally linear, then the angles θ and φ can be expressed as:

$$tan\theta = \alpha FE/x \tag{2.15}$$

$$tan\varphi = (1-\alpha)FE/x \tag{2.16}$$

Thus

$$\alpha = tan\theta/(tan\varphi + tan\theta) \tag{2.17}$$

If the intersection is symmetrical then $\varphi = \theta$ and α=1/2. Otherwise $0 \leq \alpha \leq 1/2$ or $1/2 \leq \alpha \leq 1$/ This is also depicted in Figure 2.3. In most systems α turns out to lie between 0.3 and 0.7 and it can usually be approximated by 0.5. In must be noted that the energy profile are not likely to be linear over large ranges of the reaction coordinate, that is φ and θ can be expected to change with shifts in potential. Even though α is potential-dependent, it has found to be constant over the narrow potential range over which experiments take place.

2.2.5 Equilibrium Conditions: The exchange current

At equilibrium the net current is zero and the electrodes adopt a potential based on the bulk concentration as described by the Nernst equation. At equilibrium the bulk concentrations are also found on the surface of the electrode. Even though the net current is zero at equilibrium there is still a balance of faradaic activity that can be expressed in terms of the exchange current, i_o, at the interface. The exchange current is equal in magnitude to the anodic or cathodic current.

$$i_o = FAk^0 C_A^* e^{(1-\alpha)f(E_{eq}-E^{o'})} \tag{2.18}$$

We can rearrange the Nernst equation in exponential form and raise it to the 1-α power to obtain:

$$e^{(1-\alpha)f(E_{eq}-E^{0'})} = \left(\frac{C_B^*}{C_A^*}\right)^{1-\alpha} \tag{2.19}$$

Substitution of 2.19 into 2.18 gives:

$$i_0 = FAk^0 C_A^{*\alpha} C_B^{*(1-\alpha)} \tag{2.20}$$

The exchange current is proportional to $k^0$and can be substituted for k^0 in kinetic equations.

2.2.6 The Current-Overpotential Equation

We can express the current as a function of the overpotential rather than the formal potential, $E^{0'}$.

$$i = i_0 \left[\frac{C_A(0,t)}{C_A^*} e^{(1-\alpha)fn} - \frac{C_B(0,t)}{C_B^*} e^{-\alpha fn}\right] \tag{2.21}$$

The first term on the right is the anodic current and the second term is the cathodic current. Equation 2.21 can be interpreted as follow. For large positive overpotentials the cathodic component is negligible. Similarly, for large negative overpotentials, the anodic current is negligible. In going in either direction from E_{eq}, the magnitude of the current rises quickly due to the exponential nature of the behavior, but levels off at extreme η.

For well-stirred solutions at which the surface concentrations are not that different from the bulk concentrations equation 2.21 becomes:

$$i = i_o\left[e^{(1-\alpha)f\eta} - e^{-\alpha f\eta}\right] \quad (2.22)$$

Equation 2.22 is known as the Butler Volmer equation. It is in good approximation of 2.21 when the current is less than 10% of the smaller limiting current (i_c or i_a). Since mass transfer is not involved (no concentration gradient), the overpotential only provides the activation energy to drive the kinetic heterogeneous reaction. The lower the exchange current the more sluggish the system is.

In the small limit of the overpotential, where η is still very small around E_{eq}, e^x can be approximated by $1+x$ and the current becomes

$$i = -i_0 f\eta \quad (2.23)$$

The net current is then linearly related to the overpotential in a narrow potential window around E_{eq}.

For large values of η one of the terms of 2.22 becomes negligible and the current can be expressed as:

$$i = i_0 e^{(1-\alpha)f\eta} \quad \text{or} \quad i = i_0 e^{-\alpha f\eta} \quad (2.24)$$

In the mass-transfer limited regime the approximate forms of the $i-\eta$ relationships outlined above are not valid. For large η species at the electrode surface are depleted and hence a concentration gradient drives the reactions at the surface. Usually plots of log $i\ vs.\ \eta$ are useful for examining the kinetics of slower reactions. These plots are known as Tafel plots and are

useful in examining the kinetics of systems with sluggish kinetics or large activation potentials. Such systems are usually irreversible. The Tafel plots for the cathodic and anodic branches are depicted in Figure 2.4. The slopes of these branches are given as $-\alpha F/2.3RT$ and as $1-\alpha F/2.3RT$ for the cathodic and anodic currents, respectively.

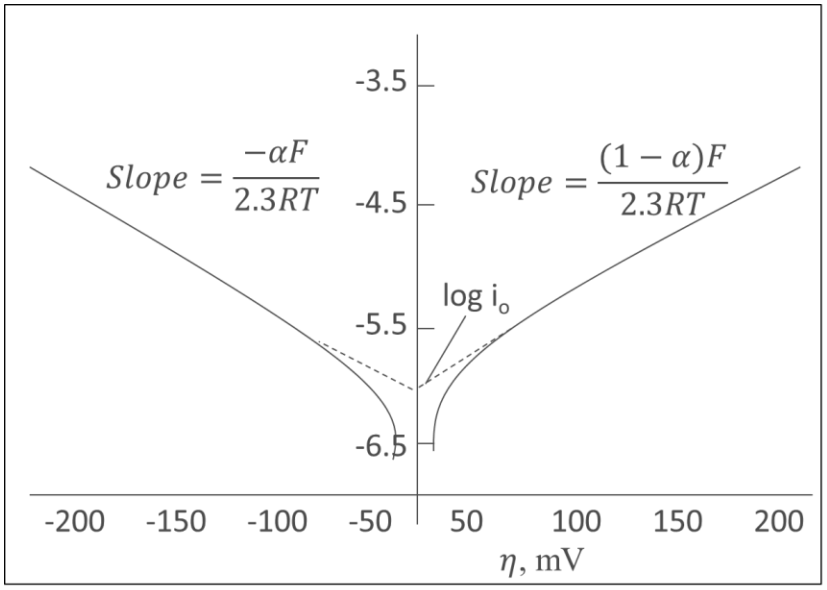

Figure 2.4 Tafel plots for the anodic and cathodic branches of the current-overpotential curve with α=0.5, T=298K and $j_o=10^{-6}$ A/cm^2.

On the other hand, for very fast kinetics, the exchange current increases and the ratio of i/i_o approaches 0. The overpotential equation given in 2.21can be expressed as:

$$\frac{C_B(0,t)}{C_A(0,t)} = \frac{C_B^*}{C_A^*} e^{f(E-E_{eq})} \tag{2.25}$$

And by substitution of the Nernst equation we obtain:

$$\frac{C_B(0,t)}{C_A(0,t)} = e^{f\left(E-E^{0\prime}\right)} \tag{2.26}$$

Which is nothing more than:

$$E = E^{0\prime} + \frac{RT}{F} ln \frac{C_B(0,t)}{C_A(0,t)} \tag{2.27}$$

Thus for reversible reactions the electrode potential and surface concentrations are related by an equation similar to the Nernst equation. No kinetic parameters are present because the kinetics are too facile. A system at equilibrium is considered reversible and hence, when the charge transfer interface is always at equilibrium, it is called reversible.

2.3 Transport in Electrochemical Processes

The current response related to the redox analyte concentration is achieved by monitoring the electron transfer of electrons during the oxidative and reduction processes. Specifically, the case of ferrocenemethanol as seen in 1.30, can be written as:

$$FcMeOH \leftrightarrow Fc^{+}MeOH + e^{-} \tag{2.28}$$

Where $FcMeOH$ and $Fc^{+}MeOH$ are the reduced(R) and oxidized(O) forms of the redox couple. This reaction will be carried out in a potential region that makes the electron transfer favorable. The resulting current is the faradaic current because it obeys Faraday's law and it is a direct measure of the rate at which the reaction is occurring. Will we be using the A and B subscripts to denote the reduced and oxidized forms of ferrocenemethanol throughout this section, to keep consistency with the notation in section 2.2.

2.3.1 The Electrical Double Layer

At the electrode surface there is an electrical double layer of charged particles/oriented dipoles. This occurs at every surface in contact with electrolyte solutions. This layer is an ionic region that compensates for any charge on the electrode. A negatively charged electrode will attract positive ions while a positively charged electrode will attract negative ones. Because the interface has to preserve charge neutrality, a counter layer of ions or dipoles of the opposite sign are attracted to the surface. Any charging background current that results from the charging of the double-layer is coined non-faradaic or capacitive and along with the faradaic component, represents the total current, seen in the current-voltage response, or voltammogram. A schematic representation of the electrical double layer is seen in Figure 2.5. We will revisit the effects of the EDL and its effects on charging currents in Chapter 4.

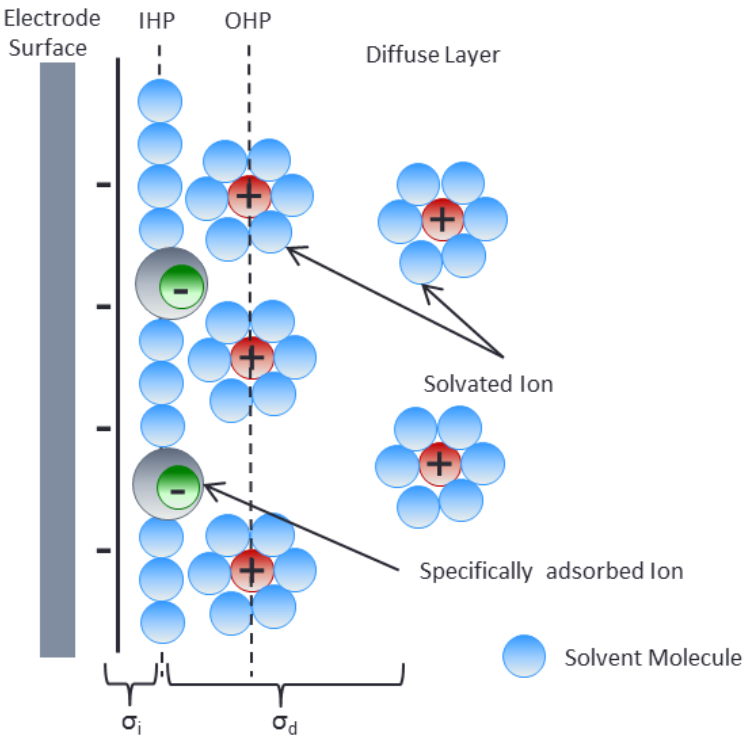

Figure 2.5 Representation of the model for the double layer region under conditions where anions are specifically adsorbed

2.3.2 Mass transfer in the Diffusion-Limited Regime

With large overpotentials, reactions take place in the mass-transfer controlled regions for oxidation and reduction of species. The potential on the electrode surfaces changes as species are reduced and oxidized according to Equation (2.1). The reactions at the electrode surface can be quite complicated and take several steps, but simplistically one can say the steps are 1) mass transfer of the electroactive species to the electrode surface, 2) electron transfer across the interface and 3) transfer of the product back to the bulk solution. This mass transfer happens through a) a diffusion gradient due to a chemical potential difference or a concentration gradient, b) ionic migration resulting from a potential gradient or c) bulk transfer happening from natural or forced convection. The three modes of mass transport are depicted in figure 2.6.

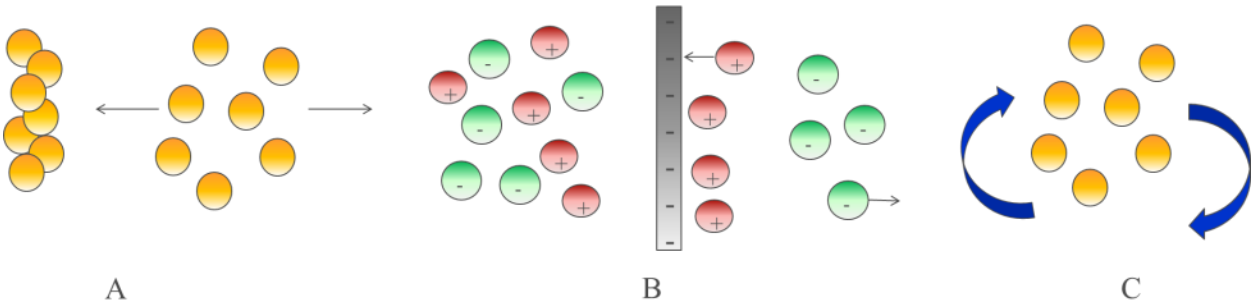

Figure 2.6 A) Transport due to diffusion. B) Transport due to a potential gradient. C) Transport due to agitation or convection.

Mass transport is measured with the correct flux (J) and it is described mathematically by the Nernst-Planck equation, given for one dimension by [139]:

$$J(x,t) = -D\,\partial C(x,t) - \frac{zF}{RT} DC\partial\varphi(x,t) + C(x,t)V(x,t) \qquad (2.29)$$

Where D is the diffusion coefficient (cm^2/s), $\delta C(x,t)/\delta x$ is the concentration gradient (distance x at time t), $\delta\varphi(x,t)/\delta x$ is the potential gradient, z is the charge of the electroactive species transferred, F is Faraday's constant, R is the gas constant, T is the temperature in Kelvin and $V(x,t)$ is the hydrodynamic velocity. Values for D in fluids usually range between 10^{-5} and 10^{-6} cm^2/s (ref). The right hand side of equation 2.29 represents the contribution of diffusion, migration and convection, respectively, to the total flux. The current is proportional to the flux and given by:

$$i = -nAFJ, \tag{2.30}$$

where n is the number of electrons transferred per molecule, A is the area, F is Faraday's constant and J is the current flux as defined in equation 2.29.

If we suppress electromigration (by using inert salts) and effects of convection, mass transfer will only be limited by diffusion. In the proximity of the electrode a concentration gradient is created as species react and deplete on the electrode relative to the bulk solution. The rate of diffusion is proportional to the concentration gradient. This is given by Fick's first law:

$$J(x,t) = -D\ \partial C(x,t)/\partial x \tag{2.31}$$

We can hence rewrite 2.30 as:

$$i = nFAD\ \partial C(x,t)/\partial x \tag{2.32}$$

Diffusional flux is time dependent. Fick's Second law describes this relationship as:

$$\frac{\partial C(x,t)}{\partial t} = D\,\frac{\partial^2 C(x,t)}{\partial x^2} \tag{2.33}$$

The change in concentration at a location x is given by the difference in flux into and flux out of an element of width dx:

$$\frac{\partial C(x,t)}{\partial t} = \frac{J(x,t) - J(x+dx,t)}{dx} \tag{2.34}$$

J/dx has units of (mol s^{-1} cm^{-2})/cm or change in concentration per unit time. The flux at any point *x+dx* can be written as:

$$J(x+dx,t) = J(x,t) + \frac{\partial J(x,t)}{\partial x}dx \tag{2.35}$$

And from equation 2.31 we obtain:

$$-\frac{\partial J(x,t)}{\partial x} = \frac{\partial}{\partial x} D\,\frac{\partial C(x,t)}{dx} \tag{2.36}$$

Combining equation 2.33 through 2.36 we get:

$$\frac{\partial C(x,t)}{\partial t} = \left(\frac{\partial}{\partial x}\right)\left[D\left(\frac{\partial C(x,t)}{dx}\right)\right] \tag{2.37}$$

The general formulation of Fick's second law for any geometry is given by:

$$\frac{\partial C}{\partial t} = D\nabla^2 C \tag{2.38}$$

Where ∇^2 is the Laplacian operator. Forms of ∇^2 for different geometries are given in Table 2.2.

Table 2.2: Forms of the Laplacian Operator for Different Geometries [139]			
Type	**Variable**	∇^2	**Example**
Linear	*x*	$\partial^2/_{\partial x^2}$	Shielded disk electrode, planar electrodes
Spherical	*r*	$\partial^2/_{\partial r^2} + (2/r)(\partial/\partial r)$	Hanging drop electrodes
Cylindrical (axial)	*r*	$\partial^2/_{\partial r^2} + (1/r)(\partial/\partial r)$	Wire electrodes, micro-pillar electrodes
Disk	*r, z*	$\partial^2/_{\partial r^2} + (1/r)(\partial/\partial r) + \partial^2/_{\partial z^2}$	Inlaid disk ultramicroelectrode
Band	*x, z*	$\partial^2/_{\partial x^2} + \partial^2/_{\partial z^2}$	Inlaid band electrode

Consider the reaction given by 1.30 where A, the electroactive species is transported purely by diffusion to the electrode surface (x=0). If no other electrode reactions occur, then the current is related to the flux of A at the electrode surface (x=0) by the equation:

$$-\partial J_A(0,t) = \frac{i}{nFA} = D_A\left[\frac{\partial C_A(x,t)}{dx}\right]_{x=0} \tag{2.39}$$

This is because the total number of electrons that are transferred in a given unit of time must be proportional to the quantity of species arriving at the electrode surface. D_A and C_A are now used to denote to designate the diffusion coefficient and concentration of reduced species A.

2.3.3 Diffusion Control at Electrode Surfaces under an Applied Potential

We have expressed the current potential characteristics in section 2.2. The first work put forward in this thesis has been done on planar electrodes (and ultramicroelectrodes) using cyclic voltammetry. We also assume kinetics for ferrocenemethanol are much faster at the electrode surface, and thus most reactions are limited by mass-transport. Thus, the derivations and analysis are examined using boundary conditions pertinent to such systems. Later in Chapter 4 we will discuss electrode voltammetry in more detail as it pertains to the specific experimental setup employed for measurement of the microelectrode array.

2.3.3.1 Qualitative Analysis

To qualitatively understand what happens at the electrode surface under an applied potential lets first consider the case where a step potential is applied to the electrode as seen in Figure 2.7a. Our analyte is species X that will oxidize at sufficiently large potential. At no applied potential it exists in its reduced form. In general, there is a potential region where faradaic processes do not occur, E_1 (ie. no oxidation). Consider E_2 to be the region at which faradaic processes do occur. At this more positive potential the kinetics for the oxidation of species X happen so fast that the reduced form of species X becomes instantaneously depleted at the surface as it reacts to donate electrons to the electrode. Because this event happens instantaneously, it requires a lot of current. Current flows subsequently to maintain the fully oxidized condition at the electrode surface. The initial oxidation has created a concentration gradient that in turn produces a continuous flow of the reduced form of the species X from the bulk solution to the electrode surface. The flux is thus

proportional to the concentration gradient. This is depicted in figure 2.7b. With time, the depletion zone thickens decreasing both the slope of the concentration profile and the current at the surface, as seen in Figures 2.7b and 2.7c. This kind of experiment is called chronoamperometry, because current is recorded as a function of time.

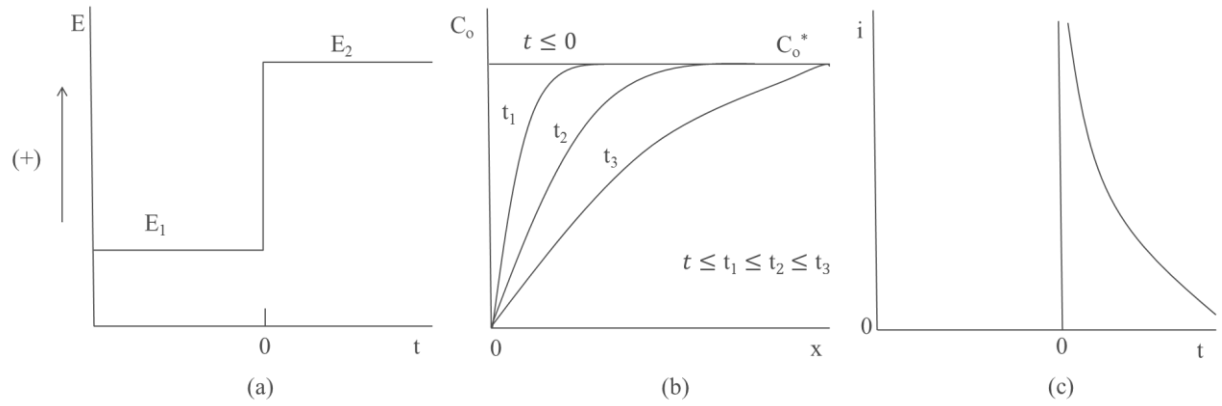

Figure 2.7 (a) Waveform for a step experiment where the species of interest is not electroactive at E1, but I oxidized at a diffusion-limited rate at E2. (b) Concentration profiles in the vicinity of the electrode surface for various times into the experiment. (c) Current flow with time. (ref from Faulkner et al)

Consider step potentials that are applied discretely over time, increasing the total applied voltage with every step, as seen in figure 2.8a. At lower voltages, namely experiment 1, the species is not yet electroactive. At steps 2 and 3, species X is oxidized but no so effectively that its surface concentration is entirely depleted. The step potentials in 4 and 5 occur in the mass-limited region. While experiment 1 yields no faradaic currents, steps 4 and 5 yield the same current. In these cases the surface concentration of reduced species X is 0; hence it arrives as fast as diffusion can bring it and the current is limited by this factor. In case 2 and 3there is still diffusion, as the number of reduced species decreases at the electrode surface as they oxidize, creating a diffusion gradient toward the electrode. However, because the gradient is less than in the mass-limited cases (4 and 5) the current is smaller. The current-time plots are depicted in

Figure 2.8b whereas a sampled-current voltammogram (I-V curve) is show in Figure 2.8c. With a linear potential sweep we can expect the current to increase as more species are readily oxidized or reduced on the electrode surface, with a limit on the peak current place on how readily species can diffuse towards the electrode surface from the bulk solution.

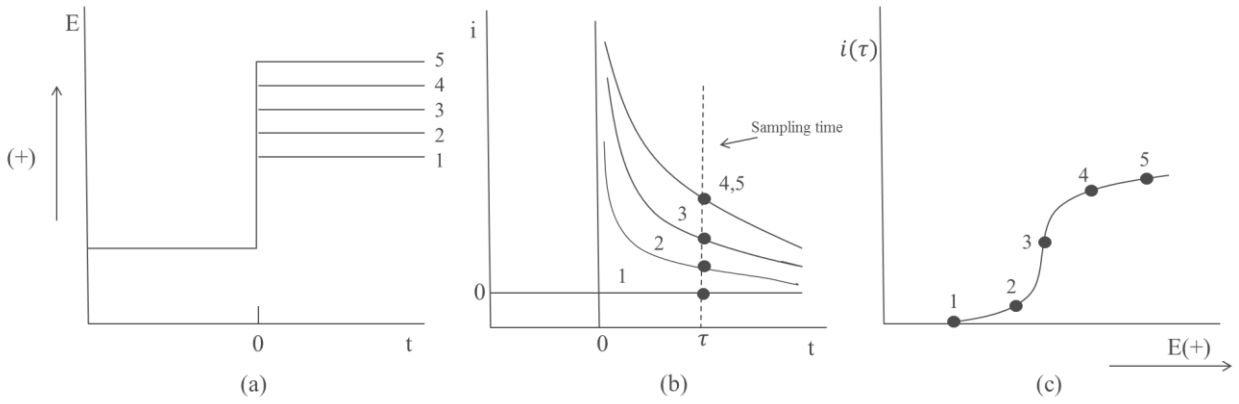

Figure 2.8 Sampled Current Voltammetry. (a)Step waveforms applied in a series of experiments. (b) Current curves observe at each potential step vs. time. (c) Sampled-current voltammogram.

2.3.3.2 Solution of the Diffusion equation for a Planar Electrode

Depending at the rate at which reactions occur on the electrode surface, we can think of 3 ways to classify a reaction: reversible, irreversible or quasi-reversible. In the reversible regime the kinetics and transfer rate constant is typically neglected as reactions occur very fast. As the electrode surface depletes with an applied potential, current is dominated and limited by mass-transfer. In the quasi-reversible regime, kinetics are much more sluggish, and thus make part of the solution to the diffusion equation. In the irreversible regime the very displacement in the potential that activate k_f also suppresses k_b, making the backward component of the electrode reaction to become less important. We can further distinguish between kinetics soon after an

applied potential or in the steady-state regime. The former is more typical of linear diffusion mechanism (planar electrodes), whereas steady state kinetics are more typically seen in small electrodes where convergent diffusion dominates the electrode response.

2.3.3.2.1 Reversible Kinetics

To quantitatively understand mass transfer for a planar electrode we must first understand the solution for the diffusion equation at a planar electrode. The calculation for the diffusion-limited current i_d, and the concentration profile $C_A(x,t)$ involves the solution of the linear diffusion equation.

$$\frac{\partial C_A(x,t)}{\partial t} = D_A \frac{\partial^2 C_A(x,t)}{\partial x^2} \tag{2.40}$$

Under the boundary conditions:

$$C_A(x,0) = C_A^* \tag{2.41}$$

$$\lim_{x\to\infty} C_A(x,t) = C_A^* \tag{2.42}$$

$$C_A(0,t) = 0 \quad for\ t > 0 \tag{2.43}$$

Condition 2.41 expresses the homogeneity of the solution before the experiment starts at t=0 and the semi-infinite condition 2.42, reflects that far away from the electrode surface electrolyte conditions are not perturbed by the experiment. The third boundary condition reflects the state of the electrode surface after the potential is applied and the species are depleted at the surface. After a Laplace transformation of (2.40) and applying conditions (2.41)-(2.43) we can rewrite the flux expression (2.39) as:

$$i(s) = nFAD_A \left[\frac{\partial C_A(x,s)}{dx}\right]_{x=0} = \frac{nFAD_A^{\frac{1}{2}} C_A^*}{s^{\frac{1}{2}}} \quad (2.44)$$

Where $s = \pi t$. The time-current response can thus be re-written as:

$$i_d(t) = \frac{nFAD_A^{1/2} C_A^*}{(\pi t)^{1/2}} \quad (2.45)$$

Expression (2.45) is known as the Cotrell Equation. In practical measurements, it must be noted that the Cotrell equation is subject to instrumental and experimental limitations such as limitations in the recording device, limitation imposed by the electrical double layer and the uncompensated resistance (more in Chapter 4) and limitations due to convection, which can cause disruptions to the diffusive layer, resulting in larger currents than those predicted [139].

The concentration profile at the electrode surface, at x=0, can be written as:

$$C_A(x,t) = C_A^* \mathrm{erf}\left[\frac{x}{2(D_A t)^{1/2}}\right] \quad (2.46)$$

Figure 2.9 shows the concentration profiles for several times after the start of a Cotrell experiment. While there is no definite thickness for the diffusion layer near the electrode surface, it is useful to think of it in terms of $(D_A t)^{1/2}$. The argument for distance, *x*, in the error function has units of length and is usually expressed in units of $2(D_A t)^{1/2}$ because it is given in units of length and denotes the distance the species has diffused in a given time, t. One can, thus, see that the diffusion layer is contained within a distance of $6(D_A t)^{1/2}$. At much greater distances than the diffusion layer thickness, the electrode has no significant effect on the species concentration,

whereas in regions that are smaller or within the diffusion layer, the electrode is very dominant. It can be observed that with increasing time the depletion region grows and the concentration gradient drops, and hence, the redox processes at the surface slow down, leading to an eventual decay in the current response [139].

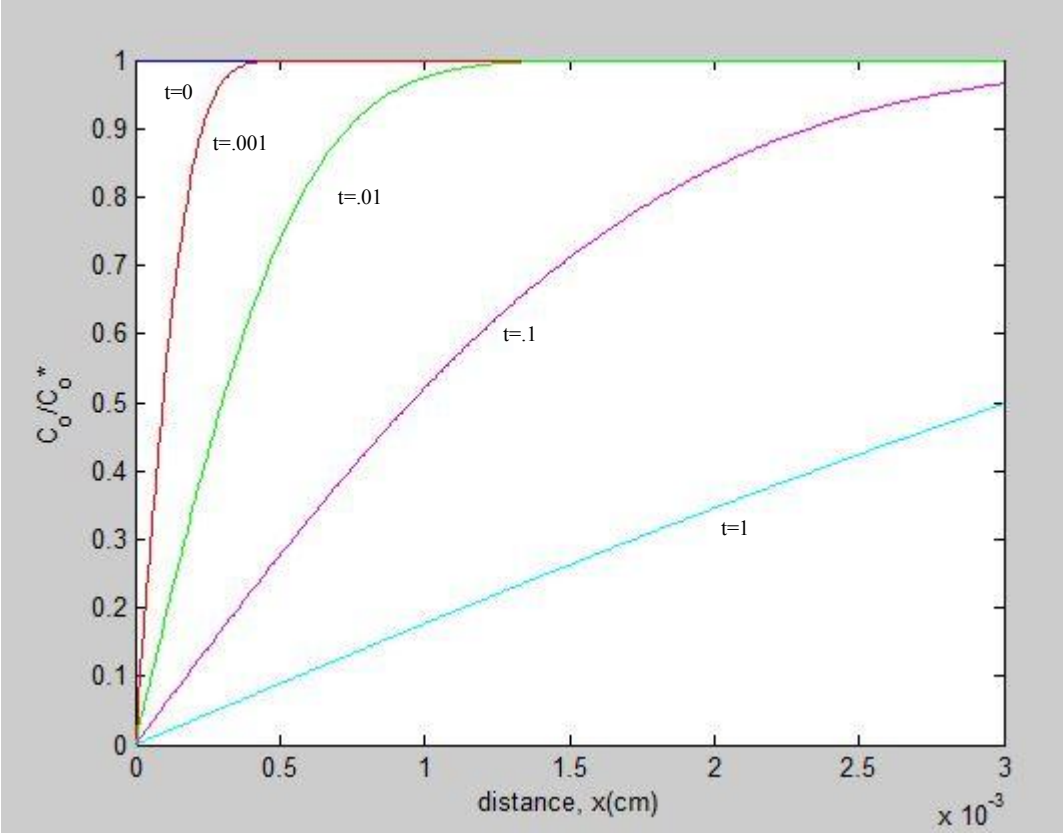

Figure 2.9 Concentration profiles for several times after the start of a Cotrell experiment. $D_o = 1\times10^{-5}$ cm^2/s.

We can expand the solution to 2.40 to both oxidative and reduction currents at the specific time at which a large potential is applied, namely at t=0. Assuming the kinetics to be very fast the electrode potential is just given by Equation 2.27 (the form of the Nernst equation). We can express the flux balance as:

$$D_A \frac{\partial C_A(x,t)}{\partial x}_{x=0} + D_B \frac{\partial C_B(x,t)}{\partial x}_{x=0} = 0 \quad (2.47)$$

Where boundary conditions may be now expressed as:

$$C_A(x,0) = C_A^* \qquad C_B(x,0) = 0 \quad (2.48)$$

$$\lim_{x\to\infty} C_A(x,t) = C_A^* \qquad \lim_{x\to\infty} C_B(x,t) = 0 \quad (2.49)$$

The Nernst relationship is expressed as:

$$\theta = \frac{C_A(0,t)}{C_B(0,t)} = -exp\left[\frac{nF}{RT}(E - E^{o'})\right] \quad (2.50)$$

We do a similar Laplace transformation as we did to equation 2.40 and account for the boundary conditions given in 2.48 and 2.49 to get:

$$\overline{C_A}(x,s) = \frac{C_A^*}{s} + A(s)e^{-\sqrt{s/D_A}x} \quad (2.51)$$

$$\overline{C_B}(x,s) = B(s)e^{-\sqrt{s/D_B}x} \quad (2.52)$$

$$D_A \frac{\partial \overline{C_A}(x,s)}{\partial x}_{x=0} + D_B \frac{\partial \overline{C_B}(x,s)}{\partial x}_{x=0} = 0 \quad (2.53)$$

Equation 2.53 can be simplified using the derivatives of 2.51 and 2.52:

$$-A(s)D_A^{\frac{1}{2}}s^{\frac{1}{2}} - B(s)D_B^{\frac{1}{2}}s^{\frac{1}{2}} = 0 \quad (2.54)$$

Thus B =-A(s)ξ where $\xi = (D_A/D_B)^{1/2}$. If we invoke reversibility (that the electrode potential is given as 2.27) and do a Laplace transform on equation 2.50 we can show that $\overline{C_A}(x,s) =$

$\theta\overline{C_B}(x,s)$ and thus:

$$\frac{C_A^*}{s} + A(s) = \xi\theta A(s) \tag{2.55}$$

As it turns out, the Cottrell equation given by 2.45 can be rewritten as:

$$i_d(t) = \frac{nFAD_A^{1/2}C_A^*}{(\pi t)^{\frac{1}{2}}(1+\xi\theta)} \tag{2.56}$$

Equation 2.45 is a special case of 2.56 in the diffusion-limited region where the applied potentials are much more positive (or negative) than $E^{O'}$ such that $\theta \rightarrow 0$.We can express the Cottrell current given by 2.45 as $i_d(t)$ and rewrite 2.56 as:

$$i(t) = \frac{i_d(t)}{1+\xi\theta} \tag{2.57}$$

We see now that for a reversible couple, the current-time curve has similar shape but the magnitude is scaled by $1/(1+\xi\theta)$ according to the potential. For very negative potentials (relative to $E^{O'}$), this scaling factor is close to 0, whereas at positive potentials it is close to unity.

From 2.57 we can extract the "reversibility" of the reaction by rewriting it at a fixed sampling time, τ, as:

$$E = E^{o\prime} + \frac{RT}{nF} ln \frac{D_R^{1/2}}{D_O^{1/2}} + \frac{RT}{nF} ln \frac{i_d(\tau)-i(\tau)}{i(\tau)} \tag{2.58}$$

When $i(\tau) = i_d(\tau)/2$, the current ration becomes unity and the third term disappears. The

potential at which this happens is the half-wave potential:

$$E_{1/2} = E^{o\prime} + \frac{RT}{nF} ln \frac{D_R^{1/2}}{D_O^{1/2}} \tag{2.59}$$

This allows us to write 2.58 as:

$$E = E_{1/2} + \frac{RT}{nF} ln \frac{i_d(\tau) - i(\tau)}{i(\tau)} \tag{2.60}$$

For a fully reversible system, the plot of E vs. log $[i_d(\tau) - i(\tau)/i(\tau)]$ should be linear with a slope of *2.303RT/nF* or 59.1mV/n mV. This is important and we see later in Chapter 4 smaller electrodes exhibit such response. As this slope increases, the system becomes less reversible.

2.3.3.2.2 Quasireversible Regime

In the quasi-reversible and reversible regimes, the slope is no longer linear. For the latter 2 cases, the kinetic parameter plays a role as it is not so fast to be transparent. The system must now be treated with semi-infinite linear diffusion where both the mass transfer and charge-transfer kinetics limit the reaction. The concentrations are now scaled with the kinetic rate constants. For reversible systems they are given by the Nernst potential [139].

The a quasi-reversible system the current flux is now expressed as:

$$\frac{i}{FA} = D_A \left(\frac{\partial C_A(x,t)}{\partial x}\right)_{x=0} = k_f C_A(0,t) - k_b C_B(0,t) \tag{2.61}$$

We have defined the forward and reverse rate constants in section 2.2.

We can do a Laplace transform of equation 2.61 as we did in the reversible case and define:

$$H = \frac{k_f}{D_A^{1/2}} + \frac{k_b}{D_B^{1/2}} \tag{2.62}$$

We can express the solution for the current as:

$$i(t) = FAk_f C_A^* \exp(H^2 t)\, erfc(Ht^{\frac{1}{2}}) \tag{2.63}$$

For the case of when the oxidized species, C_B^*, is initially present equation 2.63 becomes.

$$i(t) = FA(k_f C_A^* - k_b C_B^*) \exp(H^2 t)\, erfc(Ht^{\frac{1}{2}}) \tag{2.64}$$

Just as we did for the reversible case, we can express this current relationship as a function of overpotential:

$$i = i_o\left[e^{(1-\alpha)f\eta} - e^{-\alpha f\eta}\right] \exp(H^2 t)\, erfc(Ht^{\frac{1}{2}}) \tag{2.65}$$

It is important to note that the forms of equation 2.64 and 2.65 are in the form of:

i=[i in the absence of mass transfer effects]×[*f(H,t)*]

where *f(H,t)* accounts for the effects of mass transfer.

If we recognize that $\frac{k_b}{k_f} = \theta = -\exp[f\left(E - E^{o'}\right)]$, we find that:

$$H = \frac{k_f}{D_A^{\frac{1}{2}}}(1 + \xi\theta) \tag{2.66}$$

Now the current can be expressed in a form that includes the Cotrell current, which is the

diffusion limited current:

$$i = \frac{nFAD_A^{1/2}C_A^*}{(\pi t)^{\frac{1}{2}}(1+\xi\theta)}[\pi^{\frac{1}{2}}Ht^{\frac{1}{2}}\exp(H^2t)\,erfc\left(Ht^{\frac{1}{2}}\right)] \quad (2.67)$$

Which we can rewrite as:

$$i = \frac{i_d}{(1+\xi\theta)}F(\lambda) \quad (2.68)$$

Where

$$F(\lambda) = \pi^{\frac{1}{2}}\lambda\exp(\lambda^2)\,erfc(\lambda) \quad (2.69)$$

and

$$\lambda = Ht^{1/2} = \frac{k_f t^{1/2}}{D_A^{\frac{1}{2}}}(1+\xi\theta) \quad (2.70)$$

2.3.3.2.3 The Irreversible Regime

The irreversible regime is defined by the condition that $k_b/k_f \approx 0$ ($\theta \approx 0$) over the whole voltammetric wave. The current expression then becomes:

$$i(t) = FAk_fC_A^*\exp\left(\frac{k_f t}{D_A}\right)erfc(\frac{k_f t^{1/2}}{D_A{}^{1/2}}) \quad (2.71)$$

2.3.3.3 Semi-Infinite Spherical Diffusion: Steady State Regime

If the electrode is spherical as opposed to planar, one must solve Fick's second law for a spherical system. This is the kind of system seen at the edges of graphene. The boundary conditions are now given by:

$$C_A(r,0) = C_A^*(r > r_O) \tag{2.72}$$

$$\lim_{r\to\infty} C_A(r,t) = C_A^* \tag{2.73}$$

$$C_A(r_O,t) = 0 \quad for\ t > 0 \tag{2.74}$$

Where r is the radial distance from the electrode center and r_o is the electrode radius. The Cotrell diffusion current is now given by:

$$i_d(t) = nFAD_AC_A^*\left(\frac{1}{(\pi D_A t)^{1/2}} + \frac{1}{r_o}\right) \tag{2.75}$$

which can be written as:

$$i_d(spherical) = i_d(linear) + \frac{nFAD_AC_A^*}{r_o} \tag{2.76}$$

For a purely planar electrode then, the spherical current would be 0 as time approaches infinity. However, in the spherical case, the limit would approach the constant term on the right of equation 2.66. This nonzero limit happens because the growth of the depletion region does not interfere with the concentration gradients at the surface as it does with planar electrodes. The diffusion field is able to draw reactants from a continually larger area at its outer limit and hence, the current reaches a steady-state value quickly.

The constant term of Equation 2.75 can be rewritten to account for reversibility and rewritten as:

$$i = \frac{FAD_AC_A^*}{(1+\xi\theta)r_o} \tag{2.77}$$

This relation is the general steady-state (or ultramicroelectrode) response for a reversible system

response to an applied step potential. In the case for the diffusion-limited region, in can be rewritten as:

$$i = \frac{i_d}{1+\xi\theta} \tag{2.78}$$

Where i_d is the limiting current, $\xi = (D_A/D_B)^{1/2}$ and $\theta = -\exp[f(E - E^{o'})]$.

2.3.4 Diffusion Analysis at Ultra Microelectrodes

We now consider the case for very small disk electrodes (r < 25μm). Diffusion at very small electrodes (ie: the edge plane of graphene sheets), is spherical or radial. At short times, where the diffusion-layer thickness is small compared to the size of the electrode, the current follows the Cotrell expression defined by 2.75 and semi-infinite spherical diffusion is applicable. However, within the context of longer times, the steady state current would be governed by the constant term from equation 2.75. For a disk microelectrode this is given by [140]:

$$i_{ss} = \frac{4nFAD_O C_O^*}{\pi r_O} \tag{2.79}$$

We will find this relationship useful in our analysis of smaller electrodes in Chapter 4.

Figure 2.10 illustrates the response of a large planar electrode versus that of a microelectrode in response to the same applied forward and reversed potential. For larger electrodes, the I-V response shows a peak at the potential, E_p, where the oxidation or reduction of the species takes place. The peak height of the IV curve scales with the concentration, area, and the square root of

the scan rate, as defined by Fick's second law of diffusion, indicating that transport is, indeed, governed by diffusion of the electroactive species to a planar electrode surface. The rate of the reaction is diffusion limited, and thus, species cannot continue to oxidize fast enough to support more current, which is why the current falls off after reaching an oxidation peak.

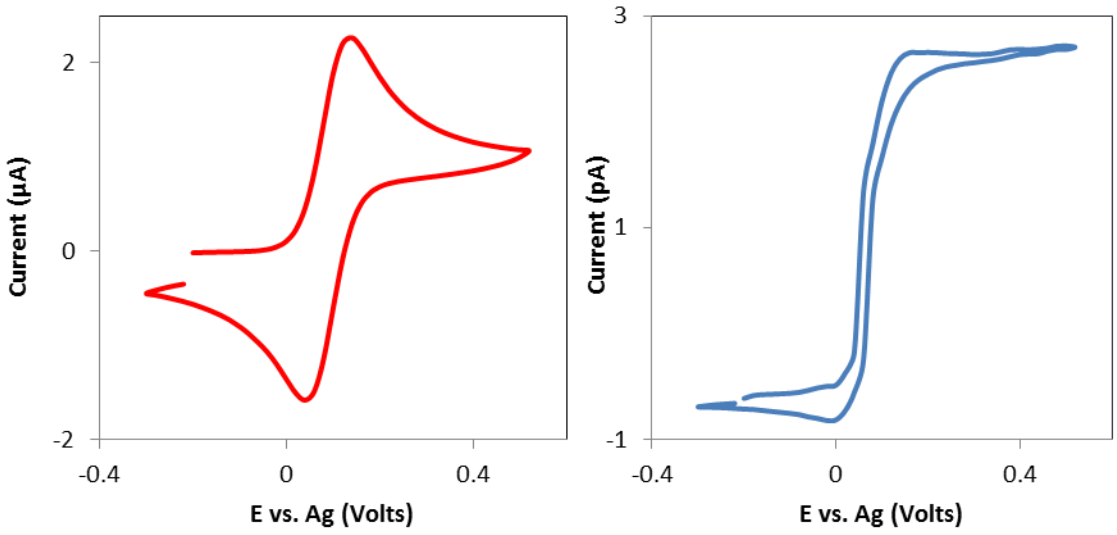

Figure 2.10 Traditional peak-shaped voltammogram(left) usually seen an large planar electrodes with linear diffusion-limited reactions versus sigmoidal response(right) observed in ultramicroelectrodes

When the electron transfer rate is fast enough, the E_p value will be independent of the scan rate; indicating a reversible electrode reaction. The potential at the electrode surface is described by the Nernst equation, and the kinetic parameters associated with the current potential characteristic, k_o and α, are not involved. If the electron kinetics are slow enough, the electrode reaction is irreversible. In the quasi-reversible limit, even though fast electron-kinetics are still at play, they are still slow enough that the E_p values will change as a function of the scan rate. Both the charge transfer and the mass transport determine the current. The Nernst equation is only approximately satisfied and the scan rate can have a considerable effect on the nature of the observed cyclic voltammogram. At sufficiently slow scan rates, quasireversible processes may

appear to be fully reversible. However, as the scan rate is increased, the kinetics of electron transfer are not fast enough to maintain (Nernstian) equilibrium

In the case of an ultramicroelectrode, given that experimental conditions do not change, a sigmoidal (without a peak) rather than a peak-shaped voltammogram is observed. The current is also much smaller (as the electrode is smaller), but much higher per unit area for the same concentration. In the steady-state condition, the rate of diffusion matches the rate of electron transfer, and thus, the current reaches a constant value. Because the size of the electrode is much smaller than a typical microelectrode (one greater than ~30 μm in radius) the contribution to the current by diffusion from the edges of the electrode now becomes relevant with respect to the total mass transport of electroactive species. In larger electrodes, this edge effect is small relative to the linear diffusion. However, for microelectrodes, the flux per unit area now becomes greater due to the radial diffusion component.

Microelectrodes are advantageous because the low currents make iR losses negligible. More importantly, smaller electrodes can make measurements in small areas, such as cell cavities, dendrite or synapses. Because the electron transfer kinetics are faster as the electrode scales down, smaller electrodes have better sensitivity per unit area. Smaller electrodes, however useful, come at the cost of many fabrication and production obstacles. As electrodes get smaller they are less tolerant to defects, have higher uncompensated resistance (See chapter 4), larger contact resistance and becomes harder to pattern with standard lithography techniques.

2.3.5 Derivation of the Nernst Planck Equation

One can arrive at the Nernst equation by making use of the chemical potential, which is the difference between the energy barriers of gaining an electron and that of giving one on the working electrode. The ratio of oxidized to reduced species then becomes the ration of the probability of being oxidized to the probability of being reduced:

$$\frac{C_B}{C_A} = \frac{\exp(-\frac{[barrier\ for\ losing\ electron]}{kT})}{\frac{\exp(-[barrier\ for\ gaining\ electron])}{kT}} = exp\left(\frac{\mu_c}{kT}\right) \tag{2.80}$$

Taking the natural logarithm of both sides and accounting for the fact that $\mu_c \neq 0$ when $\frac{C_A}{C_B} = 1$, we write:

$$\mu_c = {\mu_c}^o + kTln\frac{C_B}{C_A} \tag{2.81}$$

To convert from chemical potential to electrode potential we divide by q, and remembering that *kT/q=RT/F* we obtain the Nernst equation for the one-electron process given in Equation 2.2:

$$E = E^{o\prime} + \frac{RT}{F}\ln\frac{C_B}{C_A} \tag{2.82}$$

2.4 Standard Electrode Materials

The materials chosen for an electrochemical cell must comply with the desired performance as well as the specific safety and toxicity guidelines. The cost, robustness, and reusability of the materials also play a vital role in the development of electrochemical cells, and hence, cannot be chosen arbitrarily.

2.4.1 Working Electrodes

The working electrode (WE) is the most important component of an electrochemical cell. The electron transfer reactions monitored occur at the interface between the WE and the solution. Therefore, the selection of a working electrode material is important to the sensitivity, linearity and effectiveness of the electrochemical cell performance.

Designs of working electrodes for laboratory measurements are vast and diverse. Typically, it can be a small sphere or disc, or a short wire, but it can also be a metal foil, a single crystal of a semiconductor or metal, an evaporated thin film, or a powder pressed as discs or pellets. There are several considerations to take into account when choosing a WE material. To begin with, the material must favor redox behavior with the analyte of interest. This must be done ideally fast, in a reproducible fashion without the electrode fouling. Secondly, the potential window over which the electrode can perform without oxidizing should be as wide as possible to permit the largest range of analyte detection. Other factors to consider are the cost, its ability to be used in fabrication, toxicity and how easily it can be "cleaned" after it is used.

The most common WE materials used are *platinum*, *gold*, *carbon*, and *mercury*. Platinum is likely the favorite amongst experimentalist, as it has very robust electrochemical inertness and can be easily fabricated [14] . However, it has a high cost and can easily reduce hydrogen ions on its surface in the presence of small amounts of water or acids, leading to the formation of hydrogen gas at negative potentials. Such reaction can obscure analytical signals from the analyte.

Gold is also very commonly used, but it is limited in the positive potential range due to the oxidation of its surface. Regardless, it has been extensively used to make modified electrodes containing surface structures known as self-assembled monolayers *(SAMs)* that can enhance the selectivity of the electrodes by targeting one specific molecule.

Mercury has an excellent potential window in the cathodic direction, but can easily oxidize in the anodic direction. Due to its toxicity, its use has become more limited these days. The use of mercury films formed on the surface of solid electrodes rather than the pure metal has become more popular as an alternative to a pure mercury electrode.

Carbon electrodes have become popular because they allow scans to more negative potentials than platinum or gold, and have good anodic potential windows. The most common form of carbon electrode is glassy carbon, which is relatively expensive and difficult to machine. Regardless, the majority of most successful electrochemical sensors, including the blood glucose biosensor strip, to date, employ a screen-printed carbon-paste as the working electrode [141, 142].

The use of new materials in conjunction with standard electrode materials, specifically nanomaterials, has become increasingly attractive in the area of research in electrochemical sensors. Zhong *et al.* [142] reported a non-enzymatic hydrogen peroxide amperometric sensor based on a glassy carbon electrode modified with an MWCNT/polyaniline composite film and platinum nanoparticles. Guo *et al.* [143] also made use of CNTS to make an amperometric sensor for tryptophan by modifying a glassy carbon (GC) electrode with gold nanoparticle decorated CNTs. The advantages and limitation of the most commonly used WE materials are

listed in Table 2.3 [216].

Table 2.3 Advantages and Limitations of Commonly Used WE Materials [216]

Material	Advantages	Limitations
Platinum	available wire, flat plate & tube; large range of sizes; Pt-Rh alloy for rigidity	Low hydrogen overvoltage so cathodic potential range limited; expensive
Gold	configurations same as Pt; larger cathodic potential range	anodic window limited by surface oxidation; expensive
Carbon	many types and configurations; good cathodic potential range	quality varies greatly; hard to shape
C-paste	wide potential range; low background current; inexpensive	unstable in flow cells; cannot be used in organic solvents
Mercury	excellent cathodic window; easy to "refresh"	Limited anodic window due to mercury oxidation; forms amalgams; toxic

2.4.2 The Reference Electrode

Electrochemical sensors make use of a reference electrode. The reference electrode is used in measuring the working electrode potential. A reference electrode should have a constant electrochemical potential as long as no current flows through it. Reference electrodes should be constructed using components that are stable over time and with changing temperature. In general, the voltage of the reference electrode should be stable and reproducible; this voltage is determined by the chemistry taking place between it and the electrolytic solution around it. To keep any potential changes negligible, even in the presence of small currents, the potential of the

electrode, as given by the Nernst equation, must not fluctuate. To do this, a redox system with constant (buffered or saturated) concentrations of each participants of the redox reaction are used and redox reactions must be occurring very fast (completely reversible and very low impedance). That is why often saturated calomel or Ag/AgCl materials are used.

In electrochemistry, the hydrogen electrode is universally accepted as the primary standard with which other electrodes are compared. Hence, the hydrogen electrode serves quite appropriately as a standard reference. While a hydrogen reference electrode is relatively simple to prepare, it is too cumbersome for practical applications. Therefore, the most common lab reference electrodes are the saturated calomel electrode (SCE) and the silver/silver chloride (Ag/AgCl) electrodes. In field probes, a pseudo-reference (a piece of the working electrode material) is often used.

2.4.3 Auxiliary Electrodes

The counter, or auxiliary electrode (AE), is the conductor that completes the cell circuit. It supplies enough electrons to sustain the electrochemical reaction taking place at the WE without passing significant current through the reference electrode. To this end, it is usually chosen to be as much bigger than the WE. There are no specific material requirements for the electrode beyond it not adversely influencing reactions occurring at the working electrode (WE) surface and, hence, is usually an inert conductor like platinum or graphite. If a reduction occurs at the WE, there must be an oxidation that takes place at the AE. One should verify that the products formed at the AE do not interfere with the WE reaction. The most commonly used material for the auxiliary electrode is platinum, due to its inertness and the speed with which most electrode reactions occur at its surface. Other, less expensive materials may also be used as auxiliary

electrodes. These include carbon, copper, or stainless steel if corrosion is not an issue for a particular electrolyte solution or reaction.

2.5 Biocompatible Electrodes

Vast efforts have been made to adapt electrochemical sensors to meet the demands of biological detection. Doing so has called for new materials and material modifications to standard electrode materials. The use of nanosized scaffolds such as spheres, fibers and tubes have all recently been reported [92-94]. The aim of using such nanostructures is to reduce diffusion limitations and maximize the functional surface area to increase enzyme loading. Also, the superior diffusion and particle mobility can impact the catalytic activity of attached enzymes [96]. Enzyme stability improvement has also been reported. Nanoparticles have also yielded better electrochemistry, due to their ability to reduce the distance between the redox center of enzymes and the electrodes [110].

2.5.1 General Considerations

Within the realm of electrochemical electrodes it is important to highlight the development of a) sensors with increased specificity and b) sensors capable of simultaneous determination of species. The ability to operate in complex biological environments is critical to electrode performance. To that end, the properties that must be considered when designing and developing chemical and biological sensors include:

Biocompatibility: First and foremost the electrode design must be biocompatible with the system of interest to prevent unwanted reactions, cell death (if applicable) or false positives.

Cost: Electrochemical sensors are for the most part a low cost analytical tool. Moreover, sensors must be produced in large numbers as many applications aim single use to avoid cross-contamination and integration with disposable packaging. Hence, being able to mass manufacture sensors is critical. The state of the art manufacturing is the commercial glucose sensor test trip. It is produced in quantities of billions every year, costing a fraction of a cent for sensor.

Miniaturization: Many applications require high-resolution detection, in which the electrodes need to be very small, densely packed, and capable of measuring localized potentials or small quantities of neurotransmitter release between cells. Amongst the advantages of miniaturization are the reduction of transport times, sample volumes, reagent and energy consumption, time expenditure and cost. Coupled with portability, miniaturization has become a major incentive in sensor research, both in the scaling of already established sensing devices [78], but also in the development and application of novel sensing materials such as graphene and carbon nanotubes (CNTs).

Sensitivity: The sensitivity of a sensor is the slope of the analytical calibration curve for a given analyte. A sensor is said to be very sensitive when a small change in analyte concentration causes a large change in the response of the sensor. Sensitivity is one of the most important performance metrics of a sensor and it is highly desirable. It is often confused or interchanged

with the detection limit. The latter, however, is the smallest detectable concentration.

Sensor reproducibility: A sensor process must be easily reproduced for manufacturing purposes. For measurement consistency, it must also be able to reproduce its intended response.

Selectivity/Specificity: Selectivity is the ability of a sensor to detect one specific species in the presence of other species or interferents. A higher degree of selectivity can be achieved by immobilizing species specific to the analyte of interest, or conversely, by immobilizing species that block the detection of unwanted analytes that may also be found in the matrix.

Multi-analyte detection: Simultaneous detection of various analytes in solution is also a highly desirable feature of any sensor, as more than one analyte is usually found in a biological matrix. In the case of dopamine, for instance, uric acid and ascorbic acid are also present in solution and will oxidize with an applied potential, nearly around the same oxidation potential of dopamine. It becomes important to then have ways of having specificity and/or selectivity for one detection element.

Stability: A sensor must be able to operate over extended periods of time. For mass production purposes, its "shelf life" must be significantly longer than its predicted time frame for intended use. Moreover, stable sensors are those than can keep their properties even after tested or used under varying conditions and harsh environments.

Mechanical Safety: Sensors must be robust enough to withstand harsh sensing conditions, but

they must be designed gently enough to avoid hurting the tissue or cells it is coming in contact with, especially for implantation purposes. Sharp electrodes can perforate cells and evoke cell death. Flexible and soft surfaces are preferred to avoid damage to the interface. However, this is often a trade-off with stability.

Electrochemical Safety: The stimulation current or the application of a potential should not cause corrosion (oxidation) of the electrode, nor should it produce reaction products that are toxic or intolerable to the surrounding tissue.

It is unlikely that any one sensor exhibits optimal performance for all properties. Usually, in biological detection, sensing selectivity is compromised if higher value is placed on cost or response time. Similarly, mechanical flexibility is compromised when selectivity or cost are prioritized. Properties should always be prioritized depending on the final application of the electrode.

2.5.2 State of the Art Electrodes

Electrodes for biosensing are vast in the literature. Glass, liquid membrane and solid-state ion selective electrodes are able to detect up to a few tenths of micromolar of species in the presence of interference [14]. Biosensors take full advantage of electrochemical techniques to quantify biological processes and transduce biosignals into electrical ones. This usually entails using immobilized biomolecules that give it specificity and selectivity. Ion-selective electrodes (ISEs), particularly, have been extensively developed for the recognition of active chemical species.

Table 2.4 lists commercially available ISEs along with their interferences [139]. The latter can often prevent, obscure or mask the detection of the target species by occupying binding sites, by having similar redox potentials or simply by eliciting side reactions. Some species can be detected up to saturated concentrations, as such is the case of sodium. Most, however, exhibit a detection range from a few molar to a few micromolar.

Table 2.4 Typically Commercially Available Ion-Selective Electrodes [139]

Species	Type	Concentration Range(M)	pH Range	Interferences
Ammonium	L	10^{-1} to10^{-6}	5-8	K^+, Na^+, Mg^{2+}
Barium	L	10^{-1} to10^{-5}	5-9	K^+, Na^+, Ca^{2+}
Bromide	S	1 to10^{-5}	2-12	I^-, S^{2-}, CN^-
Cadmium	S	10^{-1} to10^{-7}	3-7	Ag^+, Hg^{2+}, Cu^{2+}, Pb^{2+}, Fe^{3+}
Calcium	L	1 to10^{-7}	4-9	Ba^{2+}, Mg^{2+}, Na^+, Pb^{2+}
Chloride	S	1 to5×10^{-5}	2-11	I^-, S^{2-}, CN^-, Br^-
Copper	S	10^{-1} to10^{-7}	0-7	Ag^+, Hg^{2+}, S^{2-}, Br^-,Cl^-
Cyanide	S	10^{-2} to10^{-6}	10-14	S^{2-}
Fluoride	S	1 to10^{-6}	5-8	OH^-
Iodide	S	1 to10^{-6}	3-12	S^{2-}
Lead	S	10^{-1} to10^{-6}	0-9	Ag^+, Hg^{2+}, Cu^{2+}, Cd^{2+}, Fe^{3+}, S^{2-}
Nitrate	L	1 to5×10^{-6}	3-10	Cl^-, Br^-, NO_2^-, F^-, SO_4^{2-}
Potassium	L	1 to10^{-6}	4-9	Ca^{2+}, Na^+, Mg^{2+}
Silver	S	1 to10^{-6}	2-9	S^{2-}, Hg^{2+}
Sodium	G	Sat'd to10^{-6}	9-12	Li^+, K^+, NH_4^+,
Sulfide	S	1 to10^{-7}	12-14	Ag^+, Hg^{2+}

Noble metal electrodes are also robustly employed in the detection of selected biological species and drug screening procedures. The noble metals such as Pt, Au, and Pd are commonly considered to be inert, and have high conductivity. However, they can become extremely reactive under certain electrochemical conditions. Table 2.5 lists some of the more common noble metal electrodes and their intended applications as biological sensors.

Table 2.5 State of the Art Biological Detection with Solid State Electrodes [79]						
Drugs	Electrode Type	Method	LOD	Potential (V)	Application	Ref
Tetracycline	Gold	CV	0.35µmL-1	1.2	Dosage forms, foods	[145]
Dopamine	mGold	CV, SWV	…*	…*	Dosage forms, foods	[146]
Nicotinic acid	Gold	CV	.27uM	.20	Dosage forms	[147]
Vitamin B_{12}	mGold	…*	10^{-9}M	.21	Dosage forms	[148]
Ethamsylate	mGold	SWV	6×10^{-8}M	…*	Dosage forms	[149]
Doxycycline	Gold	FIA with PAD	1 µM	1.15	Dosage forms	[150]
Monosaccharide	mGold	LSV, amperometry	…*	0.30	Dosage forms	[151]
Tetracycline	Gold	FIA with PAD	…*	…*	Dosage forms	[152]
Isosorbide dinitrate	Gold	LSV	$0.084\mu gmL^{-1}$	…*	Dosage forms, arterial plasma, synthetic serum	[153]
Thiram	Gold	CV, SWV	4.3×10^{-7}M	…*	Dosage forms, spikes grapes	[154]
Ascorbic Acid	mGold	FIA/amperometry	…*	…*	Dosage forms	[155]
Guanifensesin	Pt	…*	…*	0.92	Dosage forms	[156]
Naproxen	Pt	CV, LSV, DPV	$0.24\mu gmL^{-1}$	1.15	Dosage forms	[157]
Doxazosin	Pt	DPV	1.0×10^{-5}M	…*	Dosage forms	[158]
Trazodone	Pt	DPV	2.5×10^{-6}M	.30	Dosage forms	[159]
Vitamin C	Pt	DEP/FIA	…*	…*	Dosage forms	[160]
Droperidol	Pt	CV	8.0×10^{-5}M	1.45	Dosage forms	[161]
Fluphenazine	Pt	CV	…*	1.35	Dosage forms	[162]
Imipramine HCl	Pt	CV	…*	1.20	Dosage forms	[163]
Dopamine Serotonin	m-indum tin oxide	DPV	0.5nM 3.0 nM	0.07 .24	Human serum, urine	[164]
Atenolol	m-indum tin oxide	DPV	0.13µM	…*	Dosage forms, urine	[165]

Carbon-based electrodes have also achieved excellent LOD and sensitivity compared to their solid-state counterparts; with the added benefit of being biocompatible, generally nonreactive and cheaper [166]. The most popular carbon-based electrodes involve glassy carbon, carbon paste, carbon fiber, screen printed carbon strips, carbon films, diamond, pyrolytic graphite, fullerenes, wax impregnated graphite, Kelgraf, carbon nanotubes, and reticulated vitreous carbon

[79]. Within the group of organic electrodes, glassy carbon stands out because of its excellent electrical and mechanical properties, wide potential window and reproducible performance. [14, 79, 167, 168]. Carbon-paste electrodes have become widely popular for their wide-potential window, robustness, low cost and feasibility. In addition, they can easily be modified, which is desirable for enhanced selectivity and specificity. During the early 1980s, the integration for carbon-paste-based amperometric biosensors had a significant impact on biosensor commercialization. Carbon-nanotube functionalized electrodes have also had some success in enhancing detection limit and sensitivity response of various analytes and biomarkers, such as hemoglobin, glucose and folic acid [169-171]. Carbon nanotubes have some advantages over other electrode materials: they have a small size with larger surface, very high sensitivity, fast response, enhanced electron transfer kinetics when used in electrochemistry [23, 167, 172, 173, 174]. They have also been used as a new support material to tether DNA molecules in the detection of hybridization events [79]. Table 2.6 lists some of the more commonly used carbon-based electrodes and their applications.

Table 2.6 State of the Art Biological Detection with Carbon-based Electrodes [79]						
Drugs	Electrode Type	Method	LOD	Potential (V)	Application	Ref
Melatonin	CPE	Flow amperometry	9×10^{-11}M	.79	Dosage forms	[175]
Ascorbic Acid	CPE mCPE	CV Amperometry	1.2×10^{-5}M	0.1	Dosage forms	[176]
Tryptophan	mCPE	CV, DPV	-	-	Clinical prep	[177]
Dopamine	mCPE	FIA/amperometry	1.5×10^{-4}M	0.1	Dosage forms	[178]
Quatiapine	GCE	DPV, SWV	4×10^{-8}M 1.3×10^{-7}M	1.0	Dosage forms Serims	[179]
Salicylic acid	GCE	DPV	1.04µg/mL	1.09	Dosage forms	[180]
Catecholamines	GCE	CV, Coulometric titration	-	.58	Dosage forms	[181]
Vitamin C	GCE	Amperometry	-	-	Dosage forms, food samples	[182]
Histamine serotonin	DE	CV, hydrodynamic voltammetry	1µM	1.4	Bulk	[183]
Cytochrome C	DE	CV	-	0.1	Bulk	[184]
Nicotine	DE	CV, SWV	0.50mg/L	1.2	Cigarette tobacco	[185]
Estradiol	SPE	LSV	1.0×10^{-5}M	0.92	Biosensors	[186]
Creatinine	SPE	SWV	8.6µM	1.8	Urine	[187]
Hemoglobin	CNT	CV, DPV	$\sim10^{-5}$M	-0.60	Bovine blood	[169]
Uric Acid	CNT	LSV, SWV	0.12µM	0.35	Human urine	[188]
L-Histidine	CNT	Potentiometry	$\sim10^{-11}$M	-	Dosage forms Food and drinks	[189]
Dopamine	CNT	DPV	200 µM	0.31	Brain homogenate	[190]
Folic Acid	CNT	CV	1.0×10^{-9}M	-0.71	Dosage forms	[170]
Glucose	CNT	CV	2.5 mM	0.45	Raw material	[171]
Naproxen	GE	Potentiometric sensor	3.9×10^{-5}M	-0.90	Dosage forms	[191]
Myoglobin	GE	CV	2.98×10^{-6}M	0.64	Real Samples	[192]
See list of abbreviations for further reference						

2.6 Summary

- We discussed the main techniques tor electrochemical sensing, including voltammetric, potentiometric, conductimetric as well as other types of sensing techniques such as

capacitive, impedance and ion-selective electrodes. The type of sensing technique is highly contingent on the type of reaction being monitored and in such a way that doesn't obstruct it as it occurs.

- We overviewed transport in electrochemical processes and arrived at the solution of the diffusion equation, as well as its solution pertaining to planar and spherical electrodes. We introduced voltammetry and its expected response. These concepts will be key in understanding and interpreting the response of our fabricated microelectrode array, as we will see in Chapter 4.

- We reviewed the electrode requirements and materials for the different terminals of an electrochemical cell. The materials are chosen primarily to satisfy the requirements imposed by the electrode application (such as biocompatibility), to prevent material corrosion and false positives. We also took a look at the existing and most commonly utilized electrode materials, along with their advantages and disadvantages.

- Lastly, we reviewed the criteria for biocompatible electrodes. These include reproducibility, miniaturization, stability, cost and possible multi-analyte detection. We also took a look at the different state of the art types of solid state and carbon-based electrodes for chemical and biological sensing electrode stability.

CHAPTER 3

DESIGN, FABRICATION AND INTEGRATION OF GRAPHENE MICROELECTRODE ELECTRODE ARRAYS

The graphene microelectrode arrays made for this dissertation were made using conventional silicon-based micro-fabrication techniques. The main goal of the process was to prevent contamination of the graphene by photoresist residues. The most challenging aspect of the process was fabricating devices on sapphire substrates, as the graphene was very barely adhered to the substrate through weak dispersion forces [193] and easily came off even just with photoresist spinning. The graphene active areas were patterned, with metal leads interconnecting the latter to contact pads placed on the perimeter of the chip, and passivation layers separating the interconnects from active biological fluids. Chips were manufactured on randomly shaped pieces and then diced into chips before being mounted on quartz-made PCBs. There were 4 generations of devices, each one being an improvement upon the previous one. In all, around 80 chips were manufactured in 3 years, each being handled individually, as process integration was limited by sample size and number, prohibiting the use of stepper lithography to make multiple chips in one run. All fabrication and integration was carried out in the Cornell Nanofabrication Facility (CNF).

3.1 Basic Scheme

The work examined in this thesis focuses on the design, integration and testing of graphene microelectrode arrays on a diverse number of graphene substrates. The design and selection of materials wasn't straightforward, and each step had to be carefully evaluated to allow for process limitations, biocompatibility issues, testing considerations, robustness, and a limited budget. In all, the work presented is the result of over 20 process iterations, ~90 chips, tens of intermediate troubleshooting steps, lost samples, patience and hard work.

The basic circuit topology of the microelectrode array in electrolyte is depicted in Figure 3.1. The interfacial impedance at the electrode-electrolyte interface (between the working electrode and the reference electrode) includes a solution resistance, R_{Sol} , the uncompensated resistance, R_U, the quantum capacitance, C_q, the double layer capacitance, $C_{dl,}$ and the electrode-electrolyte intrinsic charge transfer resistance, R_{int}. We will examine these values in greater detail later in chapter 4, as they vary greatly with the experimental conditions. In addition to the impedances at the solution-graphene interface, there are other resistances associated with making contact to the graphene and its sheet resistance post fabrication. We will examine these in detail in this section. R_C is the contact resistance of the metal-graphene junction, R_{SH} is the sheet resistance of any one electrode and R_M is the resistance of the metal lines. Other capacitance parasitics are the passivation capacitance between the interconnects and the electrolyte (C_p), the capacitance between neighboring interconnect traces (C_{neigh}), and the capacitance between the interconnects and the substrate (C_{sub}). We will describe these in detail is section 3.4.

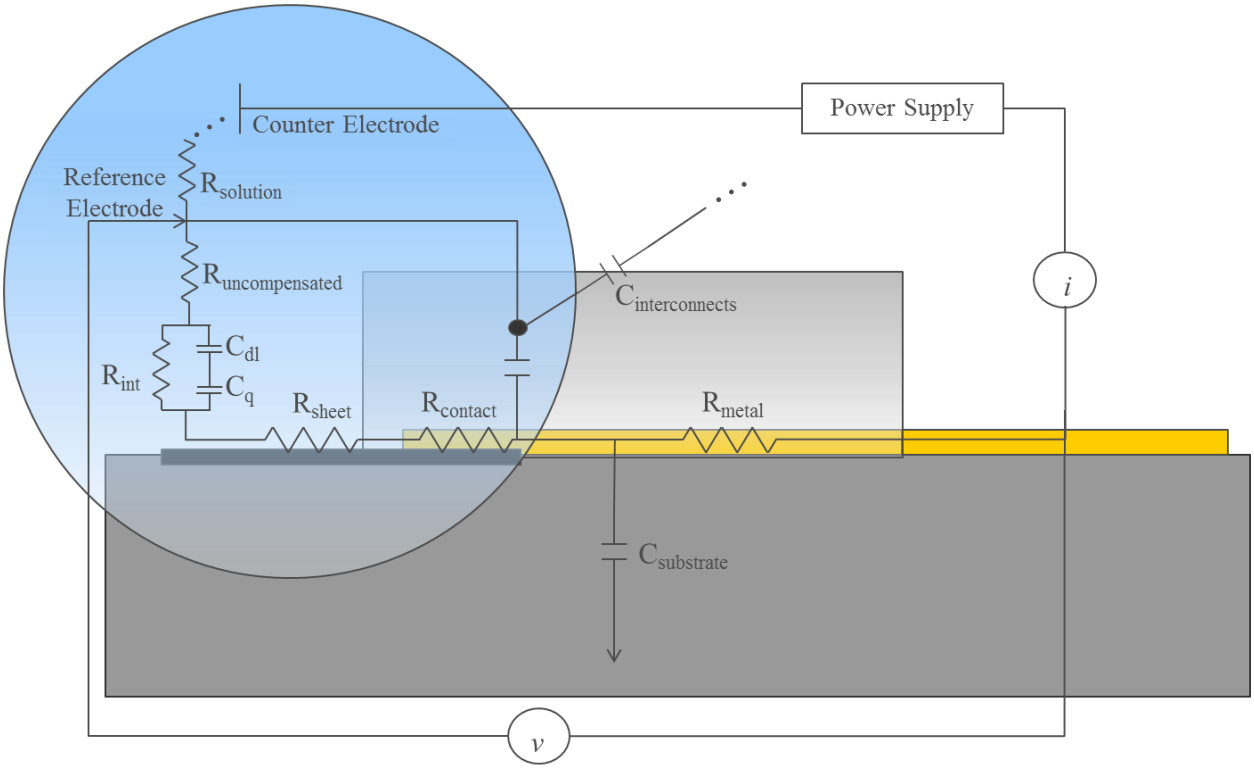

Figure 3.1 Circuit schematic of electrode parasitics associated with the device structure, intrinsic graphene properties and experimental methods.

3.1.1 General Considerations

A microelectrode's intended use must be considered prior to device design and integration. The electrodes presented in this thesis were intended for biological detection of neurotransmitters released from neural cells. Even though all experiments were carried out in an ex vivo aqueous environment, electrodes were designed as they would be for implantable devices, with materials and structures chosen and designed accordingly. The devices needed to perform in a fluid and be resistant to physiochemical processes, such as corrosion. For testing purposes and experimental consistency, we wanted devices that could be used several times. In addition, because we were not using a probe station to test chips, these had to be mounted on printed circuit boards and wire

bonded. The general consideration guidelines for biosensing electrodes were put forth in section 2.4.1 and are the same for the design and fabrication of our electrode array. The 1st generation devices are not part of this work as they exhibited considerable leakage currents.

3.1.2 Mask Design

There were four generations of devices. All four generations had a similar layout. The active graphene areas (electrodes) were always placed in the center of the chip, with contact pads for probing placed at the perimeter of the chip, making contact to the graphene active areas through metal leads. An insulation layer covered these lines, isolating the graphene from the contact pads and also preventing any signal to come from false positives due to exposure of metals to the ionic liquid interface. Chip size was limited due to sample availability and cost. Silicon carbide for epitaxial graphene growth is expensive, and thus limited the sample size to ~ $1cm^2$. Growth on sapphire was also carried out on small sample sizes, as constrained by growth chamber conditions. This resulted in our masks being limited to a $1cm^2$. A top down view of the electrode design can be seen in Figure 3.2, which is not drawn to scale. The second and third generation masks are also depicted in Figure 3.3.

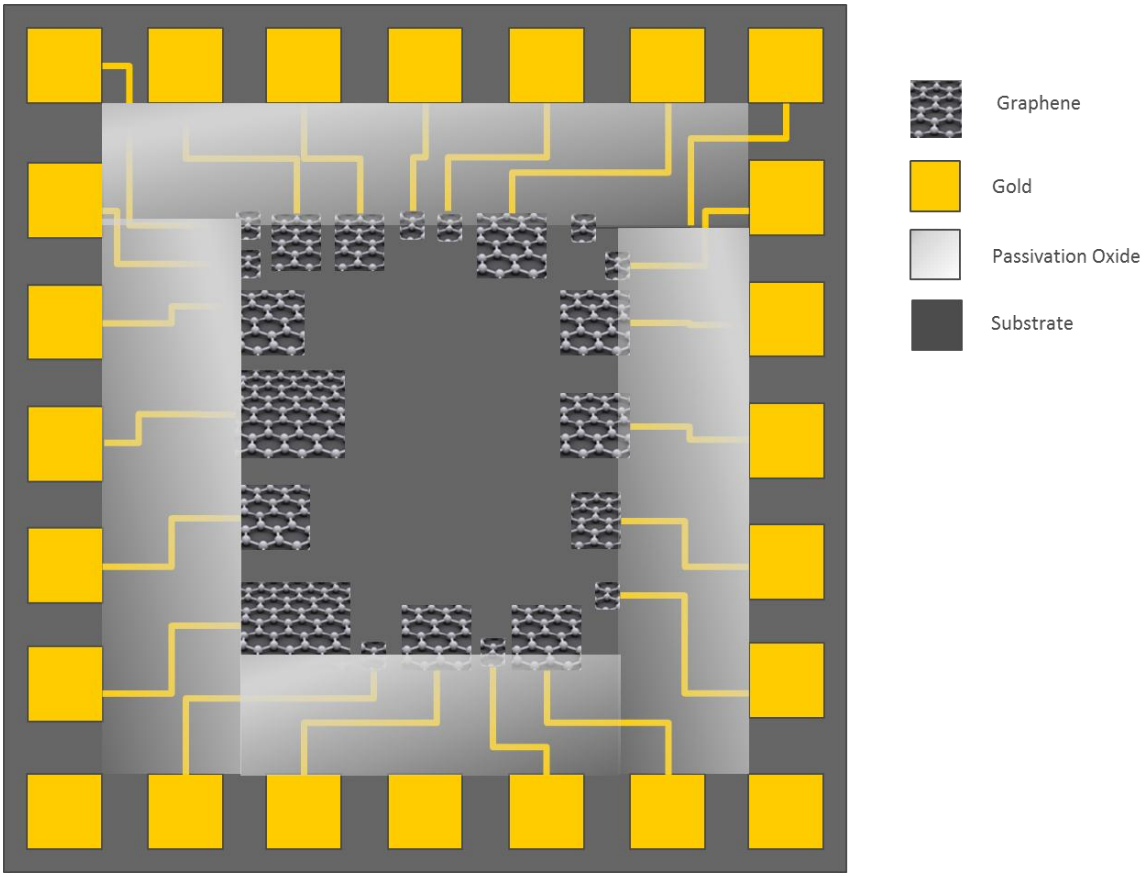

Figure 3.2 Top-view depiction of graphene microelectrode mask. The graphene areas are kept in the center and are isolated from the contact pads with silicon oxide. Devices are not drawn to scale.

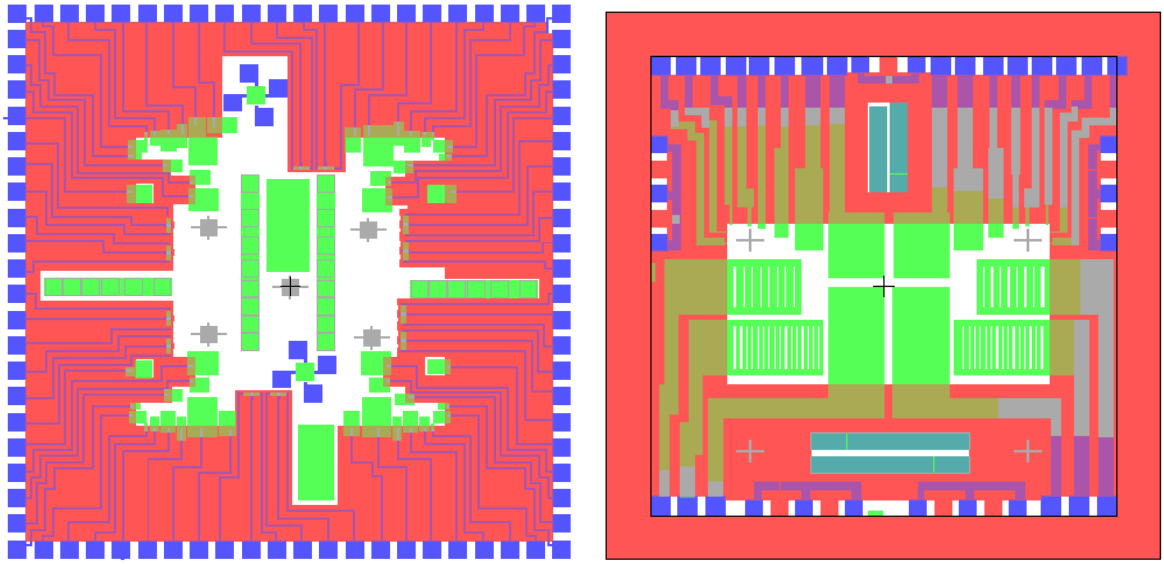

Figure 3.3 Mask layout of the second and first generation mask. Graphene active areas are patterned in green. Metal lines and contacts are in purple and insulation layer is represented in pink.

Also, to prevent false positives coming from leakage redox reactions taking place on the metal interconnects, the devices were designed to keep the lines at least 200 micron away from the exposed active area, such that fluid never sat directly on the lines, even when separated by the passivation layer. While the first generation design had very little overhead between the insulation layer and the metal lines (< 20um), this was corrected in subsequent mask designs. Later designs also incorporated the design of serpentine electrodes, to examine the effect of exposed edges had on the electrochemical properties. We will examine these in Chapter 5.

3.1.3 Materials Selection

There are three major points to consider when selecting the materials for the microelectrode arrays. To begin with, all materials chosen must be biocompatible. This means they may not be toxic to biological fluids and cells. Second, all materials must be thermally stable at 300 °C , as this is the temperature at which plasma SiO_2 is deposited in the final passivation step. Lastly, all materials must not leave a residue that might degrade the electrode performance or produce false positives. Finally, materials must be chosen as to minimize circuit parasitics while maintaining proper device operation.

3.1.3.1 Substrate

Being one layer thick and high sensitive to small perturbations, the choice of substrate is critical to device performance. Many studies [42, 43, 46] have revealed that the intrinsic mobility of graphene is limited by its underlying substrate. There were 3 different substrates used, each with

its inherent advantages and disadvantages. Graphitic materials grown via CVD were transferred to 300 nm of SiO_2. The substrate is not only 100% biocompatible, but, in addition, offers high contrast to graphene, rendering it visible on the substrate even under the naked eye, unlike material grown on sapphire and silicon carbide, where there is little to no contrast. This made it particularly hard to visually monitor the material through an optical microscope during fabrication, calling on more robust techniques like Raman spectra to ensure the stability of the material. Unlike sapphire and silicon carbide, SiO_2/Si substrates were also readily available at a low cost. On the other hand, material on sapphire and silicon carbide had the advantage of being clean of PMMA and ferric chloride ion residues, inherent with the transfer process from copper and nickel surfaces to SiO_2. Direct growth, without the use of a metal catalyst, on an insulating substrate is ideal for device fabrication.

3.1.3.1.1 SiO_2 on Silicon

The most widely used substrate for graphene device fabrication to date is silicon oxide on silicon. It is highly compatible with fabrication, but the rough surface and charged impurities in the oxide limit the intrinsic graphene mobility and shift the Dirac point by creating electron–hole charge fluctuations (or 'puddles') in the graphene, which scatter charge carriers. However, it does offer a wide range of other advantages, such as a stable surface for transfer, the ability of easily back-gating graphene and high contrast to enhance the visibility of the one-atom-thick carbon allotrope. As mentioned, silicon-oxide-on-silicon substrates are cheap and readily available. More importantly, they are biocompatible with our electrode array process.

3.1.3.1.2 Sapphire

Sapphire is otherwise known as aluminum oxide, a chemical compound of aluminum and oxygen with the chemical formula Al_2O_3. It is commonly known as alumina or sapphire. Despite being an electrical insulator, it has a relatively high thermal conductivity (30 $Wm^{-1}K^{-1}$[3]) for a ceramic material and is insoluble in water.

The ability of growing graphene directly on an insulating material at a large scale would aggressively accelerate the integration of graphene with other materials, leading to new types of electronic devices based on hybrid multilayers of graphene with other semiconductors, ferromagnets, controlled-growth thin films, metal oxides and ferroelectrics.

Sapphire was chosen for a variety of reasons. Mainly, it has hexagonal symmetry, thus increasing the likelihood of lattice-matched epitaxial growth [the in-plane lattice constant of (0001)-oriented sapphire, 4.75 Å, is about twice the graphene lattice constant, 2.45 Å]. Also, it has a very high melting point (>2000◦C) which is beneficial considering that most graphene formation via MBE or CVD processes is favored at high temperatures. Its biocompatibility and insolubility in water make it an ideal substrate for a biosensing electrode surface.

3.1.3.1.3 Silicon Carbide

Silicon carbide (SiC) is a semiconductor made up of silicon and carbon atoms in equal stoichiometric ratios. There are two different surface terminations: the Si-terminated SiC(0001)

Si-face and the C-terminated SiC(0001) C-face. While monolayer graphene growth is easily controlled in the Si-face, it is harder on the C-face, leading to multiple layers.

SiC is chemically inert, physically robust, has a large bandgap, a high breakdown voltage, a high thermal conductivity and a high saturation electron drift velocity [35-37]. Consequently, it is commonly used in power applications. Recently, it has been found to be very biocompatible, and used in medical implant devices.

More relevant to this work, it is a viable substrate for epitaxial graphene growth. Due to the higher vapor pressure of Si, silicon atoms on the Si-face of SiC can evaporate away at high temperatures and leave a surface of graphene, under the right conditions. SiC is a well-adapted wide band-gap semiconductor (2.2eV - 3.3eV),, and as such, like SiO_2 on silicon, is readily available, although a lot more costly.

3.1.3.2 Sacrificial Layer

The choice of a sacrificial layer stemmed primarily from the desire to keep graphene clean from photoresist (PR) residues. It has been reported that PR residues are unlikely to be removed once they make contact with graphene. To that end, we sought to design a fabrication protocol that could prevent any type of contaminant used during fabrication from coming in contact with the top surface of the graphitic material. It would also prove useful later on as a seeding layer was needed to passivate the electrodes via atomic layer deposition (ALD). We explored the feasibility of utilizing oxides from thermal ALD reactors as well as evaporated porous oxides deposited

through e-beam techniques. Figure 3.4 shows the Raman spectra of graphene on sapphire before and after deposition of ALD Al_2O_3 and e-beam SiO_2. Sapphire was chosen as the test substrate because it has the weakest interaction with graphene of all the other materials used. The surface tension of the sacrificial layer should not remove the graphene off the surface. 20 nm of e-beam SiO_2 proved to be porous enough to not strain the underlying graphene, but dense enough to keep PR contaminants from depositing on the graphene, while ALD and e-beam Al_2O_3 proved problematic in keeping the graphene

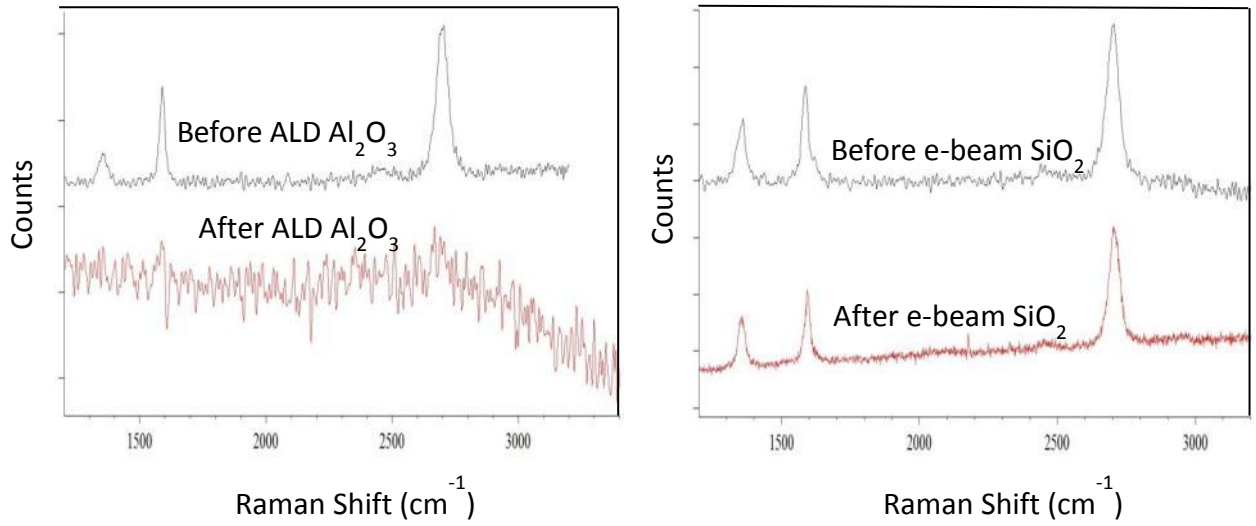

Figure 3.4: (left) Raman spectra of graphene on sapphire before and after atomic layer deposition of alumina as a sacrificial layer. Graphene comes off the surface. (right) Raman spectra of graphene on sapphire before and after an e-beam SiO_2 sacrificial oxide layer. Graphene remains on the surface.

3.1.3.3 Interconnects and Contact Pads

The materials chosen for the interconnects had to be biocompatible, be stable in fluid electrolytes, exhibit high mobility and make good contact to graphene. Generally speaking, making a good contact to pristine graphene is hard due to its inert nature. Later in this chapter we

discuss in more detail several of the technique used to enhance the contact resistivity. Chrome is toxic to cells, so it was disregarded as an adhesion layer and titanium was chosen instead. Gold is biocompatible and the preferred material for interconnects and particularly contact pads, as these will be wire-bonded thereafter. Due to the latter, the thickness of the gold layer had to be at least 100 nm with an adhesive titanium layer 10nm thick.

3.1.3.4 Insulation Layer

The insulation material was chosen as per 3 requirements: (1) It had to be a biocompatible interface; (2) it had to be dense enough to prevent any ions in the electrolyte from migrating across it and coming in contact with the underlying metal lines connecting the active graphene areas to the contact pads; and (3), it has to minimize any parasitic contribution to the overall measurement due to any capacitive effect with underlying metal lines. Silicon dioxide has a lower relative permittivity (ε_r = 3.9) than any of the other insulating oxides. Thus, a thick silicon dioxide layer (100 nm) effectively reduces any capacitive current between the interconnects and the electrolyte. It may be permeable to sodium ions, but a dummy chip without any graphene active electrodes areas was tested without leakage currents, due primarily to the use of a plasma ALD material. The silicon dioxide also provides a top hydrophilic surface which is ideal for cell adhesion.

3.1.3.5 Packaging

Chips were tested using a potentiostat. Such setup prohibited the use of a probe station, and so, all measurements had to be conducted via alligator clips. As such was the case, chips had to be mounted and wire-bonded onto a printed circuit board. Even though the PCB would not ultimately be part of an integrated solution, we decided to make it biocompatible as well. For this reason quartz was used as the primary substrate and gold was used to make the printed circuit lines onto which to wire-bond.

3.2 Graphene Synthesis and Transfer

We will now describe the different protocols utilized for sample preparation. It is important to once again highlight the fundamental role sample preparation has over overall device performance. Sample preparation contributes to the total number of ripples, crack, holes, defects and charged impurities (dopants) that affect the electrochemical response of graphene electrodes.

3.2.1 Epitaxial Graphene

Epitaxial graphene has attracted the interest of the graphene community for a variety of reasons. First and foremost, it presents a way of producing graphene at a large scale on a metal-catalyst free substrate. Most importantly, the contact resistance to epitaxial graphene has been reported to be lower than that of CVD graphene. Section 3.4 will explore this more in depth.

3.2.1.1 Growth Methods

Growth of graphene on 6H-SiC (0001) was carried out in the vertical cold walled chamber. The growths were performed at temperatures of 1500- 1650 °C under Ar pressure of 600-700Torr. A picture of the chamber is shown in Illustration 3.1. The process is similar as that described in [194].

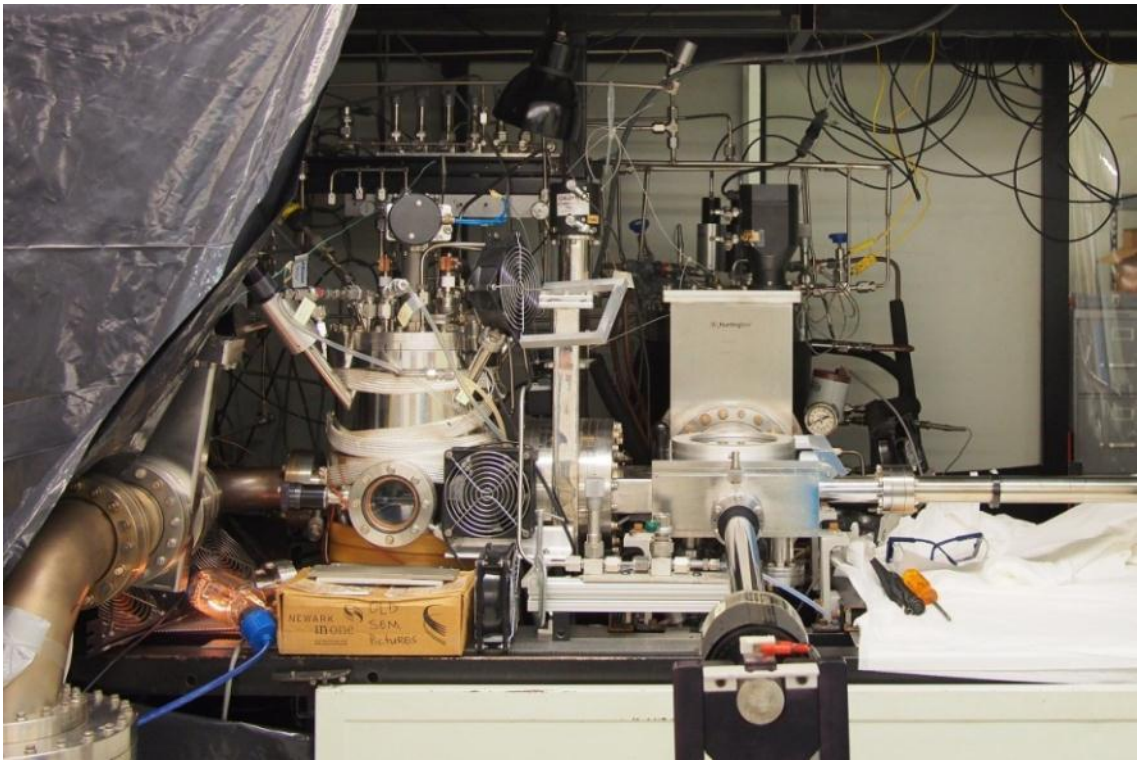

Illustration 3.1 Chamber were epitaxial graphene growth was carried out.

3.2.1.2 Materials Characterization

Epitaxial material was characterized both with Raman Spectra and Atomic Force Microscopy (AFM). Raman Spectroscopy, seen in Figure 3.6, indicated 1 to 2 monolayers of graphene were formed. An AFM image of a typical layer is also shown below in Figure 3.5. The AFM images

also depict the typical step bunching that is often observed in SiC and that often is responsible for corrugations observed in epitaxial graphene.

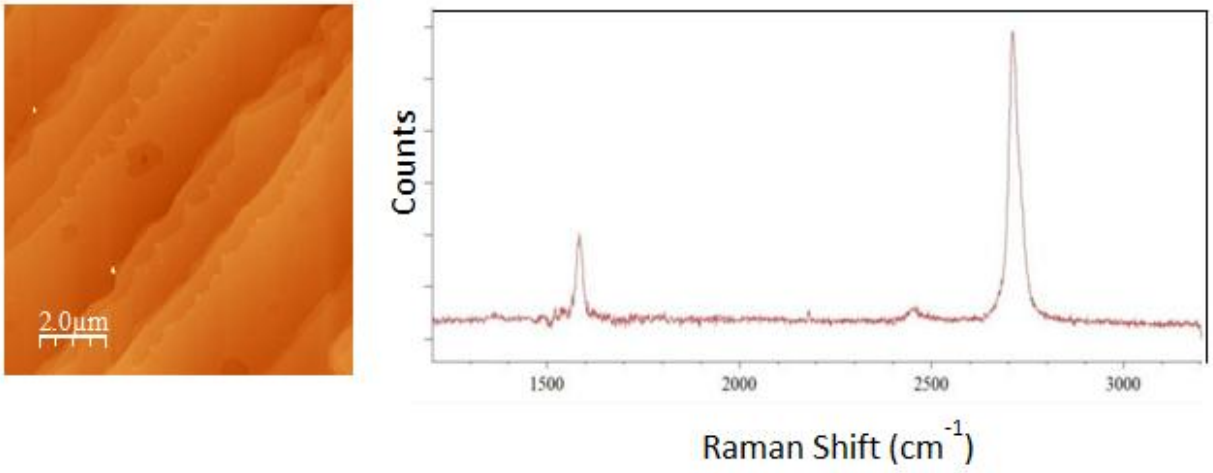

Figure 3.5 (Left) AFM image of graphene grown epitaxially on Si-face of silicon carbide. (Right) Raman spectra of epitaxial graphene reveals 1-2 layers on the surface. The background SiC signal has been subtracted.

3.2.2 CVD Graphene on Sapphire

In this thesis we present the first characterization of graphene grown via high temperature CVD on sapphire as an electrode material. Therefore, we will briefly outline the growth mechanisms, physical and electrical properties of such material. Realizing the full potential of 2D materials calls for a practical, catalyst-metal-free growth method that avoids transfer on an insulating substrate. While there have been efforts to grow graphene on sapphire and other substrates with low temperature processes (450◦) or conventional CVD (950-1000◦) [195] these have not yielded material competitive enough with materials grown on nickel or copper substrates or epitaxial material on SiC [193].

3.2.2.1 Growth Methods

This material was grown in a conventional vertical cold wall CVD system. Graphitic filaments located below the wafer carrier were heated by a DC power supply. Argon was the carrier gas ay roughly 10,000 sccm. Methane and hydrogen were introduced separately. Methane flow was between 5 and 200 sccm. It was used as a primary carbon source. Hydrogen flow was 5-15 times greater than methane, and is the first source of carbon etch through the formation of hydrocarbon gases. A growth process was optimized varying the H_2/CH_4 ratio and the chamber pressure was kept at 600 Torr. Graphene was grown directly when the methane partial pressure was greater than 0.2%. Otherwise, a two-step nucleation-nucleation/growth process was carried out. The picture of the reaction is seen in Figure 3.6.

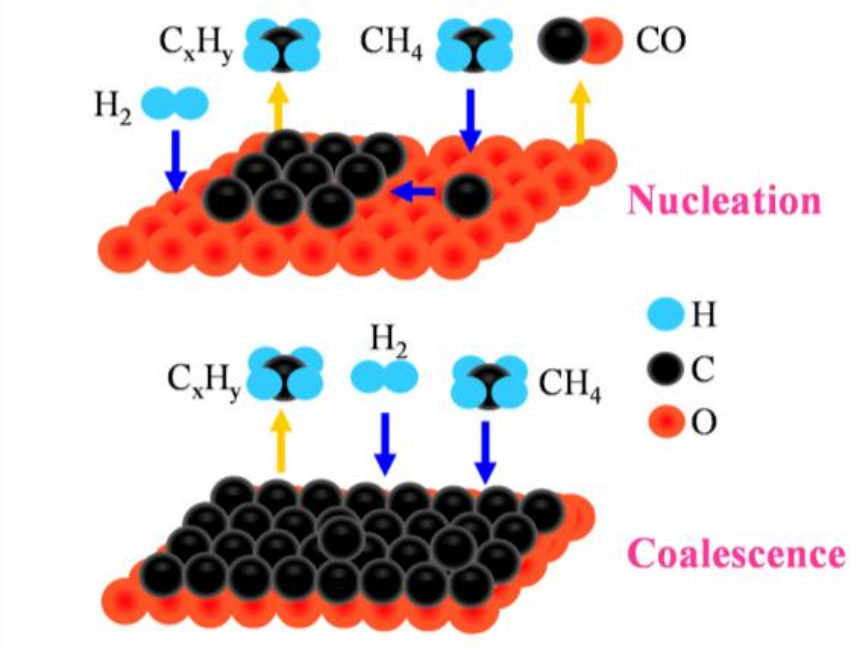

Figure 3.6 Proposed growth model for CVD graphene on sapphire. Carbon is supplied by the cracking of CH4, and it is balanced by carbon etching by hydrogen and oxygen. Aluminum atoms on the sapphire surface were not shown here for a simplified view. [193]

3.2.2.2 Materials Characterization

The Hall Effect was measured at room temperature and the mobility was found to be more than 2000 $cm^2/V{\cdot}s$. Carrier type was dependent on growth conditions. AFM measurements revealed that nucleation seeds were distributed uniformly on the substrate and the lateral growth rate was estimated to be 82 nm/min, with nuclei density measured to be ~ $24\mu m^{-2}$. Density functional theory reveals that the interaction between graphene and sapphire is predominantly weak dispersion type interactions, namely Van der Waals forces. GIXRD and LVTEM studies confirm a dominant crystal orientation for about 80-90% of the material associated with epitaxial growth [193]. A TEM of graphene grown on sapphire and transferred to a TEM grid is observed in Figure 3.7. Raman Spectra and AFM, as seen in Figure 3.8, confirm the strong presence of smaller domain sizes, and hence, a higher number of defects associated with more dangling bonds and unterminated carbon groups.

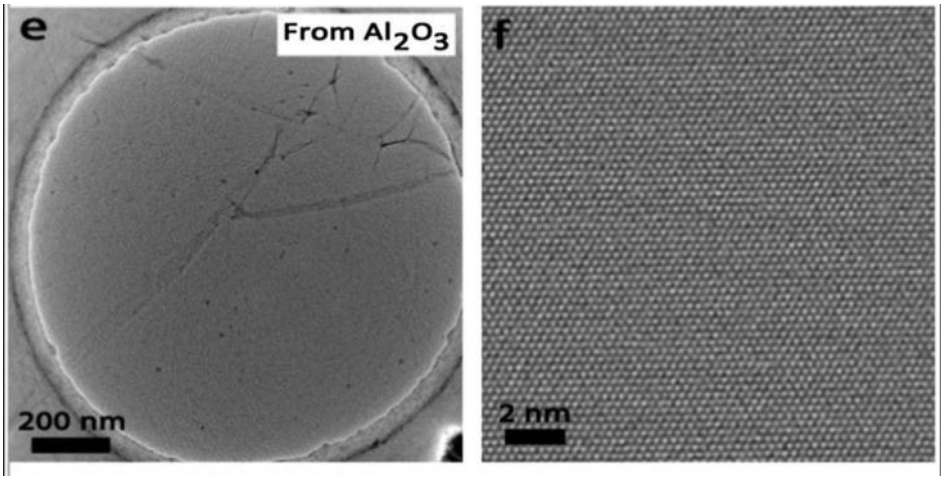

Figure 3.7 Panels e) and f) respectively show the corresponding overview and HRTEM images of monolayer graphene transferred from Al_2O_3 respectively.

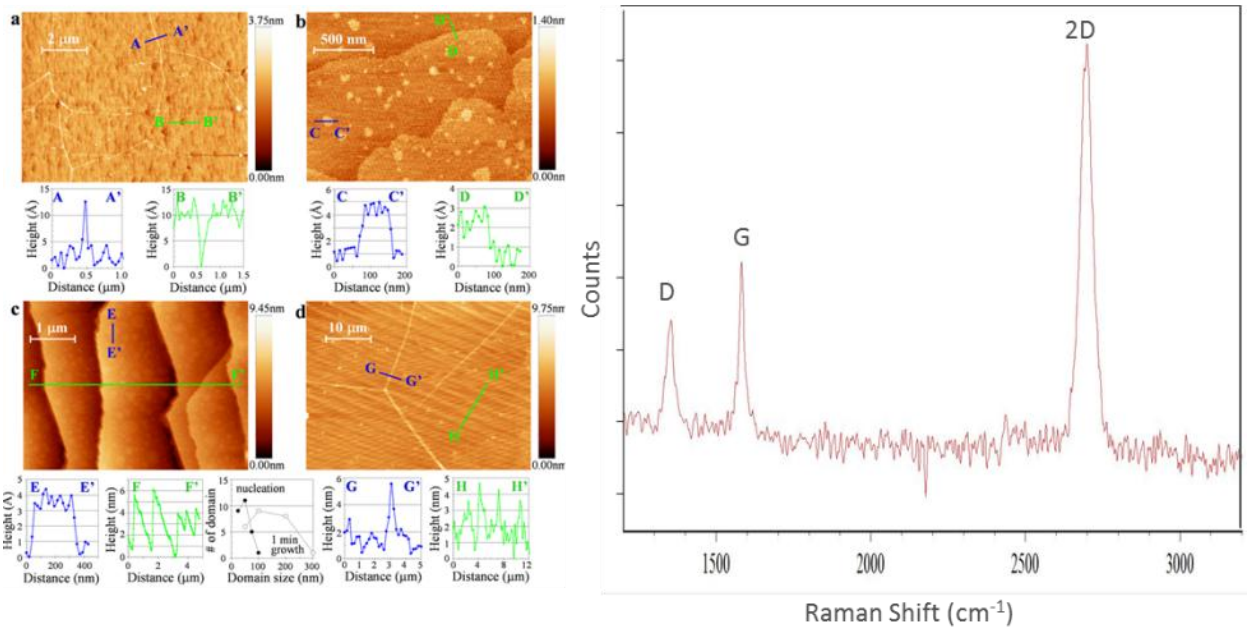

Figure 3.8 (Left) AFM analysis of graphene on sapphire. (a) Graphene was directly grown at 1550°C for 3 min with CH4 concentration of 0.8% and a H2/CH4 ratio of 12. (b) AFM of "nucleation only" sample. This sample was nucleated at 1350°C for 3 min with the CH4 concentration of 0.15% and a H2/CH4 ratio of 14 and then immediately cooled. (c) AFM of "partially grown" sample. This sample was nucleated at the same condition described in panel b and then grown at 1650°C for 1 min with a CH4 concentration of 0.15% and a H2/CH4 ratio of 10. It was an intentional incomplete growth to see the lateral growth of nucleation domains. The size distributions of the graphene domains in a 1 μm2 area are shown here together. Solid circles indicate the distribution after nucleation as seen in panel b, and the open circles represent the distribution after nucleation þ1 min short growth as seen in panel c. (d) This sample was grown by the two-step method. This sample was nucleated and then grown at the same condition of panels b and c but for 3 min at 1650 °C to complete growth. (Right) Raman Spectra showing the distinct D, G and 2D peaks. [193]

3.2.3 Graphene Transfer Process from Copper Substrates

Graphene was transferred from copper substrates via a conventional transfer method. 4% PMMA solution in anisole was spun at 2000 RPM for 45 seconds and then baked for another 45 seconds on a 160◦C hotplate. Samples were then transferred to a chemical hood where they were suspended in copper etchant (ferric chloride) for about 3-4 hours. After the copper had etched away, the PMMA with the graphene adhered to it was floating on the surface of the copper etchant bath. The samples were then carefully transferred to a DI water bath to allow for excess ferric chloride ions to wash out. The samples were transferred from one water bath to another 6

times and then left in the last water bath for about 3-4 hours. It was then carefully transferred to a 100nm silicon dioxide on silicon substrate, allowed to air dry and the put on a 90◦C hotplate to remove any wrinkles. The samples were immersed in acetone overnight to remove the PMMA and the washed with isopropyl alcohol (IPA) and DI water to remove any acetone residues. Illustration 3.2 shows step-by-step pictures of such process. The times indicated are important to note that some steps, particularly the Cu etch and water baths, require a minimum time to ensure a good quality transfer.

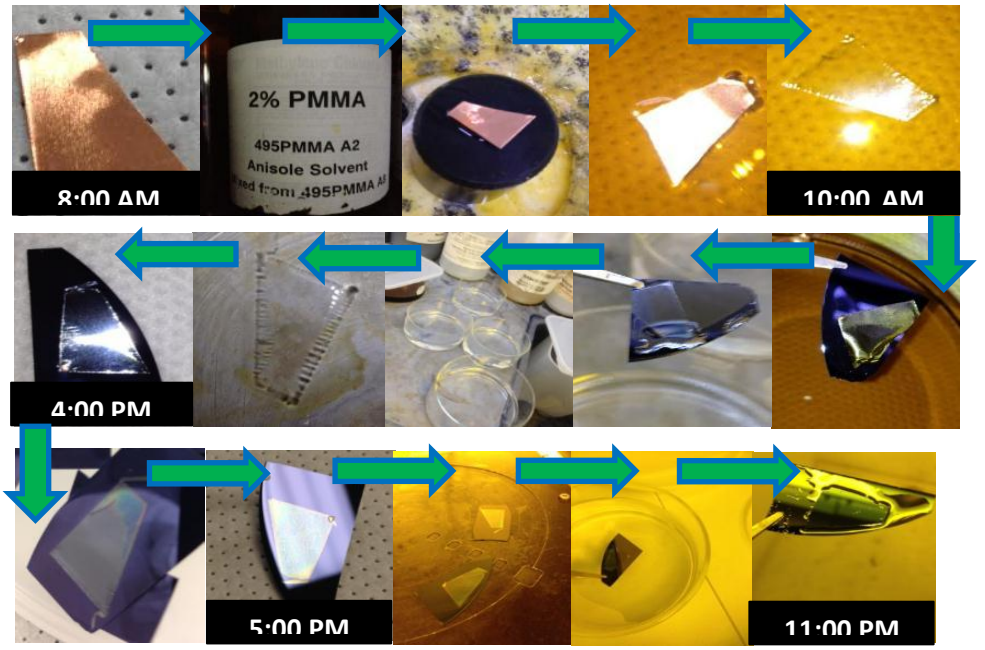

Illustration 3.2 Step-by-step images of the graphene transfer process from copper substrate to silicon dioxide.

For ease of fabrication and sample availability, some samples with transferred multilayer graphene material were directly purchased from Graphene Labs for nanofabrication. Samples were characterized via Raman spectroscopy. The Raman spectra of single layer, bilayer and multilayer graphene on SiO_2 is illustrated in Figure 3.9.

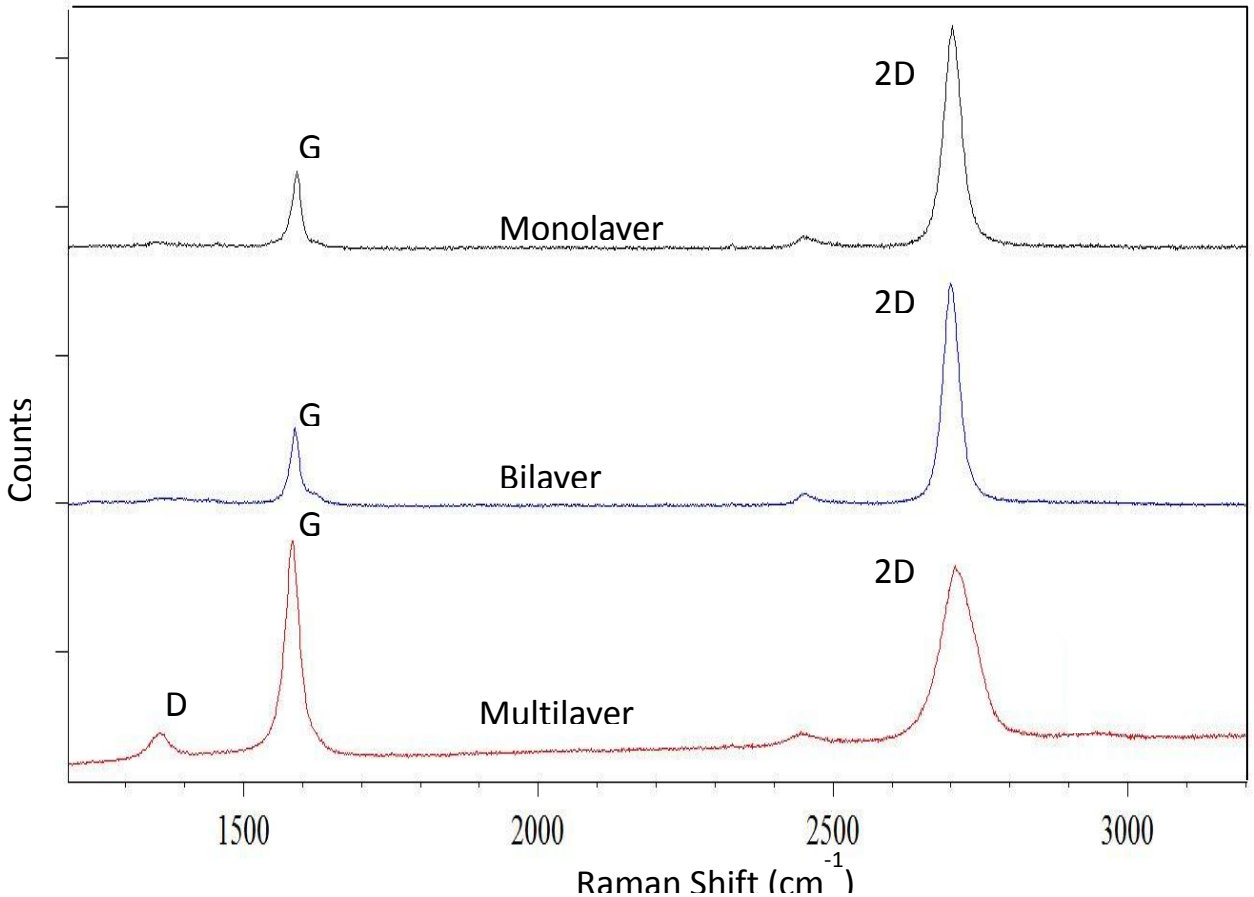

Figure 3.9 Stacked spectra of monolayer, bilayer and multilayer graphene prior to fabrication. D represents the defect peak, G represent the peak observed due to high frequency phonon process at the Brillouin zone center. The 2D peak represents the lattice vibration form two-phonon processes.

3.3 Device Fabrication

The graphene microelectrode array was fabricated utilizing traditional silicon-based micro-fabrication processing techniques. Graphene was either grown or transferred onto wafers and patterned with interconnect and passivation layers. Throughout the fabrication scheme, devices were continuously inspected with an optical microscope and Raman Spectroscopy. Lastly, samples were diced into chips before mounted on a glass PCB for wire-bonding. First generation devices proved to have some leakage due to the small overhead of the passivation over the metal lines. Subsequent designs had over 200 μm of overhead to ensure fluid didn't sit directly over the

metal lines, even if separated by the passivation

3.3.1 Processing

The fabrication procedure is depicted in Figure 3.10. The protocol was cross-compatible across different substrates and types of graphene, which was helpful in fabricating several samples in parallel, cutting down in both time and resources. Devices were made using a 3-mask positive photoresist process for chips plus one additional mask used to make the PCB. The initial fabrication process was implemented in around a 1 year period. However, once established and proven robust enough, the chip turnaround was roughly 2-3 days.

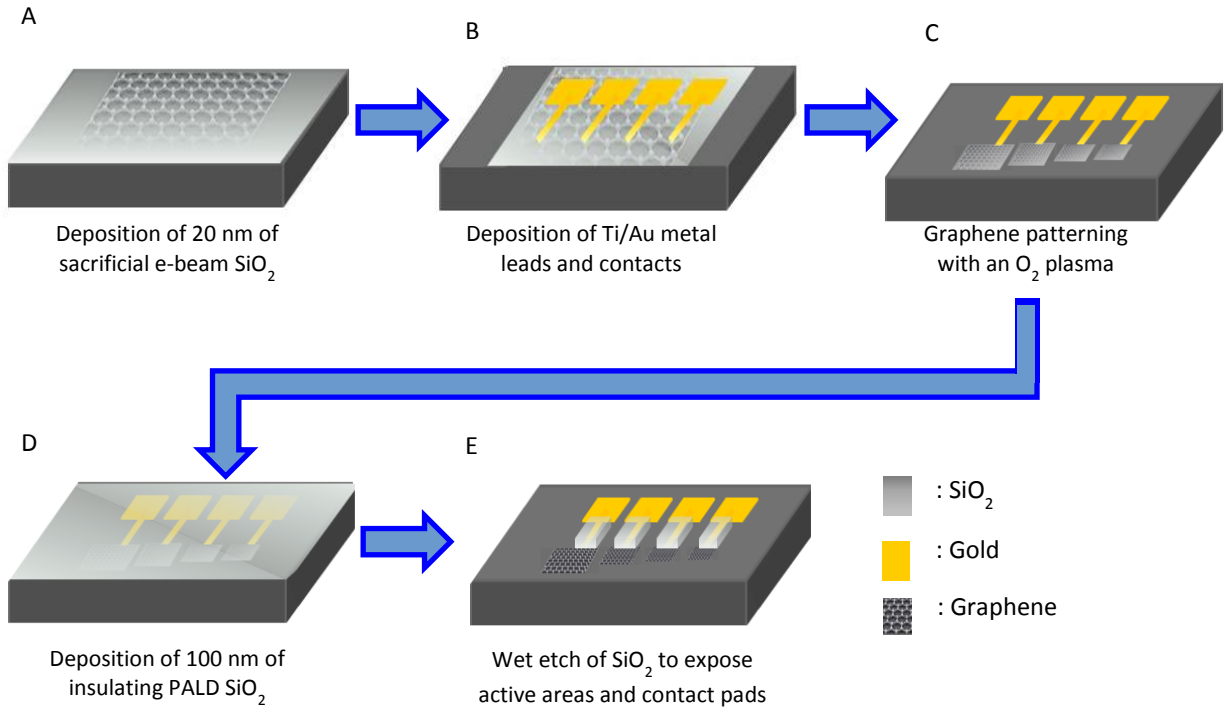

Figure 3.10 Fabrication Protocol of Graphene Microelectrode devices

3.3.1.1 Use of a sacrificial layer

After choosing the appropriate sacrificial layer through trial and error of several oxides, 20 nm of evaporated silicon oxide, chosen as the most optimal material, was deposited on our surfaces. It is important to note that the quality of the silicon oxide and the crucible holding it is critical to process integration. Any types of contaminants or residues in the oxide (or the crucible) would leave cracked, crusty, uneven or poorly adhered oxide onto the graphene samples. To this end, the oxide was replaced for every use and a crucible exclusively for silicon oxide crystals was used.

Samples were mounted on a CVC SC4500 even-hour E-gun Evaporation System. This cryopumped evaporator contains a 6 pocket electron gun source. Once samples were mounted, the evaporator was pumped down for roughly 75 minutes, allowing it to reach a pressure of 2 $\times 10^{-6}$ Torr. Power of the e-gun was manually ramped to roughly 6%, letting the deposition rate stabilize to around 0.5Å/sec, at which point the shutter was opened until 20nm were deposited. The etch rate of the material was established against Buffered Oxide Etch 30:1 (DI H_2O: HF) and found to be roughly 1.33nm/sec. Despite the established etch rate, it was important to monitor samples to prevent over-etching, as it would also tend to etch away graphene on SiO2 substrate.

3.3.1.2 Metal interconnect and Pads Patterning

SPR 220-3 μm photoresist (PR) was spun for 60 seconds at 3000RPM in the photolithography hood. Samples were primed with P-20 (20%- *hexamethyldisilazane)* prior to spinning PR to enhance adhesion of the photoresist to the substrate, as both graphene and the photoresist render hydrophobic. Samples were then baked on a 115◦C hot plate for 90 seconds and exposed, using the Layer 1 mask with a near-UV light source in contact proximity. After developing the samples in MIF-726 (2% tetramethylammonium in DI water), samples were dried out and inspected.

It was found that for first and second generation devices, with interconnect lines as thin as 20 and 40 μm, it was necessary to develop for 150-165 seconds. Developing for lesser amount of time lead to incomplete removal of the photoresist, which lead to breaks in the metal interconnects. This is seen in Illustration 3.3. Later generations of the electrodes used thicker metal lines, also as a means to improve resistivity.

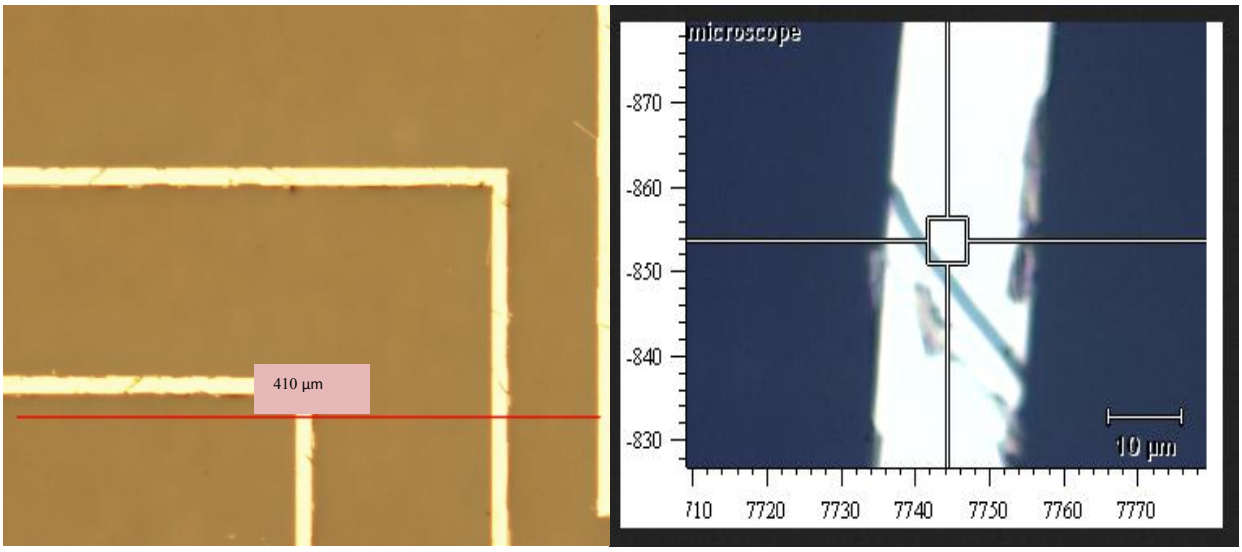

Illustration 3.3 Optical microscope photograph 20 μm lines in first generation devices. The lines reveal small break due to under-developed photoresist.

The oxide was etched for 15 seconds and samples were rinsed with DI water. At this point, it was critical to inspect samples, as any oxide remaining affects the contact resistance to the graphene. To ensure the oxide was entirely etched away, samples were allowed to over-etch slightly for 1-2 seconds until small cracks could be visible in the graphene layer underneath. Samples had to be continuously be inspected to ensure the oxide had been removed, particularly with samples grown epitaxially on SiC or sapphire. Profilommetry, visual inspection under the microscope, and Raman were utilized extensively across all process steps to verify the presence, removal and/or defects of the graphene after each process step.

Samples were then mounted on the odd-hour CVC SC4500 evaporator. The tool was allowed to pump down to 2×10^{-6} Torr, at which point the shutter was opened. 10 nm of titanium were evaporated, followed by 150 nm of gold. Post evaporation, samples were allowed to sit in acetone overnight to carry out a lift-off. They were cleaned with IPA and rinsed with DI water before proceeding to electrode patterning. An image of samples prior to gold evaporation and after lift-off is seen in Illustration 3.4.

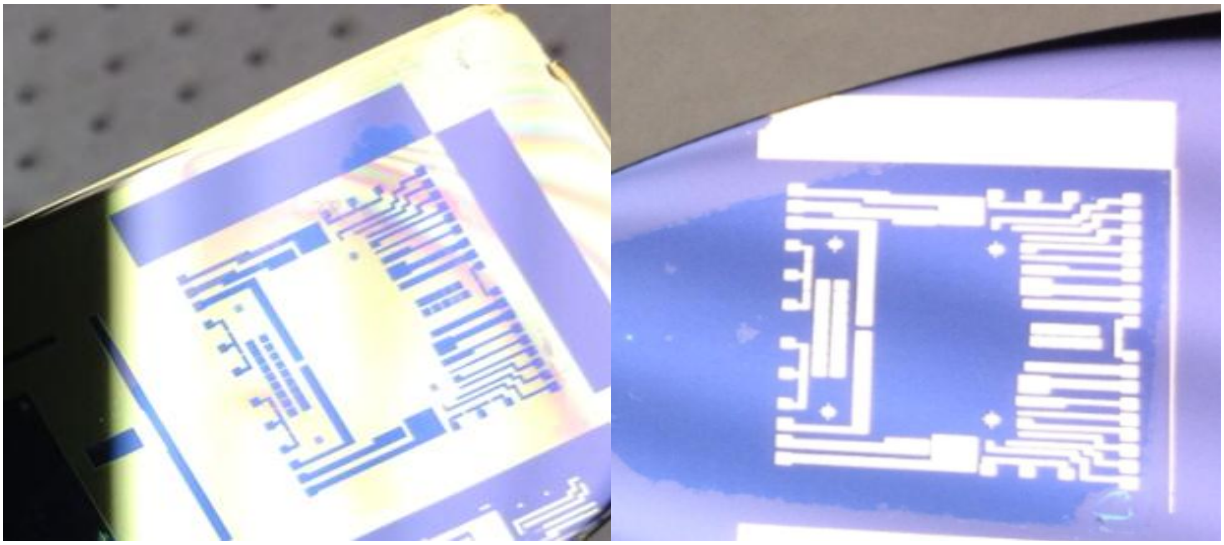

Illustration 3.4 Pictures of Second Generation Devices before (left) Ti/Au evaporation and after lift-off (right).

3.3.1.3 Electrode Patterning

Photoresist was again spun, baked and developed as describe in section 3.3.1.2, this time using the second layer mask to pattern graphene electrodes. The unmasked oxide was etched in 30:1 BOE and the samples were then etched using 50 sccm, 50W oxygen plasma for 60 seconds. Samples had been etched in a downstream plasma using the YES CV200RFS Oxygen Plasma Asher. It was a harsh treatment and unable to preserve our smallest 20 μm features. Consequently, we switched to the PT72, which offered more controlled and uniform etching. Figure 3.13 shows an image of a patterned serpentine electrode.

After patterning the graphene active areas, samples were immersed in nanostrip for about 2 hours to allow for the masking PR to be stripped away gently. They were then washed with acetone, IPA and DI water, and dried with a nitrogen gun. Patterned electrodes before and after plasma exposure are pictured in Illustration 3.5.

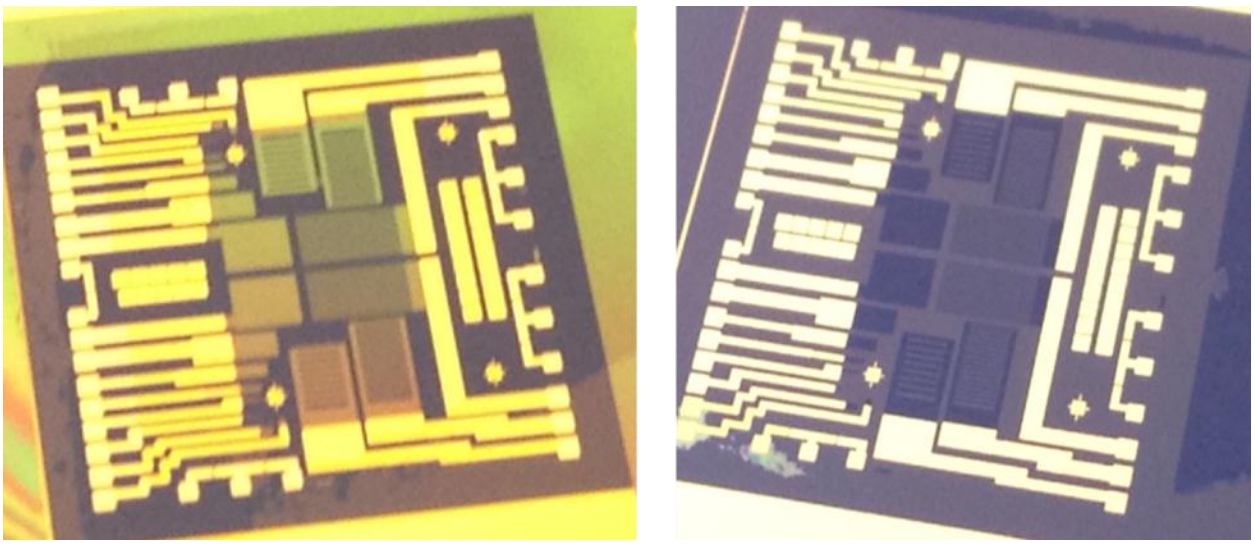

Illustration 3.5 (Left) Image of chip with electrode photoresist pattern only. (Right) Picture of patterned electrodes after oxygen plasma etch of graphene and photoresist removal. Both are images of second generation chips.

3.3.1.4 Passivation

Plasma atomic layer deposited silicon oxide was blanketed over the samples at a temperature of 300◦C in an Oxford ALD FlexAL system. The deposition rate was less than 1Å/cycle. Roughly 1200 cycles were run to meet the required 100 nm thickness. This thickness proved to be dense enough to prevent ions from leaking to the metal interconnects. After deposition, samples were once again prepared with lithography steps outlined, but exposed with Mask 3, which defined the passivation layer. An estimated etch rate for ALD SiO_2 was .94 nm/second in 30:1 BOE. Samples were etched for about 105 seconds, being careful not to over-etch as to prevent lifting off the graphene (this was the case for chips fabricated on SiO_2/Si substrates).

3.3.2 Packaging

Device integration for testing purposes required for the chip to be mounted and wire-bonded onto a printed circuit board. Device integration for implantable purposes is much more complex, and outside the scope of this thesis, and thus, not addressed. Illustration 3.6 shows a picture of the completed quartz PCB.

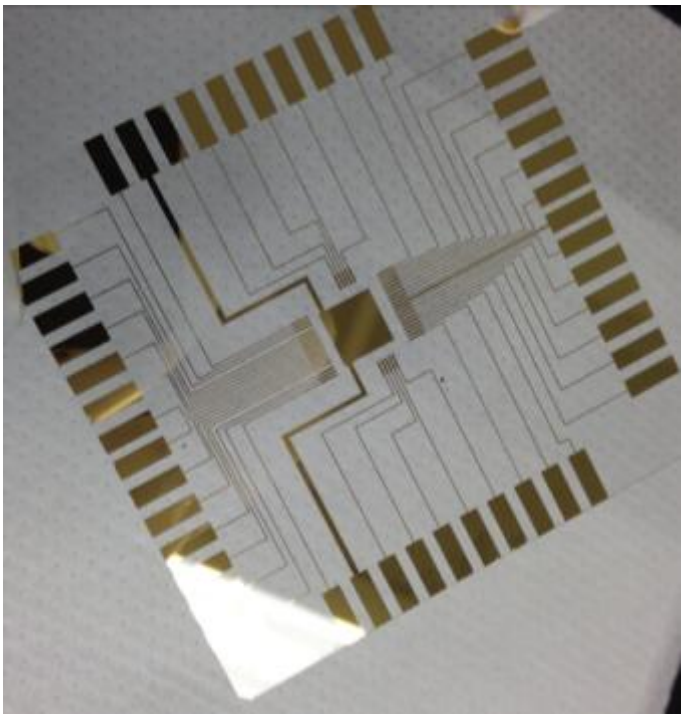

Illustration 3.6 Patterned printed circuit board with a 10/150nm chrome/gold deposition and patterned with wet chemical etch. Boards were roughly 3 x 3 inches.

3.3.2.1 PCB design and fabrication

Quartz wafers were evaporated with 10/150 nm of chrome/gold. Prior to evaporation, all wafers were Piranha cleaned to avoid lack of adhesion. Wafers were mounted onto a CHA evaporator. Post metal evaporation, photoresist was spun, baked, exposed and developed as described previously. A gold chemical etch followed by a chrome etch was used to pattern the PCB lines. The PCBs were trimmed using the K&S dicing saw.

3.3.2.2 Chip Dicing

Fabricated chips had to be diced in order to be wire bonded onto the glass PCB. To that end, each chip was individually trimmed using the K&S dicing saw, which has up to 1 mm resolution to trim miniscule edges. Chips had to be protected with photoresist prior to being diced because the tool makes use of strong water currents as it cleaves the silicon (or glass) substrate. To protect graphene from photoresist contaminants, the dicing was done prior to patterning the graphene electrodes, post lift-off. At this point in the process, samples were still protected from the photoresist with a thin oxide layer. A photograph of a chip prior and after dicing is observed in Illustration 3.7 below.

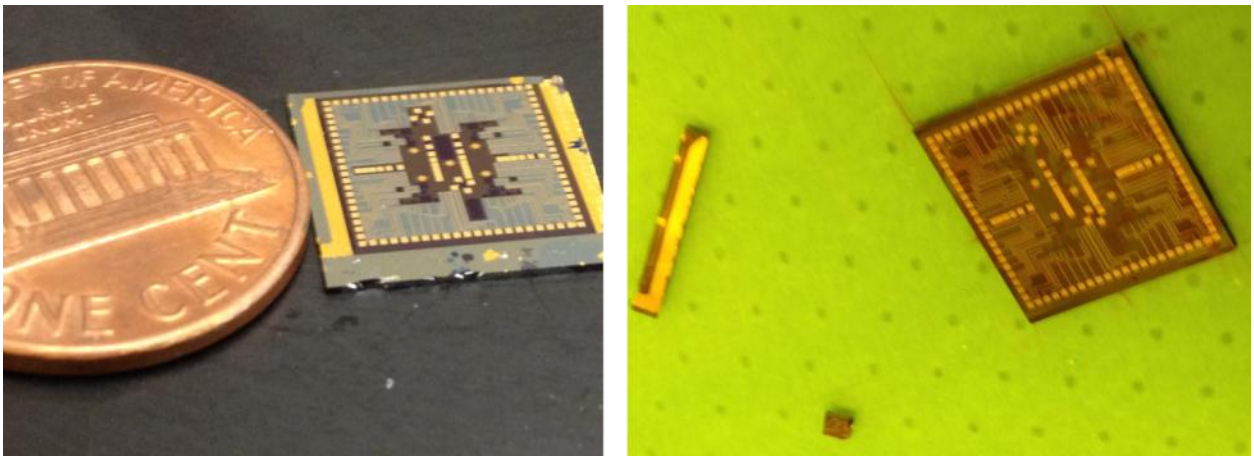

Illustration 3.7 (Right) Picture of a chip prior to dicing. Size is smaller than a penny. (Left) Image of a diced chip.

3.3.2.3 Wire-bonding and DUT setup

Chips were mounted on the PCB with conductive nickel tape and wire-bonded with aluminum bonds, at a tool power of 350W. A picture of the finalized and packaged chip is illustrated in Illustration 3.8. The contact pads had excellent adhesion to the substrate, as no pads were lifted off the chip with wire-bonding. First and second generation chips had 48 electrodes, 4 TLM

lines, 2 Van der Paw structure and 12 solution-gated transistors, which were not part of this study. Third generation chips had 22 electrodes, 6 of which were serpentine electrodes. The minimum size feature was 5 micron. However, the smallest properly pattered electrode was as small as 20 micron. (10 and 5 microns ide length devices we not achievable with contact lithography).

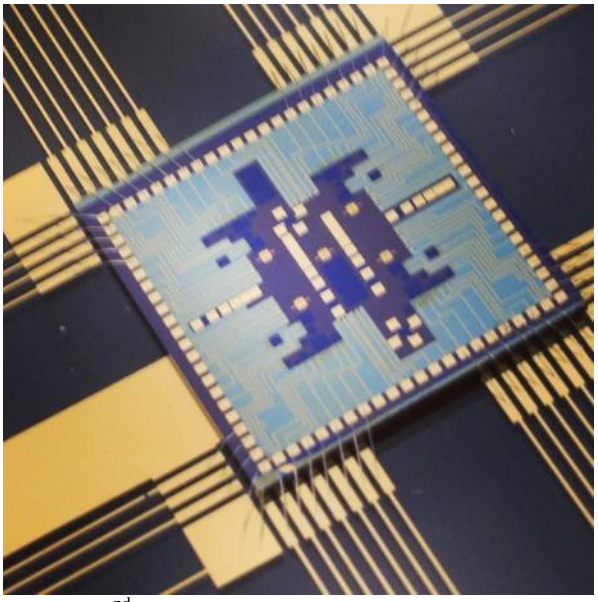

Illustration 3.8 Completed 2nd generation chip mounted onto a glass PCB and wire-bonded.

3.4 Parasitics: Calculation and measurement

We defined what the device and circuit parasitics were in section 3.1. Electron kinetics are understood by analyzing the voltammetric response of redox reactions on electrode surfaces. However, these kinetics can often be masked or affected by other impedances in the system. We will now take a closer look at the impedances associated with our electrode design and inherent to the fabrication process. In chapter 4 we will take a look at the parasitics intrinsic to the experimental setup.

3.4.1 Passivation Capacitance

Our design isolates the active electrode areas from the contact pads, found on the periphery of the chip, by using Ti/Au interconnects. In the first generation devices, these lines were kept at around 20 micron in width. However, they were as long as 3000 um. In subsequent designs the lines were as thick as 250 micron to enhance the contact resistance and avoid breaks in the lines due to under-developed photoresist. The lines were insulated to prevent our analyte from coming in contact with the gold surfaces, as this would lead to false positive results. Even though the fluid rested mostly on the active area, and there was very little overlap of it with the metal lines, there was some passivation capacitance to account for. Given the dielectric permittivity of silicon oxide and the thickness of the passivation layer the passivation capacitance was given by:

$$C = \frac{\varepsilon_{SiO2}\varepsilon_o A}{d} \tag{3.1}$$

Here, ε_{SiO2} is the relative permittivity constant of silicon dioxide, 3.9 and $\varepsilon_o$is the vacuum permittivity, 8.85×10^{-14} F/cm; *d* is given by the thickness of the oxide layer, 100 nm. The area is defined by the width of the contact and the length through which the metal lead overlaps with the fluid. The normalized capacitance was 34nF/cm^2. We will see in section 4 that this capacitance becomes negligible in our measurements.

3.4.2 Crosstalk Capacitance

In our measurements, one electrode was measured at the time, so there was no actual crosstalk between metal leads. However, it is important to discuss crosstalk for future applications, which

may involve using more than one electrode at the time for simultaneous measurements.

The cross-talk can be minimized by maximizing the distance between the leads and decreasing the thickness of the metal leads. In addition, choosing a material with a lower permittivity constant, such as silicon dioxide, helps reduce any crosstalk capacitance. As we will see in Chapter 4, the double layer capacitance is on the order of uF/cm^2, so it is important to keep the other capacitances to be much lower. As seen in Figure 3.1, the capacitances run parallel to each other. Because the distance between adjacent leads is on the order of tens or even hundreds of micron, the crosstalk capacitance becomes negligible.

3.4.3 Substrate capacitance

Because our substrates are sapphire, insulating silicon carbide and thick silicon dioxide films over silicon, the substrate capacitance contributions also become negligible in our design. While we considered electrodes on hafnium oxide or aluminum oxide over silicon substrates (and as passivation layers), the high-κ inherent to these oxide would have increased the parasitic capacitances.

3.4.4 Contact and Sheet Resistance

We used the transmission line method to extract the contact resistance, lateral sheet resistance and transfer length of the graphitic materials used. Along with the uncompensated resistance (see Chapter 4), the lateral sheet and contact resistance account for significant corrections in our measurements due to the magnitude of the currents being measured. TLM structures and Van der

Pauw structures were used within the chip. Because of the large graphene areas defined by the Van der Pauw, there were hard to test as there were introduced cracks and holes that lead to lack of continuity for a four point probe measurement.

Figure 3.11 shows a plot of the normalized measured total resistance for monolayer graphene as a function of spacing between the contacts. Contact line spacing extended past 25 micron, but for accuracy those measurements were not included, as with larger spacing there are increased number of irregularities, defects, holes and discontinuities. Transmission line measurements yield values for the contact resistance, R_C, the transfer length, L_T and the sheet resistance, R_{SH} of the semiconductor being studied.

The total resistance can be expressed as a function of the spacing length:

$$R(L) = \frac{R_{SH}}{W}(L + 2L_T) \tag{3.2}$$

Thus, from our measurements and best fit lines to the data we were able to extract mean values for the contact and sheet resistances and the transfer length. The results are summarized in Table 3.1.

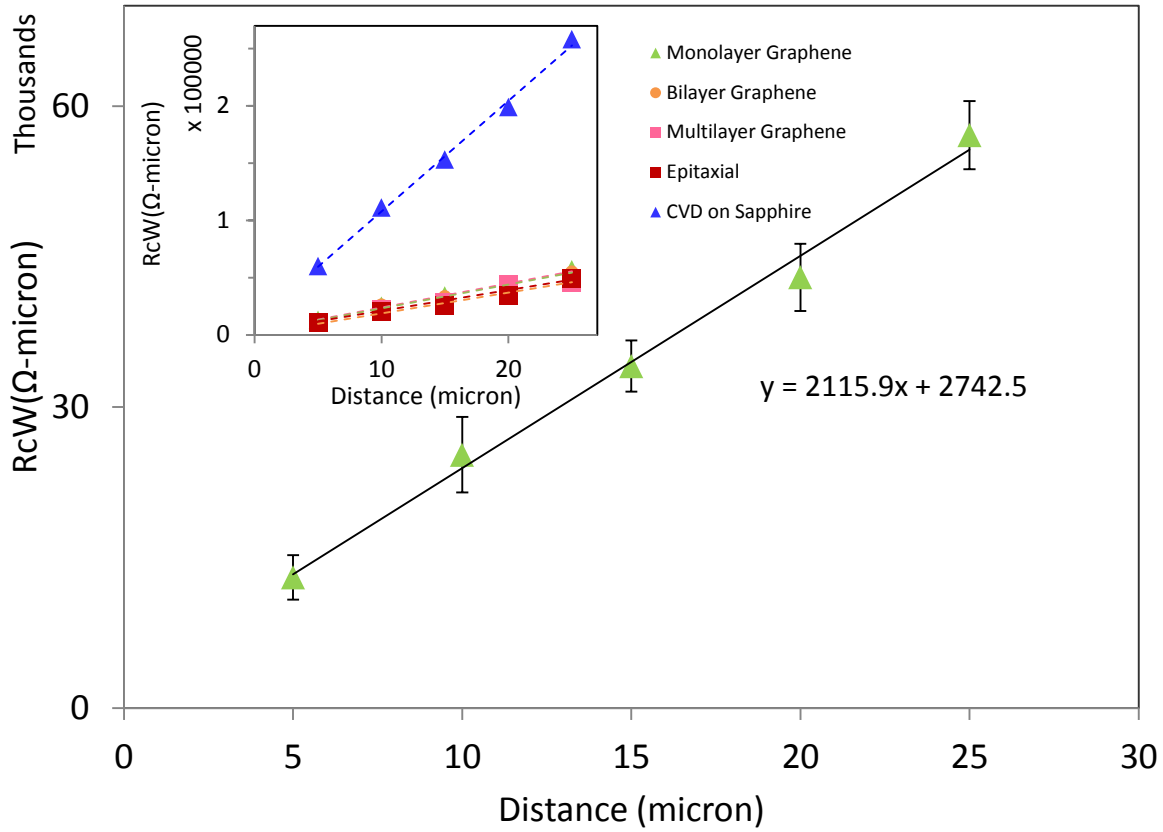

Figure 3.11 TLM analysis for monolayer graphene. The inset shows the TLM analysis for the other materials being used.

Table 3.1 Average values with standard error for TLM analysis.

Graphene Type	R_c(ohm-μm)	R_{sheet}(ohm/□)	ρ(ohm-cm^2)	Transfer length (L_T)
Single Layer	1371±239	2116±299	3.55X10^{-5}	1.29
Bi-layer	1184±283	2086±373	2.68X10^{-5}	1.13
Multilayer	1161±230	1882±406	2.86X10^{-5}	1.23
Epitaxial on SiC	753±147	1506±482	1.37X10^{-5}	0.91
Graphene on Sapphire	5544±853	9672±1984	1.27X10^{-4}	1.146

The values extracted are somewhat higher than those reported in the literature for CVD and epitaxial graphene. This was probably due to the fact that the fabrication process, despite being carefully carried out, did leave some residues or created holes in the graphene. Regardless, there

was not significant variation in contact or sheet resistance values across the different number of layers, as reported by Russo *et al*.[196]. The contact and sheet resistance for CVD material grown on sapphire was roughly 5 times greater than for any of the other materials. We hypothesize that the uneven patchy distribution of this type of material led to higher sheet and contact resistances. Chapter 4 examines the many differences seen between the voltammetric behaviors of the different graphene types, particularly as electrodes are scaled down.

3.5 Summary

- Each electrode of the array is made up of a graphene pad in the center of the chip connected to a contact pad at the edge of the chip through a metal lead. It is isolated from the contact pad via an oxide passivation layer.
- Graphene was either grown directly on sapphire substrates via CVD or epitaxially on silicon carbide. Mono-, bi and multilayer material that had been grown on copper or nickel films and transferred to 300 nm of silicon oxide was also used for chip fabrication.
- Post fabrication all chips were mounted and wire-bonded onto a PCB for experimental recordings.
- Starting materials and electrodes were characterized primarily using Raman spectroscopy during the fabrication process. Post-fabrication, electrodes were characterized using Raman Spectroscopy and AFM.
- Most capacitive impedances in our design were negligible as compared to the electrical double layer capacitance, but the contact and sheet resistances were extracted for future correction factor of experimental voltammograms.

CHAPTER 4

ELECTROCHEMICAL PROPERTIES OF GRAPHENE ELECTRODES

More than 500 electrodes were characterized in this study. Electrodes varied in size, substrate, graphene type, but encountered the same fabrication process for consistency. The reported values in this section are purely experimental results, and confirm other finding and hypothesis put forward in the literature about the electrochemical behavior of graphene. We have summarized the gathered data for the performance metric of all electrodes to establish a proper comparison and present the results in this chapter.

We now turn our attention to the electrochemical characterization of graphene electrodes. This was the first true comparison across epitaxial, CVD on SiO_2 and CVD on sapphire graphitic materials that entailed patterned electrodes with photolithographic steps. The different materials and device geometries exhibit different ratios between the basal and edge plane sites. The electrochemical characterization was consistent with other results in the literature, and offered some interesting insights into the fabrication process in itself. If was found that electrodes that had been roughened through the fabrication process (ie. had more holes and defects, without substantial material loss), exhibited faster electron transfer kinetics than those with relatively 'defect-free' graphene surfaces. The electrode behavior was found to scale down with defined area and concentration. The overall performance of epitaxial electrodes was concluded to be just as good or slightly better than that of CVD electrodes.

4.1 The Randles-Sevcik Equation

In Chapter 2 we derived the expression for the Cotrell equation and for the concentration at an electrode surface as a function of time for a step potential. In linear sweep voltammetry the electrode potential is swept at a scan rate *v* so that the potential at any time is given by:

$$E(t) = E_i + vt \qquad , \tag{4.1}$$

where E_i is the initial open circuit electrode potential. In our experiments it was found to be around .2 Volts. Because the rate of electron transfer is rapid at the electrode interface, the oxidized and reduced species will immediately adjust to the ratio dictated by the Nernst equation (2.1). We can now reorganize this equation to be a function of the applied potential, and thus time:

$$\frac{C_A(0,t)}{C_B(0,t)} = exp\left[\frac{nF}{RT}(E_i + vt - E^{o\prime}\right] \tag{4.2}$$

Equation (4.2) really becomes a boundary condition for the solution of the current at the electrode surface at any given time during a potential sweep. The solution to this equation was first considered by Randles and Sevcik and later approached by Nicholson and Shain [139]. The solution for the current expression current is given by:

$$i = nFAC_o^*(\pi D_o \sigma)^{\frac{1}{2}}\chi(\sigma t) \tag{4.3}$$

where σ is given by *(nF/RT)v* and $\chi(z)$ is given by:

$$\chi(z) = \frac{i(\sigma t)}{nFAC_o^*(\pi D_o \sigma)^{1/2}} \tag{4.4}$$

$\chi(\sigma t)$ is a pure number and relates the current to the variables. Specifically, it shows that the current is proportional to the concentration and to $v^{\frac{1}{2}}$. The current reaches a maximum value where $\pi^{\frac{1}{2}}\chi(\sigma t) = 0.4463$ and this peak current is the well-known as the Randles-Sevcik equation, given at room temperature by:

$$i_p = (2.69 \times 10^5) n^{3/2} A D_o^{1/2} C_o^* v^{1/2} \tag{4.5}$$

Where *A* is given in cm^2, D_o is given in cm^2/s, C_o^* is given in mol/cm^3, *v* is given in V/s and i_p is given in amperes. This equation is the most important equation that we will be manipulating to assess our electrode performance metrics, extract effective electrode areas, rate constants and measure detection limits. It relates the measured currents to the known and unknown experimental conditions we want to extract to evaluate not just the quality of the graphene, but also the overall robustness and stability of our fabrication process.

4.2 The Electrode-Electrolyte Interface

The electrochemical processes at the electrode-electrolyte interface not only determine the electron transfer kinetics, but also what, if any, impact it will bring to both the electrode and the

surrounding electrolyte. Good electrochemistry is critical for reliable, reproducible and accurate data acquisition. To that end, it is important for us to understand the impedances and processes that take place at the interface between a semiconducting surface and a physiological solution. In section 3.1 we presented the basic circuit scheme for our graphene electrode and, in section 3.4 we analyzed the impedances inherent to the devices structure and fabrication process. In this section, we will examine the impedances inherent to the experimental setup, namely the impedances seen at the electrode-electrolyte interface. These are depicted in Figure 4.1. The impedances presented are solely due to the interface of the working, reference and auxiliary electrodes with the analyte, and exclude parasitics associated with micro-fabrication variables.

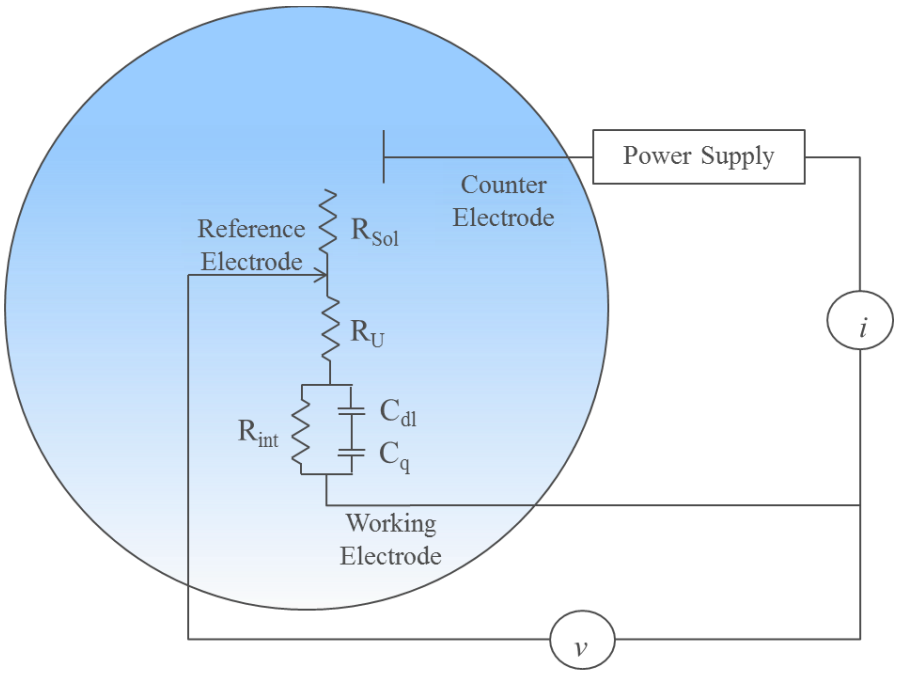

Figure 4.1 Depiction of parasitics inherent to the electrode-electrolyte interface.

Even under no applied bias, chemical reactions do take place at the interface [197]. One-step electron transfer redox processes occur, driven by thermodynamic equilibrium. As this occurs, an

excess charge layer builds up on the electrode surface. A second layer of charges, composed of ions, attracted to the surface charge via Coulombic forces electrically screens the first layer. This second layer is loosely associated with the electrode surface. It is made of free ions that move in the fluid via electric attraction and thermal motion rather than being firmly anchored. It is thus called the "diffuse layer". Once equilibrium is reached the net current across the interface is zero. Figure 2.2 schematically shows the electrical double layer. To keep a continuous current flow at the interface, there must be either a capacitive current through the double-layer formed by the excess charge on the electrode surface and the space charge (diffuse) layer in the solution, or there must be some type of resistive current through a faradaic process, in which case charge are actually transferred between the solid electrode phase and the solution. A faradaic current would encounter both a solution resistance, R_{Sol} and an interface charge transfer resistance, R_{int}. This can be seen in Figure 4.1. In addition there is an uncompensated resistance, R_U, also known as a spreading resistance due to the placement of the reference electrode.

4.2.1 The Double-Layer Capacitance

The interfacial capacitance at the electrode-electrolyte interface plays a critical role in our work, as it is responsible for any charging currents that can be observed in our measurements. These become more relevant as the concentration of analyte species is reduced. All peak currents must be measured with respect to this charging current, and, as expected, it is a function of the applied potential of the working electrode.

Close to the electrode, water dipoles in solution orient themselves to form a hydration sheath. In

figure 2.2 anions specifically adsorb to the electrode surface. The locus of the anion is usually termed the *inner Helmholtz plane (IHP).* The locus of the nearest hydrated cations is called the *outer Helmholtz plane* (OHP). Water dipoles separate these cations from the electrode surface and they are said to be nonspecifically adsorbed. Because of thermal agitation these ions dispense with a concentration gradient from the OHP to the bulk solution forming the *diffuse layer.*

4.2.1.1 The Gouy-Chapman-Stern (GCS) Model

The double layer capacitance had originally been treated by Helmholtz as a constant parallel-plate capacitor.

$$C_{dl} = \frac{\varepsilon_o \varepsilon}{d} \tag{4.6}$$

Equation (4.1) expressed the double layer (in units of Farads/cm^2) as a mere function of the permittivity of the solution and the distance between two sheets of charge at the electrode surface. However, experimental data revealed C_{dl} changed with applied potential and concentration. Because of the diffuse layer, the thickness d is actually the result of a balance between the electrostatic attraction or repulsion taking place at the electrode surface and the thermal agitation defining the diffuse layer. This concept of a diffuse layer was put forward by the Gouy-Chapman theory. Thus, higher electrode potentials or higher solution concentrations would make the C_{dl} more compact, and hence give it a larger capacitance value.

However, because of the size of solvated ions, the distance from the electrode surface can never be infinitely thin. Stern added the concept of the outer Helmholtz plane (OHP) to separate the C_{dl} into two components:

$$\frac{1}{C_{dl}} = \frac{1}{C_H} + \frac{1}{C_D} \tag{4.7}$$

C_H is the capacitance of the OHP and C_D is the diffuse layer capacitance. The C_{dl} is treated as two capacitors in series. At potentials of little to no charge accumulation, the double-layer capacitance is dominated by the diffuse layer and has strong potential dependence; at larger potentials, the outer Helmholtz capacitance dominates and the C_{dl} approaches a constant value, as originally proposed by the Helmholtz model. Solution concentration is also important because in highly concentrated electrolytes the diffuse layer is so thin that that its capacitance become rather large, and hence, negligible. In such cases the C_{dl} also approaches a constant value.

4.2.1.2 Estimate of the Double Layer Capacitance in Carbon Electrodes

The double-layer capacitance of various forms of carbon ranges widely from 1-70μF/cm^2 [168]. Along the basal plane the electrons are delocalized and can move freely. Graphene has reported high carrier mobilities repeatedly in the literature [21, 25]. However, the resistivity normal to the basal plane and in the direction of charge transfer is much higher, close to 1000 times higher. To that end, it can be considered insulating and one must include an extra space-charge capacitive component in the C_{dl} [198, 199]:

$$\frac{1}{C_{dl}} = \frac{1}{C_H} + \frac{1}{C_D} + \frac{1}{C_{SH}} \tag{4.8}$$

For intrinsic semiconductors,

$$C_{SH} = \left(\frac{2\varepsilon_0 \varepsilon_r q^2 n_i}{kT}\right)^{1/2} \tag{4.9}$$

Where n_i is the intrinsic concentration of electron and holes. The space-charge capacitance is usually much smaller than the Helmholtz or diffuse layer capacitance values, so it dominates the C_{dl}. This accounts for the overall smaller double-layer capacitance seen in graphite as compared to standard metals. Graphite edges, however, have a higher capacitance due to the contribution of surface groups. As expected, the double layer capacitance scales with the electrode area.

4.2.2 The Quantum Capacitance

In the case of graphene, in addition to the double layer capacitance, there is an additional capacitive component, the so-called quantum capacitance, C_Q. C_Q is defined as $\partial Q/\partial U_{gr}$, where Q=*e*(p-n) is the total charge in graphene and ∂U_{gr} represents the electrostatic potential in graphene, or the position of the Fermi level with respect to the Dirac point[200-201]. Therefore, the total interfacial capacitance seen at the electrode-electrolyte interface results from the series combination of the quantum capacitance and double-layer capacitance. There have been conflicting views on an exact model for the interfacial capacitance, but in accordance to the work put forward by Garrido *et. al* [200], we will use a series combination in our model. Figure 4.2 shows how the total interfacial capacitance, C_{ePB} can be described by the combination of C_Q and a C_{dl} of about 3μF/cm^2. It is important to note that for the given calculated values of the quantum capacitance around the Dirac point, the quantum capacitance, usually much smaller than the double-layer capacitance, would dominate the interfacial capacitance. However, we must note

that the presence of charged impurities both from transfer or growth processes can induce chemical doping and shift the Fermi level away from the Dirac point, thus pushing the value of the quantum capacitance up. The Dirac point can be shifted by as much as 50 volts. In such case, the interfacial capacitance is dominated by the double-layer capacitance.

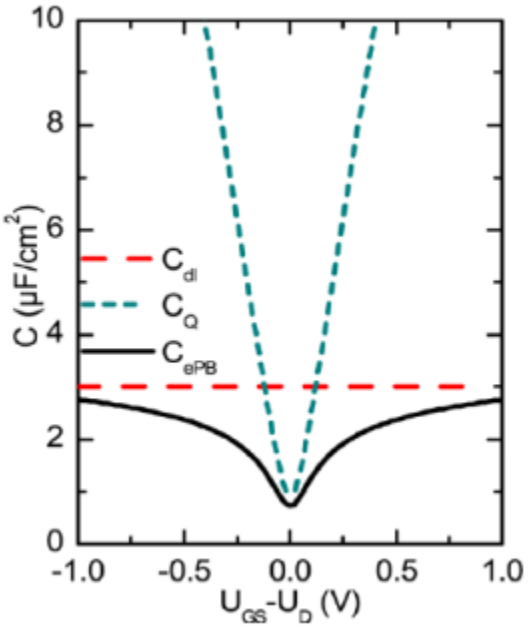

Figure 4.2 Capacitance of the graphene-water interface (CePB) calculated using an extended Poisson-Boltzmann model and its two in-series contributions: the electrolyte double-layer capacitance (Cdl) and the quantum capacitance of graphene (CQ) [201].

4.2.3 Charging Currents

For a potential step experiment at a constant-area electrode, the charging current dies away after a few time constants. However, since the potential is continuously changing as we sweep the voltage, a charging current i_c is always flowing. This current can be written as [139]:

$$|i_c| = AC_d v \tag{4.10}$$

Figure 4.3 shows the typical capacitive current measured from a .267 mm^2 monolayer graphene electrode immersed in $0.2KNO_3$ with no redox analytes in solution. The sweep rate was 200mV/sec. This allows us to extract an estimate for the double-layer capacitance to be around $34uF/cm^2$. The extracted double layer capacitance for all different types of electrodes is given in table 4.1 below and it increases with the number of defects or exposed edges.

Table 4.1 Interfacial capacitance values for tested electrodes

Graphene Type	**Extracted double layer capacitance**
Monolayer	$21 \pm 3\mu F/cm^2$
Bilayer	$55 \pm 7\ \mu F/cm^2$
Multilayer	$69 \pm 4\ \mu F/cm^2$
Epitaxial	$9.17 \pm 2\ \mu F/cm^2$
CVD on Sapphire	$105 \pm 12\ \mu F/cm^2$

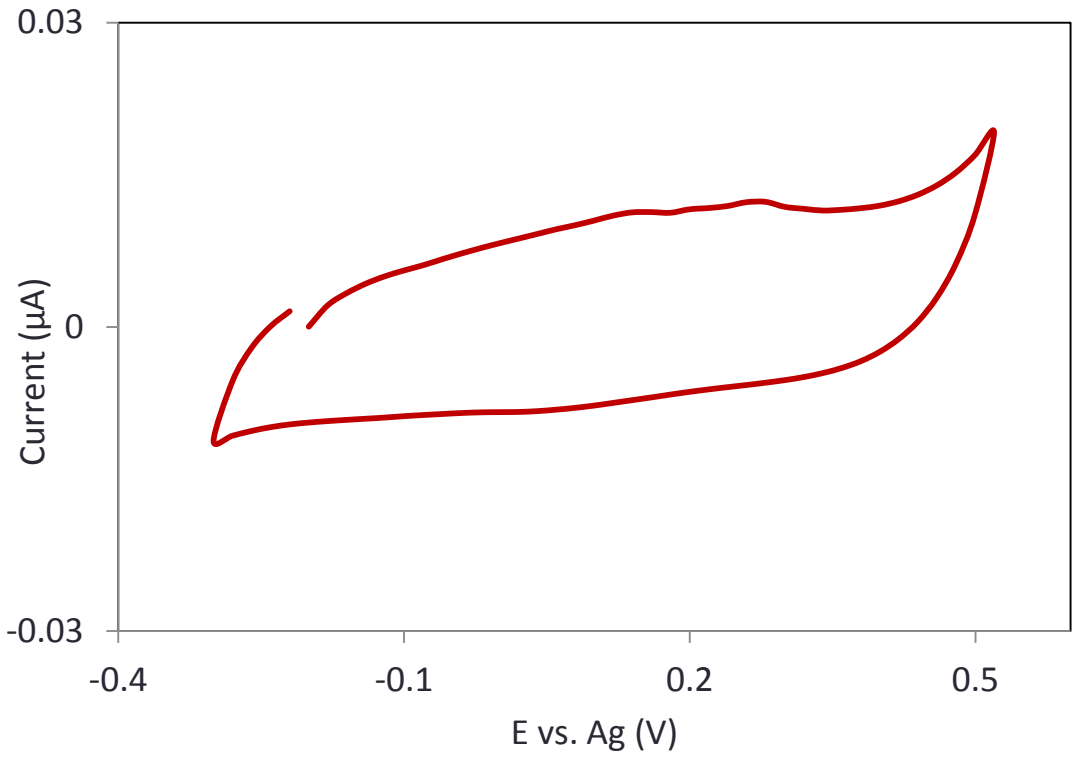

Figure 4.3 Measured capacitive/charging current in 0.2M KNO_3 on a monolayer graphene .267 mm^2 electrode. Scan rate was 200mV/s.

While i_p varies with $v^{1/2}$ for processes dominated by linear diffusion, i_c varies with v and becomes more relevant at faster scan rate. From equation (4.5) and (4.10) we can write [139]:

$$\frac{i_c}{i_p} = \frac{C_d v^{\frac{1}{2}}(10^{-5})}{2.69 n^{3/2} D_O^{1/2} C_O^*} \tag{4.11}$$

Equation 4.11 shows that a higher scan rates and lower concentrations the charging current increases relative to the peak current and inflicts severe distortion to the voltammogram, setting a limit for the useful scan rate and minimum detectable concentration.

4.2.4 The Interfacial Charge Transfer Resistance

In parallel with the double layer and quantum capacitances is the interface charge transfer impedance. This is a valuable metric of how fast electron transfer reactions take place at the electrode interface and is a function of the device geometry, sample preparation and, the ratio of edge to basal plane sites for electrocatalytic activity. The single most important metric for an electrode material is its ability to transfer charges easily or, namely, that it has a large electron transfer constant. For graphene, values as large as 0.042 cm/s have been reported [140]. It has been hypothesized that corrugation increase the heterogeneous rate transfer constant

4.2.5 The Uncompensated Resistance

The three-electrode setup is usually preferred over the two-electrode setup because it keeps the reference electrode potential stable while using an auxiliary electrode to pass the current. If we consider the potential between the working and auxiliary electrode, we can see that unless the reference electrode is placed exactly on the working electrode, some fraction of iR_{Sol} (called iR_U, the uncompensated resistance) will be included in the measurement. Given a reference capillary placed a distance x from a working planar electrode of area A, the uncompensated resistance is given by [139]:

$$R_U = \frac{x}{\kappa A} \tag{4.12}$$

From 4.12 we can see that the uncompensated resistance increases for smaller electrodes. Because the current scales linearly with the electrode area, the iR_U term remains relatively

constant regardless of the size of the electrode. It does, however, increase as we increase the separation of the reference electrode from the working electrode. In our measurements, the active area of the chip was confined to less than 4 by 4 mm. Therefore, an accurate enough estimate of this distance was roughly 2-4mm. κ is the solution conductivity. Table 4.1 lists the solution conductivity for various commonly used electrolytes, including KNO_3. From this table it is clear that choosing an electrolyte with a large electrical conductivity will help decrease the uncompensated resistance. Our carrier electrolyte, 0.2M (roughly 20.1 grams to a liter of DI water) of KNO_3 had an estimated electrical conductivity of 20.1 mS/cm.

Table 4.2 Electrical Conductivity in mS/cm for the Indicated Concentration by Mass percent

Name	**Formula**	**0.5%**	**1%**	**2%**	**5%**	**10%**	**15%**
Acetic Acid	CH_3COOH	0.3	0.6	0.8	1.2	1.5	1.7
Calcium Chloride	$CaCl_2$	8.1	15.7	29.4	67.0	117	157
Hydrogen Chloride	HCl	45.1	92.9	183			
Potassium chloride	KCl	8.2	15.7	29.5	71.9	143	208
Potassium nitrate	KNO_3	5.5	10.7	20.1	47.0	87.3	124
Sodium chloride	NaCl	8.2	16.0	30.2	70.1	126	171
Sodium hydroxide	NaOH	24,8	48.6	93.1	206		

4.3 Experimental Basis of Detection

Detection of ferrocenemethanol was carried out by examining its oxidation potential relative to a silver reference electrode through cyclic voltammetry type measurements. By sweeping the working electrode potential, it is possible to examine the concentration of species in the vicinity of the electrode surface. As species oxidize onto the surface of the working electrode, the current increases. For transport limited by linear diffusion, such as the case of larger electrodes, the current reaches a peak before it decays; because the electron transfer kinetics occur at a faster rate than the sustained diffusion, the current cannot increase with applied potential, and starts decaying. For smaller electrodes, where the mass transport of analyte species to the surface is governed by convergent diffusional processes, the current reaches a steady state, as the rate of electron transfer is comparable to that of species arriving to the surface. The electrode response, in turn, provides insight into the electrochemical behavior of the patterned electrodes, the possible pitfalls of the fabrication process and, more importantly, the ways of improving them for subsequent runs. All electrochemical measurements were made using the cyclic voltammetry technique.

4.3.1 Cyclic Voltammetry

Figure 4.4 shows the typical waveform of the applied potential onto the working electrode. Measuring the capacitive current with no analyte species allows us to get an idea of the potential window, roughly between -.5 and .6 Volts. Figure 4.3 also shows the typical voltammogram resulting from the electrode response, with 8 distinct regions. At A the applied potential is not enough to start oxidizing species, and most of the species in solution near the electrode surface

remain reduced. As the potential increases, at B, past 0 volts, the species start oxidizing. As more species oxidize, the concentration of reduced species at the surface depletes and a concentration gradient is set between the bulk solution and the electrode surface. The rate of electron transfer is faster than the rate at which species can diffuse to the electrode surface. As the applied potential increases, the current is gradually diminished as a result of the gradual expansion of the diffusion layer towards the solution bulk, which in turn will gradually decrease (according to Fick's 1st law) the flux of F_c species towards the electrode surface. Thus, the current reaches a peak, seen at C, before it starts decreasing, at D, despite the increased applied potential.

When the current is reversed a similar trend is observed as the oxidized species are now reduced. At E the potential is not negative enough to reduce the oxidized species. Once it becomes negative enough, at F, the oxidized species in the electrode vicinity start reducing until they reach a cathodic peak at G. Again, the rate at which species reduce is limited by the rate of mass transport to the electrode surface. As the potential becomes more and more negative the number of species that can reduce diminishes, as seen at H.

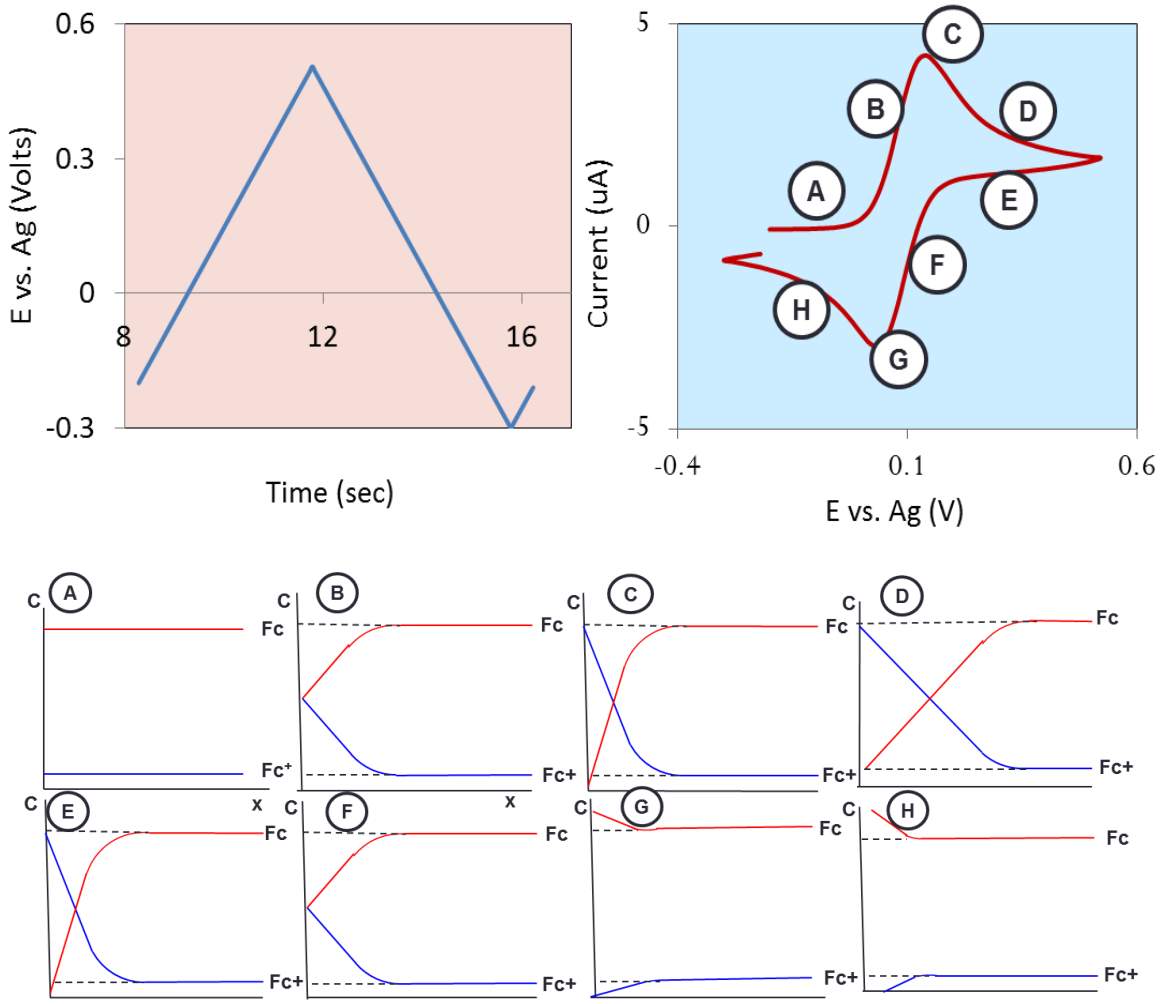

Figure 4.4 Top (left) - Samples input waveform of potential applied to WE. Top (right)-Sample voltammogram observed with 1mM of FcMeOH at 200mV/sec on monolayer graphene. Bottom- Concentration profiles at the electrode surface seen at the different parts of the voltammogram.

4.3.2 Experimental Setup, DUT and Apparatus

Our wire-bonded chip onto the PCB was set on a stage and taped down to prevent it from sliding when using alligator clips to make contact to the PCB. We used the Autolab PGSTAT128N potentiostat for all the measurements presented in this thesis. The carrying electrolyte was prepared using 20.1 grams of potassium nitrate in de-ionized water. 1mM of ferrocenemethanol (16.8 mg/100mL) was prepared in this carrier electrolyte and diluted further for smaller concentrations. The reference and auxiliary electrodes, made of silver and platinum wire,

respectively, were mounted on a manipulator using a cleaved pipette to hold the wires. After making contact to the chip and to the reference and auxiliary electrodes with the alligator clip leads, the reference and auxiliary electrode were placed in close proximity (2-4 mm away depending on the chip layout) to the working electrode, but not touching it. About 50μL of solution was pipetted onto the center of the chip, making sure the auxiliary and reference electrodes were fully immersed. Illustration 4.1 shows a picture of the setup as seen on the chip. The solution held well in the defined active area. The potentiostat was set to scan at a rate between 100mV/second and 500mV/second between -0.3 volts and 0.5 volts with sampling frequencies between 50 and 200 Hz. Sampling any higher introduced significant noise into our results. While NOVA can correct the voltammogram for uncompensated resistance, this feature was turned off in our measurements.

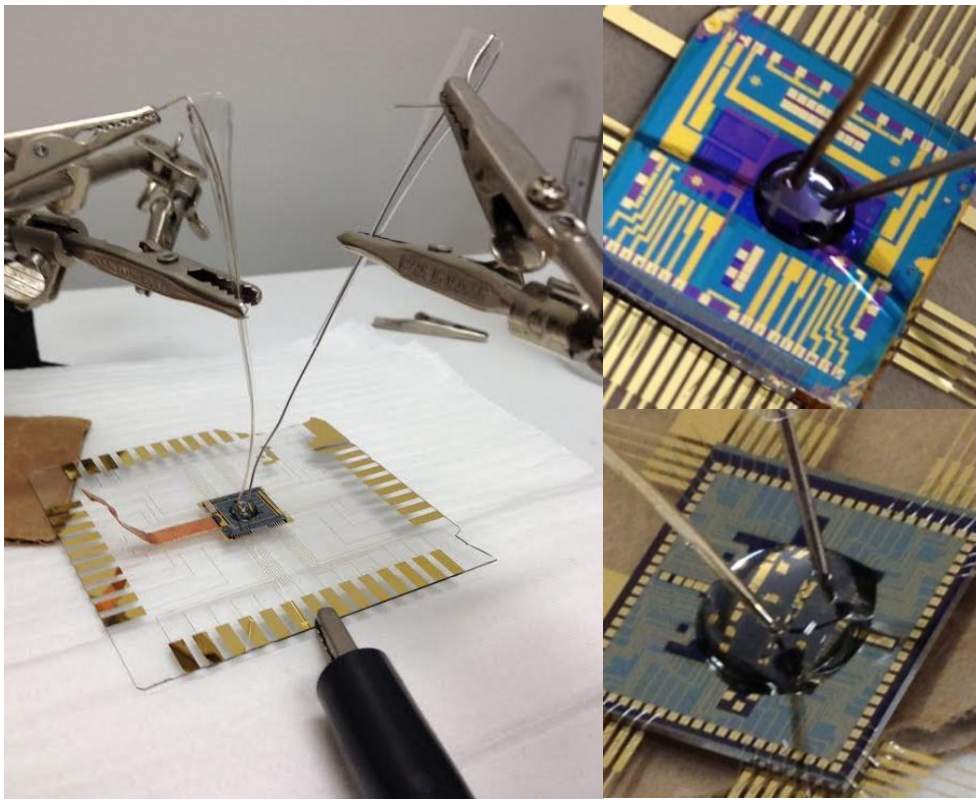

Illustration 4.1 Left- Picture of experimental setup as seen on wire-bonded chip. Right - Pictures of graphene 1st (bottom) and 2nd (top) generation microelectrode array chips with reference and auxiliary electrodes placed over the working electrodes immersed in a 1mM solution of ferrocenemethanol in 0.2 M of KNO_3

4.4 Visual and Optical Characterization of graphene electrode

Fabricated structures were inspected under a microscope and using Raman spectra. Figure 4.5 shows the Raman Spectra of the different electrodes post processing. As expected, the 2D:G ratio decreases with increasing number of graphene layers(reference). A small D peak is now observed in monolayer, bilayer and epitaxial samples, with a larger D peak observable in multilayer graphene and CVD material grown on sapphire. As mentioned, the latter materials exhibits high degree of defects with a decrease in domain size, exposing more edges and dangling bonds than CVD graphene transferred onto SiO_2 and epitaxial graphene on SiC. The background Raman signals from SiC and sapphire have been subtracted from their respective spectra.

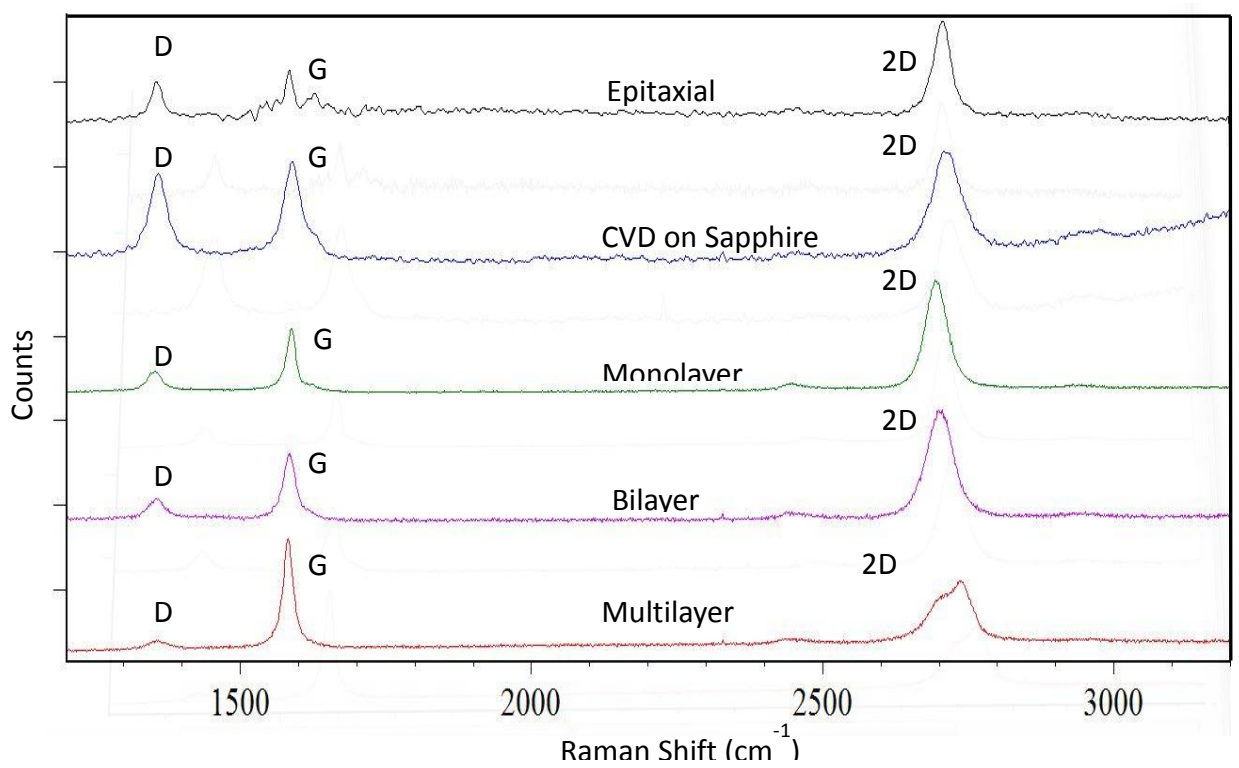

Figure 4.5 Raman Spectra of fabricated electrodes for different graphene types. D represents the defect peak, G represent the peak observed due to high frequency phonon process at the Brillouin zone center. The 2D peak represents the lattice vibration form two-phonon processes.

Atomic force microscopy (AFM) characterization of these materials has revealed domain sizes of 100-200 nm for graphene grown on sapphires and 4-6 um for material grown epitaxially on SiC. AFM images of single layer and multilayer in Figure 4.6 show significant samples thickness.

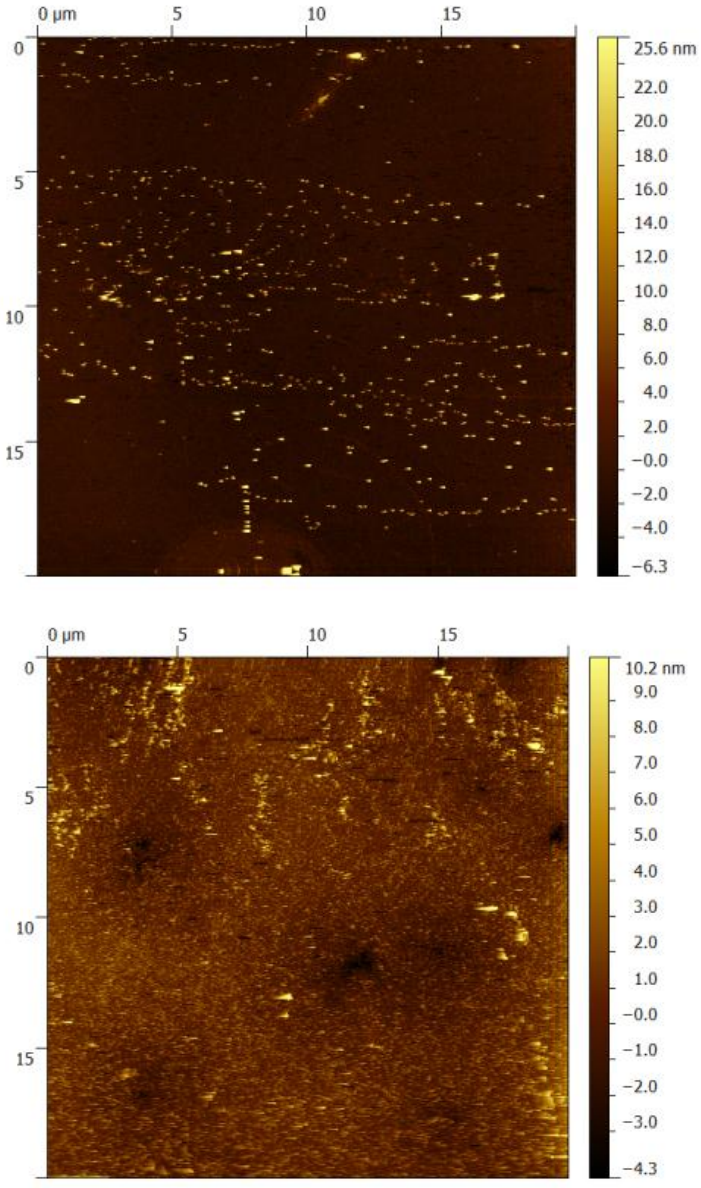

Figure 4.6 AFM images of Single Layer (top) and multilayer (bottom) graphene.

4.5 Electrochemical Characterization of Graphene Electrodes

The next section will focus on presenting a detailed summary of the performance metrics across all the different types of graphene electrodes measured. All electrodes were tested at different scan rates to test for diffusional processes, compute the effective electrode areas and extract kinetic parameters. The limit of detection was performed on 500×500 μm^2 electrodes for the case of mono-, bi- and multilayer graphene. Epitaxial and CVD electrodes on sapphire were arbitrarily chosen and found to be roughly 64767 and 38376 μm^2, respectively. The sensitivity was extracted from current vs. concentration plots and found to be highest in CVD graphene on sapphire electrodes. In addition, the electrodes were tested over the course of 2 weeks to test for current stability.

4.5.1 Scan-Rate Dependence of Peak Current

Conventional peak-shaped voltammograms associated with standard redox reactions of FcMeOH were observed for most electrodes, with observable differences seen in the peak-to-peak separations of the anodic and cathodic currents. In order to accurately interpret the voltammetric response and extract the correct electron charge transfer constant, the Ti/Au contact resistance to the graphene and the electrode sheet resistance, as well as the uncompensated resistance from the reference electrode had to be taken into account. The solution resistance is negligible due to the strong molarity of the supporting electrolyte (.2 M KNO_3).

Figure 4.7 displays the cyclic voltammogram for a single layer $1mm^2$ geometrically defined

graphene electrode at different scan rates. The inset plots the peak current as a function of the square root of the scan rate after correcting for any contribution from the charging current, which given our estimate for the double-layer capacitance, proved to always remain less than 2.5% of the total measured peak current. The linear relationship confirms diffusional transport and mass-transport-limited reactions taking place at the electrode surface. The voltammogram is representative of quasi-reversible kinetics, with a very subtle increased separation observed between the anodic and cathodic peaks with increasing scan rates. It is worth observing the resolution of this measurement was limited by the sampling frequency (~100 Hz).

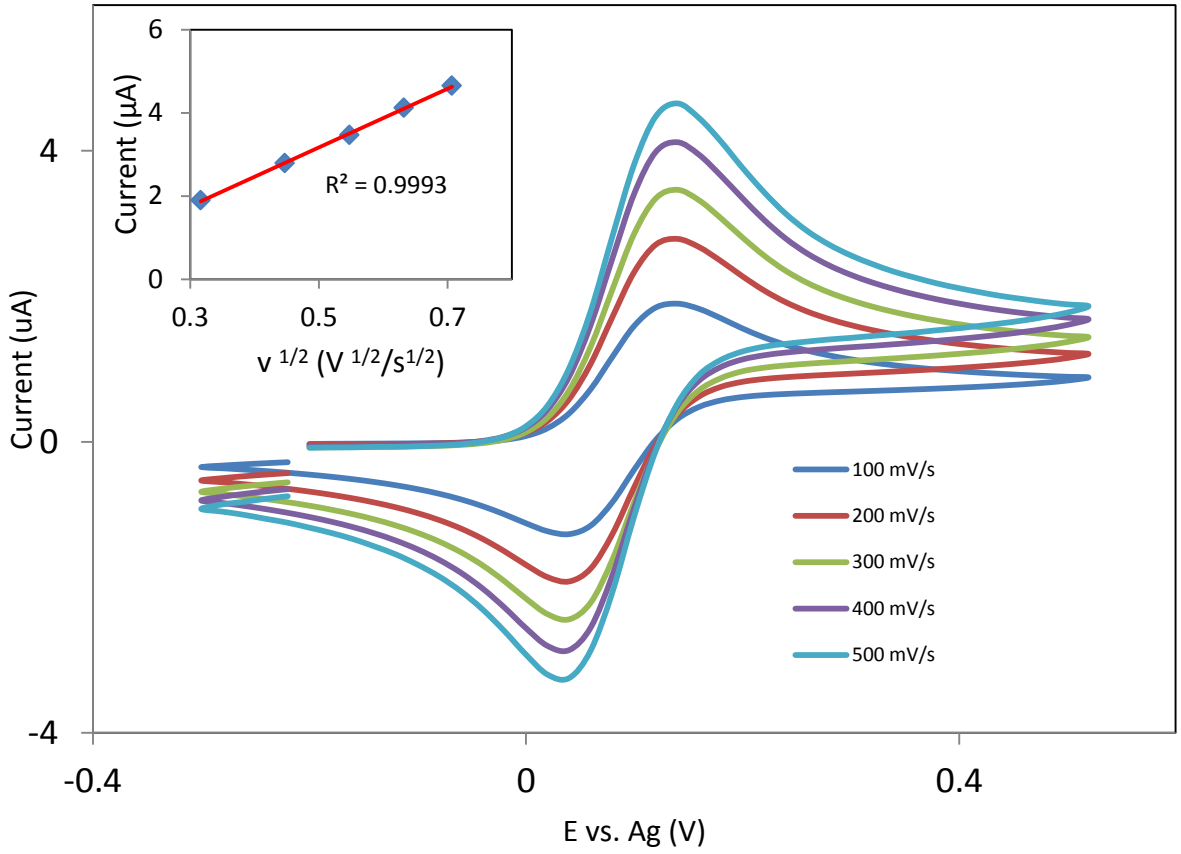

Figure 4.7 Voltammogram for different scan rates for a 1 mm^2-defined monolayer graphene electrode in 1mM of FcMeOH in 0.2KNO_3 solution.

By using the Randles-Sevcik equation we can extract the effective electrode area from the slope of the line. The diffusion coefficient is given as 7.4×10^{-6} cm^2/s. The effective area for this electrode was found to be .806mm^2, which is within reasonable limits of the defined mask electrode area. For consistency, all electrodes were tested in 1 mM solution of ferrocenemethanol.

Figure 4.8 shows the voltammetric response for bilayer, multilayer, epitaxial and sapphire electrodes. Taking into consideration the parasitics, the plots reveal that for larger electrodes (larger than 100×100 μm^2) the electron kinetics are diffusion-limited, quasi-reversible and similar for CVD transferred materials regardless of the number of graphene layers. The smaller peak-to-peak separations observed in the electrodes patterned on epitaxial graphene show somewhat faster kinetics, which is true for some, but not all, of the epitaxial electrodes. Most interesting is the voltammetric response exhibited by sapphire electrodes. We will first highlight that the extracted areas for all sapphire electrodes were much smaller than that defined by the mask, as was expected. Sapphire proves to be an incredibly inert substrate for CVD graphene, and the graphene layers are merely adhered to the substrate by Van der Waals forces. It comes as no surprise that through subsequent fabrication steps, graphene is no longer conformal on the substrate. This was confirmed by Raman and even through optical microscope images. The effective electrode area defined by the electrode shown in figure 4.9C is around 7486 μm^2. It is much smaller than the mask-defined area of 22500 μm^2. Despite having a peak current, it exhibits a more sigmoidal response, usually seen with in electrodes much smaller than ~30×30 micron, and the current decay post the peak current is much more subtle than the one seen in linear diffusion-limited transport processes alone. The inset shows the peak current relationship

to the square root of the scan rate. The response is no longer linear with increased scan rate, but rather logarithmic, reaching a steady-state limit. This was found to be true for most sapphire electrodes, regardless of the calculated effective area. The electrode current behaves like the sum of the individual current contributions of ultramicroelectrodes, representative of the high number of edge domains found in graphene grown on sapphire due to the patchwork type of material present on the substrate. The capacitive current was found to be greater for CVD graphene electrode on sapphire, mainly due to the increased number of edge sites as compared to basal ones.

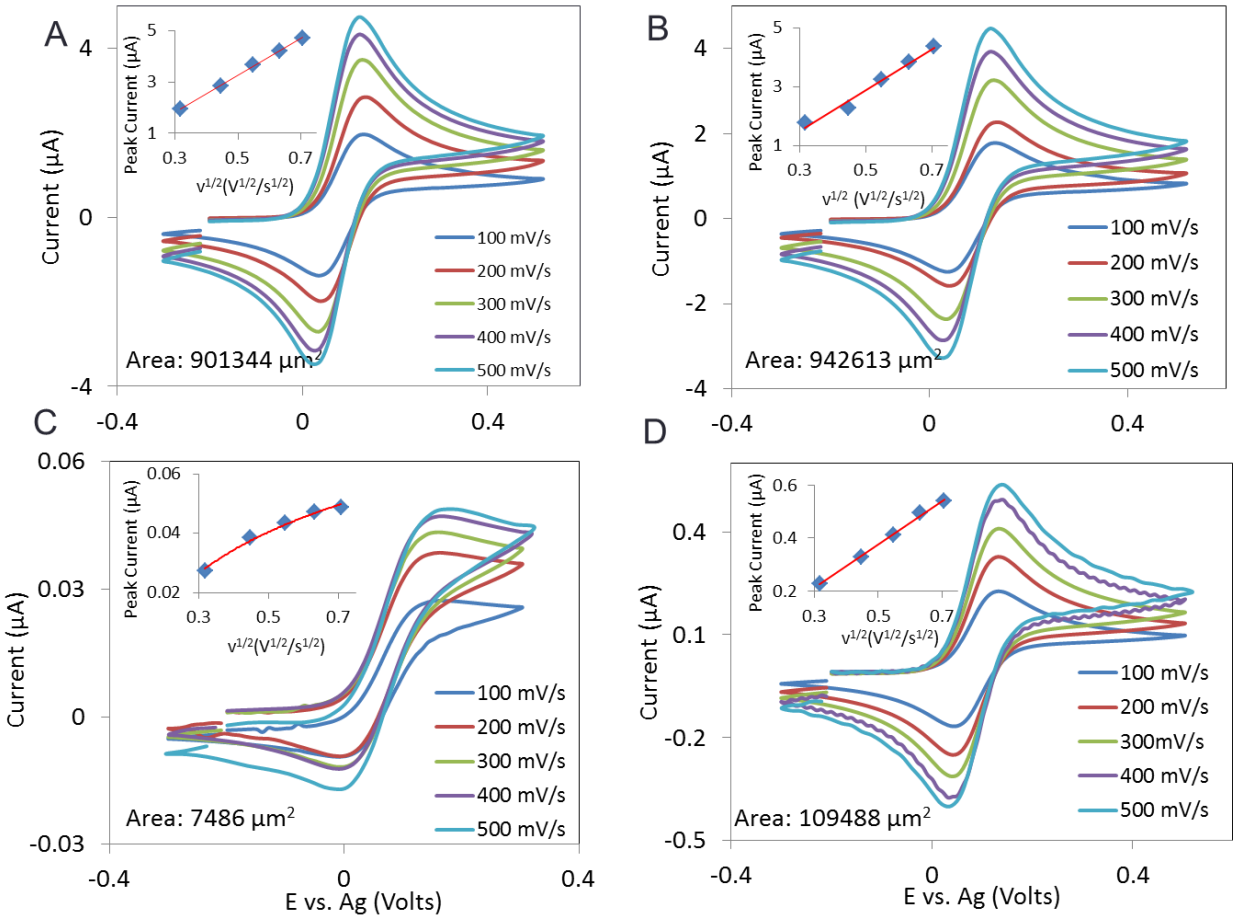

Figure 4.8 Typical voltammograms observed in A) Bilayer, B) Multilayer, C) CVD graphene on sapphire and D) epitaxial graphene electrodes. The insets plot the peak response as a function of the square root of the scan rate. The extracted effective electrode area is annotated on the bottom left corner of each voltammogram.

4.5.2 Effective Electrode Area

Figure 4.9 plots the effective electrode area against the calculated and experimental peak current for the different electrode types as given by the Randles-Sevcik equation. The areas are extracted from the linear relationships between the square root of the scan rate and the measured peak current.

Monolayer, bilayer, multilayer and epitaxial graphene all show good accordance between the expected and obtained values for peak current. The deviation from the calculated values for CVD graphene electrodes on sapphire confirm that the effective electrode area is much smaller than the defined one and hence, the fabricated structures do not have conformal graphene coverage, but rather areas where material has been lost. Previous computational studies of this type of graphene confirm that only weak dispersion forces adhere graphene to the alumina substrate (Hwang et. al), increasing the likelihood of interconnected patches of graphene as opposed to a continuous layer. The high contact and sheet resistance, as compared to that of transferred CVD graphene on silicon oxide and epitaxial graphene, are also indicative of substantial material loss. The inset plots the electrode area against the experimental current for smaller electrodes ($<30000\mu m^2$).

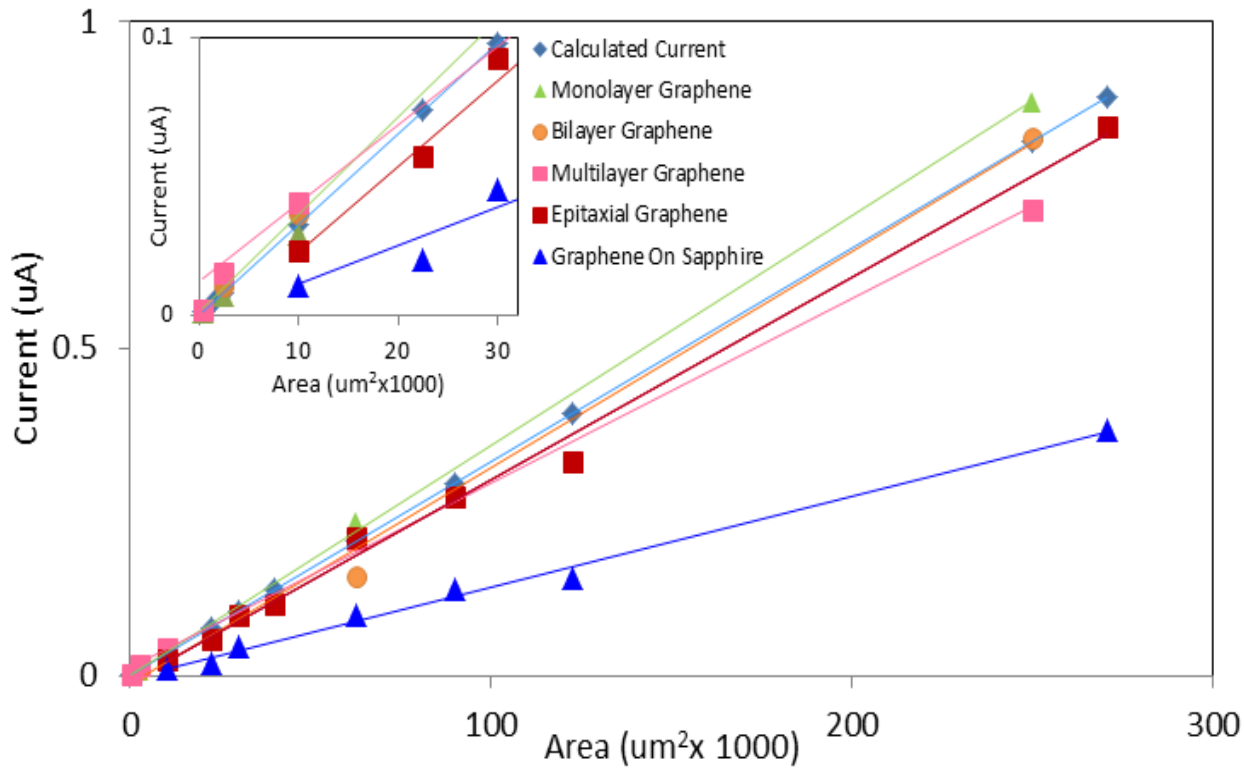

Figure 4.9 Plot of electrode area versus predicted current for different types of graphene electrodes

While larger electrodes do not show much difference between single, bi- and multilayer material, smaller electrodes show higher current sensitivity for multilayer graphene electrodes. While the difference in the number of graphene layers has not been proven to change the transfer kinetics at the basal plane, there have been reports of the charge transfer constant to be greater at the graphene edge plane as compared to the basal plane. Higher electrode sensitivity is observed in bi-layer and multi-layer electrodes that have been scaled down enough below 50 µm. In addition, the voltammetric response for multi-layer graphene electrodes starts becoming more sigmoidal, as dominated by convergent diffusion beyond 50 µm scaling. This can be attributed to a "microelectrode edge" effect, also seen in sapphire electrodes. [140]. Such effect can be negligible at a macro-electrode scale because the contribution due to this type of "convergent

diffusion" is small compared to that of planar diffusion activity. But as the electrode scales down to a few micron (~ < 50microns or so), convergent diffusion becomes more significant and changes in the voltammetric response and electrode sensitivity can be observed. The peak current for smaller multilayer graphene electrodes, therefore, is no longer just dominated by the Randles-Sevcik equation for linear diffusion, but rather has a component due to spherical or convergent diffusion as given by Equation (2.25).

Figure 4.10 shows the gradual change in current response for multilayer graphene versus monolayer graphene as electrodes are scaled from to 250 μm all the way down to 20 μm in length. It can be seen that the convergent diffusion effect is more prominent in multilayer electrodes as opposed to single layer ones. Not only is the I-V curve more sigmoidal in multilayer graphene electrodes, but it is significantly higher than that predicted by the Randles-Sevcik expression. The increased number of layers has a role in the overall electrode response as the devices scale down to a few tens of microns.

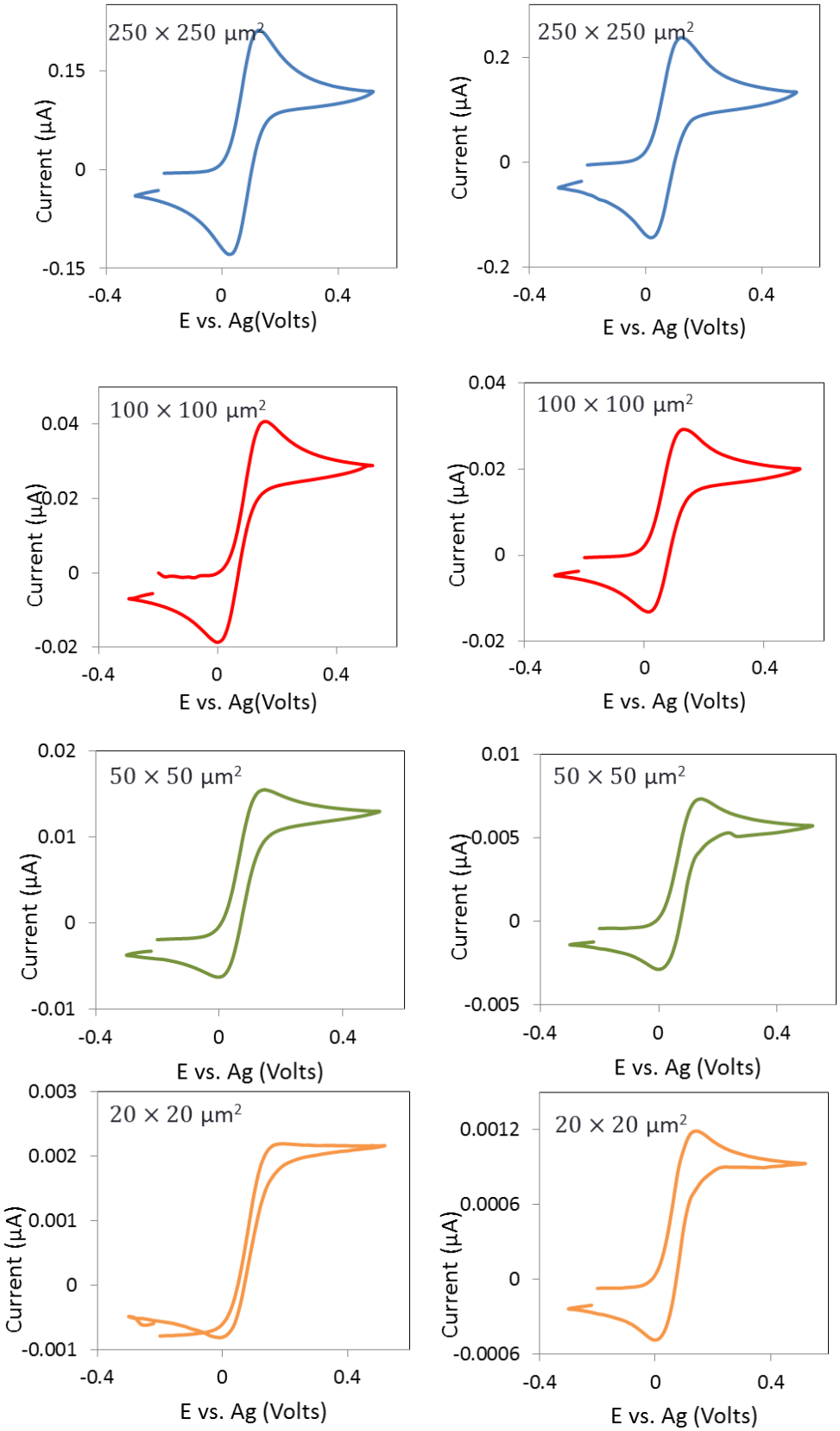

Figure 4.10 Voltammetric response of multilayer (left) versus monolayer (right) electrodes as they are scaled down.

4.5.2.1 Effective area of Ultramicroelectrodes

For an electrode solely dominated by convergent diffusion (ie: an UME) the steady state current is independent of the scan rate and is given by [140]:

$$A_{eff} = \pi \left(\frac{I_{ss}}{4nFDC_o^*} \right)^2 \tag{4.14}$$

We see such response in the smallest multilayer electrodes ($20 \times 20 \mu m$). The voltammogram behavior of such electrode is plotted in Figure 4.11. The small fluctuations in the electrode current correspond to the capacitive current, which increases linearly with the scan rate. For a steady state current of roughly 2.65 nA and a 1mM concentration of ferrocenemethanol in potassium nitrate the effective electrode area is computed to be 271±17 μm. Because the electrode is made of several layers of graphene it is likely that the electrode area is indeed somewhat smaller, as equation (4.14) is used assuming only one sheet around which convergent diffusion occurs, as opposed to many.

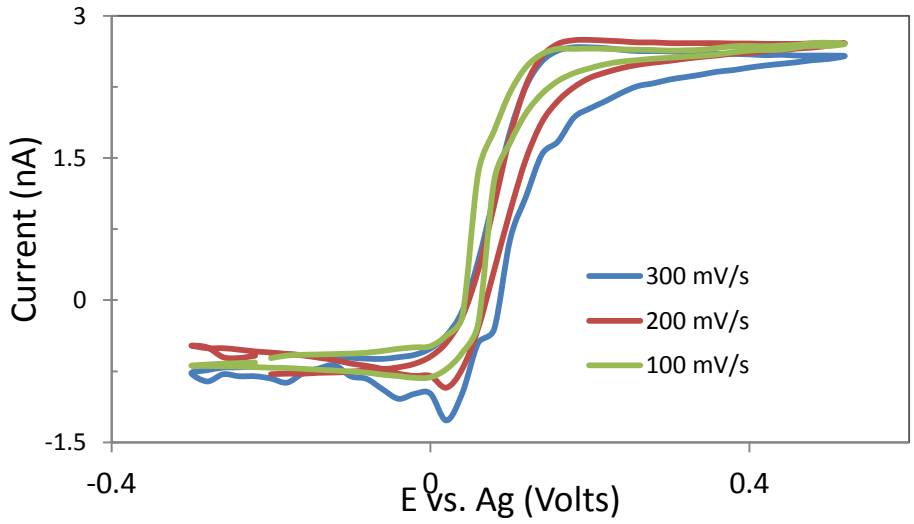

Figure 4.11 Voltammogram of FcMeOH (1mM) in KNO_3 0.2M at a multilayer graphene microelectrode

4.5.2.2 Correction to the Effective Electrode Area

The effective electrode area for the smaller CVD graphene electrodes, as well as the graphene on sapphire electrodes would not be as given by the plot in Figure 4.9 but rather, be somewhat smaller, as to account for the fact that not all diffusive transport processes are linear, but some are convergent, and thus represent higher currents for the same area. To arrive at a model we looked at the i_p vs. $v^{1/2}$ plots for these electrodes and, as given by equation (2.25) we identified two contributions to the total current measured:

$$i_p = x2.69 \times 10^5 n^{3/2} C_0 A_{tot} {D_o}^{1/2} v^{1/2} + (1-x)\frac{A_{tot}}{\pi {r_o}^2}\sqrt{\pi {r_o}^2}\frac{4nFD_oC_o}{\pi} \quad (4.15)$$

Equation (4.15) separates the current into a component due to linear diffusion (left) and a component due to convergent diffusion (right), with their weighed contributions summing up to the total peak current observed. The second component sums the individual contributions of the current due to the individual graphene domains. The total number of domains in a given electrode is given by $\frac{A_{tot}}{\pi {r_o}^2}$, where r_o is the estimated radius of each domain. For CVD graphene on sapphire this number is anywhere between 50 and 100 nm as confirmed by AFM. *x* and *1-x* are the weighing factors by which we scale the current contributions, with *x* being a decimal value between 0 and 1. Equation 4.15 is a first order approximation that assumes a linear combination between the contributions coming from the edges and those given from the basal plane electroactive sites. It can be fitted to different domain sizes and values for x. Figure 4.12 shows the simulation for a domain size with 50 nm radius and x values between .998 and .999. It also shows the experimental data points for the electrodes tested. The extracted electrode areas and

the experimental data confirms that electrode behavior is not just governed by linear diffusion only, with about 33% of the current contribution coming from convergent diffusional transport processes for scaling values of x as high as .999.

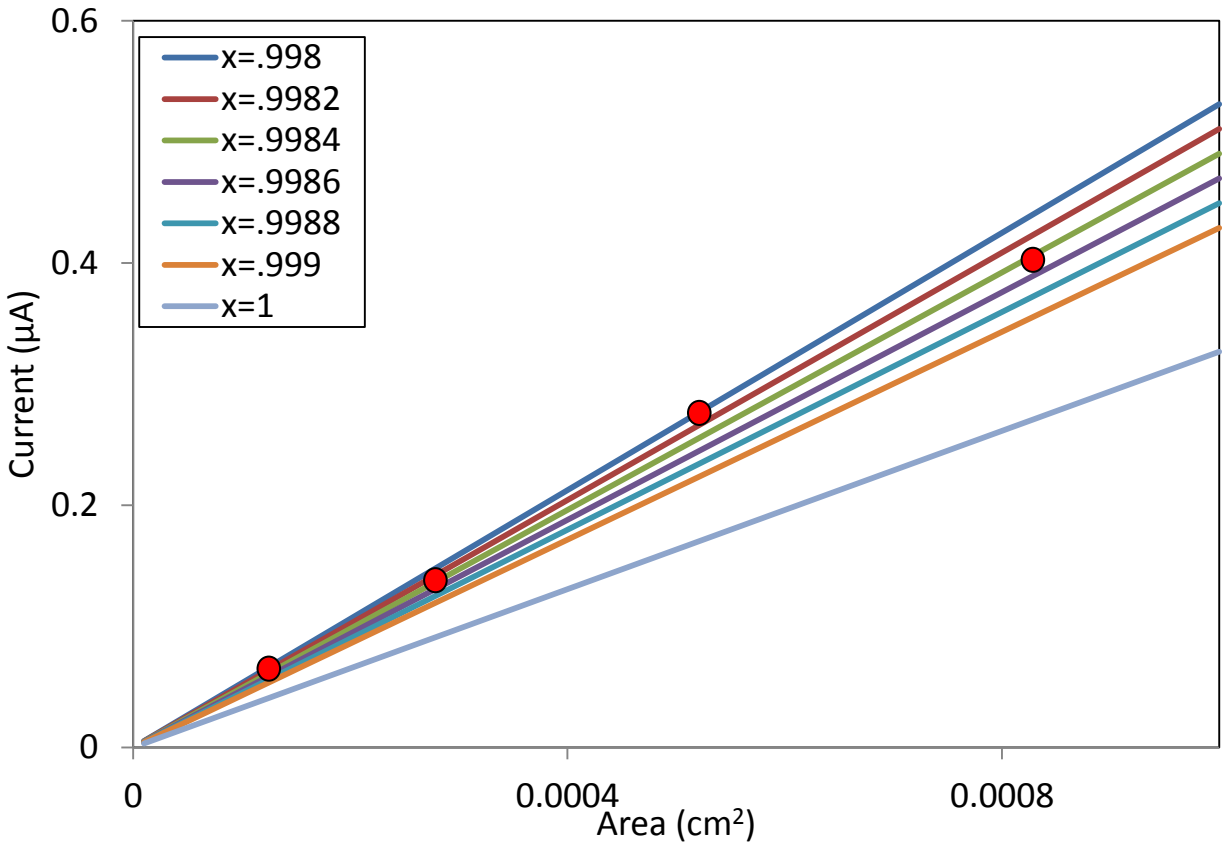

Figure 4.12 Simulated current response for electrodes showing contributions both from linear and convergent diffusion. The red dots show the experimental data from CVD graphene on sapphire electrodes.

We now turn to the case of specific CVD on sapphire electrodes measured, where we do not observe an electrode peak current but rather a steady state current, with differences seen in the capacitive current as the scan rate increased (charging current is proportional to the scan rate). This electrode response to an applied triangular wave potential is seen in Figure 4.13. This type of electrode carries a heavier weight on the contribution of current due to convergent diffusion. If we take the steady state current as given by the scan rates at 100 and 200 mV/s we can use

equation 4.14 to extract the electrode effective area to be roughly around 9000 μm^2 (or ~ 95×95 μm), which is somewhat large for convergent diffusional effects, unless the distribution of graphitic material is in patches of only a few micron in length or width. We speculate that for these electrodes fabricated on CVD graphene on sapphire, the effects of convergent diffusion arise due to the small domain sizes.

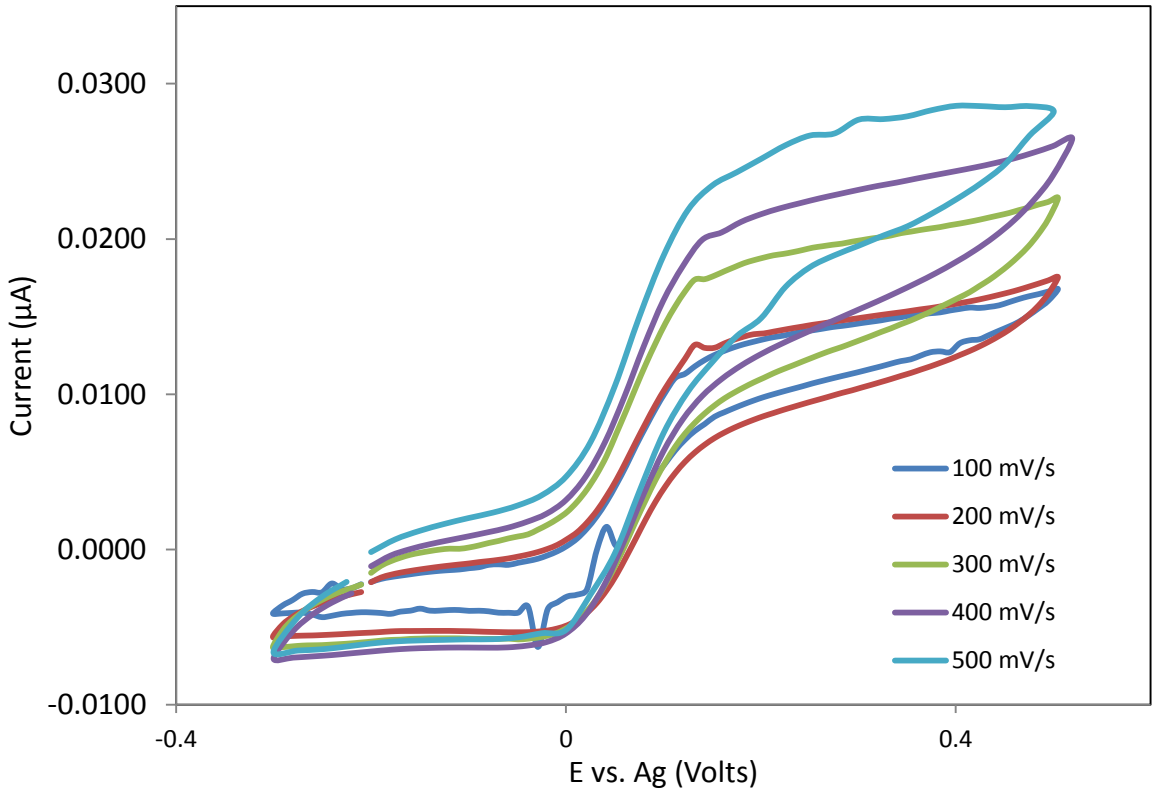

Figure 4.13 Voltammogram of a CVD graphene on sapphire electrode with area of about 9000 μm^2 . The response starts to approximate that of an ultramicroelectrode.

4.5.2 Detection Limit, Linear Range of Detection and Electrode Sensitivity

Electrodes were tested against varying concentrations of analyte to measure the range of linear detection, the detection limit and the sensitivity. Figure 4.14 shows the typical voltammogram response for an epitaxial electrode with an area of roughly 300×200 um^2.

As expected, more distortion defines the voltammograms at lower concentrations due to the increase in the ratio of the charging current to the measured peak current. The linear range of detection is observed to be roughly between 25uM and 1mM, and the smallest observable peak can still be observed at 1µM, despite the charging current.

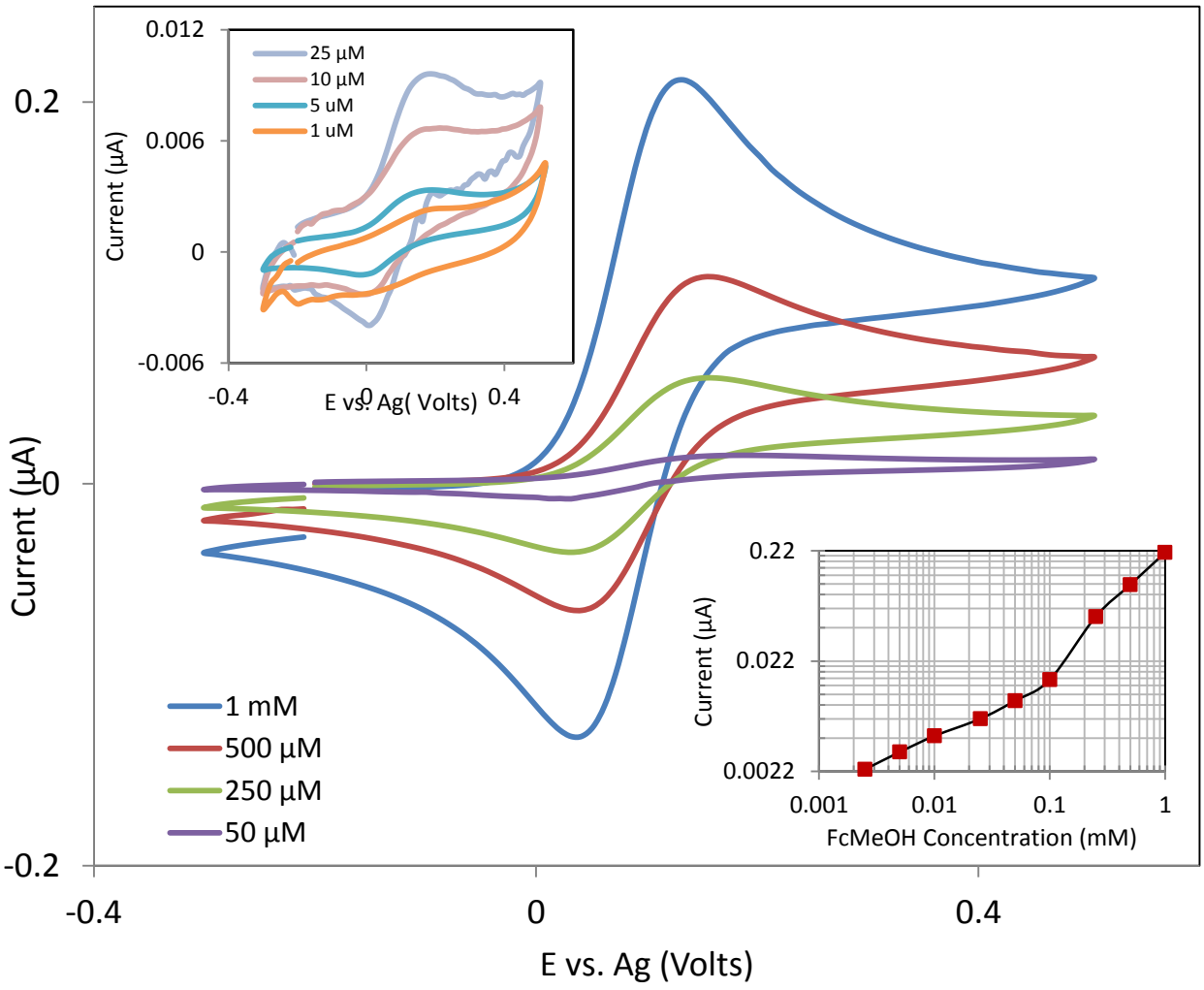

Figure 4.14 Voltammograms of a 300×200 µm^2 epitaxial graphene electrode with varying concentrations of FcMeOH in 0.2M KNO_3. The top left inset plots voltammetric response for concentration at or below 25µM. The bottom right inset plots the peak currents versus concentration response.

Identical analysis was performed on the other type of electrodes. Figure 4.15 plots the peak

current versus concentration response for single layer, bilayer, multilayer and CVD graphene on sapphire electrodes of different sizes. The effective area of the tested CVD graphene on sapphire electrode was much smaller than the CVD graphene electrodes on SiO_2, thus the smaller current scaling.

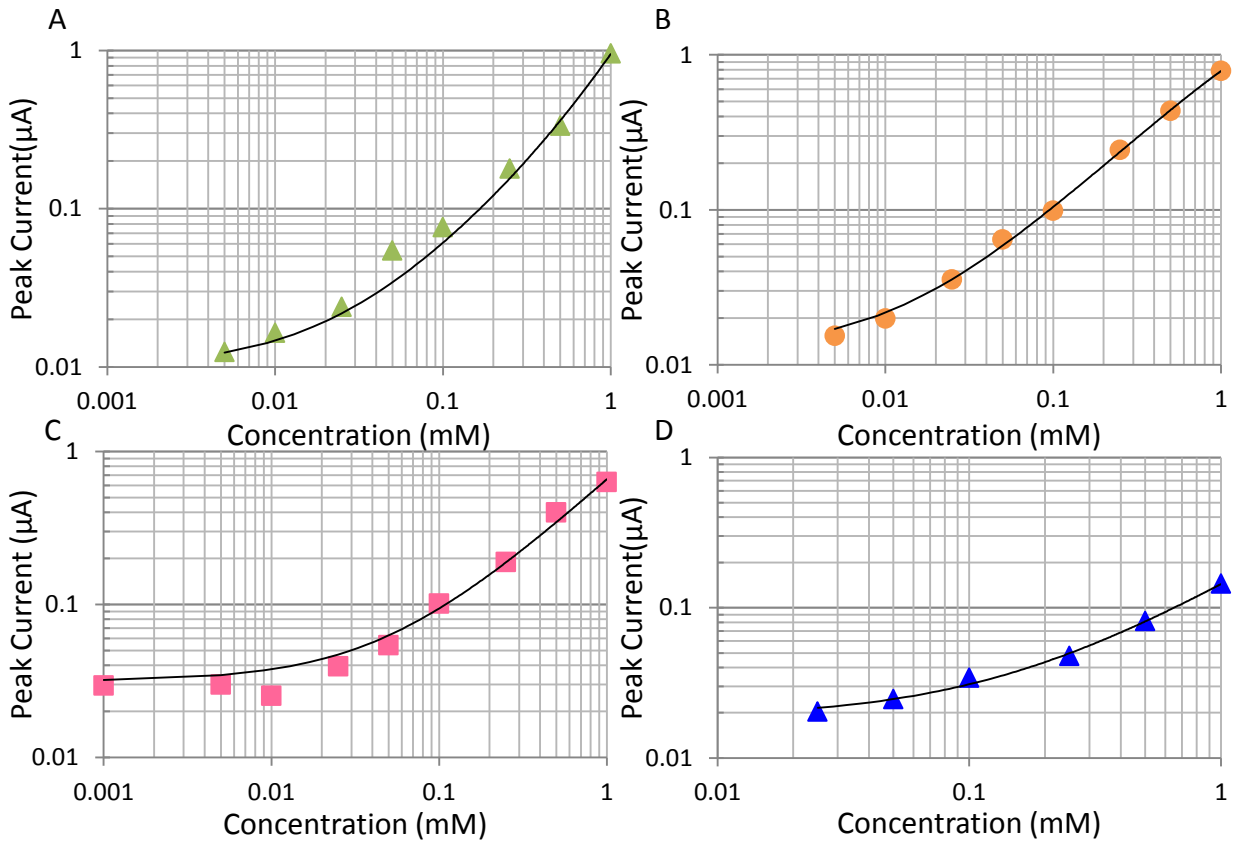

Figure 14.15 Peak current versus concentration trends for A) single layer, B) bilayer, C) multilayer and D) CVD graphene on sapphire electrodes. The electrodes areas are given by 267000, 24400, 192000, and 38376 μm^2, respectively.

The electrode sensitivity for epitaxial electrodes can be extracted from the slope of the peak current vs. concentration plot normalized to the electrode area for the linear regime (at higher concentrations), where the charging current is negligible, as given by Figure 4.16. The effect of higher distortion due to the increase in the double layer capacitance can be observed at lower concentrations, particularly for multilayer and CVD on sapphire electrodes, where the double

layer capacitance is greater than for the other materials. The highest current sensitivity for epitaxial electrodes is calculated to be 4.12pA $mM^{-1}\mu m^{-2}$, and the mean sensitivity taken across all concentrations is given by 2.95 pA $mM^{-1}\mu m^{-2}$.

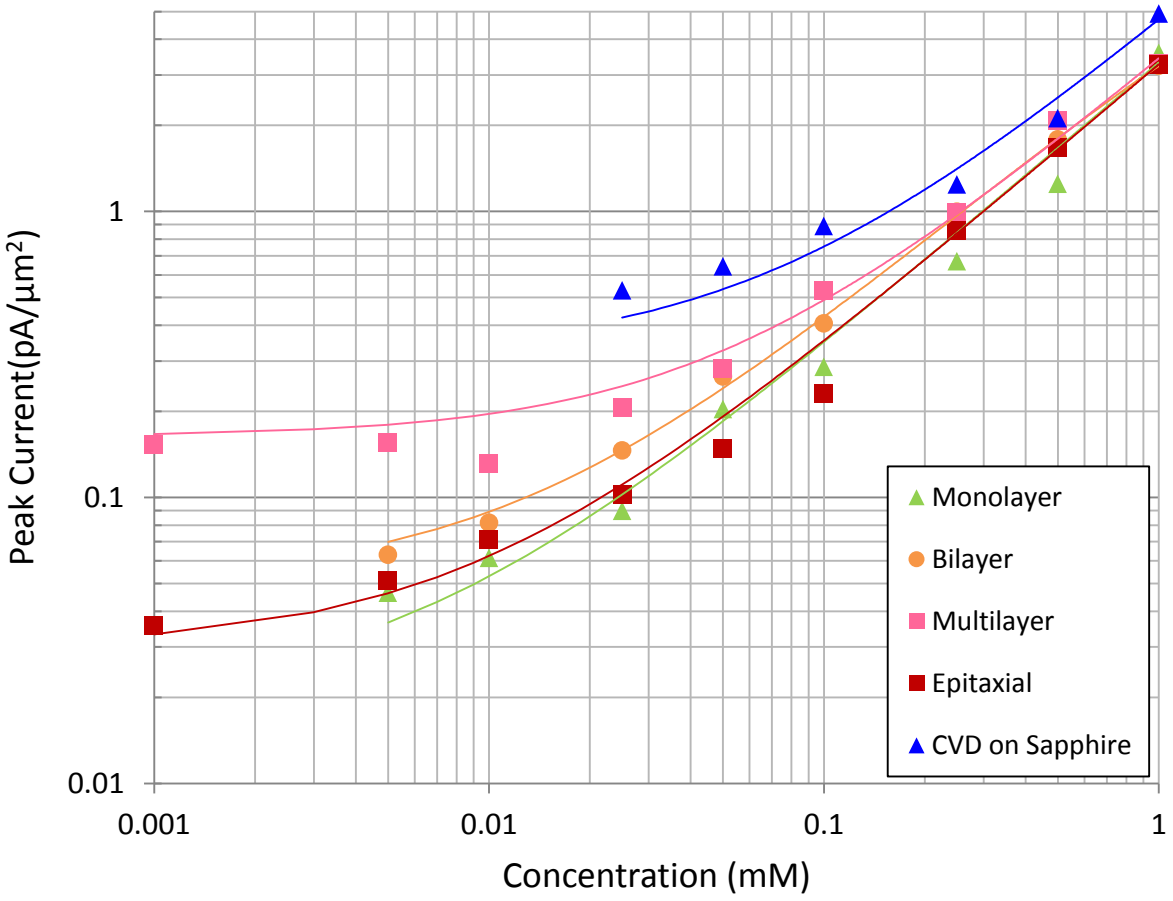

Figure 4.16 Normalized peak current vs. concentration plot for different electrode types. Higher distortion due to charging currents is observed for multilayer and CVD graphene on sapphire electrodes.

Table 4.3 Summary of the peak and mean sensitivity for characterized electrodes

Electrode Type	Peak Sensitivity(pA $mM^{-1}\mu m^{-2}$)	Mean Sensitivity(pA $mM^{-1}\mu m^{-2}$)
Monolayer	4.66	3.14
Bilayer	3.94	3.52
Multilayer	4.37	3.56
Epitaxial	4.12	2.95
CVD graphene on sapphire	6.10	3.83

Tables 4.3 summarize the peak and mean sensitivity for all electrode types for 1mM of FcMeOH. We have included the response observed across all the different size electrodes tested (do note Figure 4.17 is only representative of one electrode). Because CVD graphene on sapphire electrodes exhibit convergent diffusional transport properties, the maximum current sensitivity per μm^2 was indeed larger than that of any other type of electrode. Figure 4.17 summarizes the linear range and detection limit for all electrodes. Epitaxial, bilayer and monolayer graphene electrodes exhibit similar linearity ranges between 25µM and 1mM. The linearity range is limited by the larger double layer capacitance of CVD graphene on sapphire (105 $\mu F/cm^2$) and multilayer electrodes (69 $\mu F/cm^2$), as expected with electrodes with increased number of defects. The linearity range is given as 250µM-1mM and 50 µM-1mM, respectively. The highest detection limit was found in epitaxial electrodes, close to 1 µM, while the lowest was given at 25 µM for CVD graphene on sapphire electrodes.

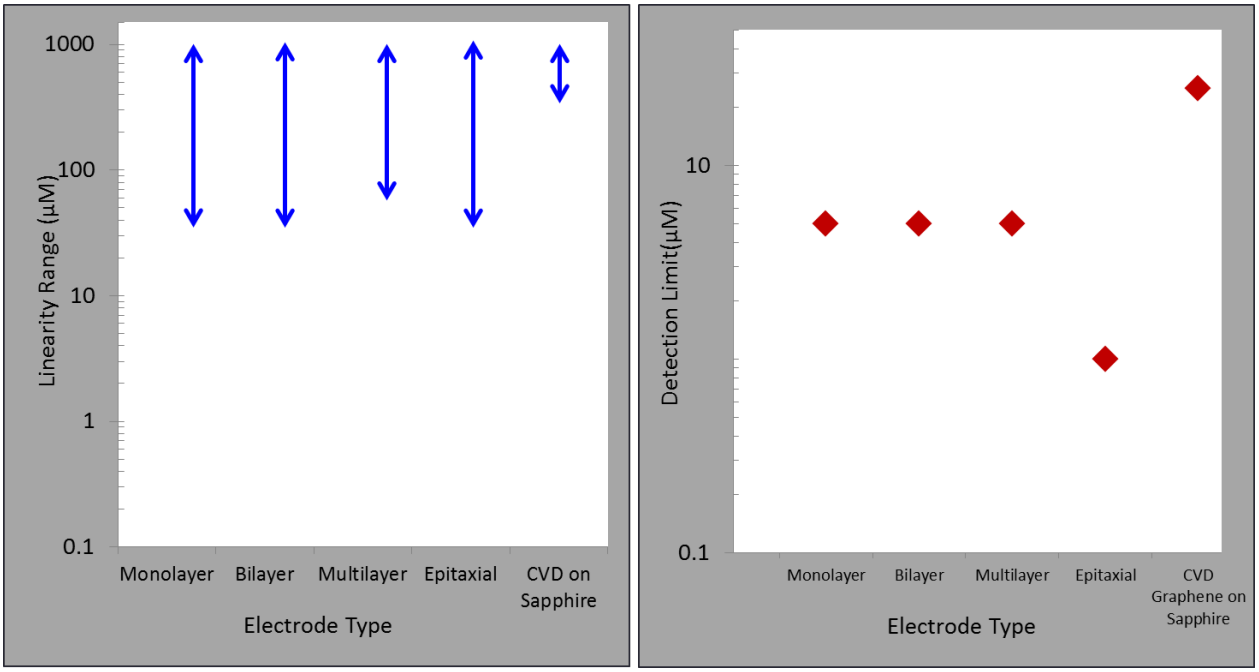

Figure 4.17 Linearity range (left) and detection limit (right) for all electrodes

4.5.3 Kinetic Parameters

The most important metric of an electrode with quasi-reversible kinetics is the rate of charge transfer. Better electrode performance is synonymous with faster electron kinetics at the surface with a given applied potential. This section summarizes the results for the charge transfer kinetics observed.

While we still use the Randles-Sevcik to relate the experimental controls to the peak current, the shape of the peaks themselves show quasi-reversible kinetic behavior. We can refer to our derivation for the current as given in section 2.3.3.2.2 where we took a look at the solution of the diffusion equation for quasireversible systems. The potential is now given by $E=E_i + vt$.

The peaks separate slightly with an applied potential. The shape of the peak and the various parameters are shown to be a function of the transfer constant, α, and a parameter Λ, defined as

$$\Lambda = \frac{k^o}{(D_A^{\alpha} - D_B^{1-\alpha} f v)^{1/2}} \tag{4.16}$$

For the case where $D_A=D_B$, as for our system, equation 4.16 becomes:

$$\Lambda = \frac{k^o}{(Dfv)^{1/2}} \tag{4.17}$$

The solution for the current under an increased potential of constant scan rate can be given as:

$$i = FAD_A^{\frac{1}{2}} C_A^* f^{\frac{1}{2}} v^{\frac{1}{2}} \Psi(x) \tag{4.18}$$

$\Psi(x)$ is a function of both α and Λ. $\Psi(x)$ is depicted in Figure 4.18 for various values of α. As Λ increases to values above 10, the system approaches the behavior of a reversible system.

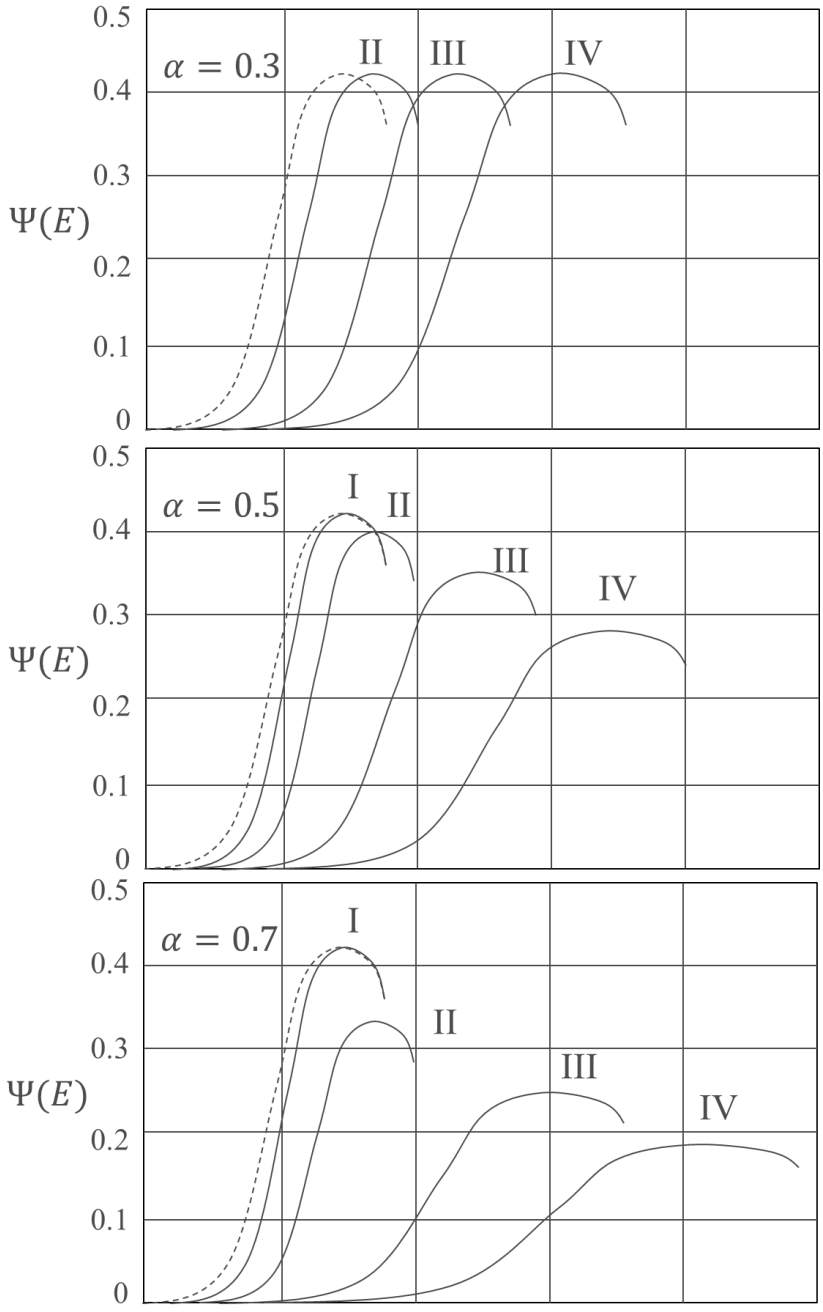

Figure 4.18 Variation of the quasireversible current function $\Psi(E)$ for different values of α for different values of Λ: (I) $\Lambda = 10$, (II) $\Lambda = 1$, (III) $\Lambda = .1$, (IV) $\Lambda = .01$. Dashed curve is for a reversible reaction. We assume the forward transfer constant to be given by 1-α, and the backward transfer constant to be given by –α [139].

The peak separation is now a function of the transfer constant, α, the scan rate, v, k^o and Λ. The curves are function of a dimensionless parameter $\psi = \Lambda\pi^{-1/2}$. For values of $0.3<\alpha<0.7$ the peak separation are almost independent of α and depend only on . Nicholson's curve relates the separation between the peaks to this dimensionless kinetic parameter [202]. This relationship is plotted in Figure 4.19.

$$\psi = k^o\sqrt{RT/\pi nFD}\,v^{-1/2} \tag{4.19}$$

The separation between the oxidation and reduction peaks was measured and plotted against the scan rate to extract kinetic parameters. Because of the high measurable currents, the correction for contact, sheet and uncompensated resistance was made across all devices.

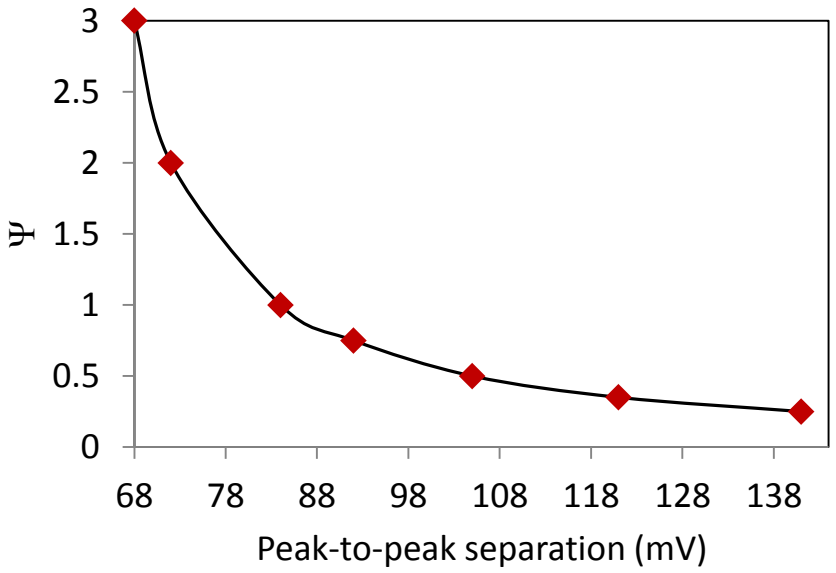

Figure 4.19 Nicholson's curve for peak separations between 68 and 144 mV.

Using the Nicholson peak separation vs. ψ curve and making for the resistance corrections that were computed in Chapter 3 and those computed earlier in this chapter, we can plot the relationship between the peak separation and Ψ for the different scan rates (or inverse square root

of the scan rates). Figure 4.20 plots this relationship for an epitaxial graphene electrode. We can extract the value for the heterogeneous transfer rate constant from the slope, as given in Equation 4.15 and find it to be roughly around .0134 $\pm$ 5% cm/s.

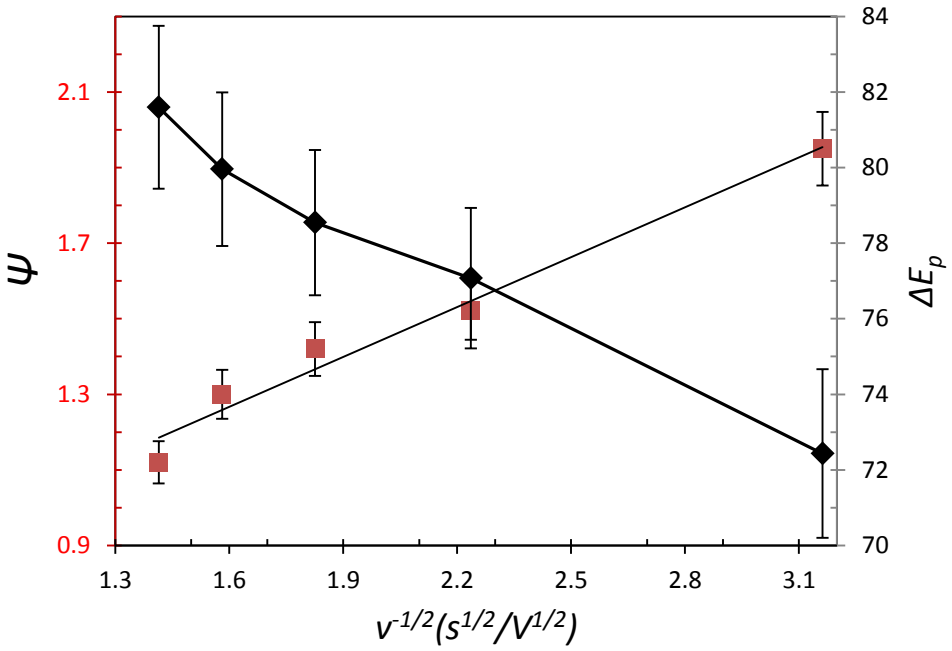

Figure 4.20 Peak separation ΔE_p and Nicholson's kinetic parameter versus the reciprocal of the square root of the potential scan ($v^{-1/2}$) epitaxial graphene electrodes.. A linear fit to the curve is used to determine the heterogeneous charge transfer rate constant, k^o.

We extrapolate this analysis to the other electrode types, mainly the large electrodes (>250×250μm), as to properly compare kinetics across all tested electrodes. Figure 4.21 plots the peak separation ΔE_p and Nicholson's kinetic parameter versus the reciprocal of the square root of the potential scan ($v^{-1/2}$) for all other materials. Like Figure 4.20, a linear fit to the curve is used to determine the standard heterogeneous charge transfer rate constant, k^o. The summary of the standard heterogeneous charge transfer rate constants is plotted in Figure 4.21 and Table 4.4. The values extracted for multilayer graphene are somewhat faster than those reported at the basal plane of bulk graphite, and slower to those observed in single layer graphene. Experimentally, the measured rate constant is faster for bilayer graphene. CVD graphene on sapphire proves to be

comparable to multilayer graphene and slower than monolayer graphene. We think that the increased number of available sites can impede charge transfer if these sites states are not available for transfer. The highest observed charge transfer constant is seen for epitaxial electrodes, at .0133 $\pm$ 6% cm/s. We suspect that in the case of sapphire electrodes, which displayed an electrode response characterized by a combination of linear diffusion and convergent diffusional transport, the transfer rate is affected by the large number of defects. Alternatively, the sheet or uncompensated resistance might have been underestimated. Epitaxial electrodes exhibit the highest charge transfer constant, primarily suspected to be due to the sheet corrugations inherent to the step bunching of silicon carbide surfaces. Most importantly, all the extracted values of k^o reflect that $\Lambda > 10$, characteristic of a system approaching reversible behavior ($(Dfv)^{1/2}$=1.92×10^{-4}).

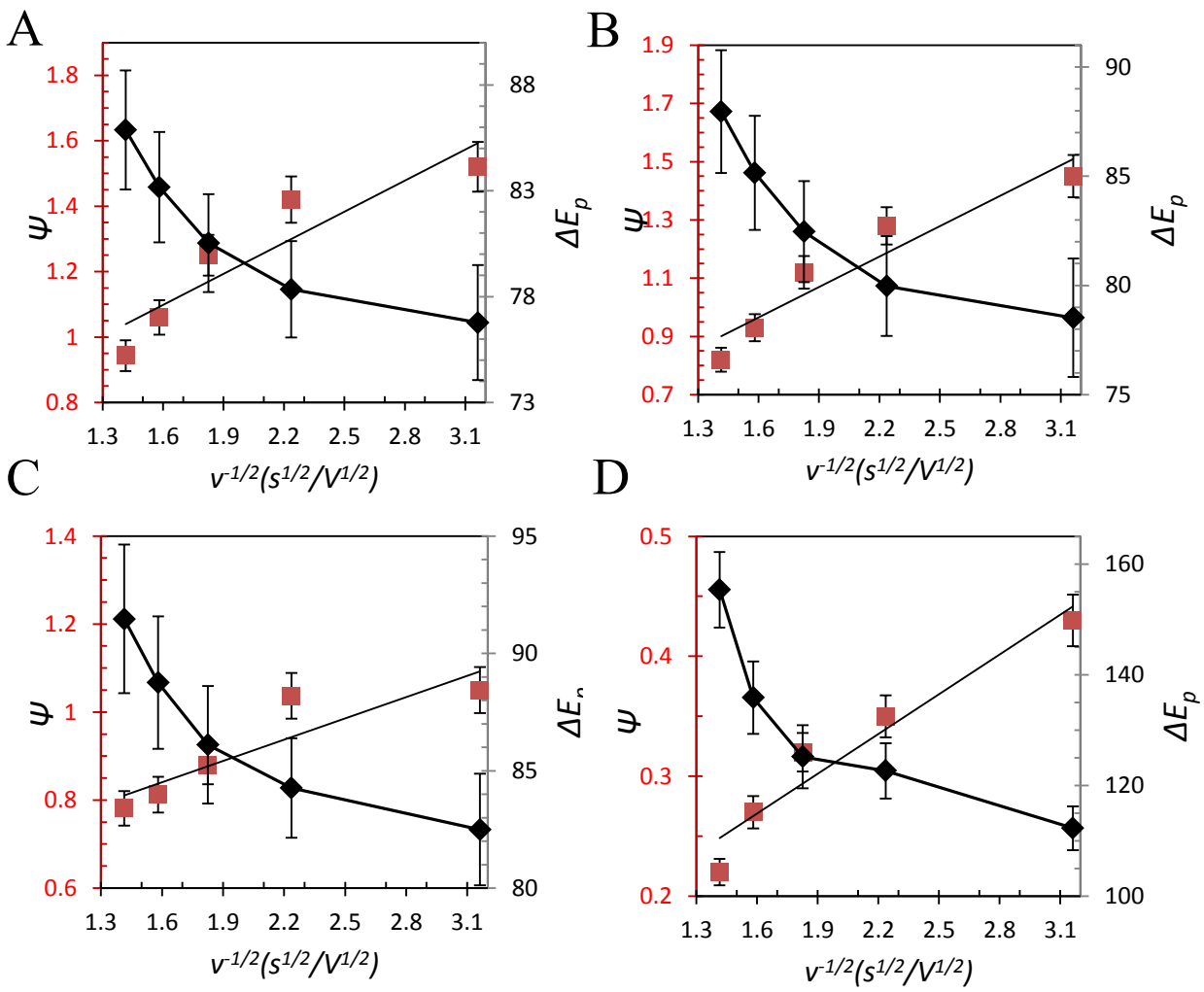

Figure 4.21 Peak separation ΔE_p and Nicholson's kinetic parameter versus the reciprocal of the square root of the potential scan ($v^{-1/2}$) for A) single layer, B) bilayer, C) multilayer and D) CVD graphene on sapphire electrodes.

Table 4.4 Extracted Heterogeneous Charge Transfer Rate Constants	
Electrode Type	**k^o**
Single Layer	$9.59\times10^{-3}\pm5\%$
Bilayer	$1.05\times10^{-2}\pm3\%$
Multilayer	$4.88\times10^{-3}\pm6\%$
Epitaxial	$1.34\times10^{-2}\pm6.2\%$
CVD Graphene on Sapphire	$3.35\times10^{-3}\pm3.2\%$

The kinetic transfer constant versus electrode type is plotted in Figure 4.22

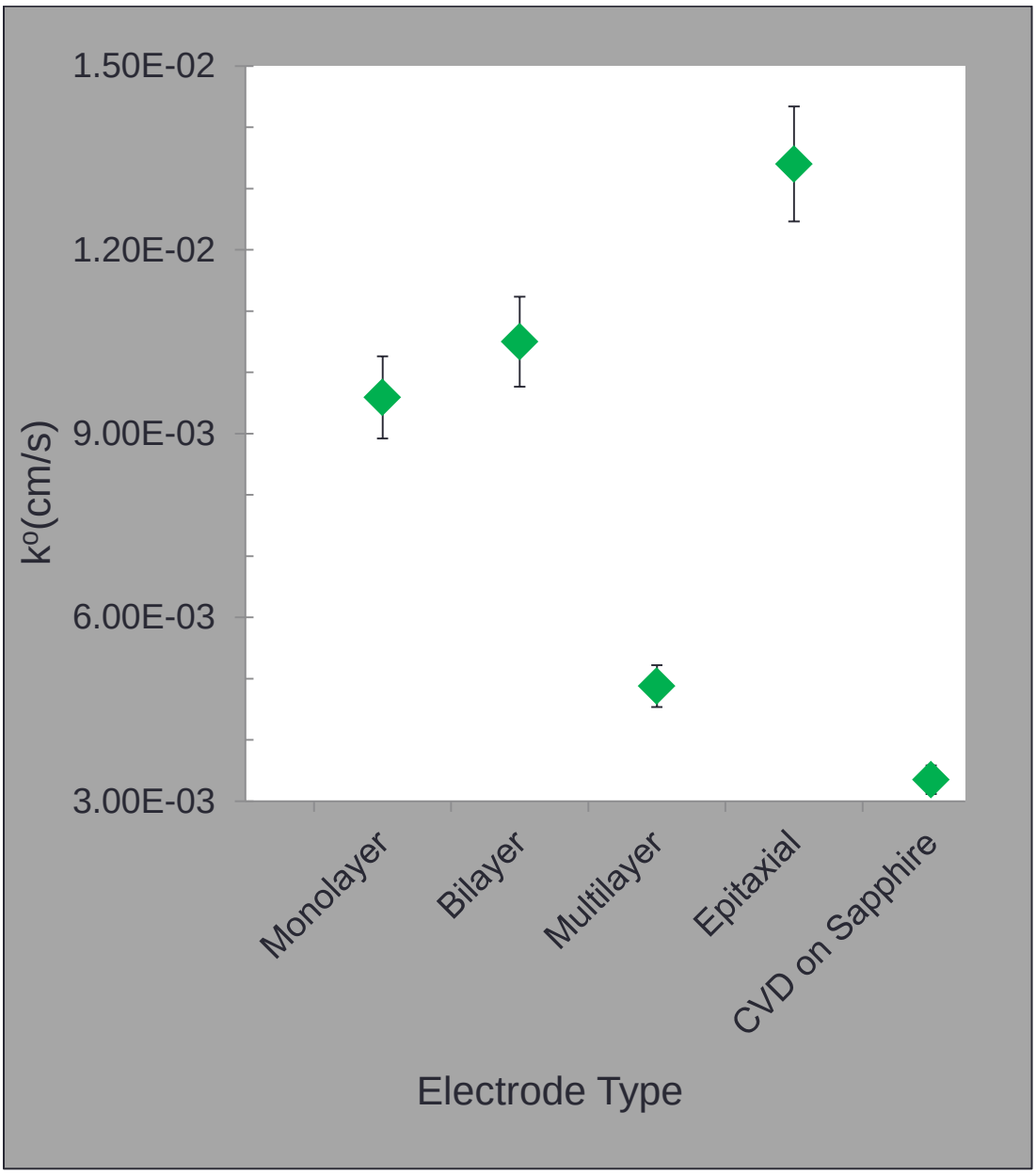

Figure 4.22 Plot of the extracted charge transfer constant versus electrode type for all characterized electrodes.

We now turn our attention to the case of multilayer microelectrodes that show purely convergent diffusional response. For these electrode the steady-state current, i_{ss}, is independent of the scan rate and any small fluctuations seen are due to the increased capacitive current. The

ultramicroelectrodes geometry allows fast reversible kinetics to be measured using cyclic voltammetry. A plot of E versus $log[(i_{ss}-i)/i]$ where i is the measured current at an applied potential E, is usually used to assess the reversibility of the reaction for UMEs. For a reversible one electron transfer reaction where the transfer rate is much greater than the rate of mass transport this plot should be linear with a slope of ≈ 59mV, increasing as the reaction rate is reduced relative to the mass transport. Figure 4.23 shows the slope of the response to be around 53 mV, confirming reversible kinetics at the multilayer graphene UME.

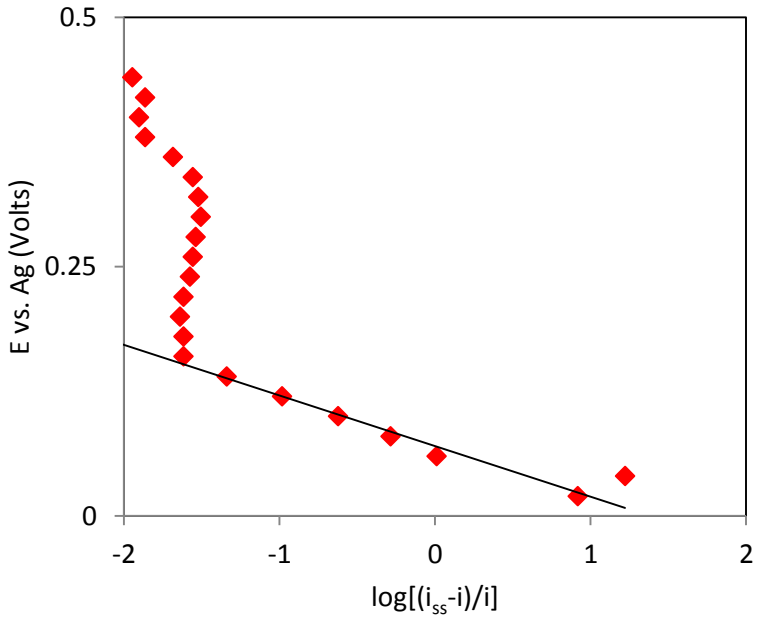

Figure 4.23 Plot of E versus $log[(i_{ss}-i)/i]$ for 20×20 μm^2 multilayer electrodes.

4.5.5 Electrode Stability

Electrodes were tested over the course of one week to monitor peak current stability. Figure 4.24 plots the electrode stability over time. Variations in the peak current response are indicative of electrode degradation and material loss over continued, extended use. Overall, monolayer, multilayer and epitaxial electrodes proved to be more stable than the other electrode types, with

total current loss being limited to less than 23, 18 and 29% off the initial current, respectively . Electrodes fabricated with CVD graphene on sapphire substrates, despite the initial higher normalized sensitivity, displayed the most unstable response and deterioration, primarily because of the weak dispersion forces that bind the graphene to the surface. The current loss was over 50% of the initially measured normalized response.

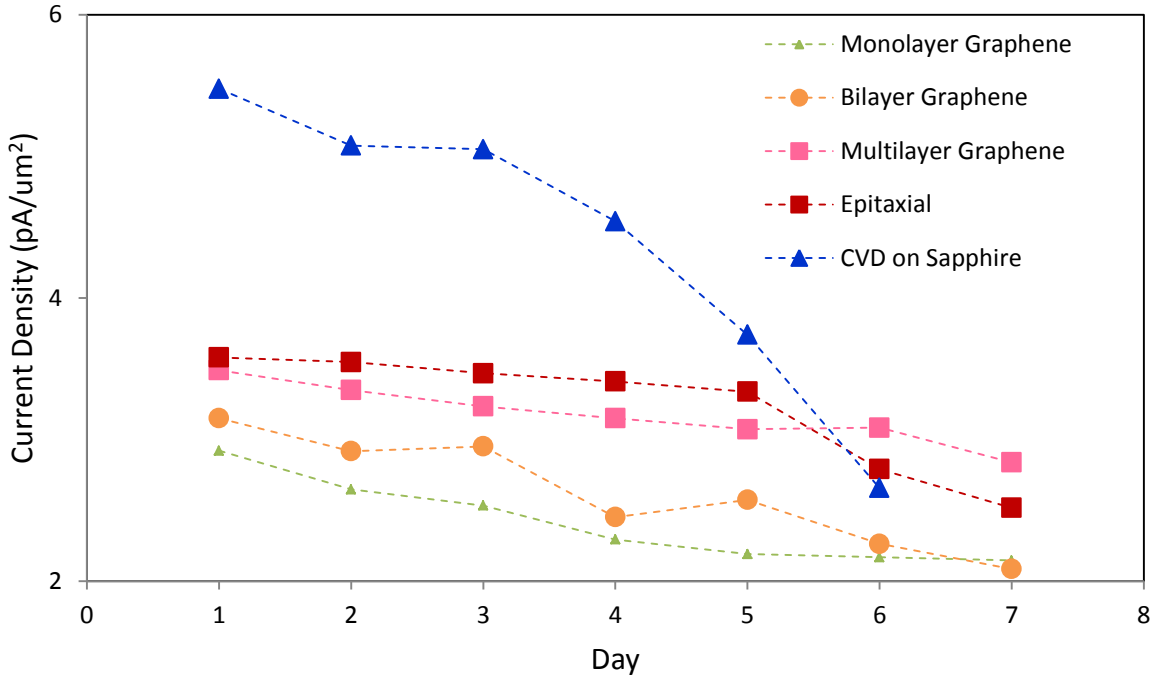

Figure 4.24 Plot of the electrode normalized peak current stability over the course of a week of continuous characterization.

4.5.6 Effects of Overcompensation on Uncorrected Resistance

Lastly, we want to briefly discuss that while the uncompensated resistance may change dramatically based on an estimate of where the reference electrode is placed with respect to the working graphene electrode, this has little to no effect when extracting the charge transfer constant from the values of Ψ. Because the latter is a function of the separation between the peaks, and these will scale linearly after the resistance correction, regardless of the value of the

uncompensated resistance, within a certain limit of values for this distance, x, the kinetics will be unaltered. Figure 4.25 shows the peak to peak separation of a CVD graphene on sapphire electrode as a function of the inverse of the square root of the scan rate for different values of x after resistance correction. The plots run parallel to one another, indicating that the change in kinetics would also, scale similarly, leading to little change due to an overcompensation factor.

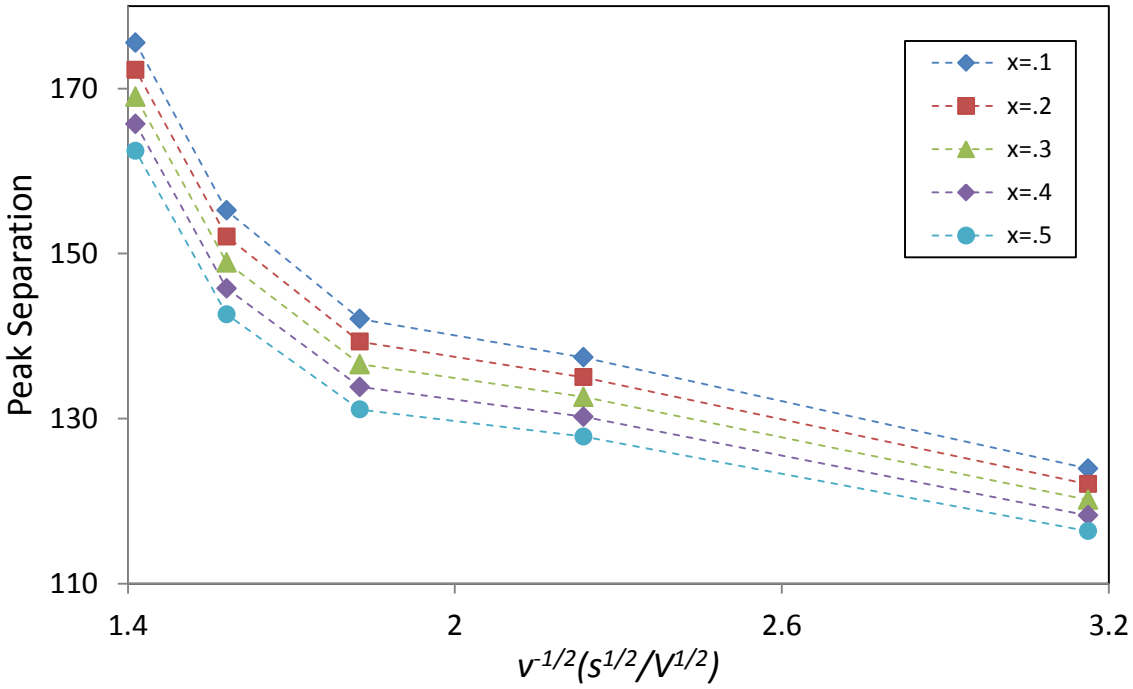

Figure 4.25 Peak separation versus the inverse square root of the scan rate for a sapphire electrode of area with different correction factors of the uncompensated resistance. *x* is given in cm.

4.6 Summary

In all, we characterized over 250 electrodes across 5 different types of materials. The key findings are summarized below:

- Most electrodes reflect transport processes dominated by linear diffusion in the quasi-reversible regime. As electrodes scale down, the effect of convergent diffusional transport become obvious and relevant to the total current. At the lower limit of 20×20 μm electrodes, multilayer graphene exhibits a purely radial diffusional response.
- Because of the patch-like graphene distribution found in CVD graphene grown on sapphire, electrodes fabricated on such substrates exhibited a combined linear and radial diffusion transport response.
- The double-layer capacitance was found to increase with higher number of defects, such as in multilayer graphene and CVD graphene on sapphire
- Electrodes made with CVD graphene on sapphire exhibited the largest current sensitivity at higher concentrations. Such effect can be attributed to the smaller graphene domain sizes (100-200 nm).
- The best detection limit was observed in epitaxial electrodes, close to 1 μM. The detection limit, sensitivity and linear range was limited by the effect of the double layer capacitance, which increases the charging current as the analyte concentration decreases.
- The quantum capacitance did not dominate the total interfacial capacitance due to the increased number of charges in the material. Better control of the fabrication process could yield devices with a Dirac point closer to the electrode standard potential. In turn, devices could exhibit less distortion at lower concentrations, larger linear ranges and lower detection limits.
- The electrode kinetics were extracted. Epitaxial graphene was shown to have the highest heterogeneous charge transfer constant, presumed to be effect of the high number of corrugations due to the step bunching of the substrate.

- It is suspected that despite higher sensitivity per square micron, electrode faster electron transfer kinetics of graphene on sapphire might have been impeded by the effect of the large double layer capacitance, or alternatively by underestimation of the sheet or uncompensated resistance.
- Electrodes were found to be relatively stable, with epitaxial, monolayer and multilayer electrodes showing the most consistent trends over a one week period. Electrodes fabricated with CVD graphene on sapphire showed the best initial normalized current response, but showed the worst instability over time.

CHAPTER 5

OPTMIZATION OF ELECTRODE PERFORMANCE WITH PATTERNING TECHNIQUES

In Chapter 4 we discussed how the increased number of edges (and thus defects) can affect the electrode response, particularly when the electrodes are scaled down to a few microns. We saw how electrodes with smaller graphene domains exhibited convergent diffusional transport and the effects that the increased number of edge defects had on the observed double layer capacitance, linear range, and quite possibly, detection limit.

In this chapter, we examine the effect geometric patterning and functionalization have on the overall electrode sensitivity and charge transfer kinetics of single layer graphene electrodes fabricated on SiO_2.

5.1 Chemical and Geometric Modification of Electrodes

The chemical and electrochemical performance of electrodes has seen improvement with chemical functionalization. The latter can be attained via different methods, whether that is by chemically attaching a functional group through surface chemistry or exposing electrodes to an ozone plasma; that is, by roughening the electrode edges. In Chapter 4, we examined the electrochemical properties of electrodes made through a fabrication process that introduced sufficient defects and holes in the graphene. In this chapter, we examine electrodes that were processed somewhat differently, with the sole purpose of leaving the graphene as pristine as

possible and avoid roughened electrodes. The passivation/sacrificial step of the fabrication process described in Chapter 3 introduced defects because to etch down to expose the active graphene areas, buffered oxide etch would also attack the underlying SiO_2 on which graphene was transferred onto, thus attacking the graphene as well. These cracks/holes/defects were visible under a microscope and also confirmed by Raman Spectroscopy. Electrodes examined in this chapter were never exposed to silicon oxide in the first place, but rather passivated with photoresist, which was cured for 12 hours at 160ºC to harden it and improve water impenetrability. The graphene, was thus, left with a smaller number of defects. To enhance the effect of the exposed patterned edges, the electrodes were exposed to a low power ozone plasma, as to functionalize the graphene surface. The results of the electrochemical performance and disadvantage of such approach are summarized in the sections to follow.

5.2 Serpentine Ladder Electrode Design and Fabrication

To evaluate the effect edges had, electrodes were patterned with a constant area, $1mm^2$, varying only the perimeter, making serpentine ladder-shaped electrodes that were roughly 2.13×, 5.32×, 5.83×, 6.43×, and 8.13× the perimeter of a standard square shaped electrode . The electrode lines were kept at 100 µm minimum width, mostly to avoid seeing current effects due to convergent diffusion, as we wanted to isolate the edge effect within the linear diffusion regime. We present a picture of the electrode mask as well as a photograph of the completed chip in Illustration 5.1 and Figure 5.1, respectively

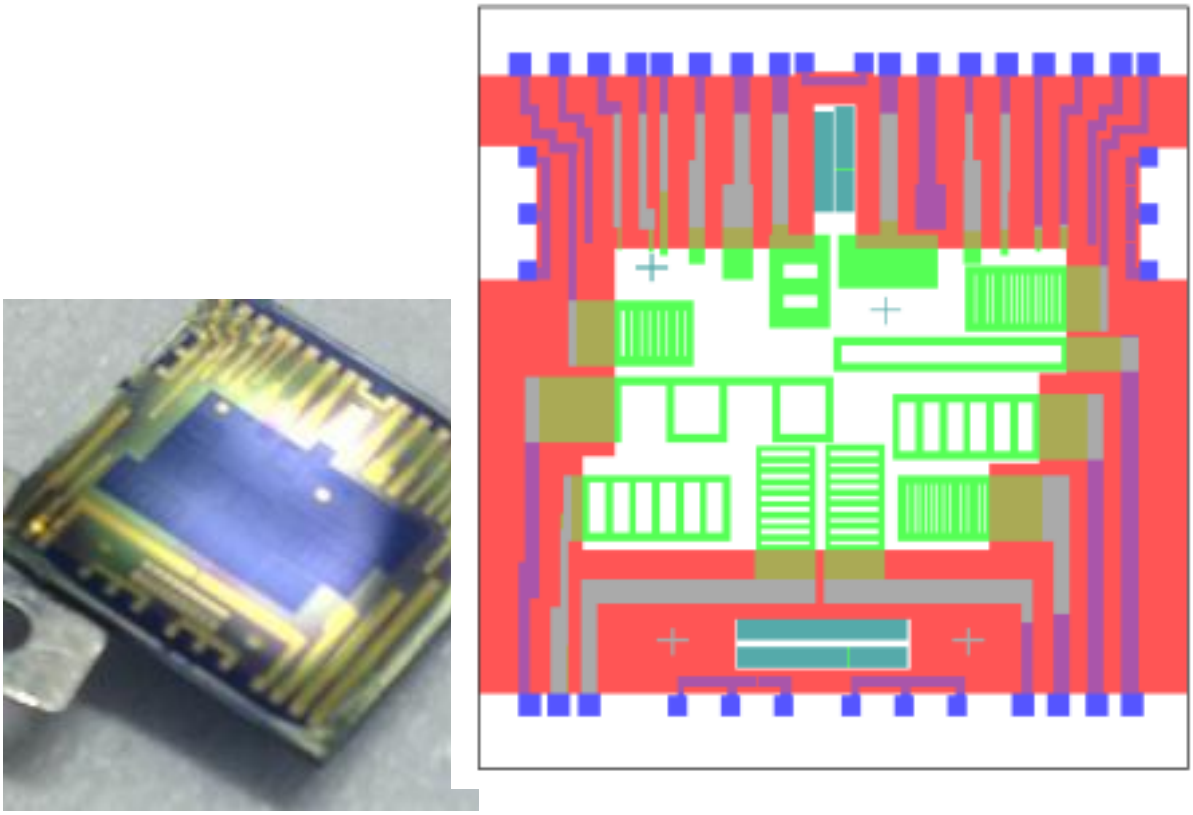

Illustration 5.1 (left) Photograph of fabricated graphene serpentine electrodes with varying perimeter: area ratios. Figure 5.1(Right) Image of mask design for ladder electrodes

Monolayer/bilayer graphene on copper foils was obtained from SMI. The graphene was transferred from the copper substrates to 100 nm of SiO_2 on silicon wafers as described in section 3.2.3. The fabrication process of this generation of devices was identical to those presented in Chapters 3 and 4, with the exception that no sacrificial layer was used to protect the graphene from the photoresist. Less holes and defects were achieved at the cost of slightly higher PR contaminants. In addition, we did not use a plasma ALD SiO_2 passivation layer to insulate the metal leads.

Post electrode patterning, the devices were just spun with PR (SPR220-3µm) , and the passivation layer was exposed, developed and cured to extract all the moisture, needed to prevent

leakage during electrode testing. Such a process yielded electrodes with more uniform surfaces, and less visible holes or patches in the graphene distribution on the 100 nm oxide surface onto which the material had been previously transferred. Because the purpose of these electrodes was to evaluate the effect that increased number of edges had, biocompatibility was not considered in the materials selection.

It is important to note the while the graphene transfer process was identical, there was variability in the origin of the graphene itself, as it came from different copper foils obtained from SMI. The slight variations amongst films did contribute to observed performance differences from one chip to the other. We try to present as consistent set of results as possible, but highlight any results that show higher sensitivity, detection limit or faster kinetics than those observed for electrodes characterized in Chapter 4. As in Chapter 4, TLM lines were also measured to extract contact and sheet resistivity.

5.3 Electrochemical characterization of Unfunctionalized Serpentine Electrodes

In our analysis we will refer to Figure 3.1, as the same impedances are applicable to this set of electrodes. The electrochemical response of a 1×1 mm^2 electrode against 1mM of FcMeOH in $0.2KNO_3$ under different scan rates is plotted in Figure 5.2. As before, the peak current scales linearly with the square root of the scan rate, confirming linear diffusional transport. However, after taking into consideration the uncompensated, contact and sheet resistance (R_U~ 1kΩ, R_{SH}~1.552 kΩ, R_C~1.65 kΩ-μm), the peak-to-peak separation between the anodic and cathodic peak is greater than the one seen for 1×1 mm^2 roughened electrodes, confirming somewhat

slower kinetics.

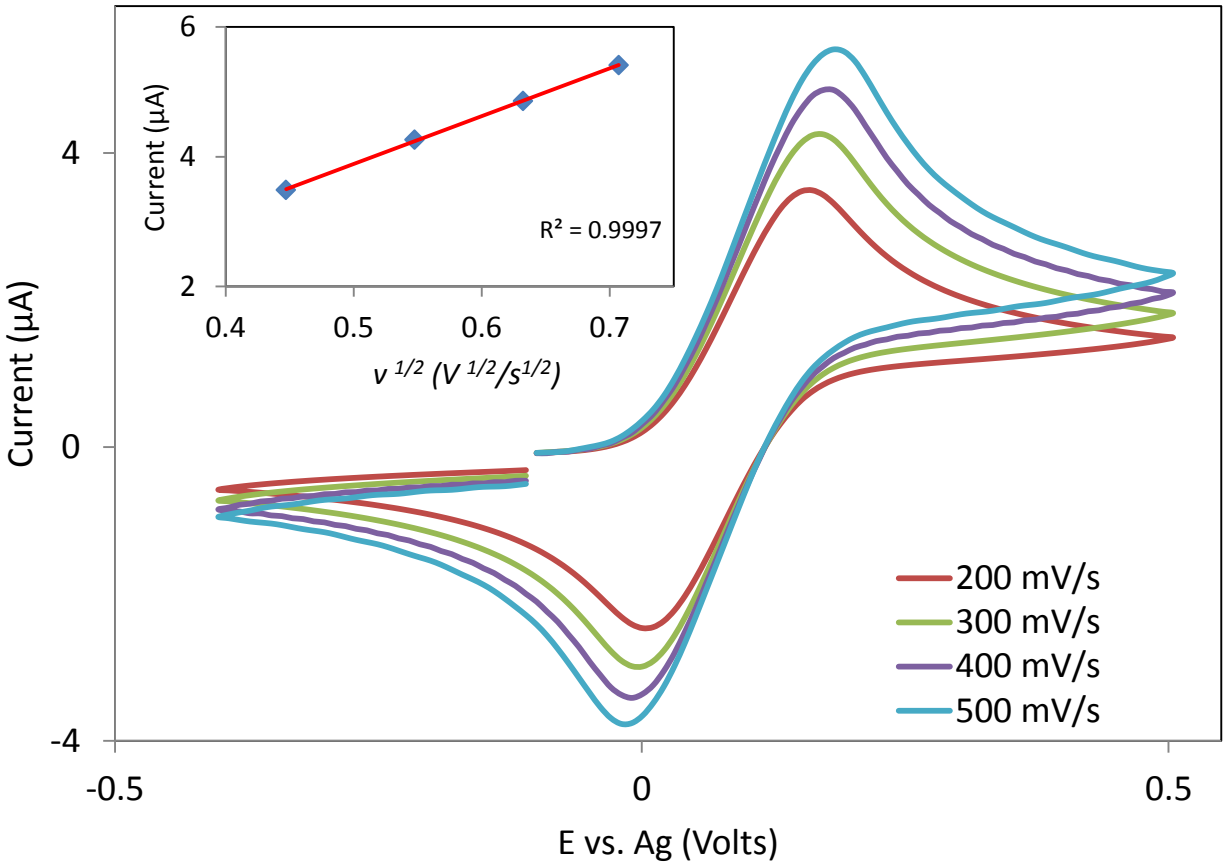

Figure 5.2 Voltammograms for a 1×1 mm^2 electrode in 1mM ferrocenemethanol at different scan rates. The inset plots the relationship of the square root of the scan rate versus the measured peak current. Charging current has been subtracted, even though it is almost negligible for such high concentration.

There were variations in the kinetic response of the electrodes, possibly due to differences in sample preparation. Even though Figure 5.2 shows a larger peak-to-peak separation (than the electrodes presented in chapter 4) between anodic and cathodic peaks, a subset of electrodes tested did exhibit faster electron kinetics. As the perimeter-to-area ratio increased so did the total effective sheet resistance of the electrode. The total intrinsic sheet resistance of the fabricated clean electrodes was found to be roughly 1552 ohm/□. To calculate the effective sheet resistance of each electrode, its geometry was taking into consideration and it was treated as a resistor

ladder or a serpentine resistor (and sometimes both). Consider the electrode with a perimeter 2.16 times as large as our control square shaped 1mm^2 electrodes, depicted in Figure 5.3. We first counted the number of squares, added them to find out the resistance along each length of the electrode, and computed the total resistance using the rules for resistors in parallel and series in a circuit as looking from the contact end. In our model we tried to account for small cracks found along the width of the lines of the electrodes. While for some electrodes with simpler design the calculation of the effective sheet resistance was straightforward, for others, it was a lot more difficult due to the small cracks in the lines. In those cases a specific range of values had to be assessed to best fit to the experimental results.

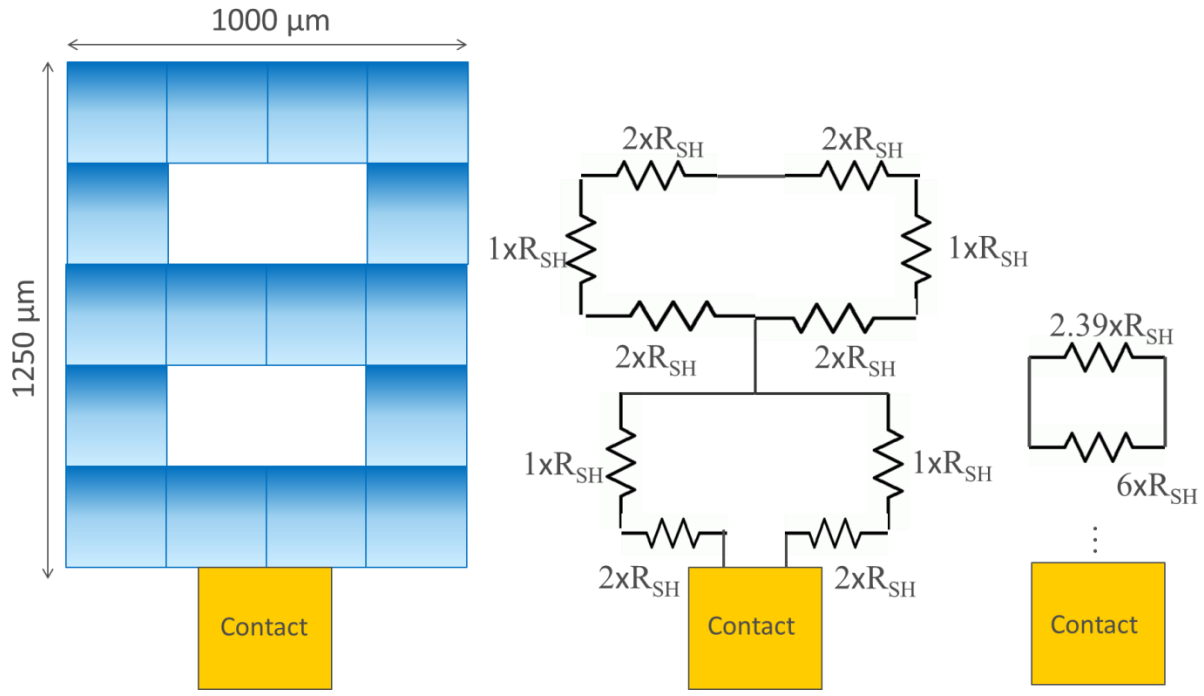

Figure 5.3 Cartoon of ladder-shaped electrode with 2X the perimeter of a 1mm^2 shaped electrode. The effective sheet resistance was extracted using a simple circuit model to collapse the resistor network as looking from the end of the contact.

The effective sheet resistance was extracted for the electrodes tested. The results are consistent with observed experimental results and summarized in Table 5.1. As the effective sheet resistance increased so did the peak-to-peak separation of the anodic and cathodic currents observed in the voltammograms (without resistance correction).

Table 5.1 Summary of Electrode Perimeter and Effective Sheet Resistance

Perimeter	Ratio to Control Electrode Perimeter	Effective Sheet Resistance
6500	2.16	$1.72\times R_{SHint}$
16000	5.32	$5.5\times R_{SHint}$
17500	5.83	$(9\text{-}10)\times R_{SHint}$
19300	6.43	$(12\text{-}14)\times R_{SHint}$
24400	8.13	$24\text{-}28\times R_{SHint}$

Figure 5.4 shows the typical voltammogram response of an electrode with an effective sheet resistance ~20 times larger and a total perimeter roughly 6.43 times as long as the control 1×1 mm^2 electrode. Not only is the peak separation larger, but the response starts to resemble that of an electrode with domains at which convergent diffusion take place, consistent with more edge sites for electrocatalytic activity.

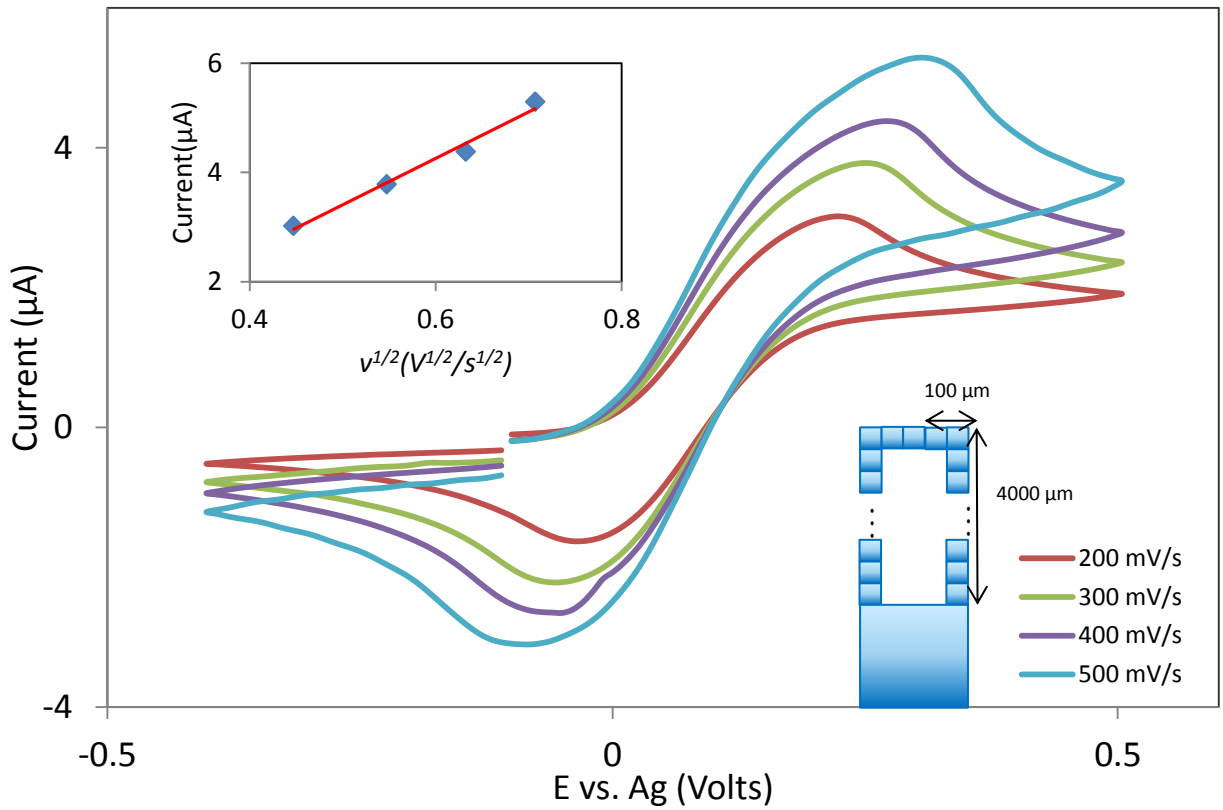

Figure 5.4 Voltammogram response at different scan rates for an electrode with 8× the perimeter length and roughly 20× the sheet resistance of a 1×1 mm^2 electrode. The inset shows the peak current plotted against the square root of the scan rate A cartoon of the electrode geometry and dimensions is shown at the bottom right.

The peak separation as a function of the scan rate is plotted in Figure 5.5, both before and after resistance correction. Because of the high magnitude of the currents and large differences in the overall effective sheet resistance of the electrodes, the peak separation will increase dramatically as the electrodes get longer. After the proper resistance correction there is no specific trend observed between the electrode responses, except for that of increasing peak separation with increasing scan rate, as is expected of heterogeneous transfer kinetics in the quasi-reversible regime. In the lower scan rate limit (~100mV/s), the response of the electrodes with 2.16, 5.32, 5.83 and 8.13 times the perimeter of the control electrode, respectively, is almost indistinguishable. At the higher scan rate limit there is also little difference seen between the peak separation of the control, the 2.16, 5.32, 6.43 and 8.13 times control perimeter electrode.

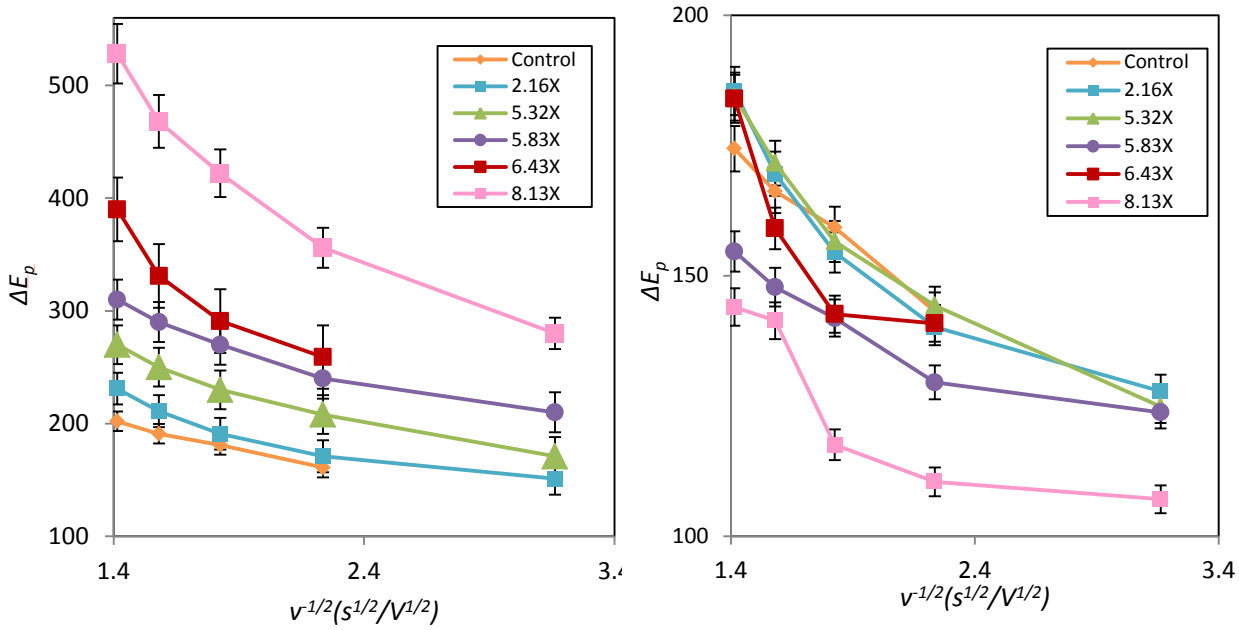

Figure 5.5 Peak separation as a function of the inverse of the square root of the scan rate for electrodes of different lengths. The left plots shows the response without correction for the sheet, contact and uncompensated resistance. The right plot shows the observed response for electrodes with proper resistance correction.

Interestingly, when characterized against ferrocenemethanol, serpentine ladder-shaped electrodes did not exhibit severe sensitivity, nor detection limit variations as compared to the square shaped electrodes. Figure 5.6 plots the relationship of the square root of the scan rate versus the peak measured current for the electrodes of different perimeter-to-area ratios, revealing nearly identical trends in the linear diffusional response. The effective electrode areas were calculated to be roughly 1mm^2 for all characterized electrodes, regardless of the perimeter: area ratio, with the area of the serpentine electrodes observed and calculated to be somewhat smaller in some electrodes due to the increased number of missing active graphene areas in the smaller segments of the electrodes.

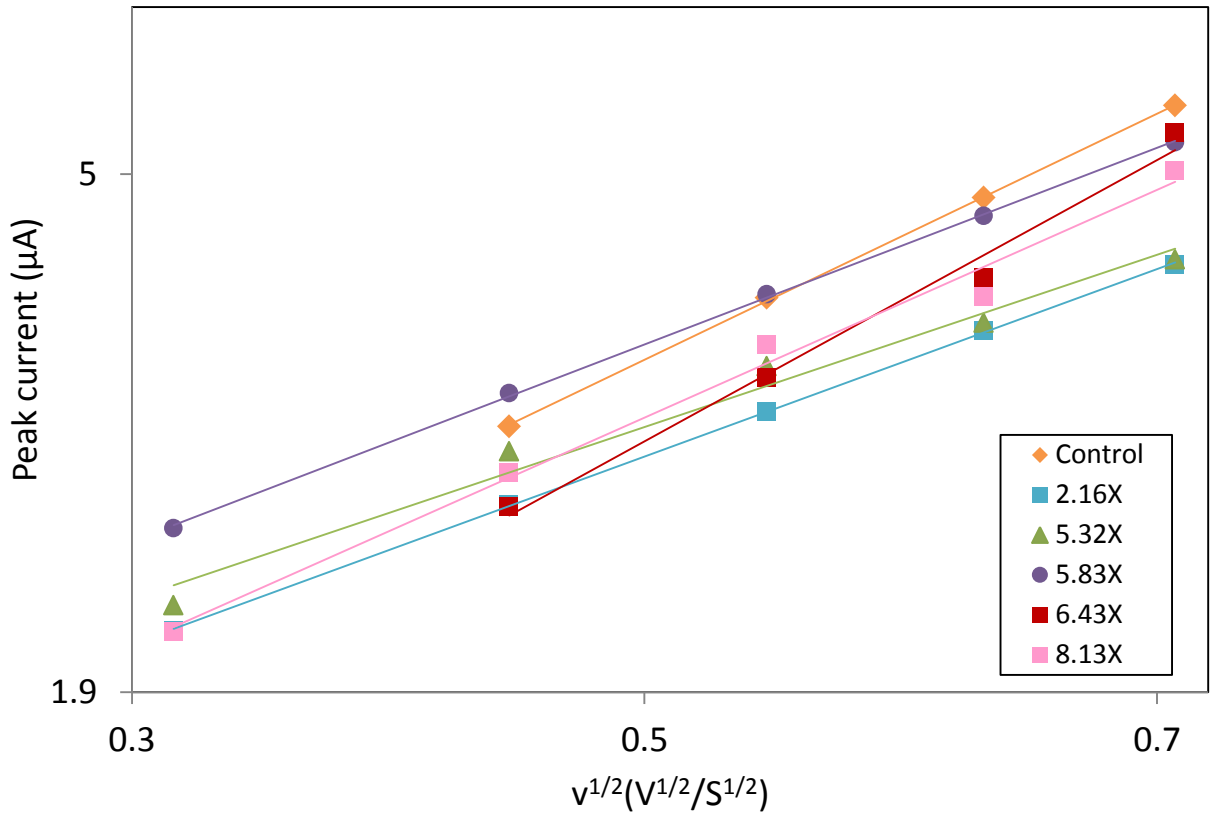

Figure 5.6 Plot of square root of the measured peak current versus square root of the scan rate for different electrodes of constant area and varying perimeters.

The detection limit was found to be about the same for all electrodes, 2.5 uM, and the similar current levels at lower concentrations were indicative of similar double-layer capacitance values despite the differences in exposed edges. The left of Figure 5.7 plots the peak current versus the concentration for electrodes of different lengths. Unfunctionalized electrodes could be tested in up to 1 mM of analyte. The curves indicate that, despite the differences in resistance and perimeter lengths, all electrodes had the same effective electrode area, and, there weren't significant changes in electrode sensitivity. Subtle differences can be attributed to slight variations in the effective double-layer capacitance, small differences in area, as well as slightly higher sensitivity with increased edges (almost negligible though) and experimental noise.

We can extract the electrode sensitivity from the current versus concentration plots. In doing so, we find that as the electrode perimeter increases the average sensitivity, taken across all data points, remains relatively unchanged, while the peak sensitivity, calculated at higher concentrations, were charging currents are negligible, increases slightly with electrode length. The results are plotted on the right plot of Figure 5.7.

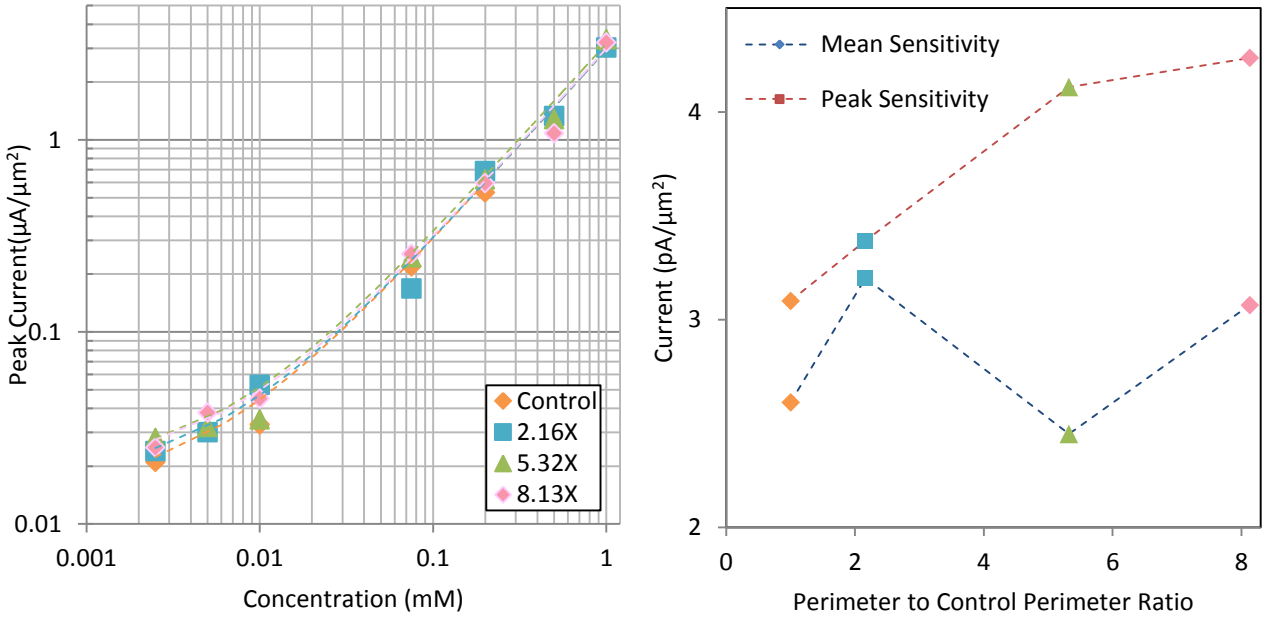

Figure 5.7 (Left) Peak current versus Concentration plot for electrodes of different geometries.(Right) Mean and peak current sensitivity normalized to electrode area.

5.4 The Effects of Plasma Functionalization

Despite graphene's astonishing characteristics, its inert nature is counterproductive to its use as an electrode material, as more electron charge transfer is seen in regions where there are more dangling bonds and defects. The contact resistance to pristine graphene has also been found to be quite high because of similar reasons. To that end, attempts at chemical functionalization or

introduction of holes or defects have been explored to enhance its electrochemical properties, as well as the contact resistance.

This thesis explores the use of a low-powered ozone plasma (<10W) to introduce just about enough defects to the edges of the patterned electrodes. The electrochemical performance is assessed post 30 seconds and post 60 seconds of plasma exposure.

5.4.1 Changing the Surface Energy with Plasma Exposure

The surface energy of graphene can be changed upon functionalizing the surface with oxygen and hydroxyl groups. The progression of this change can be seen in Figure 5.8, where the prolonged plasma exposure increases the hydrophilicity of the surface, and thus, the measured contact and receding angles.

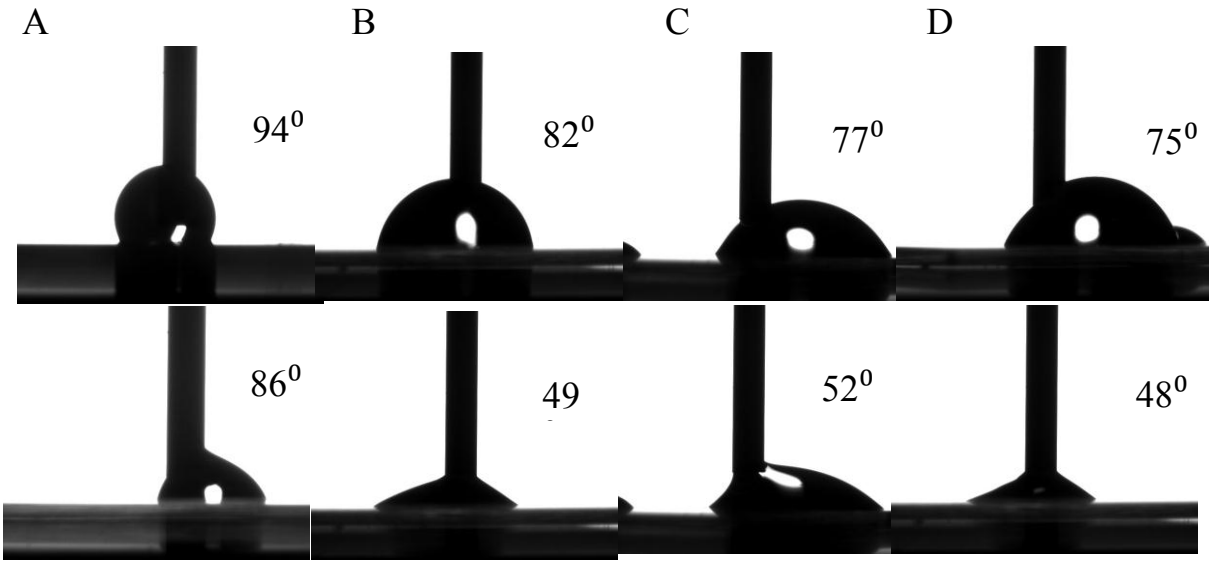

Figure 5.8 Progression of contact angle on CVD graphene under A) no applied ozone plasma, B) 5 seconds, C)10 seconds and D)15 seconds. Plasma power was kept under 10W.

With no applied plasma the contact angles of water to the surface are almost perpendicular. With increased exposure, the angles drop and the water droplet collapses onto a more hydrophilic surface. Figure 5.8 shows the progression of the contact and receding angles with 5, 10 and 15 second plasmas.

5.4.2 Using an Ozone Plasma to Enhance Contact Resistance

The effect of using a low powered plasma was first examined in the measurement of the contact resistance made to CVD graphene with Ti/Au contacts. To this end, TLM lines were fabricated as depicted in Figure 5.9 using a simple 2-mask process to define contacts and pattern graphene.

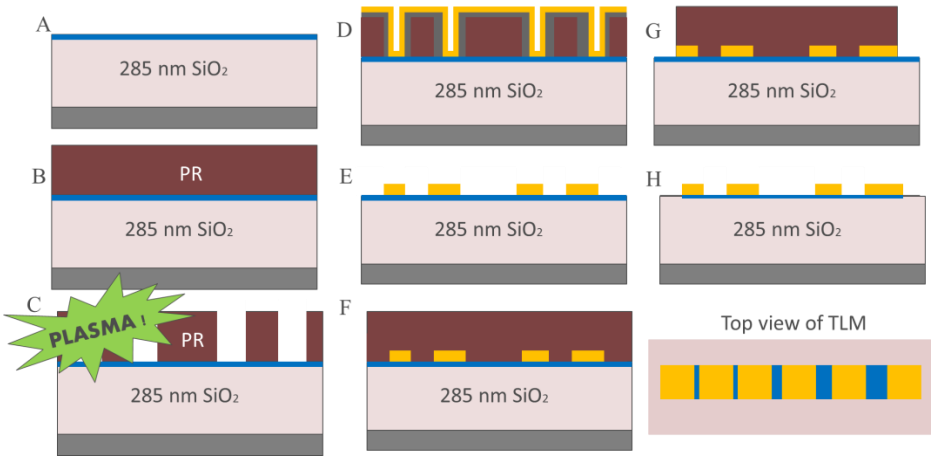

Figure 5.9 Process Flow diagrams of TLM lines. Before metallization, the samples were exposed to a 15 and 30 second low-power ozone plasma as to improve the contact resistance of the Ti/Au to the graphene.

The TLM lines were measured to extract the contact resistance to the graphene. The contact resistance values are plotted in Figure 5.10.

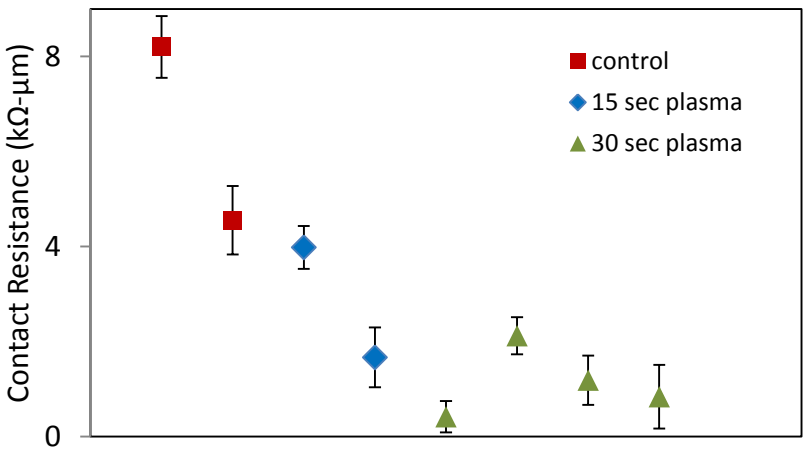

Figure 5.10 Contact resistances of TLM lines under no ozone plasma, 15 second and 30 second exposure

The plasma improved the contact to the graphene, with 30 second exposure proving to be more effective than 15 seconds. All lines were measured with a probe station and data for each point was averaged over 8 lines. Each point represents one chip. The TLM mask design is shown in Figure 5.11, featured below.

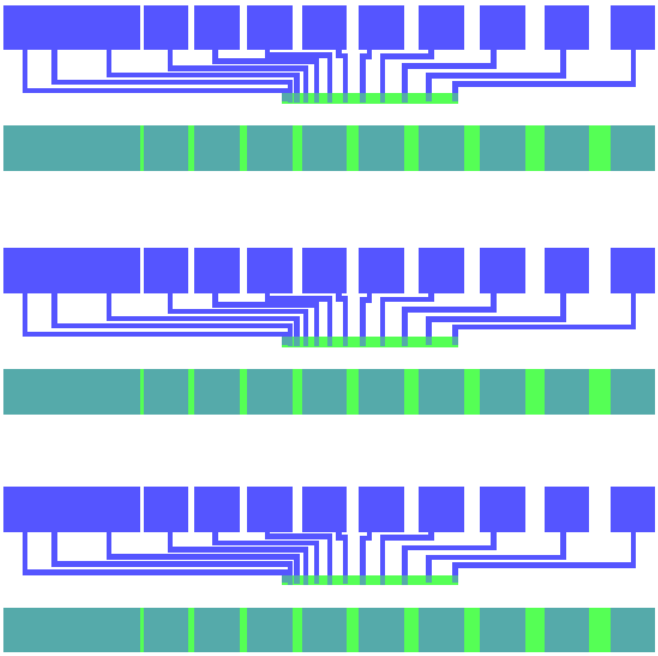

Figure 5.11 Mask for TLM line analysis. Design includes both lines made at 20μm width as well as larger 200 μm width lines. The blue areas are the gold contacts/line. Active graphene areas are shown in green.

To further understand the mechanism by which the plasma affected the graphitic surface, we exposed fabricated TLM lines to a plasma and subsequently measured the sheet resistance as well as the total resistance, to draw a comparison from controls. Figure 5.12 plots the response of a typical TLM line before and after plasma exposure. Each point was extracted over the average of 8 measurements, 2 made on the actual electrode chip and 6 made on witness TLM lines prepared under the same protocol as the electrodes. Results confirm an increase in the total sheet resistance from 1552 ohms/□ to roughly 2678 ohms/□ after 30 seconds of plasma exposure.

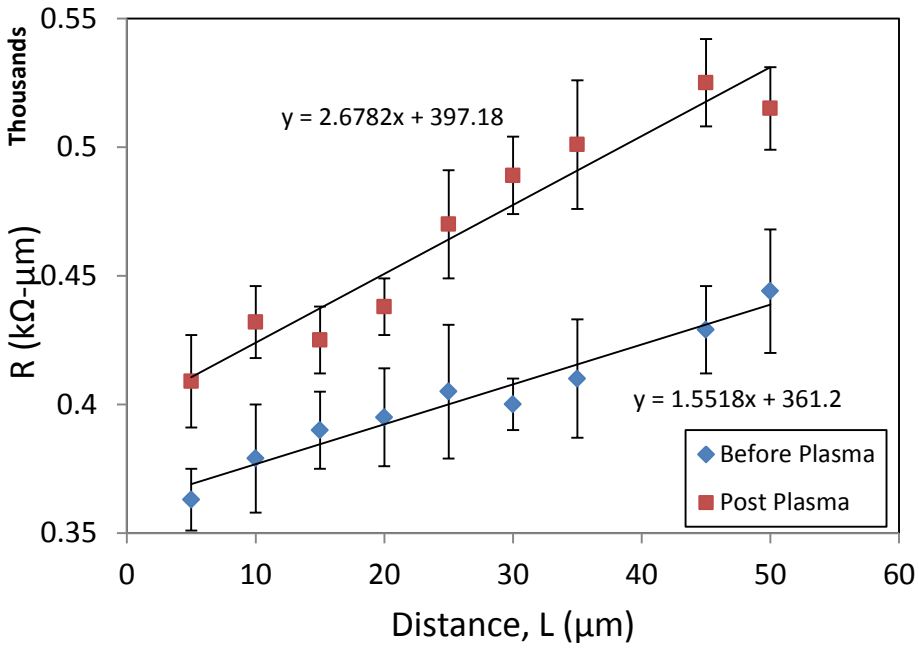

Figure 5.12 TLM analysis before (red dots) and post 30 second (blue dots) plasma exposure of the graphene surface between the contact pads of the TLM lines.

Post ozone-plasma exposure, the overall sheet resistance of the lines increases, suggesting that more defects, specifically holes and cracks, were made in the graphene. Figure 5.13 confirms this to be true with Raman spectra. There is a small observable increase in the D peak.

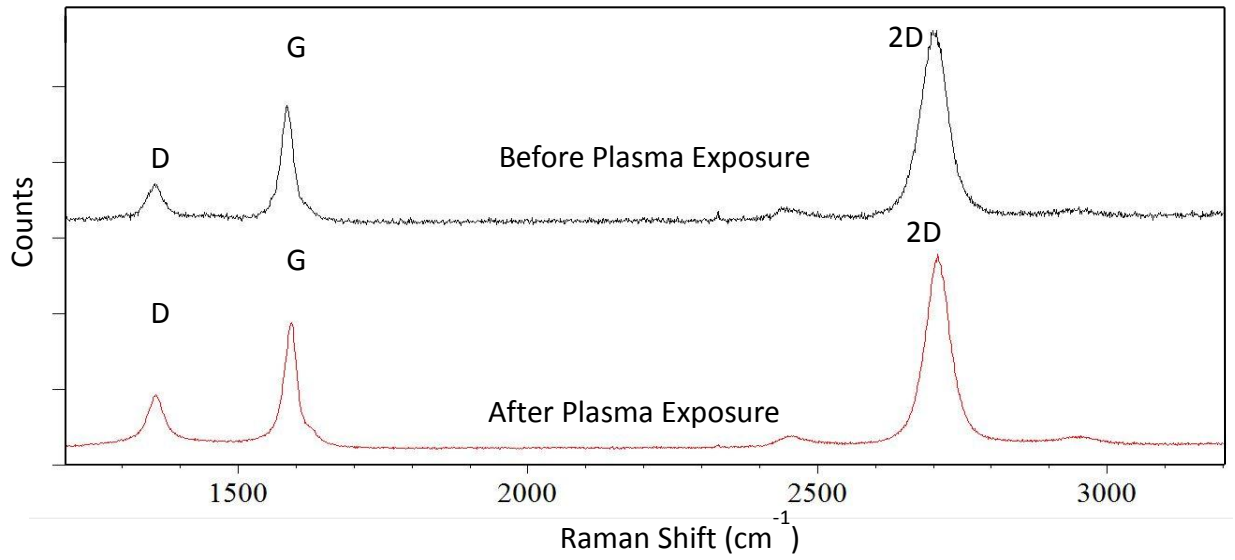

Figure 5.13 Raman spectra of monolayer graphene before and after a 30 second ozone plasma exposure.

This simple experiment suggests the plasma enhanced the contact resistance by cleaning the graphene surface from PR residues left from processing, and by possibly creating small defect sites that can increase the local density of states to enhance contacts. However, these holes can also increase the sheet resistance, as seen from the plotted results. The increase values for sheet resistance had to be taken into consideration when analyzing the kinetic trends of plasma-functionalized electrodes.

5.5 Electrochemical Characterization of Functionalized Serpentine Electrodes

We now turn our attention to the characterization of serpentine electrodes that were functionalized with an ozone plasma. Electrodes were tested against 500 µM of ferrocenemethanol in 0.2M of KNO_3 as the supporting electrolyte. Like before, chips were mounted onto a PCB made on quartz wafers and wire-bonded using aluminum thread.

5.5.1 Electrode Kinetics

Figure 5.14 shows the characteristic voltammograms at a scan rate of 200 mV/second for the different electrodes of varying lengths. All electrodes were treated with a low power (<10W) ozone plasma for 30 seconds. The electrodes exhibit linear diffusional transport in the quasi-reversible regime. Regardless, the current still scale s linearly with the scan rate, so the Randles-Sevcik equation is till applicable within this regime.

Like untreated electrodes, as the electrode perimeter increases so does the separation between the peaks of the voltammograms. Notice that the profiles are given for a smaller concentration of ferrocenemethanol in 0.2M of KNO_3, namely 500μM. The concentration had to be reduced for 2 reasons: 1) The potential window was narrower due to increased kinetics and 2) the intrinsic device resistance increased as well (due to the increased sheet resistance after plasma exposure) and the device could easily oxidize with increased applied potential at higher concentrations (more voltage would be needed to see the peak of the current, i.e.: $I=VR$). Therefore, if we compare these voltammograms to the ones seen in section 5.3, the uncorrected peak separation is actually much larger. This is in accordance with the observed increased in sheet resistance after plasma exposure.

There is also visible increased sensitivity (we will examine this in more detail later in this section) with the total peak current increasing with increased electrode perimeter. Most of the curves, with the exception of the one for the electrode with 8.13 times the control perimeter, show a larger value in the double-layer capacitance as expected. As the edges get functionalized, the double-layer capacitance increases.

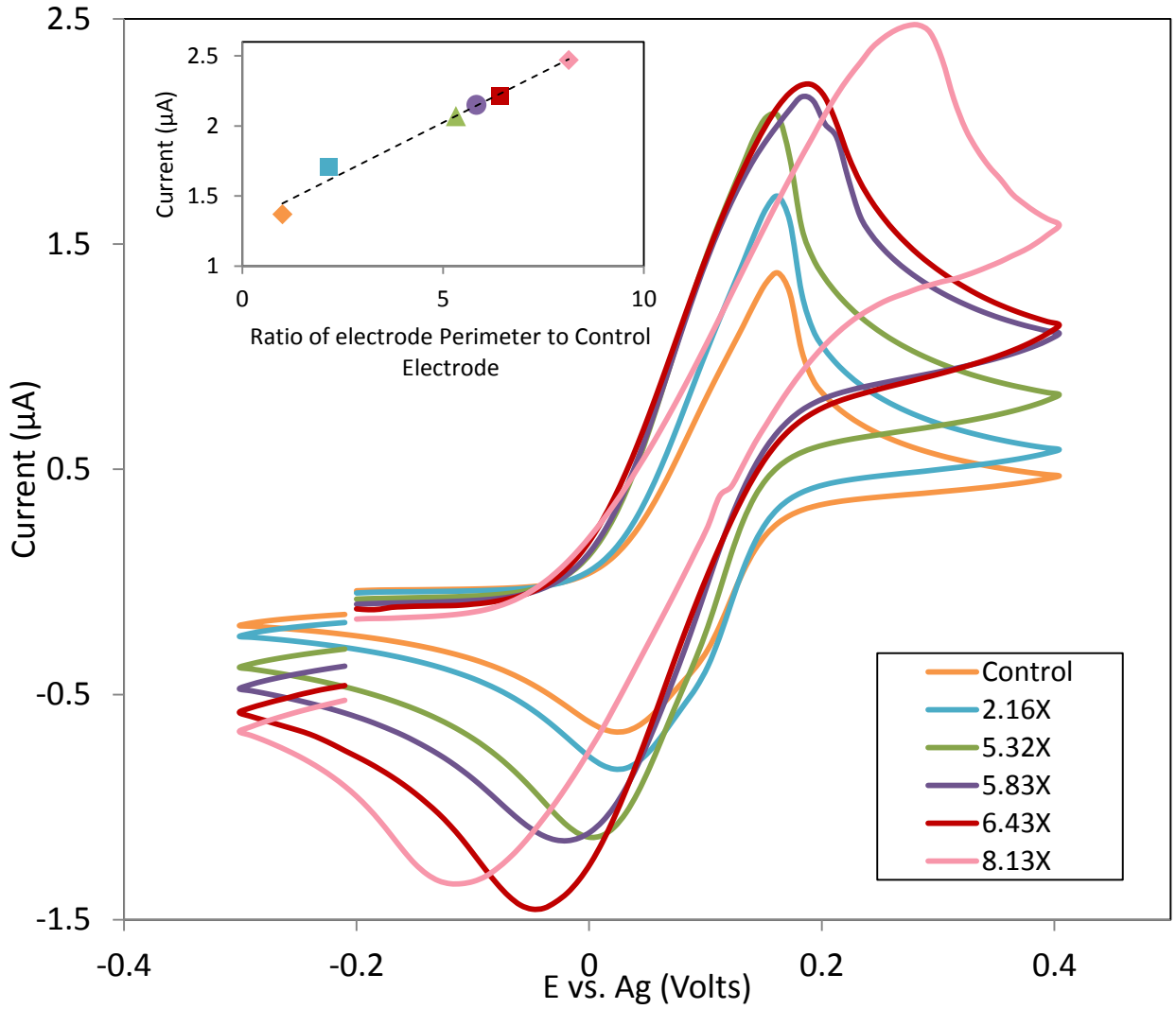

Figure 5.14 Voltammogram behaviors of serpentine ladder electrodes in 500 µM of FcMeOH in $0.2KNO_3$ at 200mV/s. The inset shows the peak current versus the ratio of the electrode to a control electrode.

If we correct for the sheet resistance (2678 ohm/□) and the uncompensated resistance (R_U~1kΩ), the separation between the peaks is actually calculated to be smaller than for control electrodes that have not been treated with an ozone plasma. An even more important and consistent result is that as the electrode perimeter increases, the separation between the peaks gets smaller. Figure 5.15 (on the left) shows the peak separation as a function of the inverse of the square root of the scan rate for all tested electrodes after the correction for the device and interface parasitics have

been taken into consideration. As the perimeter increases, the peak-to-peak separation decreases, except for the 8.13× electrodes were the measured peak-to-peak values were somewhat larger than those measured in the 6.43 × electrodes. It is important to emphasize that experimental data was subject to measurement resolution limits, roughly +/- 5mV. In addition, local variations in sheet resistance throughout the chip are likely sources of measurement errors. It is predicted that the longest electrode might have had more holes/cracks/discontinuities and thus, may have had a larger sheet resistance than the one accounted for. To ensure that the extracted kinetics were just not an effect of overcompensation, we also calculated the correction for the lower limit of the measured sheet resistance, that is, in the case the sheet resistance had not been changed at all by exposure to the plasma, namely R_{SH}~1552ohm/□. The observed trend in the peak-to-peak separation remains consistent.

We can once again use Nicholson's curve to correlate the peak separation to a dimensionless parameter, ψ. Figure 5.15 also plots this dimensionless parameter versus the inverse of the square root of the scan rate for the tested electrodes. From equation (4.19), $\Psi = k^o\sqrt{RT/\pi nFD}v^{-1/2}$, we can extract the values for the heterogeneous rate constant for each of the electrodes from the slope of the best fit line to the plotted data points.

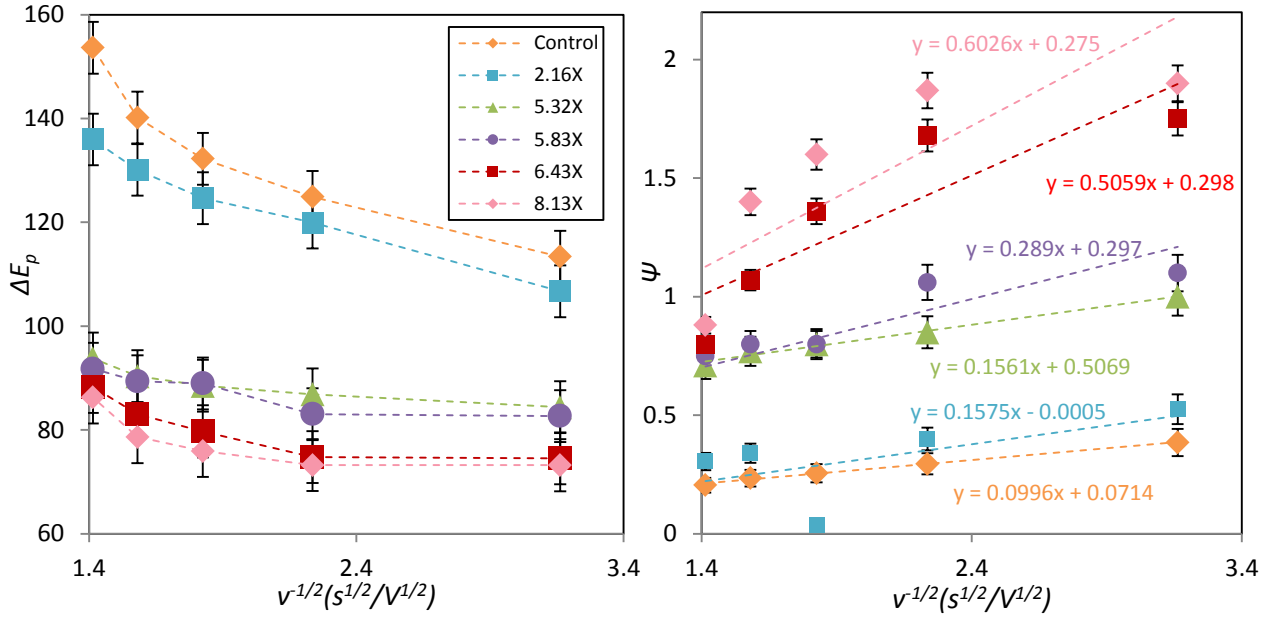

Figure 5.15(left) Potential separation between the measured anodic and cathodic peak for the different serpentine ladder electrodes versus the inverse square root of the scan rate. Respective plots for ψ on the right.

We plot the extracted heterogeneous charge transfer rate constant for the electrodes versus the perimeter-to-area ratio for electrodes that had not been treated with a plasma, and for electrodes that had been treated with it. For the latter, we plot both the case where the sheet resistance was 2678 ohm/□ and the case were it remained unchanged even after plasma exposure (the lower limit of the sheet resistance) to show how the kinetics follow the same trend regardless of the correction factor, proving that the ozone functionalization does enhance the electron transfer kinetics as the number of edges are increased. Figure 5.16 presents the single most important result of this work: that the increased number of edges with available states (functionalized) can enhance not just the current sensitivity, but also enhance the electron transfer kinetics. The transfer constant of the control square-shaped electrode is consistent with that reported for single-layer graphene in Chapter 4 (~.002-.003) and shows minimal improvement with exposure to plasma.

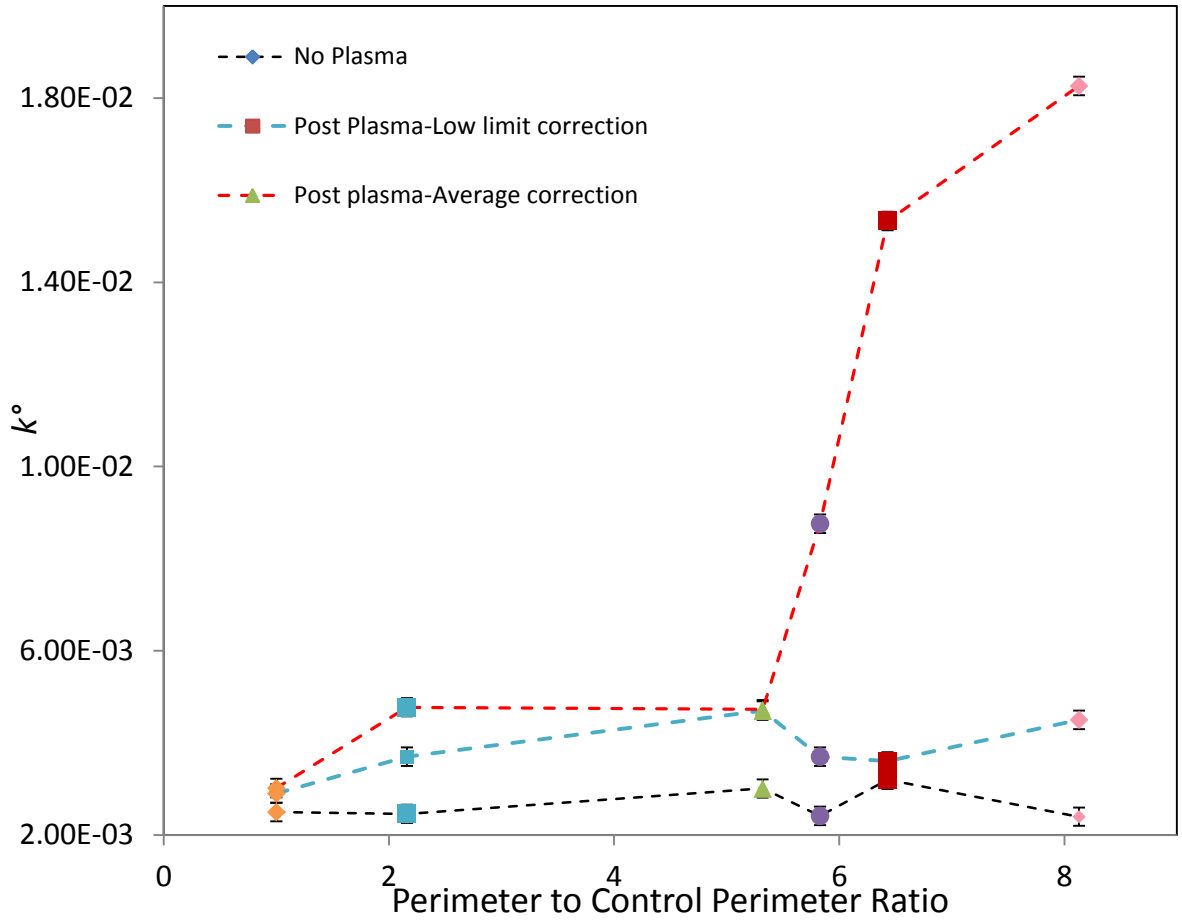

Figure 5.16 Plots of the extracted heterogeneous charge transfer constant as a function of electrode length.

5.5.2 Electrode Sensitivity

We now turn our attention to the detection limit and sensitivity of plasma-modified electrodes. While subtle, there is an increase in the double-layer capacitance with increased electrode length, even more so after plasma exposure, and this, in turn, will limit the detection limit, linear range and overall sensitivity of the patterned electrodes. Thus, when designing, it is one of the constraints to consider. An electrode may have a limit at which further lengthening comes at the cost of a lower detection limit. Figure 5.17 plots the peak current versus the concentration for electrodes of different lengths on the left. The mean and peak current sensitivity versus the

electrode length ratio is plotted on the right. The latter reflects the second most important result of this work, which is inherently coupled to the first, presented in the prior section: with increased electrode length the sensitivity is improved.

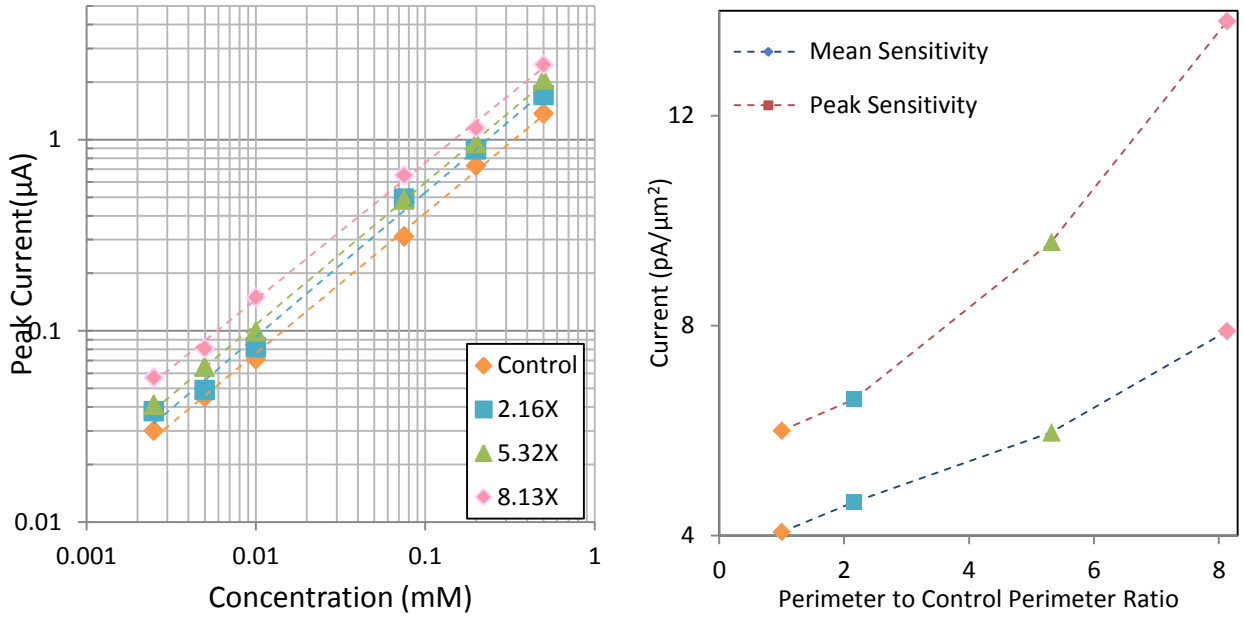

Figure 5.17 Plots of the measured peak current versus concentration (left) and plots of the measured peak and mean sensitivity for 500 µM of FcMeOH(right).

While there were improvements in both the electron transfer rate and the sensitivity, the LOD and linear range remain unchanged for all electrodes, regardless of the electrode length or the exposure to a plasma, remaining constant at 2.5 µM and 50-500µM.

To further enhance performance, electrodes were exposed to a 60 second plasma. Interestingly, the number of induced defects was so high the response was purely capacitive and no faradaic currents were observed. A sample plot of such response is observed in Figure 5.18 below.

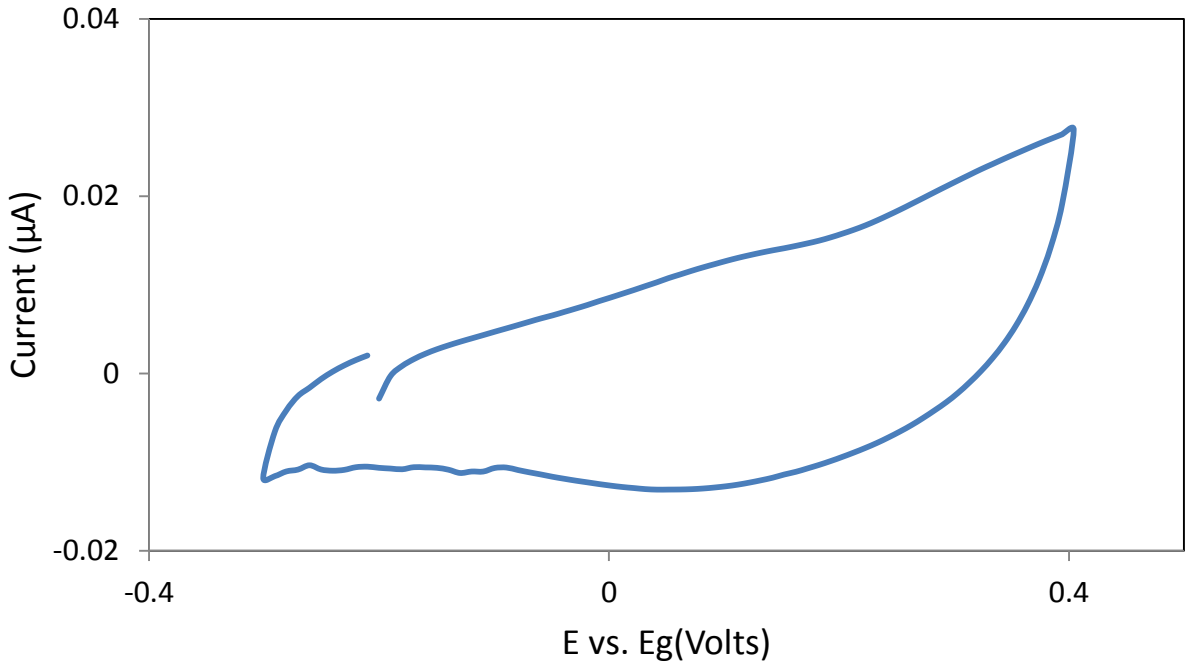

Figure 5.18 Purely capacitive response of an electrode (6.32X) post 60 seconds of plasma exposure.

5.6 Summary

This chapter explored the effect that increasing the electrode length had on the sensitivity and charge transfer kinetics of FcMeOH on single layer graphene. We summarize results below:

- The change in sensitivity was minimal in electrodes of same area and different lengths that had not been exposed to an ozone plasma
- There was little to negligible change in the transfer rate constant of electrodes of same area and different lengths that had not been exposed to an ozone plasma

- Upon exposure to a 30 second ozone plasma source, the electrode sensitivity improved and the charge transfer constant increased with increasing electrode length. Faster kinetics also narrowed the potential window, as expected.
- Raman spectroscopy confirmed increased number of defects with plasma exposure.
- It is suspected that the increased number of defects along the length of the electrodes improved the electrode performance.
- There was a small increase in the local specific capacitance of the electrode. This increase in in double-layer capacitance may limit the LOD of electrodes and is thus a design constraint when designing electrodes.
- This study would be further improved designing smaller electrodes that show convergent diffusional transport (<20μm lines). Our study was limited by photolithographic process. A process with e-beam patterning would allow patterning much thinner serpentine electrodes.

CHAPTER 6

ELECTROCHEMICAL DETECTION OF NEUROTRANSMITTERS

The mammalian nervous system uses hundreds of chemicals, amongst them neurotransmitters and neuromodulators, to transmit signals across the brain and the body. Dopamine (DA) is one of the most important catecholamine neurotransmitters [203]. It is responsible for regulating mood, movement, addictive behaviors, sleep, learning, attentions and pleasurable reward, amongst others. Dopamine is produced in the dopaminergic neurons in the ventral tegmental area (VTA) of the midbrain, the *substantia nigra pars compacta*, and the arcuate nucleus of the hypothalamus [204].

Regulation of dopamine is highly critical; any excess or lack of it produces imbalances in the body. For instance, if there is a deficiency in dopamine in the brain, movements may become delayed and uncoordinated. However, in the presence of an excess of dopamine, the brain would cause the body to make unnecessary repetitive movements.

Abnormal DA concentration may also result in brain disease, one such example being Parkinson's disease [204]. To this date, there are many approaches have been developed for dopamine detection. These include capillary electrophoresis with laser-induced native fluorescence (Park *et. al*) [205], high performance liquid chromatography–mass spectrometry (Carrera *et. al*, 2007) [206], colorimetric detection based on silver or gold nanoparticles (Kong *et. al*, 2011; Lin *et. al*., 2011) [207, 208]. Such techniques are very involved, unreliable and time-

consuming.

Electrochemical techniques have proven advantageous for a variety of reasons. They offer rapid and sensitive detection, ease of use and low cost miniaturized platforms that can often be re-used. The determination of DA has been extensively investigated in the past few decades. (Njagi et al., 2010; Strawbridge et al., 2000; Wu et al., 2005) [209, 210, 211]. One of the biggest challenges, however, is the detection of dopamine in the presence of ascorbic acid (AA) and uric acid (UA), which are also oxidized at potentials close to that of DA at solid electrodes, resulting in overlapped voltammetric response. This makes their discrimination difficult. AA, DA and UA usually coexist in the extra cellular fluid of the central nervous system and serum. Thus, it is important, that for realizable applications, their signals can be discriminated.

6.1 History of Dopamine Detection on Carbon-Based Sensors

There have been many initiative and studies conducted to address the simultaneous detection of DA , UA and AA , both on solid-state and carbon-based electrodes. Chen *et. al*, for instance, used phosphonic acid terminated self-assembled layers assembled on a gold surface to sensitively and selectively detect dopamine (DA) in the presence of highly concentrated ascorbic acid (AA) [212]. Liu *et. al*, on the other hand, designed a polycalconcarboxylic acid (CCA) modified glassy carbon electrode (GCE) by electropolymerization and then successfully used to simultaneously determine ascorbic acid (AA), norepinephrine (NE) and uric acid (UA) [213]. On the graphene end of applications, Sheng *et. al* used nitrogen-doped graphene oxide to measure the electrocatalytic activity towards AA, DA and UA [214] while Wu *et al.* used a new type of

porphyrin-functionalized graphene for highly selective and sensitive detection of dopamine (DA) [211]. The aromatic $\pi - \pi$ stacking and electrostatic attraction between positively-charged dopamine and negatively-charged porphyrin-modified graphene can accelerate the electron transfer whereas weakening ascorbic acid (AA) and uric acid (UA) oxidation. Their reported detection limit was as low as .01μM. Table 6.1 summarizes the performance, as measured by detection limit, of various research efforts, towards the detection of dopamine.

Table 6.1 State of the Art Dopamine Detection with Solid State and Carbon-Based Electrodes [79]

Drugs	Electrode Type	Method	LOD	Potential (V)	Application	Ref
Dopamine	mGold	CV, SWV	…*	…*	Dosage forms, foods	[146]
Dopamine Serotonin	m-indum tin oxide	DPV	0.5nM 3.0 nM	0.07 .24	Human serum, urine	
Dopamine	CNT	DPM	200 μM	0.31	Brain homogenate	[190]
Dopamine	mCPE	FIA/amperometry	1.5×10^{-4}M	0.1	Dosage forms	[178]
Dopamine	porphyrin-functionalized graphene	CV	.01μM	0.2	Dosage forms	[211]
Dopamine	Nitrogen-doped graphene	DP	2.2 μM	0.2	Dosage forms	[214]
Dopamine	PCF	DPV/LSV	.04 μM	…*	Dosage forms	[215]

6.2 Detection of Dopamine on Monolayer Graphene Electrodes

In this work, we conducted detection of dopamine on monolayer graphene electrodes. We also examined the oxidation potentials of DA in the presence of ascorbic and uric acid. The electrodes utilized were characterized and described as in Chapters 3 and 4. We used a 0.1M PBS buffer as the supporting electrolyte and measured electrocatalytic activity for a range of 250μM-10pM.

Figure 6.1 shows the voltammogram response for the different concentrations of analyte on an electrode of area 0.875 mm^2. The electrode response shows irreversible kinetics, typical of dopamine redox reactions. The inset plots a calibration curve. Because the relationship no longer follows the Randles-Sevcik equation, we cannot extract the diffusion coefficient from the slope, but rather approximate it using the equation [139]:

$$i(t) = FAk_f C_A^* \exp\left(\frac{k_f t}{D_A}\right) erfc\left(\frac{k_f t^{1/2}}{D_A{}^{1/2}}\right) \tag{6.1}$$

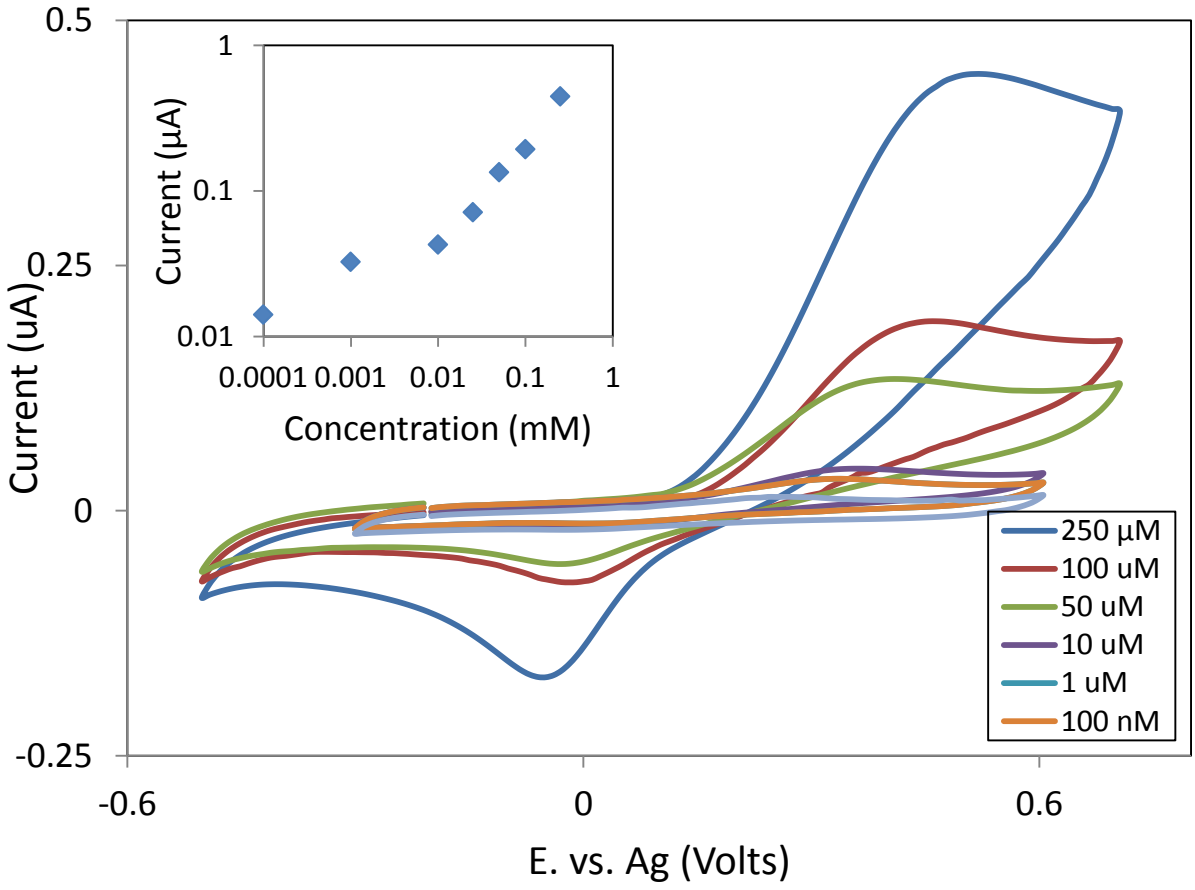

Figure 6.1 Voltammogram of .875mm^2 graphene monolayer electrode response against varying dopamine concentrations in a 0.1mM PBS buffer. The inset shows the peak current versus concentration.

The oxidation potential for dopamine is seen around 0.5 volts. The lack of symmetry reflects that

the energy barrier associated with donating an electron is much smaller that the energy needed to accept one, thus the larger oxidation currents in the first half of the reaction.

6.3 Dopamine Detection in the Presence of Uric and Ascorbic Acid

We also monitored the detection of dopamine in the presence of uric acid and ascorbic acid. It was found that the response was lumped as one peak, where the dopamine response was masked by the presence of ascorbic acid and/or uric acid. Figure 6.2 shows the individual response of 1mM of ascorbic acid as well as the combined response of 250 μM of DA in 1 mM of ascorbic acid. The oxidation peak for ascorbic acid is observed at 0.7 volts. While the current magnitude is representative of the sum of the individual currents, there is not distinct separation of the peaks in the voltammogram.

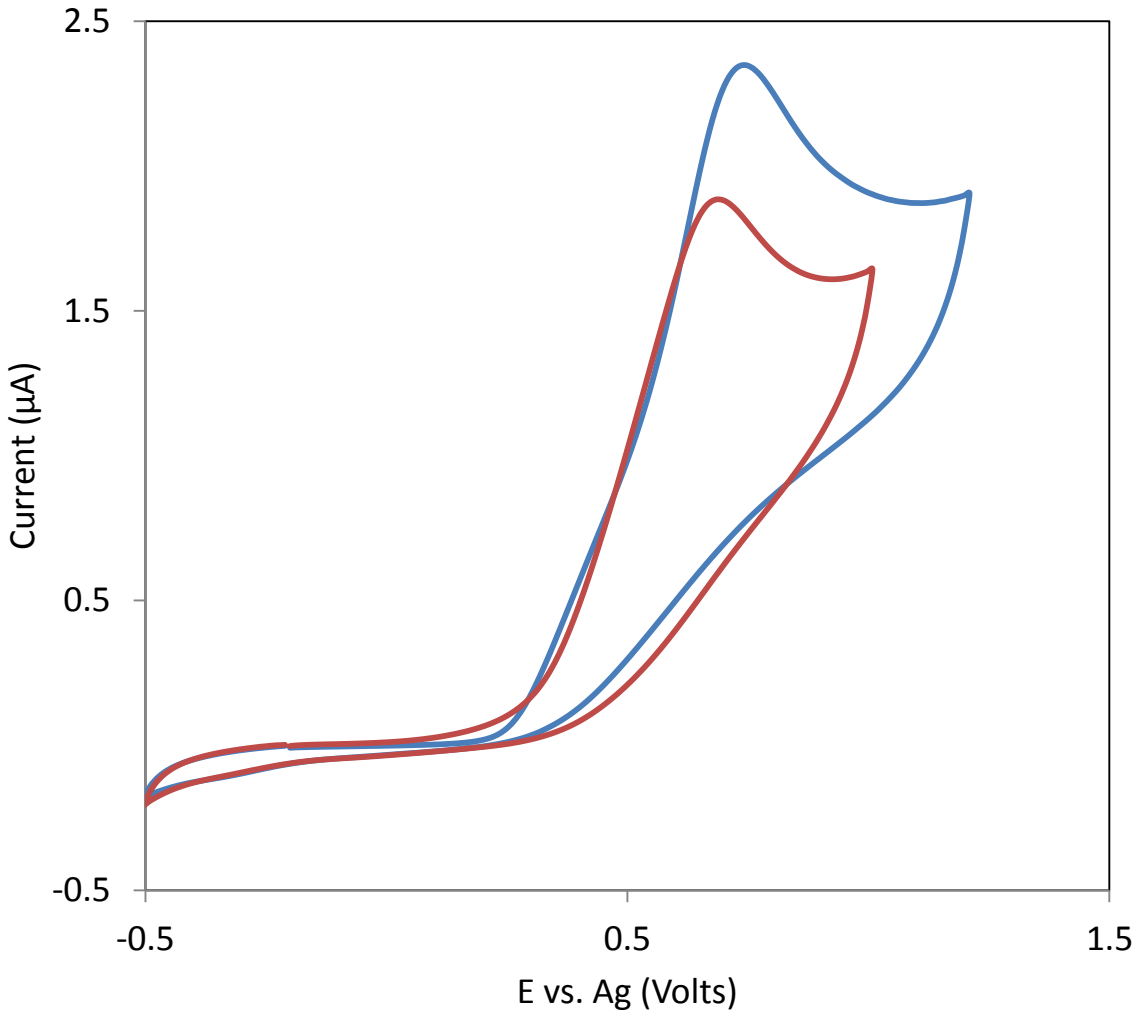

Figure 6.2 Response against 1 mM ascorbic acid (red) and combined response of 250 µM of dopamine and 1 mM ascorbic acid in PBS (blue).

A similar response is observed in the case of 400 µM of uric acid combined with 250 µM of DA. However, there is a small distinguishable peak observed for DA at 0.5 Volts. The oxidation peak for UA is seen around 1 volt.

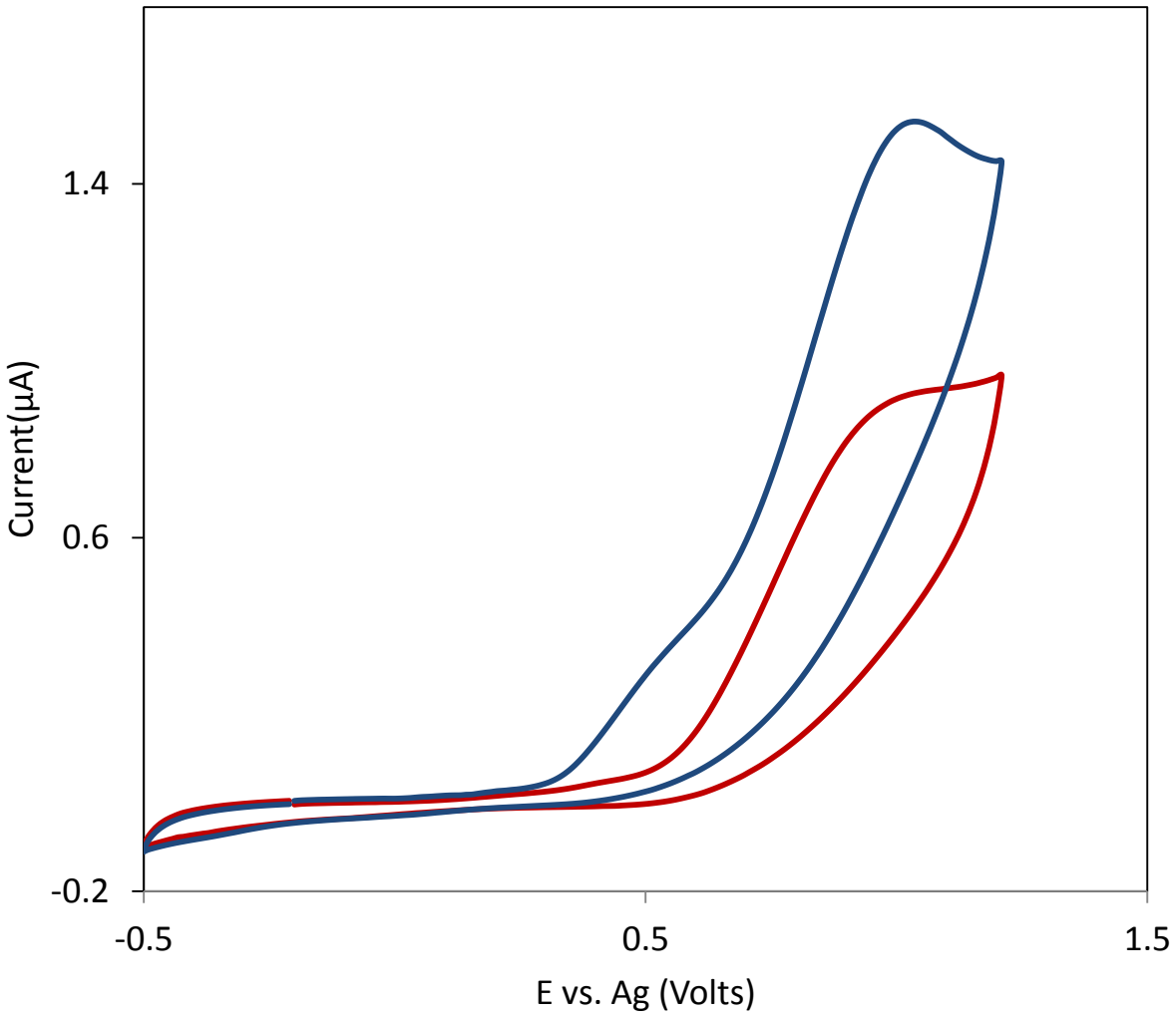

Figure 6.3 Response against 400 µM uric acid (red) and combined response of 250 µM of dopamine and 400 µM uric acid in PBS (blue).

We did not examine the simultaneous response of DA, UA and AA.

6.4 Summary

- Monolayer graphene electrodes were tested against varying concentrations of dopamine in a PBS buffer. The detection limit was as low as 0.1 µM with a linear range observed between 10-250 µM.

- DA was tested in the presence of AA. It was undistinguishable from the 1 mM voltammetric response of AA.
- DA was tested in the presence of UA. It was subtlety distinguishable from the 1 mM voltammetric response of AA. A small peak was observed around 0.5 volts.

6.5 Concluding remarks and Future Direction

This work characterized the electrochemical properties of different types of graphene as an electrode material in the context of an array. We also examined the role activated edge sites had on electrode performance through patterning and functionalization. Experimental results confirmed that the number of graphene layers increased charge transfer rate constant and overall sensitivity as electrodes were scaled past below 20μm. Results also confirm that epitaxial graphene had the largest measurable sensitivity and fastest kinetics across all materials examined. We presume the corrugations inherent to the underlying step bunching of the silicon carbide of such material to be responsible for its improved performance. In addition, at the cost of detection limit due to increased double-layer capacitance, electrodes fabricated on graphene on sapphire showed the highest mean sensitivity. While not perfectly well understood, better control of the quantum capacitance through better fabrication protocols to control doping of the material is suspected to potentially being able improve the overall sensitivity and linear response of the electrodes by reducing the interfacial capacitance.

Optimization of electrode response was achieved through patterning and functionalization of electrodes with increased exposed edges. After exposure to an ozone plasma, sensitivity was

found to increase with increased length. The charge transfer rate constant was also experimentally observed to increase after proper resistance correction.

Lastly, electrodes were used to detect dopamine in the presence of uric acid and ascorbic acid. Dopamine was detected as low as 0.1 μM, with a linear range between 10-250 μM. In the presence of uric acid and ascorbic acid, the signal was masked by the dominant responses of the latter, with only a small subtle peak observed when combined with 400 μM of uric acid.

As a continued effort to integrate graphene as a biosensing platforms, this work, as well as the solution-gated transistors integrated on chip, will be used towards detection of action potential from neuron cells found along myenteric plexus of the intestine.

APPENDIX A

A.1 Matlab Code for Cotrell Concentration Profiles

```
Do=.00001
x=[0:.00001:.003];
y0=erf(x/(2*sqrt(Do*0)));
y1=erf(x/(2*sqrt(Do*.001)));
y2=erf(x/(2*sqrt(Do*.01)));
y3=erf(x/(2*sqrt(Do*.1)));
y4=erf(x/(2*sqrt(Do*1)));
plot(x,y0);
hold
Current plot held
plot(x,y1,'red');
plot(x,y2,'green');
plot(x,y3,'magenta');
plot(x,y4,'cyan');
ylabel('C_o/C_o*')
xlabel('distance, x(cm)');
```

A.2 Matlab Code for Dispersion Relation of Graphene

```
lattice=1.42;
k_vec_x=linspace(-2*pi/(lattice),2*pi/(lattice),100);
k_vec_y=linspace(-2*pi/(lattice),2*pi/(lattice),100);
 [k_meshx, k_meshy]=meshgrid(k_vec_x,k_vec_y);
 t=3;
 energy_mesh=NaN([size(k_meshx,1),size(k_meshy,2),2]);
for a=1:size(k_meshx,1)
energy_mesh(:,a,1)=sqrt(4*t^2*((cos(k_meshy(:,a)/2*lattice).^2)+cos(sqrt(3)/2*k_meshx(:,a)*lat
tice).*cos(k_meshy(:,a)/2*lattice))+1/4);
energy_mesh(:,a,2)=-
sqrt(4*t^2*((cos(k_meshy(:,a)/2*lattice).^2)+cos(sqrt(3)/2*k_meshx(:,a)*lattice).*cos(k_meshy(
:,a)/2*lattice))+1/4);
end
surf(k_meshx, k_meshy,real(energy_mesh(:,:,1)))
hold
Current plot held
surf(k_meshx, k_meshy,real(energy_mesh(:,:,2)))
```

A.3 Matlab Code for Density of States of Graphene

```
%energy t
 t=1.0;

maxE=5*1;
deltaE=1e-3;
Energy=-maxE:deltaE:maxE;
dimE=size(Energy,2);

%The DOS(y-axis) set to 0
DOS=zeros(size(Energy));

%k-point sampling density
keps=1E-2;
keps=1E-3;

%Number of sampled points (to be incremented)

n=0;
%loop over k-point gird
%points are using the special Monkhorst-pack grid
%in the irreducible BZ(1/8 of square)

for kx=keps/2:keps:pi

for ky=kx:keps:pi

%The energy at this point
E=-2*t*(cos(kx)+cos(ky));

%This line finds the enrgy bin in the Energy array
i=floor((E/maxE+1)/2*dimE)+1;

%Increment the bin associated with this energy
DOS(i)=DOS(i)+8;

%increment the point count
n=n+8;

end %ky

end %kx

%Divide total number of points samples
DOS=DOS/n;

plot(Energy,DOS);
xlabel('Energy [t]')
ylabel('Density of States [states per unit cell per t]');
```

REFERENCES

1. Rice, R. J.; McCreery, R. L. Quantitative Relationship between Electron Transfer Rate and Surface Microstructure of Laser-Modified Graphite Electrodes. *Anal. Chem.* **1989,** 61, 1637-1641.

2. Robinson, R. S.; Sternitzke, K.; McDermott, M. T.; McCreery, R. L. Morphology and Electrochemical Effects of Defects on Highly Oriented Pyrolytic Graphite. *J. Electrochem. Soc.* **1991,** 138, 2412-2418.

3. Cline, K. K.; McDermott, M. T.; McCreery, R. L. Anomalously Slow Electron Transfer at Ordered Graphite Electrodes: Influence of Electronic Factors and Reactive Sites. *J. Phys. Chem.* **1994,** 98, 5314-5319.

4. Banks, C. E.; Compton, R. G. Edge Plane Pyrolytic Graphite Electrodes in Electroanalysis: An Overview. *Anal. Sci.* **2005,** 21, 1263-1268.

5. Edwards, M. A.; Bertoncello, P.; Unwin, P. R. Slow Diffusion Reveals the Intrinsic Electrochemical Activity of Basal Plane Highly Oriented Pyrolytic Graphite Electrodes. *J. Phys. Chem. C* **2009,** 113, 9218-9223.

6. Wang, J.; Yang, S.; Guo, D.; Yu, P.; Li, D.; Ye, J.; Mao, L. Comparative Studies on Electrochemical activity of Graphene Nanosheets and Carbon Nanotubes. *Electrochem. Comm.* **2009,** 11, 1892-1895.

7. Jean-Noel Fuchs and Mark Oliver Goerbig, Introduction to the Physical Properties of Graphene, *Lecture Notes 2008*, Université Paris-Sud.

8. Kissenger, P.T.; Heineman, W.R. Eds. **1996**. *Laboratory Techniques in Electroanalytical Chemistry*. 2nd Ed., Marcel Dekker, New York.

9. Wang, J. (Ed.). **2000**. *Analytical Electrochemistry*. Wiley-VCH Pub., New York.

10. Smyth, M.R.; Vos, J.G. (Eds). **1992**. *AnalyticalVoltammetry*. Vol.XXVII, Elsevier Science Pub., Amsterdam.

11. Kh., Neyman, E *Electroanalytical Stripping Methods*. Vol. 26, (Series Ed. J.D. Winefordner) John Wiley & Sons, New York NY **1993**.

12. Wang, J. (Ed). *Electroanalytical Chemistry*. 3rd Ed., Wiley-VCH Pub., New Jersey **2006**.

13. Wang, J.; Lu, J.; Hocevar, S.; Farias, P.; Ogorevc, B. *Anal. Chem*., **2000**, *72*, 3218.

14. Uslu, B.; Ozkan, S.A. *Anal. Lett*., **2007**, *40*, 817.

15. McCreery, Richard. *Chem Review* **2008**, 108, 2646-2687

16. Wightman, R. M. *Science*, **2006**, 311, 1570–1574

17. Hutton, H. D.; Huang, W.; Alsmeyer, D.; Kometani, J.; McCreery, R. L.; Neenan, T.; Callstrom, M. R. *Chem. Mater.* **1993**, *5*, 1110.

18. Iwasita, T.; Schmickler, W. *Ber. Bunsen-Ges.* **1985**, *89*, 138–42.

19. Royea, W. J.; Hamann, T. W.; Brunschwig, B. S.; Lewis, N. S. *J. Phys. Chem. B* **2006**, *110*, 19433–19442.

20. Hutton, H. D.; Alsmeyer, D. C.; McCreery, R. L.; Neenan, T. X.; Callstrom, M. *Polym. Mater. Sci. Eng.* **1992**, *67*, 237.

21. Novoselov, K. S. *et al. Science* 306, 666-669

22. Radushkevich LV, Lukyanovich VM. O struktkture ugleroda, obrazujucegosja pri termiceskom razlozenii okisi ugleroda na zeleznom kontakte. Zurn Fisic Chim **1952**; 26:88-95.

23. Iijima, S. *Nature*, **1991**, *354*, 56.

24. (a) P. R.Wallace, *Phys. Rev.*, 1947, 71, 622–634; (b) D. R. Dreyer, R. S. Ruoff and C. W. Bielawski, Angew. *Chem., Int. Ed.,* **2010,** 49, 9336–9344; (c) A. K. Geim, *Phys. Scr*., 2012, 2012, 014003.

25. Novoselov, K. S. *et al.,* Two-dimensional gas of massless Dirac fermions in graphene. *Nature* 438, 197-200 (**2005**).

26. Zan *et al.* Atomic Structure of Graphene and h-BN Layers and Their Interactions with Metals Nanotechnology and Nanomaterials. Advances in Graphene Science, book edited by Mahmood Aliofkhazraei, ISBN 978-953-51-1182-5, Published: July 31, **2013**.

27. Berger C, Song Z, Li X, Wu X, Brown N, Naud C, Mayou D, Li T, Hass J, Marchenkov A N, Conrad E H, First P N, and de Heer W A, **2006**, *Science* 312 1191

28. Ohta T, Bostwick A, Seyller T, Horn K and Rotenberg E, **2006**, *Science* 313 951

29. Riedl C, Starke U, Bernhardt J, Franke M and Heinz K, **2007**, *Phys. Rev.* B 76 245406

30. Emtsev K V, Bostwick A, Horn K, Jobst J, Kellogg G L, Ley L, McChesney J L, Ohta T, Reshanov S A, Rotenberg E, Schmid A K, Waldmann D, Weber H B and Seyller T, **2009**, *Nature Materials* 8 203

31. Lin Y-M, Dimitrakopoulos C, Jenkins K A, Farmer D B, Chiu H-Y, Grill A, Avouris P, **2010**, *Science* 327 662

32. van Bommel A J, Crombeen J E and van Tooren A, **1975,** *Surf. Sci.* 48 463

33. Forbeaux I, Themlin J-M and Debever J-M **1998** *Phys. Rev.* B 58 16396

34. Virojanadara C, SyvÄajarvi M, Yakimova R, Johansson L I, Zakharov A A and Balasubramanian, T, **2008** *Phys. Rev. B* 78 245403

35. Gierz I, Riedl C, Starke U, Ast C R and Kern K **2008** *Nano Letters* 8 4603

36. Coletti C, Riedl C, Lee D-S, Krauss B, Klitzing K v, Smet J and Starke U **2010** *Phys. Rev.* B 81 235401

37. Riedl C, Coletti, C, Iwasaki, T, Zakharov A A and Starke U **2009** *Phys. Rev. Lett.* 103 246804

38. A. Dahal and M. Batzill, *Nanoscale*, **2014**, 6, 2548-2562

39. X. Li, W. Cai, J. An, S. Kim, J. Nah, D. Yang, R. Piner, A. Velamakanni, I. Jung, E. Tutuc, S. K. Banerjee, K. Sanjay, L. Colombo and R. S. Ruo, *Science* **2009**, 324, 1312-1314.

40. S. Goranthia *et al*, *Nanoscale*, Volume 6, Issue 2, p. 889.

41. http://www.aps.org/publications/apsnews/200605/graphene.cfm

42. Aniruddha Konar, Tian Fang, and Debdeep Jena, *Phys Rev Lett*. B 82 **2010** 115452

43. *D Jena,* A. *Konar,* E. H. Hwang, S. Adam and S. Das Sharma, *Phys. Rev. Lett.* 98, 186806 (**2007**)

44. Chen *et al*., *Nature Nanotechnology*, Vol. 3, April **2008**

45. Novoselov, K. S. *et al.* Proc. Natl Acad. Sci. USA 102, 10451-10453

46. Das Sarma, S. & Hwang, E. H. ***(2003)*** *Phys. Rev. B 68(19), 195315–195324.*

47. Gardiner, D.J. (1989). *Practical Raman spectroscopy*. Springer-Verlag. ISBN 978-0-387-50254-0.)

48. A. Ferrari and D. Basko,, Nature Nanotechnology 8, 235–246 (**2013**)

49. (a)M. S. Goh and M. Pumera, Anal. Chem., 2010, 82, 8367–8370; (b) M. S. Goh and M. Pumera, *Anal. Bioanal. Chem.,* **2011**, 399, 127–131.

50. T. J. Davies, M. E. Hyde and R. G. Compton, *Angew. Chem., Int. Ed.,* **2005**, 44, 5121–5126.

51. T. J. Davies, R. R. Moore, C. E. Banks and R. G. Compton, *J. Electroanal. Chem.,* **2004**, 574, 123–152.

52. C. E. Banks and R. G. Compton, *Analyst*, **2006**, 131, 15–21.

53. (a) M. A. Edwards, P. Bertoncello and P. R. Unwin, J. Phys. Chem. C, **2009**, 113, 9218–9223; (b) C. G. Williams, M. A. Edwards, A. L. Colley, J. V. Macpherson and P. R. Unwin, Anal. Chem., **2009**, 81, 2486–2495; (c) S. C. S. Lai, A. N. Patel, K. McKelvey and P. R. Unwin. *Angew. Chem.,* Int. Ed., **2012**, 51, 5405–5408.

54. Melina Blees, *APS March Meeting 2014*, Volume 59, Number 1, March 3–7, **2014**; Denver, Colorado, Abstract ID: BAPS.2014.MAR.L30.11

55. Yuan *et al.* Scientific Reports 3, Article number: 2248

56. Davies, T. J., Hyde, M. E. & Compton, R. G. Nanotrench arrays reveal insight into graphite electrochemistry. Angew, Chem.-Int. Edit. 44, 5121–5126 (**2005**).

57. Pumera, M., Ambrosi, A., Bonanni, A., Chng, E. L. K. & Poh, H. L. Graphene for electrochemical sensing and biosensing. TrAC, Trends Anal. Chem. 29, 954–965 (**2010**)

58. Banerjee, S. *et al.* Electrochemistry at the edge of a single graphene layer in a nanopore. ACS Nano 7, 834–843 (**2012**).

59. Brownson, D. A. C. & Banks, C. E. CVD graphene electrochemistry: the role of graphitic islands. Phys. Chem. Chem. Phys. 13, 15825–15828 (**2011**)

60. Banks, C. E., Davies, T. J., Wildgoose, G. G. & Compton, R. G. Electrocatalysis at graphite and carbon nanotube modified electrodes: edge-plane sites and tube ends are the reactive sites. Chem. Commun. 829–841 (**2005**)

61. Anne, A. S., Cambril, E., Chovin, A., Demaille, C. & Goyer, C. D. Electrochemical atomic force microscopy using a tip-attached redox mediator for topographic and functional imaging of nanosystems. ACS Nano 3, 2927–2940 (**2009**).

62. Patel, A. N. *et al.* A New View of Electrochemistry at Highly Oriented Pyrolytic Graphite. J. Am. Chem. Soc. 134, 20117–20130 (**2012**).

63. Brownson *et al.*, *Chem. Soc. Rev.*, **2012**, 41, 6944–6976

64. M. C. Henstridge, E. Laborda, N. V. Rees and R. G. Compton, *Electrochim. Acta*, **2011**.

65. R. Nissim, C. Batchelor-McAuley, M. C. Henstridge andR. G. Compton, *Chem. Commun.*, **2012**, 48, 3294–3296.

66. (a) N. M. R. Peres, L. Yang and S.-W. Tsai, New J. Phys., 2009, 11, 095007; (b) R. L. McCreery and M. T. McDermott, *Anal. Chem.*, **2012**, 84, 2602–2605.

67. D. Jiang, B. G. Sumpter and S. Dai, *J. Chem. Phys*., **2007**,126, 134701.

68. M. Pumera, *Chem. Soc. Rev.*, **2010**, 39, 4146–4157.

69. Y. Shimomura, Y. Takane and K. Wakabayashi, *J. Phys. Soc. Jpn.*, **2011**, 80, 054710.

70. R. Sharma, J. H. Baik, C. J. Perera and M. S. Strano, *Nano Lett.*, **2010**, 10, 398–405

71. Valota, Anna. Electrochemical Behavior of Monolayer and Bilayer Graphene. *University of Manchester.*

72. T. J. Davies, R. R. Moore, C. E. Banks and R. G. Compton, *J. Electroanal. Chem*., **2004**, 574, 123–152.

73. C. E. Banks and R. G. Compton, Analyst, **2006**, 131, 15–21.

74. C. E. Banks, T. J. Davies, G. G. Wildgoose and R. G. Compton, *Chem. Commun.*, **2005**, 829–841.

75. K. R. Ward, N. S. Lawrence, R. S. Hartshorne and R. G. Compton, *Phys. Chem. Chem. Phys.*, **2012**, 14, 7264–7275.

76. T. J. Davies, M. E. Hyde and R. G. Compton, *Angew. Chem., Int. Ed*., **2005**, 44, 5121–5126.

77. Banks, C.E.; Compton, R.G. *Analyst*, **2006**, *131*, 15.

78. Mc Creery, R.L.; Cline, K.K., Carbon Electrodes. Kissenger, P.T.; Heineman, W.R.(Eds). **1996**. *Laboratory Techniques in Electroanalytical Chemistry*. 2nd Ed., Marcel Dekker, New York.

79. Bengi Uslu and Sibel A. Ozkan, *Combinatorial Chemistry & High Throughput Screening*, **2007**, *10*, 495-513

80. J. R. Stetter and G. J. Maclay, in *Advanced Micro and Nano Systems*, Vol. I, Chap. 10, p. 357.

81. C. C. Liu, P. Hesketh, and G. W. Hunter, *Electrochem. Soc. Interface,* 12(2), 22 (**2004**).

82. M. Madou, *Fundamentals of Microfabrication*, CRC Press, Boca Raton, FL (**1997**).

83. I. Lundstrom, M. S. Shivaraman, and C. M. Svensson, J. Appl. Phys., 46, 3876 (**1975**).

84. G. W. Hunter, C. C. Liu, D. B. Makel, in *MEMS Handbook*, Chap. 22, M. Gad-el-Hak, Editor, CRC Press LLC, Boca Raton, FL (**2001**).

85. G. W. Hunter, L. Chen, P. G. Neudeck D. Makel, C. C. Liu, Q. H. Wu, and D. Knight, Tech. Rep. 34th AIAA/ASME/ SAE/ASEE Joint Propulsion Conference, Cleveland, OH (**1998**)

86. *Exner et al. , ACS Appl. Mater. Interfaces*, **2013**, 5 (5), pp 1575–1582.

87. Sanseep K, Vashist, A Review of Microcantilevers for Sensing Application, *Open Access Rewards System*, June 18, **2007**

88. Joseph R. Stetter, William R. Penrose, and Sheng **Yao** *Journal of The Electrochemical Society*, **150** (2) S11-S16 (**2003**)

89. Z. Cao, W. J. Buttner, and J. R. Stetter, *Electroanalysis*, **4**, 253 (**1992**).

90. Yang M, *et al.*, (**2011**), Site - Specific Immobilization of Gold Binding Polypeptide on Gold Nanoparticle - Coated Graphene Sheet for Biosensor Application, *Nanoscale*, 3: 2950-2956.

91. Ahmadalinezhad A., Wu G. S., and Chen A. C., (**2011**), Mediator-free electrochemical biosensor based on buckypaper with enhanced stability and sensitivity for glucose detection, *Biosensors & Bioelectronics*, 30: 287-293.

92. Yehezkeli O, Tel-Vered R, Reichlin S, and Willner I, (**2011**), Nano - Engineered Flavin -Dependent Glucose Dehydrogenase / Gold Nanoparticle - Modified Electrodes for Glucose Sensing and Biofuel Cell Applications, *ACS Nano*, 5: 2385-2391.

93. Wipawakarn P, Ju HX, and Wong DKY, (**2012**), A Label - Free Electrochemical DNA Biosensor Based on a Zr(IV) - Coordinated DNA Duplex Immobilised on a Carbon Nanofibre Chitosan Layer, *Analytical and Bioanalytical Chemistry*, 402: 2817-2826.

94. Lahiff E, *et al.*, (**2010**), The Increasing Importance of Carbon Nanotubes and Nanostructured Conducting Polymers in Biosensors, *Analytical and Bioanalytical Chemistry*, 398: 1575-1589.

95. Ansari S. A. and Husain Q., (**2012**), Potential applications of enzymes immobilized on/in nano materials: A review, Biotechnology Advances, 30: 512-523.

96. Xiao Y, *et al.*, (**2003**), "Plugging into Enzymes": Nanowiring of Redox Enzymes by a Gold Nanoparticle, Science, 299: 1877-1881.

97. Zayats M, Willner B, and Willner I, (**2008**), Design of Amperometric Biosensors and Biofuel Cells by the Reconstitution of Electrically Contacted Enzyme Electrodes, *Electroanalysis*, 20: 583-601.

98. Sia SK and Chin CD, (**2011**), Analytical Chemistry: Sweet Solution to Sensing, *Nature Chemistry*, 3: 659-660.

99. S. Yao, Y. Shimizu, N. Miura, and N. Yamazoe, *Chem. Lett.*, **1990**, 2033.

100. Shang F, *et al.*, (**2009**), Selective Nanomolar Detection of Dopamine Using a Boron-Doped Diamond Electrode Modified with an Electropolymerized Sulfobutylether - β - Cyclodextrin - Doped Poly (N - Acetyltyramine) and Polypyrrole Composite Film, *Analytical chemistry*, 81: 4089-4098.

101. Yan J, *et al.*, (**2008**), An Electrochemical Sensor for 3, 4 - Dihydroxyphenylacetic Acid with Carbon Nanotubes as Electronic Transducer and Synthetic Cyclophane as Recognition Element, *Chemical Communications*: 4330-4332.

102. Cremer M, (**1906**), Über die Ursache der elektromotorischen Eigenschaften der Gewebe, zugleich ein Beitrag zur Lehre von den polyphasischen Elektrolytketten, Zeitschrift fur Biologie, 47: 562 - 608.

103. Haber F and Klemensiewicz Z, (**1909**), Über elektrische Phasengrenzkräfte Zeitschrift für *Physikalische Chemie*, 67: 385 - 431.

104. Lubert KH and Kalcher K, (**2010**), History of Electroanalytical Methods, *Electroanalysis*, 22: 1937-1946.

105. Petr Zuman and Philip J. Elving, *J. Chem. Educ.*, **1960**, 37 (11), p 562.

106. Hickling, A. (**1942**). "Studies in electrode polarisation. Part IV.-The automatic control of the potential of a working electrode". *Transactions of the Faraday Society* **38**: 27–33

107. Clark LC, (**1956**), Monitor and Control of Blood and Tissue Oxygen Tensions, *Transactions American Society for Artificial Internal Organs*, 2: 41-46.

108. Clark LC and Lyons C, (**1962**), Electrode Systems for Continuous Monitoring in Cardiovascular Surgery, *Annals of the New York Academy of Sciences*, 102: 29-45.

109. Hu CG *et al.*, (**2012**), Inkjet Printing of Nanoporous Gold Electrode Arrays on Cellulose Membranes for High-Sensitive Paper-Like Electrochemical Oxygen Sensors Using Ionic Liquid Electrolytes, *Analytical Chemistry*, 84: 3745-3750.

110. Aoife C. Power and Aoife Morrin, *Electroanalytical Sensor Technology*, Chapter 7

111. Vire, J.C.; Kauffmann, J.M. *Curr. Top. Electrochem.*, **1994**, *3*, 493.

112. Janata, J. *Chem. Rev*., **1990**, *90*, 691.

113. Vytras, K. *J. Pharm. Biomed. Anal*., **1989**, *7*, 789.

114. Kulapina, E.G.; Barinova, O.V. *Pharm. Chem. J.*, **1997**, *31*, 667.

115. Bakker, E.; Pretsch, E. *Trends Anal. Chem.*, **2001**, *20*, 11.

116. Bakker, E.; Pretsch, E.; Buhlmann, P. *Anal. Chem*., **2000**, *72*, 1127.

117. Yukinori, T.; Yoshio, U. *Sensor Lett.*, **2005**, *3*, 99.

118. Wang, J. (Ed). *Electroanalytical Chemistry*. 3rd Ed., Wiley-VCH Pub., New Jersey **2006**

119. Alexandre Brolo, Nature Photonics 6, 709–713 (**2012**)

120. J.H.T. Luong and G.G. Guilbault, "Analytical Applications of Piezoelectric Crystal Biosensors," *Biosensor Principles and Applications,* ed. L.J. Blum and P.R. Coulet (New York: Marcel Dekker (**1991**), pp. 107-138.

121. G.G. Guilbault, "Detection of Formaldehyde with an Enzyme-Coated Piezoelectric Crystal Detector," *Anal. Chem.*, 55 (**1983**), pp. 1682-1684.

122. J. Ngeh-Ngwainbi *et al.*, "Parathion Antibodies on Piezoelectric Crystals," *J. Am. Chem. Soc.*, 108 (**1986**), pp. 5444-5447.

123. G.G. Guilbault, B. Hock, and R. Schmid, "A Piezoelectric Immunobiosensor for Atrazine in Drinking Water," *Biosensors Bioelectronics,* 7 (**1992**), pp. 411-420.

124. M. Minunni, P. Skladal, and M. Mascini, "A Piezoelectric Quartz Crystal Biosensor for Atrazine," *Life Chemistry Reports*, 11 (**1994**), p. 391.

125. M. Minunni, P. Skladal, and M. Mascini, "A Piezoelectric Quartz Crystal Biosensor as a Direct Affinity Sensor," *Anal. Lett.*, 27 (**1994**), p. 1475.

126. K. Nakanishi *et al.*, "Detection of the Red Tide-Causing Plankton Alexandrium Affine by a Piezoelectric Immunosensor Using a Novel Method of Immobilizing Antibodies," *Anal. Lett.*, 29 (**1996**), pp. 1247-1258.

127. M.Minunni, P. Skladal, and M. Mascini, "A Piezoelectric Quartz Crystal Biosensor as a Direct Affinity Sensor," *Anal. Lett.*, 27 (**1994**), pp. 1475-1487.

128. Taylor RF, Marenchic IG, Cook EJ. *Anal. Chim. Acta*. **1988**; 213:131.

129. Bontidean I, Berggren C, Johansson G, Csoregi E, Mattiasson B, Lloyd JA, Jakeman KJ, Brown NL. *Anal. Chem*. **1998**;70:4162.

130. Yin F. Anal. Lett. **2004**;37:1269.

131. Hleli S, Martelet C, Abdelghani A, Burais N, Jaffrezic-Renault N. *Sens. Actuators, B.* **2006**;113:711.

132. Yang LJ, Li YB, Griffis CL, Johnson MG. *Biosens. Bioelectron.* **2004**;19:1139.

133. Radke SM, Alocilja EC. *IEEE Sens. J.* **2005**;5:744.

134. K'Owino IO, Sadik OA. *Electroanalysis*. **2005**;17:2101.

135. Mishra NN, Retterer S, Zieziulewicz TJ, Isaacson M, Szarowski D, Mousseau DE, Lawrence DA, Turner JN. Biosens. Bioelectron. **2005**; 21:696.

136. Stelzle M, Weissmuller G, Sackmann E. J. Phys. Chem. **1993**; 97:2974.

137. Knoll W, Yu F, Neumann T, Schiller S, Naumann R. *Phys. Chem. Chem. Phys.* **2003**; 5:5169.

138. Xian Huang, Siqi Li, Erin Davis, Dachao Li, Qian Wang, and Qiao Lin, J *Microelectromech Syst.* Jun 20, **2013**; 23(1): 14–20

139. Allen J. Bard and Larry R. Faulkner , *Electrochemical Methods: Fundamentals and Application, Wiley*; 2 edition (December 18, **2000**)

140. Li *et al.*, ACS Nano. **2011** Mar 22;5(3):2264-70.

141. Morrin A, (**2012**), Inkjet Printed Electrochemical Sensors, In Korvink JG, *et al.*, *Inkjet-based Micromanufacturing*, Wiley-VCH: 295-309.

142. Newman JD and Turner APF,Home Blood Glucose Biosensors: A Commercial Perspective, *Biosensors & Bioelectronics* (**2005**), 20: 2435-2453.

143. Zhong HA, *et al.*, Non - Enzymatic Hydrogen Peroxide Amperometric Sensor Based on a Glassy Carbon Electrode Modified with an MWCNT / Polyaniline Composite Film and Platinum Nanoparticles, *Microchimica Acta*, (**2012**), 176: 389-395.

144. Guo YJ, Guo SJ, Fang YX, and Dong SJ, (**2010),** Gold nanoparticle/carbon nanotube hybrids as an enhanced material for sensitive amperometric determination of tryptophan, *Electrochimica Acta*, 55: 3927-3931.

145. Masawat, P.; Slater, J.M. *Sens. Actuators B*, **2007** (in press).

146. Codognoto, L.; Winter, E.; Paschoal, J.A.R.; Suffredini H.B.; Cabral M.F.; Machado, S.A.S.; Rath, S. *Talanta*, **2007**, *72*, 427.

147. Wang, X.; Yang, N.; Wan, Q. *Electrochim. Acta,* **2006**, *52*, 361.

148. Yang, N.; Wan, Q.; Wang, X. *Electrochim. Acta,***2005**, *50*, 2175.

149. Zhang, X.H.; Wang, S.F. *Sens. Actuators B*, **2005**, *104*, 29.

150. Charoenraks, T.; Palaharn, S.; Grudpan, K.; Siangproh, W.; Chailapakul, O. *Talanta*, **2004**, *64*, 1247.

151. Mohammadi, H.; Amine, A.; El Rhazi, M.; Brett, C.M.A. *Talanta,* **2004**, *62*, 951.

152. Palaharn, S.; Charoenraks, T.; Wangfuengkanagul, N.; Grudpan, K.; Chailapakul, O. *Anal. Chim. Acta*, **2003**, *499*, 191.

153. Parham, H.; Zargar, B. *Talanta*, **2001**, *55*, 255.

154. Hernandez-Olmos, M.A.;Agüi, L.; Yanez-Sedeno, P.; Pingarron, J.M. *Electrochim. Acta*, **2000**, *46*, 289.

155. Munoz, R.A.A.; Matos, C.M.; Angnes, L. *Talanta*, **2001**, *55*, 855.

156. Tapsoba, I.; Belgaied, J.-E.: Boujlel, K. *J. Pharm. Biomed. Anal*., **2005**, *38*, 162

157. Adhoum, N.; Monser, L.; Toumi, M.; Boujlel, K. *Anal. Chim. Acta,* **2003**, *495*, 69.

158. Altıokka, G. *J. Pharm. Biomed. Anal*., **2001**, *25*, 387.

159. Dogrukol-Ak, D.; Zaimoglu, V.; Tunçel, M. *European J. Pharm. Sci.*, **1999**, *7*, 215.

160. Abulkibash, A.M.S.; Koken, M.E.; Khaled, M.M.; Sultan, S.M. *Talanta,* **2000**, *52,* 1139.

161. Biryol, I.; Ozkan, S.A. *J. Pharm. Biomed. Anal*., **1997**, *15*, 1695.

162. Sentürk, Z.; Ozkan, S.A.; Uslu, B.; Biryol, I. *J. Pharm. Biomed.Anal.*, **1996**, *15*, 365.

163. Uslu, B.; Biryol, I. *STP Pharma. Sci.*, **1997**, *7*, 248.

164. Goyal, R.N.; Gupta, V.K.; Oyama, M.; Bachheti, N. *Talanta*, **2007**

165. Goyal, R.N.; Gupta, V. K.; Oyama, M.; Bachheti, N. *Electrochem. Commun*., **2006**, *8*, 65

166. Buckshire, Melissa *An Overview of Carbon Fiber Electrodes Used in Neurochemical Monitoring.* Master's Thesis, University of Pittsburgh (**2008**).

167. Wang, J. (Ed). *Electroanalytical Chemistry*. 3rd Ed., Wiley-VCH Pub., New Jersey **2006**.

168. Kinoshita, K. *Carbon: Electrochemical and Physicochemical Properties*, Wiley-VCH Pub, New York.

169. Li, M.X.; Li, N.Q.; Gu, Z.N.; Sun, Y.L.; Wu, Y.Q. *Anal.Chim.Acta*, **1997**, *356*, 225.

170. Wang, C.; Li, C.; Ting, L.; Xu, X.; Wang, C. *Microchim. Acta*, **2006**, 152, 233.

171. Gao, M.; Dai, L.; Wallace, G.G. *Electroanalysis*, **2002**, 15, 1089.

172. Merkoci, A. *Microchim. Acta*, **2006**, *152*, 157.

173. He, P.; Xu, Y.; Fang, Y. *Microchim. Acta*, **2006**, *152*, 175.

174. Wang, J. *Electroanalysis*, **2005**, *17*, 7.

175. Cortujo-Antuna, J.L.; Martinez-Montequin, S.; Fernandez-Abedul, M.T.; Costa-Garcia, A. *Electroanalysis,* **2003**, *15*, 773.

176. Avand, M.; Sohrabnezhad, S.; Mousavi, M.F.; Shamsipur, M.; Zanjanchi, M.A. *Anal. Chim. Acta* **2003**, *491*, 193.

177. Kotkar, R.M.; Srivastava, A.K. *Sens. Actuators B.*, **2006**, *119*, 524.

178. Bezerra, V.S.; Lima Filho, J.L.; Montenegro, M.C.B.S.M.; Araujo, A.N.; Silva, V.L. *J. Pharm. Biomed. Anal*., **2003**, *33*, 1025.

179. Ozkan, S.A.; Dogan, B.; Uslu, B. *Microchim. Acta*, **2006**, *153*, 27.

180. Torriero, A.A.J.; Ruiz-Diaz J.J.J.;Salinas, E.; Marcevsky, E.J.;Sanz, M.I.; Raba, J. *Talanta* **2006**, *69*, 691.

181. Goyal, R.N.; Singh, S.P. *Talanta*, **2006**, *69*, 932.

182. Thangamutlu, R.; Kumar, S.M.S.; Pillai, K.C. *Sens. Actuators B*, **2007**, *120*, 745.

183. Sarada, B.V.; Rao, T.N.; Tryk, D.A.; Fujishima, A. *Anal. Chem*, **2000**, *72*, 1632.

184. Marken, F.;Paddon, C.A.; Asogan, D. *Electrochem.Commun*., **2002**, *4*, 62.

185. Suffredini, H.B.; Santos, M.C.; De Souza, D.; Codognoto, L.; Homem-de-Mello, P.; Honorio, K.M.; Silva, A.B.F.; Machado, S.A.S.; Avaca, L.A. *Anal. Lett.* **2005**, *38*, 1587.

186. Ozkan, D.; Karadeniz, H.; Erdem, A.; Macsini, M.; Ozsoz, M. *J. Pharm. Biomed. Anal.*, **2004**, *35*, 905.

187. Chen, J.C.; Kumar, A.S.; Chung, H.H.; Chien, S.H.; Kuo, M.C.; Zen, J.M. *Sens. Actuators B*,**2006**, *115*, 473.

188. Goyal, R.N.; Gupta, V.K.; Sangal, A.; Bachheti, N. *Electroanalysis*, **2005**, *17*, 2217.

189. Stefan-van Staden, RI.; Lal, B.; Holo, L. *Talanta*, **2006**, *71*, 1434.

190. P.J.; Santhanam, K.S.V.; Ajayan, P.M. *Bioelectrochem. Bioenergetics*, **1996**, 41, 121.

191. Gao, W.; Song, J.; Wu, N. *J. Electroanal. Chem.*, **2005**, 576, 1.

192. Zhang, J.D.; Oyama, M. *Microchem. J*., **2004**, 78, 217.

193. Hwang et al., *ACS Nano*, **2013**, 7 (1), pp 385–395

194. K. V. Emtsev, A. Bostwick, K. Horn, J. Jobst, G. L. Kellogg, L. Ley, J. L. McChesney, T. Ohta, S. A. Reshanov, J. Ŕohrl, E. Rotenberg, A. K. Schmid, D. H. Waldmann, B. Weber and Th. Seyller, *Nat. Mater*., **2009**, 8, 203–207.

195. Hu *et al*., *Carbon*, Volume 50, Issue 1, January **2012**, Pages 57–65

196. S. Russo et al., *Physica E: Low-dimensional Systems and Nanostructures*, Volume 42, Issue 4, p. 677-679.

197. Ke Wang, *A Carbon Nanotube Microelectrode array for Neural stimulation*, Dissertation, Stanford University, **2006**, p. 43.

198. Randin, J.P. and E. Yeager, Differential capacitance study of stress-annealed pyrolytic graphite electrodes. *Journal of the Electrochemical Society*, **1971**. 118(5): p.711-14.

199. Randin, J.P. and E. Yeager, Differential Capacitance Study On Basal Plane Of Stress-Annealed Pyrolytic-Graphite. Journal of *Electroanalytical Chemistry*, **1972**. 36(2): p. 257-&.

200. Dankerl *et al.*, *Adv. Funct. Mater*. **2010**, 20, 3117-3124.

201. Hess *et. a., Applied Phys. Let.* 99, 033503 (**2011**).

202. Nicholson *et al., Anal. Chem.Vol.* 37, No. 11, Oct. **1965**

203. Wightman, R.M., May, L.J., Michael, A.C., **1988**. *Anal. Chem*. 60, 769A–779A.

204. http://www.news-medical.net/health/Dopamine-Functions.aspx

205. Park, Y.H., Zhang, X., Rubakhin, S.S., Sweedler, J.V., **1999**. *Anal. Chem*. 71, 4997–5002.

206. Carrera, V., Sabater, E., Vilanova, E., Sogorb, M.a., **2007**. *J. Chromatogr. B* 847, 88–94.

207. Kong, B., Zhu, A., Luo, Y., Tian, Y., Yu, Y., Shi, G., **2011**. *Angew. Chem. Int. Ed*. 123, 1877–1880.

208. Lin, Y., Chen, C., Wang, C., Pu, F., Ren, J., Qu, X., **2011**. *Chem. Commun*. 47, 1181–1183.

209. Njagi, J., Chernov, M.M., Leiter, J.C., Andreescu, S., **2010**. *Anal. Chem*. 82, 989–996.

210. Strawbridge, S.M., Green, S.J., Tucker, J.H.R., **2000**. *Chem. Commun*., 2393–2394.

211. Wu, W.Z., Huang, W.H., Wang, W., Wang, Z.-L., Cheng, J.-K., Xu, T., Zhang, R.-Y., Chen, Y., Liu, J., 2005. *J. Am. Chem. Soc*. 127, 8914–8915.

212. Chet *et al., Bioelectrochemistry.* **2009** Apr;75(1):26-31.

213. Liu *et al., Biosensors and Bioelectronics,* 23 (**2008**) 1488–1495

214. Sheng *et al., Biosensors and Bioelectronics* 34 (**2012**) 125– 131

215. M. Hadi anf A. Rouhollahi, *Analytica Chimica Acta* 721 (**2012**) 55– 60.

216. http://www.asdlib.org/onlineArticles/ecourseware/Kelly_Potentiometry/PDF-16-WorkingElec.pdf